

## REPORT DOCUMENTATION PAGE

Public reporting burden for this collection of information is estimated to average 1 hour per response, including the time for reviewing instructions, searching existing data sources, gathering and maintaining the data needed, and completing and reviewing this collection of information. Send comments regarding this burden estimate or any other aspect of this collection of information, including suggestions for reducing this burden, to Washington Headquarters Services, Directorate for Information Operations and Reports (0704-014302). Respondents should be aware that notwithstanding any other provision of law, no person shall be subject to any penalty for failing to comply with a collection of information if it does not have a valid OMB control number. PLEASE DO NOT RETURN YOUR FORM TO THE ABOVE ADDRESS.

AFRL-SR-AR-TR-02-

0262

e  
g  
itly

1. REPORT DATE (DD-MM-YYYY) July 26, 2002		2. REPORT TYPE Final		3. DATES COVERED (From - To) 9/01/1995 to 12/31/2001	
4. TITLE AND SUBTITLE Large Area Inspection of Aircraft Structures Using Vibrational Nondestructive Evaluation Methods				5a. CONTRACT NUMBER	
				5b. GRANT NUMBER F49620-95-1-0518	
				5c. PROGRAM ELEMENT NUMBER	
6. AUTHOR(S) Roberto A. Osegueda and Carlos M. Ferregut				5d. PROJECT NUMBER	
				5e. TASK NUMBER	
				5f. WORK UNIT NUMBER	
7. PERFORMING ORGANIZATION NAME(S) AND ADDRESS(ES) FAST Center for Structural Integrity of Aerospace Systems The University of Texas at El Paso Burges Hall, Room 206 El Paso, Texas 79968				8. PERFORMING ORGANIZATION REPORT 20020903 049	
9. SPONSORING / MONITORING AGENCY NAME(S) AND ADDRESS(ES) US Air Force of Scientific Research/NM 801 North Randolph St. Arlington, VA 22203-1977				10. SPONSOR/MONITOR'S ACRONYM(S) AFOSR	
				11. SPONSOR/MONITOR'S REPORT NUMBER(S)	
12. DISTRIBUTION / AVAILABILITY STATEMENT Approved for public release; distribution unlimited.					
13. SUPPLEMENTARY NOTES					
14. ABSTRACT The research work performed on the development of vibrational nondestructive evaluation methods to infer damage over a large area of aircraft structures using laser Doppler Velocimeter accompanied with data fusion techniques is documented. The Vibrational methods rely on the response characteristics before and after damage. Damage is reflected in changes in the vibrational characteristics which are used to quantify modal strain energy differences between the structure in the damaged and healthy states. These differences provide features that can be used to localize and quantify the damage. The collection set of modal strain energy differences for the available modes are combined using averaging and data fusion techniques to provide damage indicators. The Vibrational and fusion methodologies were developed and refined considering a series of controlled damage experiments on simple beams, a stiffened plate panel, a vertical stabilizer assembly, and a stiffened shell specimen. Modal vibration tests were conducted on these test objects using conventional accelerometers and/or a laser Doppler Velocimeter to obtain their dynamic characteristics before and after inflicted on controlled damage. Damage evaluation results are documented for each case in this report. The methods developed seem to have a major potential to detect defects that cause a stiffness change in hidden members or members deep inside aircraft structures without disassembly.					
15. SUBJECT TERMS Aircraft Structures, Global Vibrational NDE, Damage Detection, Large Area NDE					
16. SECURITY CLASSIFICATION OF:			17. LIMITATION OF ABSTRACT	18. NUMBER OF PAGES	19a. NAME OF RESPONSIBLE PERSON
a. REPORT Unclassified	b. ABSTRACT Unclassified	c. THIS PAGE Unclassified	Unclassified	186	Roberto Osegueda
					19b. TELEPHONE NUMBER (include area code) (915) 747-7891

# **LARGE AREA INSPECTION OF AIRCRAFT STRUCTURES USING VIBRATIONAL NONDESTRUCTIVE EVALUATION METHODS**

**A Final Report**

**Grant No. F49620-95-1-0518**

**Prepared by**

**Roberto A. Osegueda**

**Carlos M. Ferregut**

**FAST Center for Structural Integrity of Aerospace Systems**

**The University of Texas at El Paso**

**Burges Hall, Room 206**

**El Paso, Texas 79968**

# **FAST**

**Center for Structural  
Integrity of Aerospace Systems**

**Submitted to**

**US Air Force of Scientific Research/NM**

**801 North Randolph St.**

**Arlington, VA 22203-1977**

**Program Manager: Dr. Spencer Wu**

**July 26, 2002**

# **LARGE AREA INSPECTION OF AIRCRAFT STRUCTURES USING VIBRATIONAL NONDESTRUCTIVE EVALUATION METHODS**

## **EXECUTIVE SUMMARY**

This report documents the research work performed on the development of vibrational nondestructive evaluation methods to infer damage over a large area of aircraft structures using laser Doppler Velocimeter accompanied with data fusion techniques to process the modal information before and after damage. Vibrational NDE for damage detection and assessment rely on experimental modal analysis testing to obtain the response characteristics before and after damage. Since damage causes changes in the structural stiffness, it is reflected in changes in the vibrational characteristics that can be measured. The vibrational NDE methods considered are based on quantifying modal strain energy differences between the structure in a damaged state and a healthy state. From structural mechanics relationships, the differences in the strain energy can be evaluated using the measured modal shapes. Damage in an element causes changes in the modal shapes in the vicinity of or at the location of damage. The damage location is indicated as an apparent strain energy increase. The damage detection formulation relies on the features of the differences of modal strain energy giving collection sets of modal strain energy differences for the available modes. The distribution of the normalized strain energy differences also provides the mechanism to extract probabilities in support of damage and no damage. The combination of information from each modal pair is then combined using data fusion techniques.

The Vibrational NDE and fusion methodologies were developed and refined considering a series of controlled damage experiments on simple beams, a stiffened plate panel, a vertical stabilizer assembly, and a stiffened shell specimen. Modal vibration tests were conducted on these test objects using conventional accelerometers and/or a laser Doppler Velocimeter to obtain their dynamic characteristics before and after controlled damage is inflicted. The data collected from the experiments served as the basis for the development of the methods documented here. The damage evaluation results are documented in this report.

The methods developed seem to have a major potential to detect defects that cause a stiffness change in hidden members or members deep inside aircraft structures without disassembly.

The following people participated in the work documented here as students.

### **Ph.D. Graduates**

Dr. Cesar Carrasco, Ph.D. graduate, Material Science and Engineering.

### **Master Level Graduates**

Raul Meza, Master of Science in Civil Engineering. (1996)

Luis Perez, Master of Science in Civil Engineering, (1997)

Leopoldo Pereyra, Master of Science in Civil Engineering (1998)

Gabriela Andre, Master of Science in Civil Engineering. (1999)

Murali Krishna, Master of Science in Computer Science (1999)

Sudhir Prabhu, Master of Science in Mechanical Engineering (1999)  
 Ravi Venugopalan, Master of Science in Electrical Engineering (1999)  
 Moises Macias, Master of Science in Civil Engineering. (2000)  
 Helder Lopez, Master of Science in Civil Engineering (2000)  
 Sergio Castillo, Master of Science in Civil Engineering (2001)

## **BS Graduates**

David Meza, Bachelor of Science, Civil Engineering, (1998)  
 Brian Harms, Bachelor of Science, Civil Engineering (1998)  
 James Brown, Bachelor of Science, Mechanical Engineering (1998)  
 Jose Gutierrez, Bachelor of Science, Electrical Engineering (1997)  
 Douglas Demming, Bachelor of Science, Electrical Engineering (1997)  
 Oscar Moguel, Bachelor of Science, Mechanical Engineering (1999)  
 Benjamin Lopez, Bachelor of Science, Civil Engineering (1999)  
 Alina Nunez, Bachelor of Science, Mechanical Engineering Major (1998)  
 Miguel Kanakoqui, Bachelor of Science, Mechanical Engineering (2000)  
 Ana C. Holguin, Bachelor of Science, Mechanical Engineering (2001)

The following publications stemmed from these research efforts:

- Carlos Ferregut, Roberto A. Osegueda, Yohans Mendoza, Vladik Kreinovich, and Timothy J. Ross, "Aircraft Integrity and Reliability", In: Jane Booker, Jerry Parkinson, and Timothy R. Ross (eds.), *Combined Fuzzy Logic and Probability Applications*, SIAM, Philadelphia, 2001 (to appear).
- Roberto A. Osegueda, Seetharami R. Seelam, Ana C. Holguin, Vladik Kreinovich, and Chin-Wang Tao. "Statistical and Dempster-Shafer Techniques in Testing Structural Integrity of Aerospace Structures", *Proc. of International Conference on Intelligent Technologies*, Bangkok, Thailand, December 13-15, 2000, pp. 383-389.
- Osegueda, C. Ferregut, V. Kreinovich, S. Seetharami and H. Schute, "Fuzz (Granular) Level of Quality, with Applications to Data Mining and to Structural Integrity of Aerospace Structures," *PeachFuzz 2000*, pp. 348-352, Atlanta, GA, July 2000.
- R.A. Osegueda, M. Macias, G. Andre, C.M. Ferregut and C. Carrasco, "Fusion of Modal Strain Energy for Health Monitoring of Aircraft Structures," in Nondestructive Evaluation of Aging Aircraft, Airports and Aerospace Hardware IV, Ajit. K. Mal, Ed., *Proceedings of SPIE Vol. 3994*, 2000. (Awarded best paper of Conference on NDE for Health Monitoring and Diagnostics Conference after peer review)
- R.A. Osegueda, H. Lopez, L. Pereyra and C. M. Ferregut, "Localization of Damage using Fusion of Modal Strain Energy Differences," *Proc. of International Modal Analysis Conference XVIII, SEM, Vol. I*, San Antonio, TX, Feb. 7-10, 2000, pp. 695-701.
- L. R. Pereyra, R. A. Osegueda, C. Carrasco and C. Ferregut, "Detection of Damage in a Stiffened Plate from Fusion of Modal Strain Energy Differences," *Proc. of International Modal Analysis Conference XVIII, SEM, Vol. II*, San Antonio, TX, Feb. 7-10, 2000, pp. 1556-1562.
- G. V. Garcia and R. A. Osegueda, "Combining Damage Index Method and ARMA Method to Improve Damage Detection," *Proc. of International Modal Analysis Conference XVIII, SEM, Vol. I*, San Antonio, TX, Feb. 7-10, 2000, pp. 668-673.



- R. A. Osegueda, G. Andre, C. Carrasco, C. M. Ferregut and L. Pereyra, "Effects of Mode Pairing in Strain Energy-Based Damage Detection Methods Applied to an Aerospace Structure," Proc. of International Modal Analysis Conference XVIII, SEM, Vol. II, San Antonio, TX, Feb. 7-10, 2000, pp. 1218-1224.
- G. Andre, R.A. Osegueda, C.M. Ferregut, C. Carrasco, L. Pereyra UTEP, G. James and M. Grygier, "Comparison of Strain Energy-Based Vibrational NDE Methods Applied to a Complex Aerospace Structure", in Nondestructive Characterization IX, Ed. R. Green, American Institute of Physics, AIP Conf. Proceedings 497, Sydney, Australia, June/July 1999, pp 561-568.
- Pereyra, L.R., Osegueda, R.A., Carrasco, C. and Ferregut, C., "Damage Detection in a Stiffened-Plate Using Modal Strain Energy Differences", in Nondestructive Evaluation of Aging Aircraft, Airports and Aerospace Hardware III, Ed. A. K., Mal, Proceedings of SPIE, Vol. 3586, Paper 3586-29, pp 211-222, March 1999.
- Osegueda, R.A., Revilla, A., Pereyra, L., and Moguel, O., "Fusion of Modal Strain Energy Differences for Localization of Damage," in Nondestructive Evaluation of Aging Aircraft, Airports and Aerospace Hardware III, Ed. A. K., Mal, Proceedings of SPIE, Vol. 3586, Paper 3586-28, pp. 189-199, March 1999.
- Garcia, G.V., Osegueda, R. and Meza, D., "Damage Detection using ARMA Model Coefficients," in Smart Systems for Bridges, Structures, and Highways, Ed. S.C. Liu, SPIE, Vol. 3671, Paper 3671-30, March 1999.
- Garcia, G.V., Osegueda, R. and Meza, D., "Damage Detection Comparison between Damage Index Method and ARMA Method", in Proc. of 17<sup>th</sup> International Modal Analysis Conference, IMAC XVII, SEM, Orlando, FL, February 8-11, 1999.
- Pereyra, L.R., Osegueda, R.A., Carrasco, C., Ferregut, C. M., "Structural Defects Detection Using Low Frequency Modal Testing with a Laser Vibrometer", in Proc. ASNT Fall 1998 Conference, The American Society of Nondestructive Testing, Columbus, OH, Oct. 1998, pp 63-66.
- Andre, G.C., Carrasco C.J., Osegueda, R.A., Ferregut, C. M., James III, G.H. and Grygier, M., "Comparison of Accelerometer and Laser Modal Tests of a Vertical Stabilizer Assembly," SPACE 98, ASCE, April 1998, pp.132-139.
- Garcia, G.V., Osegueda, R. and Meza, D., "Comparison of the Damage Detection Results Utilizing an ARMA Model and an FRF Model to Extract the Modal Parameters." In Smart Structures and Materials 1998: Smart Systems for Bridges, Ed. S.C. Liu, SPIE Proceedings, Vol. 3325, ISBN: 0-8194-2769-1, San Diego, CA, March 1-5, 1998, Paper 3325-30.
- Ferregut, C.M., Osegueda, R.A., and Nuñez, A., (Editors), Intelligent NDE Sciences for Aging and Futuristic Aircraft, FAST Center for Structural Integrity of Aerospace Systems, The University of Texas at El Paso, ISBN: 97404-279-8, El Paso, Texas, January 1998.
- Osegueda, R., Ferregut, C., George, M.J., Gutierrez, J.M. and Kreinovich, V., "Maximum Entropy Approach to Optimal Sensor Placement for Aerospace Non-Destructive Testing," in Maximum Entropy and Bayesian Methods, Eds. G. Erikson and J. T. Rychert, Kluwer Academic Publishers, Dordrecht, 1997, pp. 277-289.
- Osegueda, R.A., Carrasco, C. J. and Meza, Jr., R., "A Modal Strain Energy Distribution Method to Localize and Quantify Damage," 15<sup>th</sup> International Modal Analysis Conference, IMAC XV, Society of Experimental Mechanics, Orlando, Florida, pp. 1298-1304, Feb. 3-6, 1997.
- Carrasco, C.J., Osegueda, R.A., Ferregut, C. M. and Grygier, M., "Damage Localization in a Space Truss Model Using Modal Strain Energy Distribution," 15<sup>th</sup> International Modal Analysis Conference, IMAC XV, Society of Experimental Mechanics, Orlando, Florida, Vol. II, pp. 1786-1792, Feb. 3-6, 1997.

- Meza, Jr. R., Carrasco, C.J., Osegueda, R.A., James, G., and Robinson, N., "Damage Detection in a DC-9 Fuselage Using Laser Doppler Velocimetry," 15<sup>th</sup> International Modal Analysis Conference, IMAC XV, Soc. of Experimental Mechanics, Orlando, FL, Vol. II, pp. 1779, 1785, Feb. 3-6, 1997.
- Carrasco, C. J., Osegueda, R.A., Ferregut, C.M. and Grygier, M., "Localization and Quantification of Damage in a Space Truss Model Using Modal Strain Energy," Smart Structures and Materials 1997: Smart Systems for Bridges Structures, and Highways, San Diego, March 3-6, (1997), pp. 181-192.
- Meza, Jr. R., Carrasco, C.J., Osegueda, R.A., James, G. and Robinson, N., "Damage Evaluation in a DC-9 Fuselage Using Laser Doppler Velocimetry Measurements," Smart Structures and Materials 1997: Smart Systems for Bridges Structures, and Highways, San Diego, CA, March 3-6, (1997).
- Perez, L., Ferregut, C.M., Osegueda, R.A., Paez, T., Barney, P., and Hunter, N., "Statistical Validation of a Plate Finite Element Model for Damage Detection," accepted for the SPIE's 1997 Smart Structures and Materials Symposium, San Diego, CA, March 3-6, 1997.
- Gutierrez, J.M., Ferregut, C., and Osegueda, R.A., "A Comparative Study on Two Types of Mode Sensitive Neural Networks for Damage Assessment," Nondestructive Evaluation of Utilities and Pipelines, M. Prager and R.M. Tilley (Eds.), Proc. SPIE 2947, 1996, pp. 224-235.
- Carrasco, C., Osegueda, R.A., Ferregut, C.M., Harms, B., Meza, D., and Grygier, M., "Comprehensive Modal Tests of a Space Truss Model for Damage Assessment," In Proc. Fifth International Conference on Space '96, June 1-6, 1996, Albuquerque, NM, pp. 1141-1147.

## ACKNOWLEDGMENTS

The efforts documented here were sponsored by the Air Force Office of Scientific Research, Air Force Materiel Command, USAF, under grant number F49620-95-1-0518. The US Government is authorized to reproduce and distribute reprints for Governmental purposes notwithstanding any copyright notation thereon. The continuing mentoring of Dr. Spencer Wu, program Manager, are greatly appreciated. The fruitful involvement of all the students listed in the executive summary is greatly acknowledged. Without their desire to obtain an education, this work would not have been possible.

## TABLE OF CONTENTS

	<u>Page</u>
CHAPTER 1 -- INTRODUCTION .....	1
1.1 Introduction.....	1
1.2 Background .....	1
1.3 Objectives .....	3
CHAPTER 2 -- VIBRATIONAL DAMAGE DETECTION METHODS .....	5
2.1. Introduction.....	5
2.2. Damage Detection from Modal Analysis Data.....	5
2.3. Modal Strain Energy Difference Method .....	7
2.4. Combining Damage Indictors and Data Fusion.....	11
Likelihood Ratios.....	13
Bayes Statistics .....	13
Evidential Reasoning .....	14
Damage Magnitude.....	16
Probability Mass Function Formulation .....	17
Weighted Averaging and PMF Formulations .....	18
2.5. Limitations of Modal Strain Energy Methods .....	19
CHAPTER 3 -- VIBRATIONAL NON-DESTRUCTIVE EVALUATION IN BEAMS .....	21
3.1 Introduction.....	21
3.2 Description of Structural System .....	21
3.3 Instrumentation .....	21
3.4 Experimental Set-Up.....	23
3.5 Damage Scenarios.....	23
3.6 Experimental Procedure.....	25
3.7 Damage Localization Process .....	26
3.8 Damage Assessment .....	28
3.9 Summary.....	33
CHAPTER 4 -- EXPERIMENTAL PROGRAM STIFFENED PLATE SPECIMEN .....	35
4.1 Introduction.....	35
4.2 Description of the Stiffened Plate Model.....	35
4.3 Instrumentation and Experimental Procedure.....	36
4.4 Description of Damage Scenarios.....	38
4.5 Summary of Acquired Data .....	41
4.6 Description of Damage Localization Procedure .....	43
4.7 Summary and Discussion of Damage Localization Results .....	43
4.8 Conclusions using Averaging .....	48
4.9 Damage Detection Results Using Likelihood Ratio and Evidential Reasoning .....	49
4.10 Conclusions using Fusion by Likelihood Ratio and Evidential Reasoning.....	51

	<u>Page</u>
CHAPTER 5 - DAMAGE DETECTION TESTS IN VERTICAL STABILIZER	
STRUCTURE .....	53
5.1 Introduction.....	53
5.2 Description of Test Article.....	53
5.3 Description of Damage Test Program.....	56
5.4 Baseline and Damaged Scenarios .....	61
5.5 Modal Parameter Extraction, MAC Analysis and Z-Function Analysis .....	62
5.6 Damage Localization Procedure .....	63
5.7 Damage Localization Results .....	65
5.8 Damage Detection Maps for All Cases.....	74
5.9 Comparison of Performance of Damage Detection Algorithms.....	79
CHAPTER 6 -- FURTHER ANALYSES OF VSA TESTS.....81	
6.1 Introduction.....	81
6.2 Finite Element Model Updating.....	81
6.3 Description of Damage Maps .....	82
6.4 Comparison of Performance of Damage Detection Methods .....	84
6.5 Conclusions.....	88
CHAPTER 7 -- DAMAGE EVALUATION IN CURVED SHELL TEST	
ARTICLE .....	89
7.1 Introduction.....	89
7.2 Description of Test Object.....	89
7.3 Instrumentation and Test Set-up .....	91
7.4 Description of Damage Test Program in Shell Specimen .....	93
7.5 Damage Localization Results .....	101
7.6 Conclusions from the Shell Tests .....	105
CHAPTER 8 -- SUMMARY AND CONCLUSIONS .....	
8.1 Summary .....	107
8.2 Conclusions.....	109
REFERENCES .....	
113	
APPENDIX A -- EXTRACTION OF MODAL SHAPES AND STRAIN	
ENERGY FROM DISCRETE MEASUREMENTS .....	115
A.1 Introduction.....	115
A.2 Curve-Fit Approach for Beam-like Structures.....	115
A.3 Mode Curve-Fit Algorithm for Plate-like Structures.....	119
A.4 Finite Element Approach for Complex Structures.....	125

	<u>Page</u>
APPENDIX B -- PROCEDURE TO DETERMINE MODE WITH SIGNIFICANT CHANGE BETWEEN DAMAGED AND UNDAMAGED SCENARIOS .....	127
B.1. Introduction.....	127
B.2. Approach for Comparison.....	127
B.3. Typical Results of Z-Function Analysis .....	129
APPENDIX C -- DAMAGE MAPS OBTAINED FOR THE VSA TEST OBJECT USING IMPROVED FE MODEL .....	131
APPENDIX D -- DAMAGE PREDICTION MAPS FOR SHELL SPECIMENS.....	157

## LIST OF FIGURES

	<u>Page</u>
Figure 2.1. Schematic of a Structure Before and After Damage.....	6
Figure 2.2. Fusion Process for Damage Localization. ....	12
Figure 2.3. PDF of Normalized Strain Energy Differences for mode k.....	12
Figure 2.4. Probability of Damage Detection Model. ....	14
Figure 2.5. Probability Mass Functions as Evidence in Support of Hoi and Hai.....	15
Figure 2.6. Evidential Intervals (Belief vs. Plausibility).....	16
 Figure 3.1. Structural System Set-Up.....	 22
Figure 3.2. Schematic of Instrumentation. ....	22
Figure 3.3. (a) Accelerometer with Mounting Stud, (b) Force Transducer and (c) Electromagnetic Shaker.....	23
Figure 3.4. Damage Scenarios for Beams 1 & 2. ....	24
Figure 3.5. Typical Mode Shapes Corresponding to Measured Data (base_01).....	26
Figure 3.6. Damage Localization Process Flow Chart. ....	27
Figure 3.7. Fusion Results for C1dam5.....	29
 Figure 4.1. Front View of Experimental Stiffened Plate Model. ....	 36
Figure 4.2. Rear View of Experimental Stiffened Plate Model. ....	36
Figure 4.3. Schematic Representation of Instrumentation. ....	37
Figure 4.4. Location of Shakers. ....	38
Figure 4.5. Frequency Response Functions for Reciprocity Test. ....	39
Figure 4.6. Location of Damage Cases. ....	39
Figure 4.7. Examples of Cut Damage. ....	39
Figure 4.8. Typical Mode Shapes.....	42
Figure 4.9. Mode Shape Before and After Damage - Case 1e. ....	42
Figure 4.10. Damage Localization Process Flow Chart. ....	44
Figure 4.11. Scale for Damage Index in Damage Maps. ....	45
Figure 4.12. Summary of Best Damage Maps for Case 1.....	45
Figure 4.13. Summary of Best Damage Maps for Case 2.....	46
Figure 4.14. Summary of Best Damage Maps for Case 3.....	46
Figure 4.15. Summary of Best Damage Maps for Case 4.....	46
Figure 4.16. Summary of Best Damage Maps for Case 5.....	47
Figure 4.17. Summary of Best Damage Maps for Case 6.....	47
Figure 4.18. Summary of Best Damage Maps for Case 7.....	48
Figure 4.19. Summary of Best Damage Maps for Case 8.....	48
Figure 4.20. Log of Damage Likelihood Ratio and Evidential Reasoning Results.....	50

Figure 5.1.	Front View of Test Article.....	54
Figure 5.2.	Close-up View of Shaker Test Article Attachment .....	54
Figure 5.3.	Geometry of Sensor and Tape Locations.....	55
Figure 5.4.	Laser and Computer Set-up. ....	55
Figure 5.5.	Damage Inflicted in Case 4.....	57
Figure 5.6.	General Location of Inflicted Damages in Case 5. ....	58
Figure 5.7.	Illustration of Rivets Removed in Cases 5a through 5d. ....	58
Figure 5.8.	Illustration of Damage Levels in Cases 5e through 5j.....	59
Figure 5.9.	General Location of Inflicted Damages in Case 6. ....	59
Figure 5.10.	Inflicted Damage Levels for Case 6.....	59
Figure 5.11.	General Location of Inflicted Damages in Case 7. ....	60
Figure 5.12.	Inflicted Damages in Case 7. ....	60
Figure 5.13.	General Location within the Right RSB of Inflicted Damages in Case 8.....	61
Figure 5.14.	Inflicted Damages in Case 8. ....	61
Figure 5.15.	Damage Localization Process Flow Chart.....	65
Figure 5.16.	Damage Map for Middle Elements for Case 4a - ASN Method.....	67
Figure 5.17.	Damage Map for Middle Elements for Case 4a - WASN Method. ....	67
Figure 5.18.	Damage Map for Middle Elements for Case 4a - PMF Method.....	68
Figure 5.19.	Damage Maps for Case 4a Using WPMF Method. ....	74
Figure 5.20.	Damage Maps for Case 4b Using WPMF Method. ....	75
Figure 5.21.	Damage Maps for Case 4c Using ASN Method. ....	75
Figure 5.22.	Damage Maps for Case 5a Using WPMF Method. ....	76
Figure 5.23.	Damage Maps for Case 5b Using WPMF Method. ....	76
Figure 5.24.	Damage Maps for Case 5c Using WPMF Method. ....	77
Figure 5.25.	Damage Maps for Case 5h Using WPMF Method. ....	77
Figure 5.26.	Damage Maps for Case 6c Using WPMF Method. ....	78
Figure 5.27.	Damage Maps for Case 7b Using WPMF Method. ....	78
Figure 5.28.	Damage Maps for Case 8f Using WASN Method.....	79
Figure 6.1	Sample Damage Maps, using Improved FE model. ....	83
Figure 7.1.	Front View of Stiffened Curved Plate Model. ....	90
Figure 7.2.	Rear View of Stiffened Curved Plate Model. ....	90
Figure 7.3.	Front and Side Views of Shell Specimen. ....	91
Figure 7.4.	Top (Left) and Bottom (Right) End Attachments.....	91
Figure 7.5.	Instrumentation .....	92
Figure 7.6.	Schematic of Instrumentation Set-up.....	93
Figure 7.7.	Identification Map for Rivets, Ribs and Stringers. ....	94
Figure 7.8.	Damage Location for Case 1.....	95
Figure 7.9.	Damage Location for Case 2.....	95
Figure 7.10.	Damage Location for Case 3.....	96
Figure 7.11.	Location of Damage for Case 4. ....	96



	<u>Page</u>
Figure 7.12. Location of Damage for Case 5. ....	97
Figure 7.13. Location of Damage for Case 6. ....	97
Figure 7.14. Location of Damage for Case 7. ....	98
Figure 7.15. Location of Damage for Case 8. ....	98
Figure 7.16. Location of Damage for Case 9. ....	99
Figure 7.17. Typical Modes for the Curved Shell Test Object .....	101
Figure 7.18. Z-Function Results for (a) Base01-Case1a and (b) Base02-Case2a. ....	102
Figure 7.19. Damage Map Results for Case 4a with Baseline 4. ....	103
 Figure A.1 Example Measured Mode Shape for a Beam.....	 116
Figure A.2 Fitted Curvature (First Iteration).....	117
Figure A.3 Final Fitted Mode Shape after Eight Iterations.....	119
Figure A.4 Figure A.4 Fitted Modal Curvature after Eight Iterations. ....	119
Figure A.5 Typical Measured Mode Shape Over a Rectangular Area.....	120
Figure A.6 Example of Plate Bending and Twisting Curvatures Obtained by Curvefitting. ....	 124
Figure A.7 Final Bending and Twisting Curvatures. ....	125
 Figure B.1 Average of Normalized FRF Magnitude Differences of All 84 Measured Points in VSA Test Article for One Case.....	  130

## LIST OF TABLES

	<u>Page</u>
Table 3.1. Description of Damage Scenarios for Beam #1.....	24
Table 3.2. Description of Damage Scenarios for Beam #2.....	25
Table 3.3. Summary of Fusion Results for C1dam5.....	30
Table 3.4. Detectability Results for Damage Cases in Beam 1. ....	32
Table 3.5. Detectability Results for Damage Cases in Beam 2. ....	33
 Table 4.1 Description of Damage Cases. ....	 40
Table 5.1. Summary of Damage and Baseline Cases. ....	62
Table 5.2. Summary of Detection Results Using Mode-Pairs with MAC > 0.5.....	70
Table 5.3. Summary of Detection Results Using Mode-Pairs with MAC > 0.9.....	71
Table 5.4. Summary of Detection Results Using Mode-Pairs with MAC > 0.5 and Indicated as Significant by the Z-Function Analysis. ....	72
Table 5.5. Summary of Detection Results Using Mode-Pairs with MAC > 0.9 and Indicated as Significant by the Z-Function Analysis. ....	73
Table 5.6. Summary of Detection Methods' Performance According to Mode- Selection Criteria. ....	80
 Table 6.1. Summary of Damage Detection Results Using Mode-Pairs with MAC > 0.5. ....	 85
Table 6.2. Summary of Damage Detection Results Using Mode-Pairs with MAC > 0.5 and Indicated as Significant by the Z-Function Analysis.....	86
Table 6.3. Summary of Damage Detection Results After FEM Updating, Using Mode-Pairs with MAC > 0.5 and Indicated as Significant by the Z-Function Analysis.....	87
Table 6.4. Summary of Detection Method's Performance According to Mode- Selection Criteria. ....	88
 Table 7.1. Case Description with Corresponding Baseline. ....	 100
Table 7.2. List of damage maps that showed the highest level of detection.....	104

# **CHAPTER 1**

## **INTRODUCTION**

### **1.1 Introduction**

Most commonly used NDE methods for the inspection of aircraft structures are capable of providing detailed information only about a limited region of the structure. The most developed and utilized methods are those based on visual inspection, electromagnetics (i.e. eddy current) and ultrasonics. One major problem faced, however, is the detection of defects in hidden members or members deep inside the aircraft. Although, the above mentioned techniques are effective in detecting cracks and other forms of damage, these require access so that sensors and/or instrumentation be placed at/or near the vicinity of the flaw. For these methods to be effective to detect flaws in hidden or deep structural members, disassembly is almost always mandatory. Disassembly requires grounding of the aircraft for weeks. Thus alternative methods for aircraft inspection, that could reduce the time airplanes are out of service, are desirable. This report documents the work performed at The University of Texas at El Paso on large area inspection of aircraft structures using vibrational nondestructive evaluation techniques.

### **1.2 Background**

The recent trend to extend the life of old military aircraft, rather than replacing them with new models, has increased their probability of structural failure as a result of aging. This trend has added a great degree of urgency to the ongoing needs for reliable and efficient NDE methods. Inspection of aging aircraft using current technology is time consuming, demands great attention to details by the inspectors and, in many cases, requires a costly disassembly of the structure. The reliability of the test results depends heavily on the type of instrument used, the condition of the instrument, the methods and environment under which it is used and above all, the interpretation of the inspectors. The inspector's interpretation depends critically on his/her experience and attentiveness.

Most NDE methods that are used for inspection in field conditions provide detailed information about a limited region of the structure. These methods include, but are not limited to, penetrating radiation, optics, electromagnetics, ultrasonics, acoustic emission and magnetic flux analysis. By far, the most developed and utilized methods are those based on visual inspection, electromagnetics (i.e. eddy current) and ultrasonics. The method to be used in a given situation depends on the expected nature of the defect to be detected, the required sensitivity, reliability of the measurement, the cost and practicality of inspection. Furthermore, one major problem faced is the detection of defects in hidden members of the structure. Although methods such as ultrasonics, Eddy currents, and thermography are effective in detecting cracks and other forms of damage, they require access to the structure so that sensors and/or instrumentation are placed at or in the near vicinity of the flaw. Moreover, to detect damage in hidden or deep structural members, disassembly is usually mandatory. One family of inspection methods, based on the changes in the global dynamic response of the structure obtained from modal analysis and referred to as vibrational non-destructive evaluation (NDE) methods, has the

capability of identifying locations of damage from global measurements taken on exterior points of the structure. Vibrational NDE methods, however, have detectability limitations that depend on the sensitivity of the defect location on the dynamic structural response. Vibration-based NDE methods to detect damage in structures are based on measurements of the dynamic response of the structure in a reference state, and similar measurements taken when the structure contains damage. Since damage cause changes in the stiffness of the structure, the methods utilize changes in the measurable global response to infer the locations of stiffness changes synonymous to damage.

The vibrational NDE methods take advantage of the fact that structures have a unique set of resonant frequencies, modal damping ratios, and characteristic mode shapes. These fundamental quantities are unique functions of the mass, stiffness and the damping characteristics of the structure. A change in any one of the latter produces a change in the modal response. In principle, aircraft structures can be monitored periodically to detect changes in their response and the information can be used to detect, locate and quantify defects and material degradation. Traditionally, vibrational NDE methods have depended on the determination of the modal parameters via experimental modal analysis using transducer sensors such as accelerometers that are mounted on several points of the structure. This poses a limitation on the amount of effort associated with mounting a large number of sensors notwithstanding that the mass of the structure is artificially increased. The added mass could be significant when the number of sensors is large. To overcome these limitations laser optical sensing instruments currently exist that allows for a rapid set-up of the required instrumentation required. Furthermore, the laser sensing also allow higher density of measurements without adding extra mass or even contacting the specimen. This technology is making the vibrational approach more attractive as a potential tool for inspecting large areas in aircraft structures.

The vibrational NDE techniques that were investigated primarily relied on measurements obtained with a Laser Doppler Velocimeter (LDV) accompanied with data fusion methodologies to develop damage assessment tools with limited information. The LDV is a device based on the Michelson's interferometer that provides non-contact measurements of dynamic velocity. The LDV used in the investigations has scanning mirrors that allow for the targeting of the laser beam on any point within an area limited by  $25^\circ$  by  $25^\circ$  of mirror rotation. In addition, the LDV is capable of obtaining velocity measurements from objects at a distance of 200-meters, which allows for scanning large structural areas. The LDV has two advantages over the conventional sensor: 1) it is a non-contact technique that eliminates the entire sensor placement and cables associated with contact sensors, 2) it gives the ability of using a dense array of points without adding mass, and 3) the problem of incorrect readings caused by dislodged accelerometers is eliminated.

The vibrational NDE methods considered are based on modal strain energy differences between the elements of the structure at a damaged and a healthy state. The method uses the strain energy in the structural elements due to modal deformation, and compares them to similar energy quantities for a healthy reference state to obtain indicators of damage as a function of the structure location. The damage severity can be determined from the relative changes in the modal strain energy. The method, however, require a mode-pairing process to match the mode shapes of the damaged state to those of the healthy state. The mode-pairing seems to have an

effect on the detectability of damage. The differences in the element strain energy due to the deformations of the paired modes then provide features for the detection of damage. Furthermore, the mode pairs may lack sensitivity to detect damage at given locations, especially if the locations have relatively low modal strain energy content. For this reason, damage is usually detected using several pairs of modes. Then the issue is how to best combine the information extracted from individual mode-pairs to make a final determination of the potential damage.

Several innovative data processing methods were implemented for the analysis of the experimental modal information. The majority of the methods were based on data fusion techniques (Gros 1997). The premise behind these techniques is that the NDE data gathered from several sources (e.g. sensors, modes, experts, etc.) can be combined to obtain better information about the structures than when data from each source are analyzed independently. Application of these techniques to NDE data is relatively new. However, they proved to be a robust tool. This report presents the most promising techniques in terms of damage detection reliability. They include: averaging methods, probability mass functions, Bayesian methods and methods based on evidential reasoning.

For the most part, vibrational methods combined with data fusion techniques have shown success when applied to simple systems such as beams (Osegueda, *et al.* 1997), plates (Meza 1996), and trusses (Carrasco, *et al.* 1996). The structures considered are relatively uniform without significant variations in the stiffness. Complex aerospace structures contain closely spaced modes and the mode pairing and selection criteria between the damaged and healthy structure become issues.

### **1.3 Objectives**

The objective of this report is to document the research work on the development of vibrational NDE methods to infer damage over a large area of aircraft structures using laser Doppler Velocimeter (LDV) accompanied with data fusion techniques to process the modal information before and after damage.

Chapter 2 documents the theoretical developments of the vibrational NDE method and the data fusion methodologies. Chapter 3 describes the work performed on beam tests for the purpose of developing the vibrational NDE techniques and to refine the fusion methods. Chapter 4 describes the work performed on a large Aluminum stiffened plate laboratory structure which resembles aircraft construction to localize damage when the modal measurements are obtained with a LDV and the data is processed using the fusion techniques. Chapter 5 describes the research performed on a prototype of the vertical stabilizer assembly of NASA's shuttle orbiter. This is an example of how the large area inspection techniques could be implemented for aircraft structures. The purpose of the tests documented in Chapter 5 was to obtain a database for developing, calibrating and testing damage identification techniques. The application of four damage detection algorithms is documented in Chapter 5. Chapter 6 includes additional fusion approaches applied to the VSA test structure and also considered improved finite element models. Chapter 7 documents the work performed in a laboratory shell structure that resembles a fuselage structure.



## CHAPTER 2

### VIBRATIONAL DAMAGE DETECTION METHODS

#### 2.1. Introduction

Experimental modal analysis has been the mechanism to obtain frequency response data to perform Non-Destructive Evaluation (NDE) and Damage Detection (NDD). Since all forms of damage may cause changes in the structural stiffness, the damage may be reflected in the vibrational characteristics. Changes in the stiffness and/or mass of the structure cause changes in structure's dynamic characteristics. Since the dynamic characteristics of a structure are altered by the damage, then changes in frequencies, mode shapes and damping ratios or any value that derives from these changes can be used to detect damage.

The vibrational NDE method considered in this report is based on modal strain energy differences (Carrasco, *et. al.*, 1996; Pereyra, 1998). This technique considers the static shapes of the individual modes. From these shapes, the strain energy distribution within the structure is computed by curvefitting or using finite element models. The energy distributions for the same mode before and after damage are normalized and compared to provide indications of the location of damage. The damage location is indicated as an apparent strain energy increase. Damage in an element causes changes in the modal shapes in the vicinity of or at the location of damage. From structural mechanics relationships, the differences in the strain energy can be evaluated using the measured modal shapes. Since experimental modes are only obtained at the sampling points, curve-fitting and/or finite element techniques are required to complete the missing components of the modes.

In order to combine information from multiple modes of different magnitudes, a standard normalization is proposed. The damage detection formulation relies on the features of the differences of modal strain energy when the modes are equally normalized giving collection sets of modal strain energy differences for the available modes. The distribution of the normalized strain energy differences also provides the mechanism to extract probabilities in support of damage and no damage at each location of the structure given the information in each mode.

Information from each modal pair is then combined using data fusion techniques. This chapter includes a summary of all the fusion techniques that were considered in this research. The work described in this chapter is based on the Master theses of (Andre 1999, Macias 2000, Pereyra 1998, and Lopez 2000).

#### 2.2. Damage Detection from Modal Analysis Data

Experimental modal analysis has been the mechanism to obtain frequency response data to perform Non-Destructive Evaluation (NDE) and Damage Detection (NDD). The methods rely on the fact that the vibrational characteristics for the structural systems are functions of the mechanical properties (stiffness, mass and damping). Since all forms of damage may cause changes in the structural stiffness, the damage may be reflected in the vibrational characteristics,



namely the resonant frequencies, damping ratios and associated modal shapes. The theory behind all the damage detection methods is that when stiffness and/or mass of the structure changes, the dynamic characteristics also change. This change in stiffness and/or mass is caused by the presence of damage in the structure. Therefore, if damage is present in a structure its dynamic characteristics are not the same as when the structure was undamaged. Since the dynamic characteristics of a structure are altered by the damage, then changes in frequencies, mode shapes and damping ratios or any value that derives from these changes can be used to detect damage. The vibrational characteristics of a structure can be determined experimentally by sampling the dynamic response from sensors due to known input excitations. This line of experiments falls within the domain of experimental modal analysis, whose techniques are well established. The Vibrational NDE and NDD methods described in this chapter use the measurements of the vibrational characteristics at a reference state (undamaged) and compare them to the measurements obtained at the damaged state. Figure 2.1 shows a schematic of this process.

The conventional way to perform modal analysis experiments is the utilization of accelerometers mounted at discrete points of the structure to provide the response and the use of dynamic shakers. Through the use of frequency spectrum analyzers, the time histories of the input forces from force sensors attached in the shaker and the output response from the accelerometers are converted to the frequency domain. This is typically done by averaging for the reduction of noise. The average ratio of the response-to-input signals is referred to as the frequency response functions (FRF). The set of FRFs collected from several points provide information of the global dynamic response of the structure as a function of frequency. Through the use of standard modal analysis software, the FRFs are processed to extract the resonant frequencies, damping ratios and associated modal shapes. The use of accelerometers, however pose limitations on the number of points on the structure to monitor.

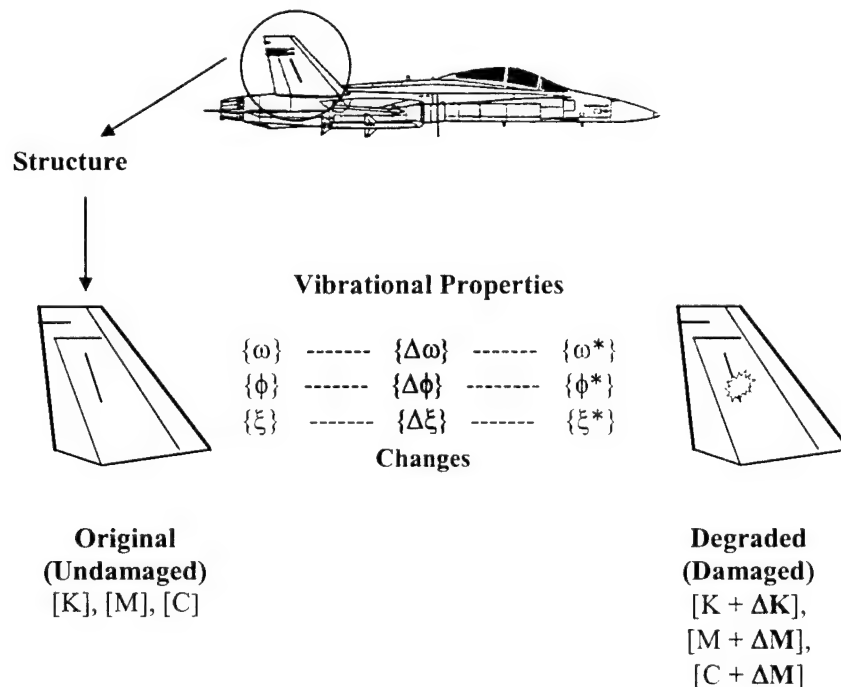


**Figure 2.1. Schematic of a Structure Before and After Damage.**

A major advancement in experimental modal analysis techniques has been the development of laser systems to measure dynamic signals of vibrating objects non-contactly. More importantly, these devices are usually accompanied with scanning mirrors that permit targeting to an unlimited number of points on the structure. The Laser Doppler Velocimeter (LDV) is a device based on the Michelson's interferometer that provides non-contact measurements of velocity. The LDV used in the investigations has scanning mirrors that allow for the targeting of the laser beam on any point within an area limited by  $25^\circ$  by  $25^\circ$  of mirror rotation. Even though the area is limited by the rotation of the mirrors, the laser has a 200-meter reach, which allows for large scanning areas to be defined. The LDV has two advantages over the conventional sensor. 1) It is a non-contact technique that eliminates the entire sensor placement and cables associated with contact techniques. 2) It gives the ability of using a dense array of points without adding mass. 3) The probability of incorrect readings caused by dislodged accelerometers is reduced.

### 2.3. Modal Strain Energy Difference Method

One vibrational NDE method that has been successfully applied for the localization of damage is the modal strain energy difference method (Carrasco, *et. al.*, 1996; Pereyra, 1998). This technique considers the static shapes of the individual mode shapes. From these shapes, the strain energy distribution within the structure is computed by curvefitting or via finite element models. The energy distribution for the same mode before and after damage are normalized and compared to provide indications of the location of damage. The damage location is usually indicated as an apparent strain energy increase. Also from the strain energy differences the magnitude of the damage may be calculated.

The basic idea of the modal strain energy difference method (MSED) is that the distribution of the relative strain energy stored in a mode of a structure will change around the location of the damage. If a structural member experiences a reduction in its stiffness (damage), then that element will have larger deformations as a result of the same amount of modal strain energy. Since the damage location is not known ahead of time, the damage is reflected as an apparent increase in the modal strain energy. Since, stiffness reductions cause deviation from the original strain energy distribution of the undamaged structure, then, the difference in the strain energy distributions of the undamaged and damaged structures provide indications of what elements are likely to have experienced damage (with increases in the modal strain energy). Therefore, the modal strain energy differences can be used to detect and locate damage.

The method considers the pairs of matching mode shapes for the structure in the undamaged and damaged states. Damage in an element causes changes in the modal shapes in the vicinity of or at the location of damage. Consider an arbitrary structure generically defined with stiffness, mass and damping properties  $[K]$ ,  $[M]$  and  $[C]$ . Then, let  $[\bar{K}]$ ,  $[\bar{M}]$  and  $[\bar{C}]$  be similar properties for the structure but in the damaged state. Assume that pairs of resonant frequencies and mode shapes are available. The vibrational characteristics can be defined as:

$$\{\omega\}^T = [\omega_1 \quad \omega_2 \quad \cdots \quad \omega_k \quad \cdots \quad \omega_{nm}] \quad (2.1a)$$

$$\{\bar{\omega}\}^T = [\bar{\omega}_1 \quad \bar{\omega}_2 \quad \cdots \quad \bar{\omega}_k \quad \cdots \quad \bar{\omega}_{nm}] \quad (2.1b)$$

$$[\Phi]^T = [\{\phi_1\} \quad \{\phi_2\} \quad \cdots \quad \{\phi_k\} \quad \cdots \quad \{\phi_{nm}\}] \quad (2.1c)$$

$$[\bar{\Phi}]^T = [\{\bar{\phi}_1\} \quad \{\bar{\phi}_2\} \quad \cdots \quad \{\bar{\phi}_k\} \quad \cdots \quad \{\bar{\phi}_{nm}\}] \quad (2.1d)$$

Where,  $\omega_k$  is the resonant frequency of the  $k^{\text{th}}$  mode in the undamaged state,  $\{\phi_k\}$  is a column vector of size  $ndof$  containing the mode shape in the undamaged state, the same quantities with the bar notation correspond to the structure in the damaged state. The parameter  $nm$  is the number of experimental modes available. It is assumed that the mode shapes in the damaged and undamaged states of the structure are normalized in similar fashions. It should be noted that the resonant frequencies are obtainable from the FRFs. However, the mode shapes can be extracted from the FRFs only at the measuring locations. Thus, the experimental mode shapes are incomplete and their order is usually less than the order of the model describing the structure. Curve-fitting and/or finite element techniques are required to complete the missing components of the modes. Therefore, for the purpose of derivations, it is assumed that complete modes are available. Appendix A contains the procedures that can be used to obtain estimates of the complete modes by either curve-fitting techniques or through the use of finite element models.

The strain energy stored in the structure due to the modal deformations of a single mode can be expressed by the classical equation:

$$U_k = \frac{1}{2} \{\phi_k\}^T [K] \{\phi_k\} \quad (k = 1, 2, \dots, nm) \quad (2.2)$$

Where  $U_k$  is referred to as the total modal strain energy stored in the structure due to mode  $k$ . A similar expression exists for the structure in the damaged state. This equation, however, can be decomposed according to the contributions of strain energy by the individual structural elements of the structure,  $U_{ik}$ . This gives:

$$U_k = \sum_{i=1}^{ne} U_{ik} = \frac{1}{2} \sum_{i=1}^{ne} \{\phi_{ik}\}^T [k_i] \{\phi_{ik}\} \quad (k = 1, 2, \dots, nm) \quad (2.3)$$

Where  $[k_i]$  is the stiffness matrix of the undamaged  $i^{\text{th}}$  element,  $\{\phi_{ik}\}$  is a subset of  $\{\phi_k\}$  containing the undamaged mode shape components associated with the degrees of freedom of element  $i$ , (conformal with  $[k_i]$ ). For the structure in the damaged state, the strain energy expression for the  $k^{\text{th}}$  mode, using a bar notation, is given by:

$$\bar{U}_k = \sum_{i=1}^{ne} \bar{U}_{ik} = \frac{1}{2} \sum_{i=1}^{ne} \{\bar{\phi}_{ik}\}^T [\bar{k}_i] \{\bar{\phi}_{ik}\} \quad (k = 1, 2, \dots, nm) \quad (2.4)$$

Observe that  $[\bar{k}_i]$  is not known for the elements that are damaged.

The changes in the element contribution to the modal strain energy are obtained by subtracting the element strain energies of (2.4) to those of (2.3) to give:

$$\Delta U_{ik} = \frac{1}{2} \{ \bar{\phi}_{ik} \}^T [\bar{k}_i] \{ \bar{\phi}_{ik} \} - \frac{1}{2} \{ \phi_{ik} \}^T [k_i] \{ \phi_{ik} \} \quad (2.5)$$

$(i = 1, 2, \dots, ne), (k = 1, 2, \dots, nm)$

Where  $\Delta U_{ik}$  is the strain energy difference of the  $i^{\text{th}}$  element in the  $k^{\text{th}}$  mode. The difference is obtained by subtracting the strain energy of the damaged structure from that of the undamaged structure. If the structure experiences no damage, then equation (2.5) should equate to zero. However, since the stiffness of the elements in the damaged state are not known, then (2.5) is evaluated assuming that  $[\bar{k}_i] = [k_i]$ , that is:

$$\Delta U_{ik} = \frac{1}{2} \{ \bar{\phi}_{ik} \}^T [k_i] \{ \bar{\phi}_{ik} \} - \frac{1}{2} \{ \phi_{ik} \}^T [k_i] \{ \phi_{ik} \} \quad (2.6)$$

$(i = 1, 2, \dots, ne), (k = 1, 2, \dots, nm)$

When this is done, positive differences in  $\Delta U_{ik}$  indicate the modal deformations at the degrees of freedoms associated with the  $i^{\text{th}}$  element have increased and thus, the  $i^{\text{th}}$  element is potentially damaged according to the  $k^{\text{th}}$  mode.

Equation (2.5) can be used to estimate the magnitude of the change of the stiffness matrix of the  $i^{\text{th}}$  element. Assuming that the stiffness matrix of the damaged element is a fraction of that of the undamaged element, and then the following expression arises:

$$[\bar{k}_i] = [k_i] + \alpha_i [k_i] \quad (2.7)$$

Where,  $\alpha_i$  is the fractional change of the stiffness matrix of element  $i$ . Since, the change in the modal strain energy should be zero, (2.5) is equated to zero, substituting (2.7) and letting  $\alpha_{ik} = \alpha_i$ , because an expression exists for each  $k^{\text{th}}$  mode, gives:

$$\alpha_{ik} = \frac{\{ \phi_{ik} \}^T [k_i] \{ \phi_{ik} \}}{\{ \bar{\phi}_{ik} \}^T [k_i] \{ \bar{\phi}_{ik} \}} - 1 = \frac{U_{ik}}{\bar{U}_{ik}} - 1 \quad (k = 1, 2, \dots, nm) \quad (2.8)$$

A value for  $\alpha_i$  can therefore be computed by averaging the values obtained from all modes.

$$\alpha_i = \frac{1}{nm} \sum_{k=1}^{nm} \alpha_{ik} \quad (2.9)$$

If the structure is beam-like, the modal strain energy equations are obtained from the following strain energy expression evaluated over the length of the beam segment.

$$U_{ik} = \frac{1}{2} \int_{x_i}^{x_i + \Delta x_i} EI_i \left( \frac{d^2 \phi_k(x)}{dx^2} \right)^2 dx, \quad (2.10)$$

Where:  $d^2 \phi_k(x)/dx^2$  is the modal bending curvature of the beam,  $E$  is the modulus of elasticity of the material and  $I_i$  moment of inertia of the  $i^{\text{th}}$  location along the beam. The evaluation of the modal strain energy, however, requires the determination of the second partial derivatives of the modal shapes. A mode shape curve-fit algorithm is used to determine the modal bending curvatures; the features for the modal curvature extraction algorithm are described later in this chapter.

If the structure were to be a plate-like structure, all equations above would apply, except for the modal strain energy expression. This expression requires the bending and twisting curvatures of the mode according to the equation:

$$U_{ik} = \frac{1}{2} \int_A \left\{ D_{xi} \left( \frac{\partial^2 \phi_k(x, y)}{\partial x^2} \right)^2 + D_{yi} \left( \frac{\partial^2 \phi_k(x, y)}{\partial y^2} \right)^2 + D_{xyi} \left( \frac{\partial^2 \phi_k(x, y)}{\partial x \partial y} \right)^2 \right\} dA_i \quad (2.11)$$

Where  $D_{xi}$  and  $D_{yi}$  are the plate bending stiffness in the x- and y-directions, respectively and  $D_{xyi}$  is the plate twisting stiffness, all corresponding to the  $i^{\text{th}}$  element. Note that the evaluation of modal strain energies requires the determination of  $\frac{\partial^2 \phi_k(x, y)}{\partial x^2}$ ,  $\frac{\partial^2 \phi_k(x, y)}{\partial y^2}$  and  $\frac{\partial^2 \phi_k(x, y)}{\partial x \partial y}$  corresponding to the second partial derivatives of the mode shapes. The determination of the curvatures of Equation (2.11) can be accomplished by a curve-fitting procedure reported by Pereyra, *et al.* (1999).

Regardless of the type of system, the changes in the modal strain energy of the elements of the structure provide indications of potential damage. Therefore, if  $nm$  modes of a structure are available, then, modal strain energy changes can be defined as a set of strain energy differences for each mode pair  $k$  computed for all elements by either Equation (2.6) or a form of Equation (2.10) or (2.11) as follows:

$$[\Delta U_k] = [\Delta U_{1k} \quad \Delta U_{2k} \quad \cdots \quad \Delta U_{ik} \quad \cdots \quad \Delta U_{nek}] \quad (k = 1, 2, \dots, nm) \quad (2.12)$$

When the array of values contained in (2.12) is observed, values corresponding to locations with potential damage would exhibit the larger positive values. In practice, however, the number of modes available for inspection is limited and the values contained in (2.12) contain uncertainties from the experiments and models. Thus, the modal strain energy difference requires a combination of the information in (2.12) from several modes in order to predict damage.

In order to combine information from multiple modes of different magnitudes, a standard normalization is proposed. The damage detection formulation relies on the features of the differences of modal strain energy when the modes are equally normalized giving collection sets of modal strain energy differences for the available modes (Osegueda, *et al.*, 1999; Pereyra, *et al.*, 1999; Osegueda, *et al.* 2000a, Carrasco, *et al.*, 1997). The mean value and standard deviation of the modal strain energy differences in such a set can be computed by the equations:

$$\mu_{\Delta U_k} = \frac{1}{ne} \sum_{i=1}^{ne} \Delta U_{ik} \quad (2.13a)$$

$$\sigma_{\Delta U_k} = \sqrt{\frac{\sum_{i=1}^{ne} (\Delta U_{ik} - \mu_{\Delta U_k})^2}{ne - 1}} \quad (2.13b)$$

Thus, the set of modal strain energy differences of (2.12) can be normalized with respect to its mean and standard deviation. This method of normalization is referred to as the standard norm and the corresponding transformation equation is given by:

$$Z_{ik} = \frac{\Delta U_{ik} - \mu_{\Delta U_k}}{\sigma_{\Delta U_k}} \quad (2.14)$$

Where,  $Z_{ik}$  is the  $k^{\text{th}}$  modal strain energy difference normalized with respect to the mean and standard deviation of the strain energy differences of all elements.

## 2.4. Combining Damage Indictors and Data Fusion

The parameter of (2.14) can be viewed as a damage indicator for element  $i$  obtained from mode  $k$ . The simplest way to combine the indicators obtained from all available modes is to take the average; that is:

$$Z_i = \frac{1}{nm} \sum_{k=1}^{nm} Z_{ik} \quad (2.15)$$

Other methods can be formulated through the use of data fusion concepts. Data Fusion can be defined as the synergistic use of information from multiple sources in order to assist the understanding of a phenomenon (Gros, 1997). Fusion techniques are routinely applied for combining inspections from various types of sensors in Non-Destructive Evaluation (NDE) applications. In this context, this work uses data fusion tools to combine information from multiple mode shapes to localize damage. Figure 2.2 shows a schematic of the fusion process for damage localization. In the process, each pair of modes is assumed to be the equivalent of a statistical independent sensor.

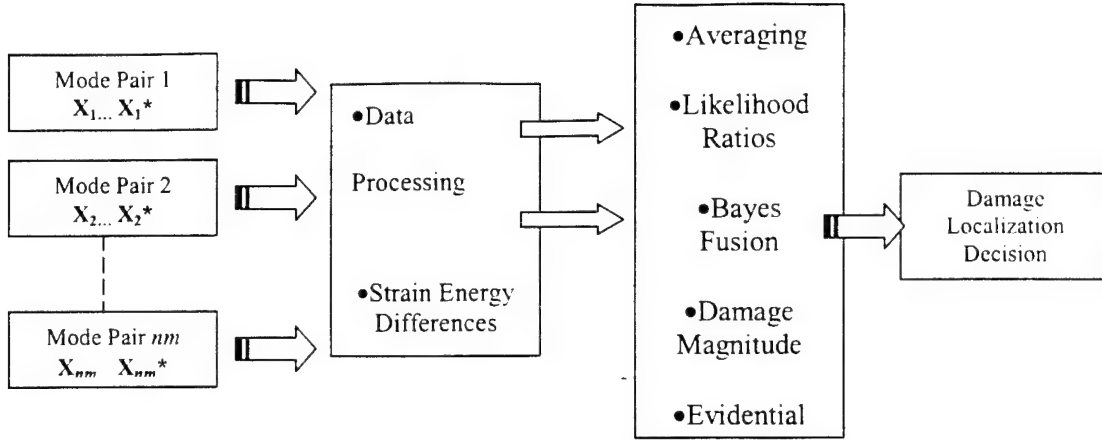


**Figure 2.2. Fusion Process for Damage Localization.**

Common methods of fusion include averaging, likelihood ratios, Bayes statistics, evidential reasoning and others; most of them employ statistics and probability theory to combine the information (Osegueda, *et al.* 2000a). These statistics arise by interpreting the distribution of the normalized strain energy differences of equation (2.14) of all the elements of a structure for a mode  $k$  as a random variable  $Z_k$  with a probability density function (PDF) as shown in Figure 2.3. Since the PDF may not follow a common distribution such as a Gaussian distribution, numerical estimates of the PDF can be obtained numerically using Kernel Density Estimators [20]. The fitted PDF provides the means to compute the probabilities by numerically integrating the area under the curve of  $F_{Z_k}$  (Silverman, 1994). The computed probabilities would support the hypotheses of damage ( $H_{oi}$ ) and no damage ( $H_{ai}$ ) at location  $i$  given the inspection event with the mode pair  $k$  ( $M_k$ ) (Osegueda, *et. al.*, 2000b).

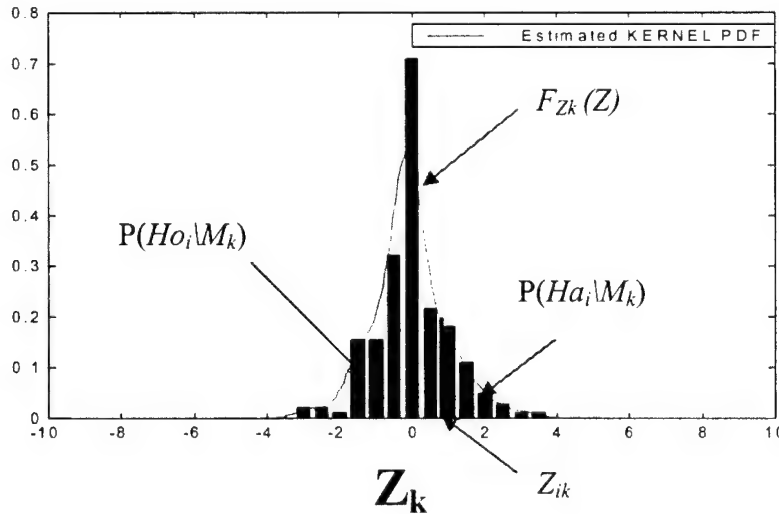


**Figure 2.3. PDF of Normalized Strain Energy Differences for mode  $k$ .**



For a given realization or event  $Z_k$  ( $z = Z_{ik}$ ), the conditional probabilities in support of Damage ( $Ho_i$ ) and No Damage ( $Ha_i$ ) at location  $i$ , given the inspection event of mode  $k$  ( $M_k$ ) (Osegueda *et al.*, 2000a; Pereyra *et al.*, 2000), are respectively:

$$P(Ho_i | M_k) = \int_{-\infty}^{z=Z_{ik}} f_{Z_k}(z) dz \quad (2.16a)$$

$$P(Ha_i | M_k) = 1 - P(Ho_i | M_k) \quad (2.16b)$$

These probabilities allow the combination of damage detection inspection from multiple modes.

### Likelihood Ratios

In context to probabilities, the features for each location  $i$  and mode  $k$  ( $M_k$ ), can be converted into probabilities by means of Equations (2.16.a) and (2.16b). From these a Damage Likelihood Ratio  $l_{ik}$  (Tappert, *et al.*, 1995) for each location  $i$  and mode  $k$  ( $M_k$ ), may be determined with the following expression:

$$l_{ik} = \frac{P(Ho_i | M_k)}{P(Ha_i | M_k)} \quad (2.17)$$

The ratios from multiple mode pairs are multiplied to determine a fused parameter  $t_i$ :

$$t_i = \prod_{k=1}^m l_{ik} \quad (2.18)$$

### Bayes Statistics

Averaging and the likelihood ratio approaches do not consider the ability and/or sensitivity of the modes to detect damage. It has been documented in the literature that damage is difficult to detect with a mode pair if the mode has a region of low strain energy at a possible damage location (Carrasco, *et al.*, 1997). Thus, the probabilities of a mode to detect damage and produce false calls are direct functions of the relative modal strain energy content and damage magnitude. Subjective models for the probability of detection (POD) and the probability of false calls (PFC) can be assumed as *prior* probabilities using log-logistics functions (Gros, 1997) of the relative strain energy content as shown in Figure 2.4.  $U_k$  is the strain energy of mode  $k$  and  $U_{kmax}$  is the maximum value of the strain energy stored in the mode; the constants  $a$  and  $b$  are subjective and can be adjusted from experimental observations. The prior probabilities of the inspection with mode  $k$  to support damage ( $Ho_i$ ) and no damage ( $Ha_i$ ) at location  $i$  are assumed respectively as:

$$P'(M_k | Ho_i) = POD_{ik} \overline{POD_{ik}} \quad (2.19a)$$

$$P'(M_k | Ha_i) = PFC_{ik} \overline{PFC_{ik}} \quad (2.19b)$$

Approaches following Bayes rules of inference have significance for damage detection where information available is invariably limited and subjective judgement is often necessary (Ang & Tang, 1975). Estimates of posterior probabilities of the inspection event with mode  $k$ , to support the hypotheses, can be made using Bayes Theorem with the following:

$$P''(M_k | Ho_i) = \frac{P(Ho_i | M_k) \cdot P'(M_k | Ho_i)}{\sum_{j=1}^m P(Ho_i | M_k) \cdot P'(M_k | Ho_i)} \quad (2.20a)$$

$$P''(M_k | Ha_i) = \frac{P(Ha_i | M_k) \cdot P'(M_k | Ha_i)}{\sum_{j=1}^m P(Ha_i | M_k) \cdot P'(M_k | Ha_i)} \quad (2.20b)$$

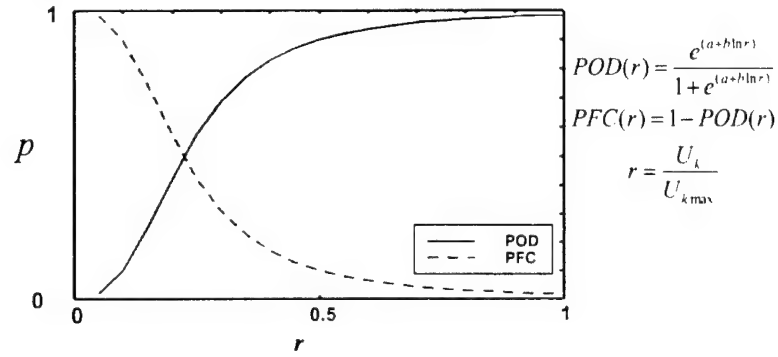


**Figure 2.4. Probability of Damage Detection Model.**

The total probabilities in support of the hypotheses damage ( $Ho_i$ ) and no damage ( $Ha_i$ ) at location  $i$  can be computed with:

$$P(Ho_i) = \sum_{k=1}^m P(Ho_i | M_k) \cdot P''(M_k | Ho_i) \quad (2.21a)$$

$$P(Ha_i) = \sum_{k=1}^m P(Ha_i | M_k) \cdot P''(M_k | Ha_i) \quad (2.21b)$$

A fused damage likelihood ratio  $l_{ik}$  for location  $i$  can be determined from the equations above:

$$l_{ik} = \frac{P(Ho_i)}{P(Ha_i)} \quad (2.22)$$

### Evidential Reasoning

Evidential reasoning referred to also, as the Dempster-Shafer theory is the generalization of the Bayesian method (Gros, 1997). For the damage detection problem  $Z_k$  provides evidence of

potential damage if the values are positive (support  $Ho_i$ ), or potential no damage if they are negative (support  $Ha_i$ ). Figure 2.5 illustrates the normalized strain energy differences for a given mode pair along a beam. Note how the positive and negative areas of  $Z_k$  (Figures 2.5b and 2.5c respectively) are used to build probability mass functions  $Pmf$  in support of the hypotheses by scaling and assuming the results to be probability masses.

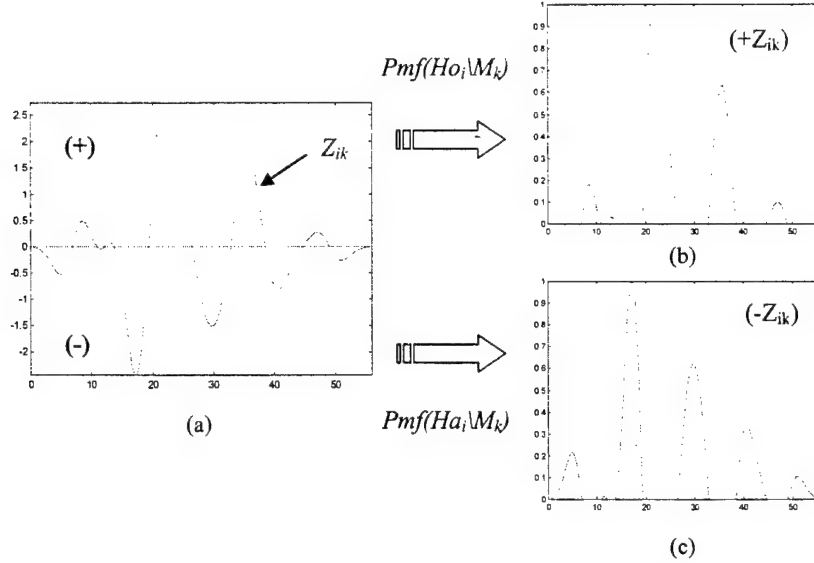


**Figure 2.5. Probability Mass Functions as Evidence in Support of  $Ho_i$  and  $Ha_i$ .**

This process yields discrete probability masses  $pm$  for all elements and modes which are can be expressed as:

$$pmf(Ho_i | M_k) = [pm_{ho_{1k}} .. pm_{ho_{2k}} ..... pm_{ho_{nek}}] \quad (2.23a)$$

$$pmf(Ha_i | M_k) = [pm_{ha_{1k}} .. pm_{ha_{2k}} ..... pm_{ha_{nek}}] \quad (2.23b)$$

The Belief ( $Bel$ ) that the hypotheses are true given the evidence in multiple modes is determined through Dempster's rule of combination (Gros, 1997). This involves the orthogonal sum of the probability masses with a re-scaling process which involves forcing the maximum value of the probability mass equal to a unit and is symbolized by:

$$Bel(Ho_i | M_1, ..., M_k) = \oplus \sum_{k=1}^{nm} pmf(Ho_i | M_k) \quad (2.24a)$$

$$Bel(Ha_i | M_1, ..., M_k) = \oplus \sum_{k=1}^{nm} pmf(Ha_i | M_k) \quad (2.24b)$$

Since location  $i$  is either damaged ( $Ho_i$ ) or undamaged ( $Ha_i$ ), the following relationship must be satisfied:

$$0 \leq Bel(Ho_i \cup Ha_i) \leq 1 \quad (2.25)$$

Plausibility ( $Pls$ ) of damage ( $Ho_i$ ) is defined as a measure of evidence that supports the hypothesis and is given by:

$$Pls(Ho_i) = 1 - Bel(Ha_i) \quad (2.26)$$

The combined range of values obtained for the Belief ( $Bel$ ) and Plausibility ( $Pls$ ) create evidential intervals from which decisions in favor of the hypothesis are made. Figure 2.6 illustrates the graphical representation of the evidential intervals associated with support of  $Ho_i$ .

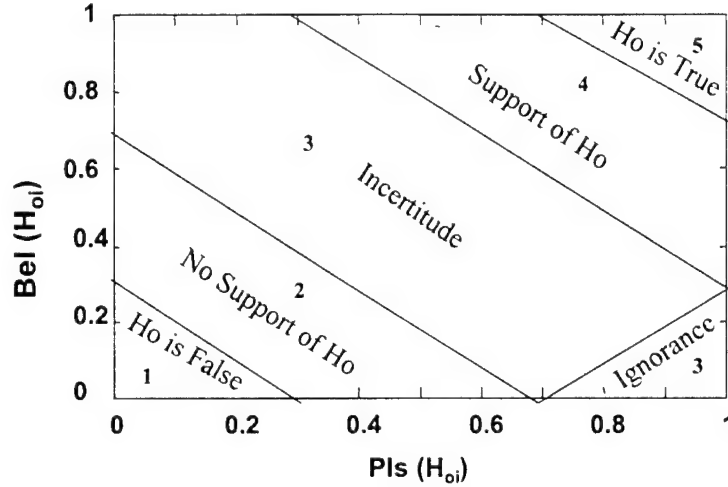


Figure 2.6. Evidential Intervals (Belief vs. Plausibility).

In order to visualize the intervals as a function of location within the structure, it is necessary to use the number code assigned in the graph. For example a certain location  $i$  along the beam has a plausibility of 0.79 and a belief of 0.83 in support of the hypotheses of damage ( $Ho_i$ ), it would be in zone 4.

### Damage Magnitude

Computations of damage magnitudes using (2.8) and (2.9) may also be used as a tool to support the decision that location  $i$  is damaged. However, these two expressions have numerical instabilities related to its energy content. First, the numerator of (2.8) may take values much greater than the denominator, and second, the denominator may approach zero. In both situations,  $\alpha_{ik}$  has a tendency to give a large value and approach infinity at certain locations. As a way to filter, Equation (2.9) can be averaged using the posterior probabilities of (2.20a) as weights. That is:

$$\alpha_i = \frac{\sum_{k=1}^m \alpha_{ik} P''(M_k | Ho_i)}{\sum_{k=1}^m P''(M_k | Ho_i)} \quad (2.27)$$

The posterior probabilities tend to approach zero at the locations with numerical instabilities.

### Probability Mass Function Formulation

The treatment of the normalized modal strain energy differences as statistical quantities permit the estimation of probabilities in support of damage at each location for each mode using (2.16a). These probabilities can be converted to probability masses. Define  $P_{D_{ik}}$  as the relative probability that element  $i$  is damaged in comparison to the rest of the elements of the structure as indicated by mode  $k$ . The parameter  $P_{D_{ik}}$  has the following property:

$$\sum_{i=1}^{ne} P_{D_{ik}} = 1 \quad (\text{for all } k = 1, 2, \dots, nm) \quad (2.28)$$

The collection of probability masses for a given mode gives rise to a probability mass function (PMF). The PMF gives the relative probability that an element is damaged according to mode  $k$ , and is expressed by the following set of probabilities:

$$PMF_k(X) = [P_{D_{1k}} \quad P_{D_{2k}} \quad \dots \quad P_{D_{ik}} \quad \dots \quad P_{D_{nek}}] \quad (k = 1, 2, \dots, nm) \quad (2.29)$$

A damage detection event may be defined as the union operator of all damage detection events with the individual modes. Each individual event is the event of detecting damage with each particular mode. Damage is located at elements where one or more of the modes indicate that damage is likely. Mathematically, this can be represented as:

$$D_i = \bigcup_{k=1}^{nm} D_{ik} \quad (\text{for all } i = 1, 2, \dots, ne) \quad (2.30)$$

Where  $D_i$  is the damage detection event at element  $i$ . Thus, the probability of detecting damage in element  $i$  is given by:

$$P_{D_i} = P(D_i) = P\left[\bigcup_{k=1}^{nm} D_{ik}\right] \quad (\text{for all } i = 1, 2, \dots, ne) \quad (2.31)$$

Where, the usually known rules for computing the probability of a union of events can then be applied. A convenient way of computing the probability of the union of events can be obtained by using deMorgan's rule. Thus,

$$\begin{aligned} P\left[\bigcup_{k=1}^{nm} D_{ik}\right] &= 1 - P^*\left(\bigcup_{k=1}^{nm} D_{ik}\right) \\ &= 1 - P(D_{i1}^* D_{i2}^* D_{i3}^* \dots D_{inm}^*) \quad (\text{for all } i = 1, 2, \dots, ne) \end{aligned} \quad (2.32)$$

Where the asterisk denotes complementary probability of the events.

### Weighted Averaging and PMF Formulations

Both, averaging and the PMF methods to combine information can be further refined by assuming that a certain level of modal strain energy is required in an element for that particular mode to be effective in detecting damage in that element. For example, a mode is insensitive to damage at those elements where the modal strain energy is zero or close to zero. Based on this criterion, a simple weight function can be assigned to the structural elements for each mode. A weight of 0 can be given to all elements that have values of modal strain energy less than a threshold, otherwise, a value of 1 is assigned. This weight function can be defined for the mode  $k$  in the undamaged and damaged states of the structure and it is used to filter out the irrelevant information from each mode. The modal weight function can be defined for the modes in the undamaged and damaged states of the structure. This function can be indicated as follows:

$$[W_k] = [W_{1k} \quad W_{2k} \quad \cdots \quad W_{ik} \quad \cdots \quad W_{nek}] \quad (k = 1, 2, \dots, nm) \quad (2.33a)$$

$$[\bar{W}_k] = [\bar{W}_{1k} \quad \bar{W}_{2k} \quad \cdots \quad \bar{W}_{ik} \quad \cdots \quad \bar{W}_{nek}] \quad (k = 1, 2, \dots, nm) \quad (2.33b)$$

Where,  $W_{ik}$  is the modal weight factor of the  $i^{\text{th}}$  element for mode  $k$  corresponding to the undamaged structure. This factor takes values of zero or one according to criterion mentioned above. The Weighted Average Standard Norm Method (WASN) can be formulated with the following expression:

$$\tilde{Z}_i = \frac{\sum_{k=1}^{nm} Z_{ik} W_{ik} \bar{W}_{ik}}{\sum_{k=1}^{nm} W_{ik} \bar{W}_{ik}} \quad (2.34)$$

The above expression forms the basis of the Weighted Average Standard Norm (WASN) method. The PMF formulation can also be slightly modified so that the PMF function only considers elements of modal strain energy levels larger than the threshold. This can be accomplished by multiplying the terms of (2.11) by the modal weight factors:

$$[\Delta U_k] = [W_{1k} \bar{W}_{1k} \Delta U_{1k} \quad \cdots \quad W_{ik} \bar{W}_{ik} \Delta U_{ik} \quad \cdots \quad W_{nek} \bar{W}_{nek} \Delta U_{nek}] \quad (k = 1, 2, \dots, nm) \quad (2.35)$$

The rest of the PMF formulation is exactly identical to Equations (2.28) through (2.32). This formulation is referred here as the Weighted Probability Mass Function (WPMF) method. Nonetheless, all four formulations to locate damage described in this chapter are based on modal strain energy differences between the undamaged and damaged states of the structure.

## **2.5. Limitations of Modal Strain Energy Methods**

The abilities of strain energy methods to detect and locate damage are limited by the following factors:

- (1) The number of available modes.
- (2) Quality of the available modes.
- (3) Numerical techniques to estimate the complete modes to evaluate the strain energy levels of all elements.

Typically, the greater the number of modes available, the greater the chances to locate damage in all parts of the structure. The quality of the modes is in reality dictated by the type of instrumentation used and the electronic noise in the instruments. The greater the noise, the greater the uncertainties on the amplitude of the mode shape. Furthermore, these uncertainties will adversely propagate into the determination of the mode shape components at those degrees of freedom not instrumented and into the modal strain energy. Therefore, one of the critical elements in the detection of damage in a complex structure using strain energy methods is the calculation of the mode shape components at the rest of the degrees of freedom. This is accomplished by curve-fitting and/or the use of finite element models as described in Appendix A.





## CHAPTER 3

### VIBRATIONAL NON-DESTRUCTIVE EVALUATION IN BEAMS

#### 3.1 Introduction

The work described in this chapter was performed by Lopez (2000) for the purpose of developing the vibrational damage evaluation techniques and to refine the fusion methods that are required to extract and combine the features from the modal strain energy differences of several modes. The fusion methods described in the previous Chapter were tested using data obtained from experimental tests conducted on two different C-shaped aluminum beams. The beams were simply supported at 48 inches on two 16-inch high, structural frames, with 6-inch overhangs at each end. Modal vibration testing was conducted on the beams to obtain their dynamic characteristics including, resonant frequencies, damping ratios and mode shapes. The measurement instrumentation attached to the aluminum channel section consisted of 13 accelerometers placed 4 inches apart and one force transducer. The excitation force was provided by an electro-magnetic shaker. The two aluminum beams were subjected to 54 damage scenarios at different magnitudes and included damage at multiple locations. The different damage magnitudes helped test the ability and sensitivity of the methods to detect small defects (flaws or cuts) on the system. For each baseline and damage scenario, sets of FRFs and Coherence functions, which were used to extract the modal parameters, were obtained. Only the first five bending modes were considered. Graphical representations of the fusion results are provided. They assist in the visualization of potential damage.

#### 3.2 Description of Structural System

The fusion methodologies described in Chapter 2 were tested using data obtained from experimental tests conducted on two different C-shaped aluminum beams. The C-shaped section beams were 60 inches in length, with a thickness of 1/8 inch, and width and depth dimensions of one inch. The beams were simply supported at 48 inches on two 16-inch high supports (for shaker positioning) with 6-inch overhangs at each end. Modal vibration testing was conducted on the beams to obtain their dynamic characteristics including, resonant frequencies, damping ratios and mode shapes. The measurement instrumentation attached to the aluminum channel section consisted of 13 PCB accelerometers placed 4 inches from each other and one PCB force transducer. Hexagonal mounts were glued to the beams to provide a mount surface for the accelerometers. To provide excitation force to the system, a 2 lb. electro-magnetic shaker was used. The structural system is as illustrated in Figure 3.1.

#### 3.3 Instrumentation

The instrumentation was divided into two main parts, body and central processing unit. The main component of the instrumentation's body was a multiple channel Zonic Analog to Digital (A/D) analyzer workstation. This workstation is a real time Fast Fourier Transform (FFT) computational analyzer and data acquisition system. A PCB Piezotronics ICD Signal Conditioner (SC) provided the capability of acquiring the output from 13 accelerometers, as well as the input from the force transducer of the electro-magnetic shaker. A Realistic power

amplifier amplified the signal coming from the Zonic A/D analyzer to the V411 model shaker, capable of producing a very dynamic sensitive force and a maximum displacement of 0.35 inches. The instrumentation set-up and instrumentation are shown in Figure 3.2.

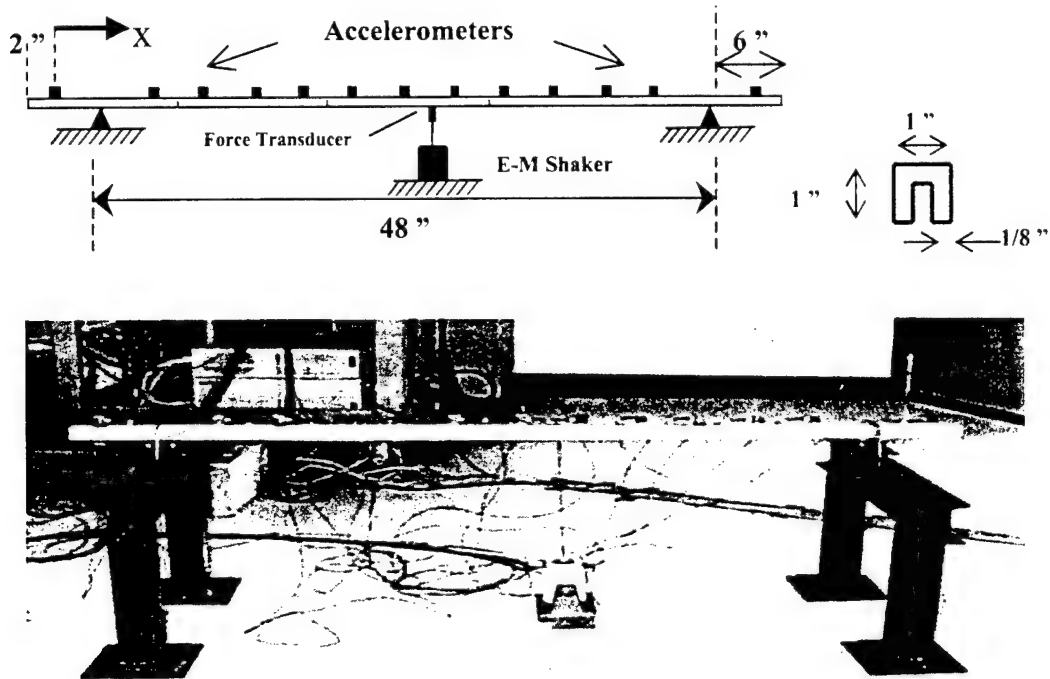


**Figure 3.1. Structural System Set-Up.**

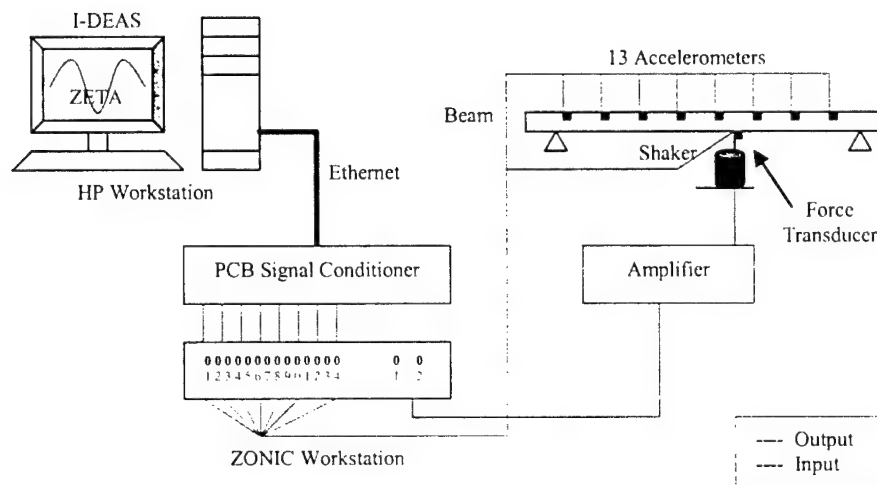


**Figure 3.2. Schematic of Instrumentation.**

### 3.4 Experimental Set-Up

To provide excitation, a 2-lb. shaker was placed directly under each beam, located at coordinates 33 and 32 in. from the origin (first accelerometer along the beam  $x = 0$ ) for the first and second beam respectively. The particular location of the shaker was chosen from analyzing previous experimental results. The location chosen contains significant modal amplitudes for the first five bending modes. The shaker had a steel stinger and a force transducer glued to the lower surface of the beam using a mounting stud. Accelerometers were equally spaced at 4 in., mounted on the upper surface of the beam as shown in Figure 3.3. The accelerometers measured the beam's transverse response (accelerations) and the force transducer measured the magnitude of the input signal provided to the system.

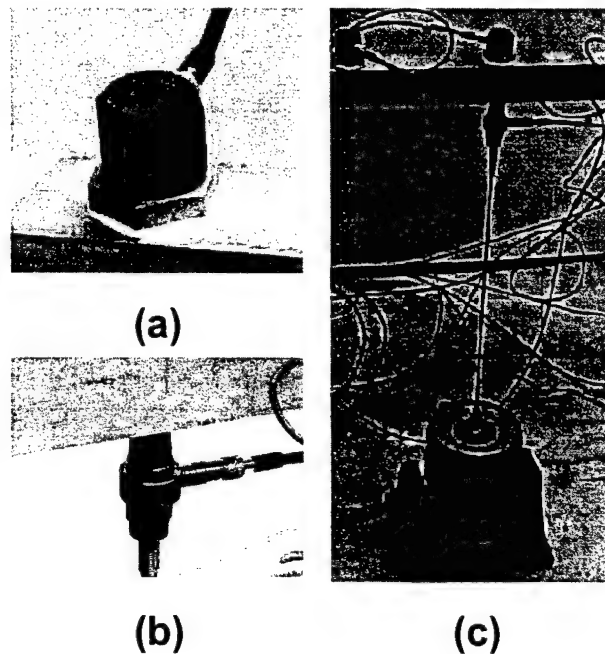


**Figure 3.3. (a) Accelerometer with Mounting Stud, (b) Force Transducer and (c) Electromagnetic Shaker.**

### 3.5 Damage Scenarios

The two aluminum beams were divided into 5 damage cases subdivided in 54 damages. Different progressive saw cuts were made at  $a/d$  ratios of 2, 5, 6, 10, 15, 20, 25, 30, 40, 45 and 50 % these varying from case to case. Here,  $a$  is the depth of the cut and  $d$  is the depth of the beam. Descriptions of the damage scenarios for each beam are presented in Tables 3.1 and 3.2. Damages, manifested as saw cuts, are illustrated in Figure 3.4 and were introduced using a dremel tool. The inflicted saw cuts had a width of 1/16 of an inch. The different damage magnitudes helped test the ability and sensitivity of the method to detect small defects (flaws or cuts) on the system.

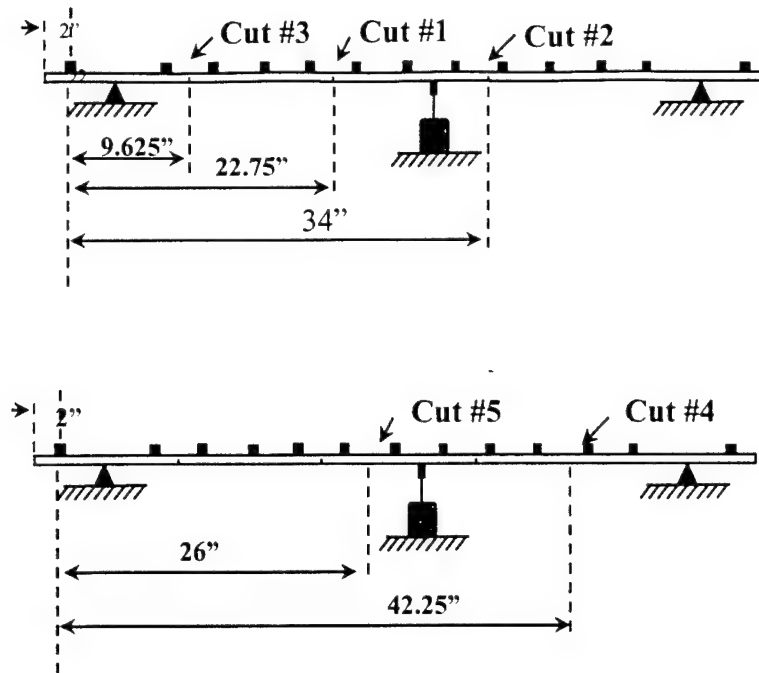


Figure 3.4. Damage Scenarios for Beams 1 & 2.

Table 3.1. Description of Damage Scenarios for Beam #1.

Case	Damage	Location X (in.)	Magnitude (a/d)
1	C1dam1	22.75	0.02
	C1dam2	22.75	0.05
	C1dam3	22.75	0.10
	C1dam4	22.75	0.20
	C1dam5	22.75	0.30
	C1dam6	22.75	0.50
2	C2dam1	34.125 + C1d6	0.02
	C2dam2	34.125 + C1d6	0.05
	C2dam3	34.125 + C1d6	0.10
	C2dam4	34.125 + C1d6	0.20
	C2dam5	34.125 + C1d6	0.30
	C2dam6	34.125 + C1d6	0.50
3	C3dam1	9.625 + C1d6 + C2d6	0.02
	C3dam2	9.625 + C1d6 + C2d6	0.05
	C3dam3	9.625 + C1d6 + C2d6	0.10
	C3dam4	9.625 + C1d6 + C2d6	0.20
	C3dam5	9.625 + C1d6 + C2d6	0.30
	C3dam6	9.625 + C1d6 + C2d6	0.50

**Table 3.2. Description of Damage Scenarios for Beam #2.**

Case	Damage	Location X (in.)	Magnitude (a/d)
4	C4dam1	42.25	0.02
	C4dam2	42.25	0.05
	C4dam3	42.25	0.10
	C4dam4	42.25	0.20
	C4dam5	42.25	0.30
	C4dam6	42.25	0.50
5	C5dam1	26 + C4d6	0.02
	C5dam2	26 + C4d6	0.05
	C5dam3	26 + C4d6	0.10
	C5dam4	26 + C4d6	0.20
	C5dam5	26 + C4d6	0.30
	C5dam6	26 + C4d6	0.50

### 3.6 Experimental Procedure

Prior to any formal testing for data acquisition, the accelerometers and force transducer were properly calibrated to assure data acquisition of the highest quality measurements possible. The beam was mounted onto the testing system and was excited by means of the shaker. This force was measured to guarantee that experimental cases had excitation forces as similar as possible.

The experimental procedure to measure the dynamic characteristics of the beam can be summarized as follows (refer to Figure 3.2):

1. -The Zonic Analog to Digital (A/D) analyzer workstation, in conjunction with the ZETA software, generated a random signal with a frequency range between 10-1000 Hz. This frequency included various natural frequencies of the system.
2. -The Power Amplifier amplified the signal coming out from the ZONIC Digital S. C. Module in order to give enough energy to the electro-magnetic shaker.
3. -The electro-magnetic shaker produced a dynamic excitation on the aluminum beam. The force signal was preset to produce a bandpass waveform random signal with a burst time 0.8 seconds on and 0.7 seconds off.
4. -The 13 accelerometers sensed the acceleration time histories of the beam using 10 averages. The acceleration signals were channeled into the PCB Signal Conditioner.
5. -The signals were then filtered into the ZONIC channel data acquisition system. The time histories of all thirteen accelerometers and force transducer were measured and recorded. The Zeta data acquisition was set to use block size of 4096 points with a full-scale frequency of 1000 Hz., on a transient capture mode.
6. -Ethernet was used to communicate between the Zonic workstation and the host computer (Hewlett Packard workstation).

The modal vibration tests were conducted on the baseline and damage scenarios.

The test measurements consisted of a series of Frequency Response Functions (FRF's) corresponding to each of the accelerometers mounted onto the beam. The FRF's were used for the extraction of the modal parameters through the use of SDRC's I-DEAS/TDAS modal

analysis software package (Lawry, 1996). The modal parameters, with primarily focus of first five mode shapes, were extracted using the polyreference curve-fitting technique method built into I-DEAS. Figure 3.5 illustrates the typical mode shapes corresponding to the measured data sets.

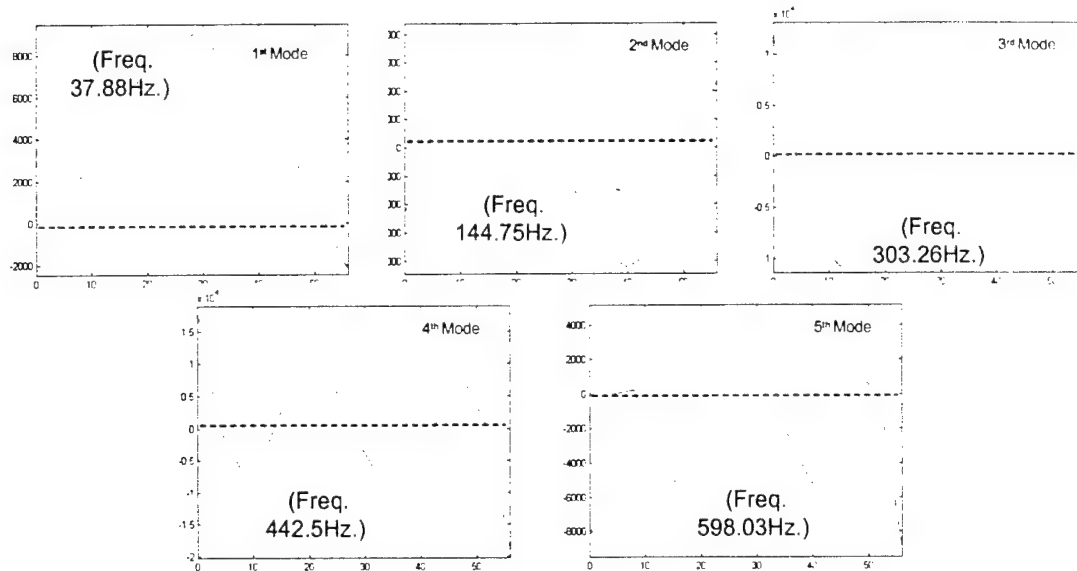


**Figure 3.5. Typical Mode Shapes Corresponding to Measured Data (base\_01).**

### 3.7 Damage Localization Process

The process starts with the extraction of the modal parameters from the FRF's to obtain the vibrational characteristics of the structure in both the original and degraded state. The five lower bending mode shapes were obtained and exported to a Universal File Format (UNV) for processing. The second step was to obtain the modal bending curvatures for all the modes of the undamaged and damaged structure, using the iterative curve-fit method described in Section A.2 of Appendix A. The curvatures were then saved in files containing now a much denser set of points than those obtained experimentally; given that an initial 15 measured points 4 inches apart were registered, and the program output provided interpolated values at 0.2 in. increments, for a total of 281. The third step in the process was the computation of the modal strain energy from Equation 2.10 using the curvatures obtained from the curve-fit algorithm. The next step was to identify pairs of modes between the undamaged and damaged structure. Then, the modal strain energy differences were computed between the identified mode pairs normalized with respect to the mean and standard deviation by means of Equation (2.14). The fifth step involved the use of Kernel density estimators' to fit a PDF and assign probabilities to the strain energy differences of each mode pair identified according to Equation (2.16). The output of the processed information was fused using some of the techniques described in Chapter 2. These were averaging, likelihood ratio, Bayes fusion, damage magnitude and evidential reasoning. The last and most important step of all involves the graphic representation of the fusion results, these graphs provide global visualization of the results for damage assessing and localization.

were averaging, likelihood ratio, Bayes fusion, damage magnitude and evidential reasoning. The last and most important step of all involves the graphic representation of the fusion results, these graphs provide global visualization of the results for damage assessing and localization.

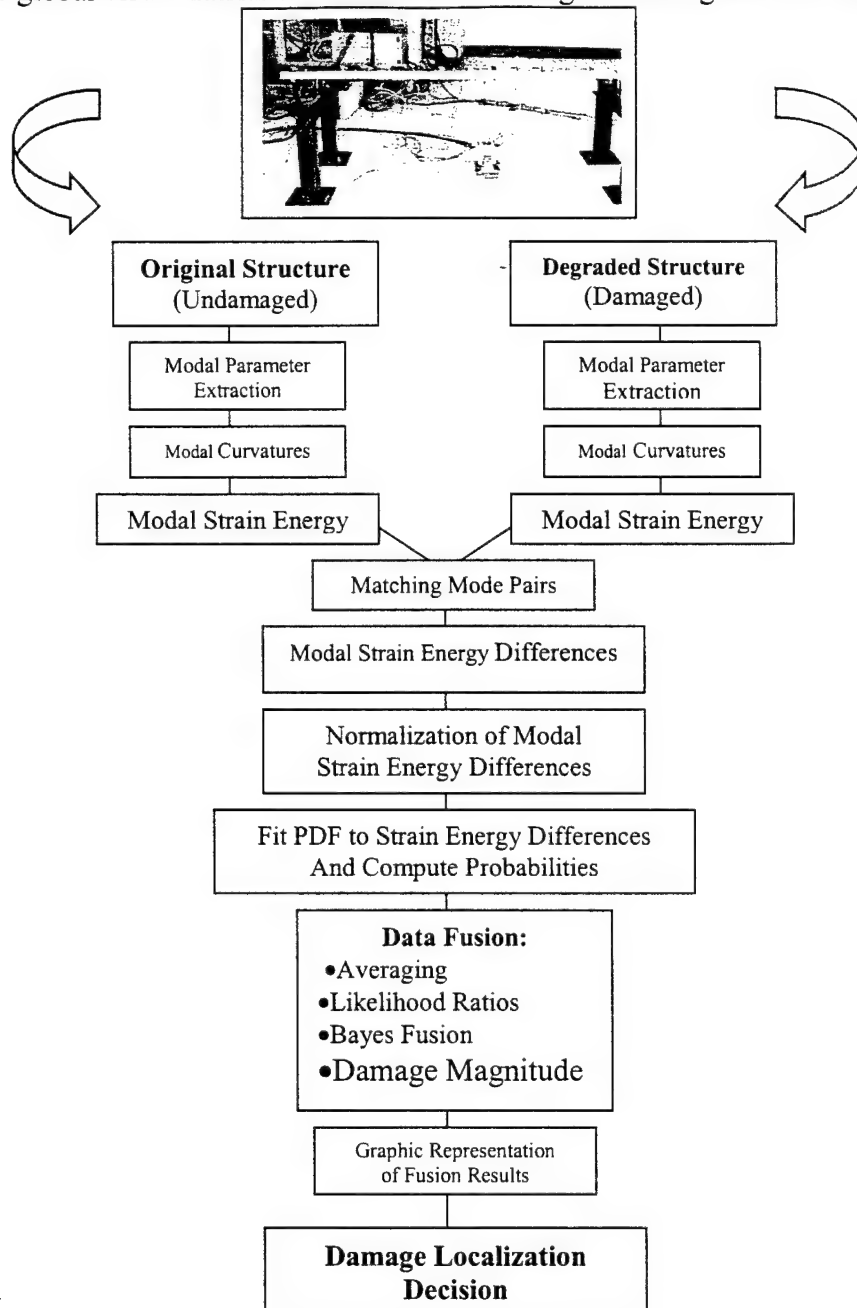


**Figure 3.6. Damage Localization Process Flow Chart.**



### 3.8 Damage Assessment

Damage indicators obtained from all the available pairs of matching modes were fused applying the data fusion techniques described in Chapter 2. The results were plotted in a figure consisting of four plots and a color code. A sample set of results is included in Figure 3.7. The first plot in the figure illustrates the **(a) average** normalized strain energy differences of Equation (2.15) for the beam location vs. the x-coordinate of the location. The averages of the normalized strain energy differences  $Z_i$  provide good indications of presence of damage. Positive differences of strain energy are indicators of possible damage; the graph's vertical axis is set to visualize only the positive values. The second subplot shows the **(b) likelihood ratios** computed with Equation (2.18) in a semi-log scale which indicates the ratio of the probability of damage  $P(Ho_i)$  to that of no damage  $P(Ha_i)$ . The third graph illustrates the **(c) Bayes fusion** computed from Equation (2.22), which involves the total and posterior probabilities of Equations (2.19) through (2.21). This graph should be analyzed with caution; the calculation of posterior probabilities implies that if the *prior* probability of their being damage is high for a certain location  $i$ , its *posterior* probability will tend to increase if the probability of detection (POD) for that mode is also high, meanwhile the posterior probability of not being damaged decreases. Thus the ratio between these quantities will have a tendency of revealing more peaks than the likelihood ratio and consequently false indications may arise when computing it. The **(d) damage magnitude** is shown in the fourth graph, computed with Equation (2.27); damage is indicated with fraction stiffness loss at a particular location throughout the structure. This graph helps support decision-making and is not exactly a way of fusion, although it is one of the more truthful and reliable methods, since considerable losses in stiffness on the system will be immediately sensed and detected. The results of the **(e) Dempster-Shafer** evidential reasoning are shown with the color code in the x-axis of each graph. This is done to facilitate visualization when analyzing each method individually and not as part of the Fusion Process. This color code represents the interval in which the belief-plausibility coordinate falls in Figure 2.3. The belief and plausibility are computed using Equations (2.23) through (2.26). From the evidential color codes assigned the most important intervals are those that tend to reddish like tonality. The most important are: red #5 and magenta #4 (reddish purple like) intervals that support true presence and evidence of damage respectively. Note that if a method has a damage indication and the evidential reasoning supports damage, then most likely that location is damaged. This of all the fusion methodologies is the most assertive, although false calls are not rare. In a majority of the cases the evidential intervals will support presence of damage where damage is true. Thus, this method is by far the most reliable when assessing damage, with exceptions in cases where the resulting intervals when *fused* with the other methods resulted in a *false call* (damage indication where damage is not present). It is to be noted that positive peaks on the plots are to be considered as possible damage indications with exception to the *damage magnitude* plot where negative peak values are indicators. Each of the plots generated for each of the cases was considered individually and the results were summarized.

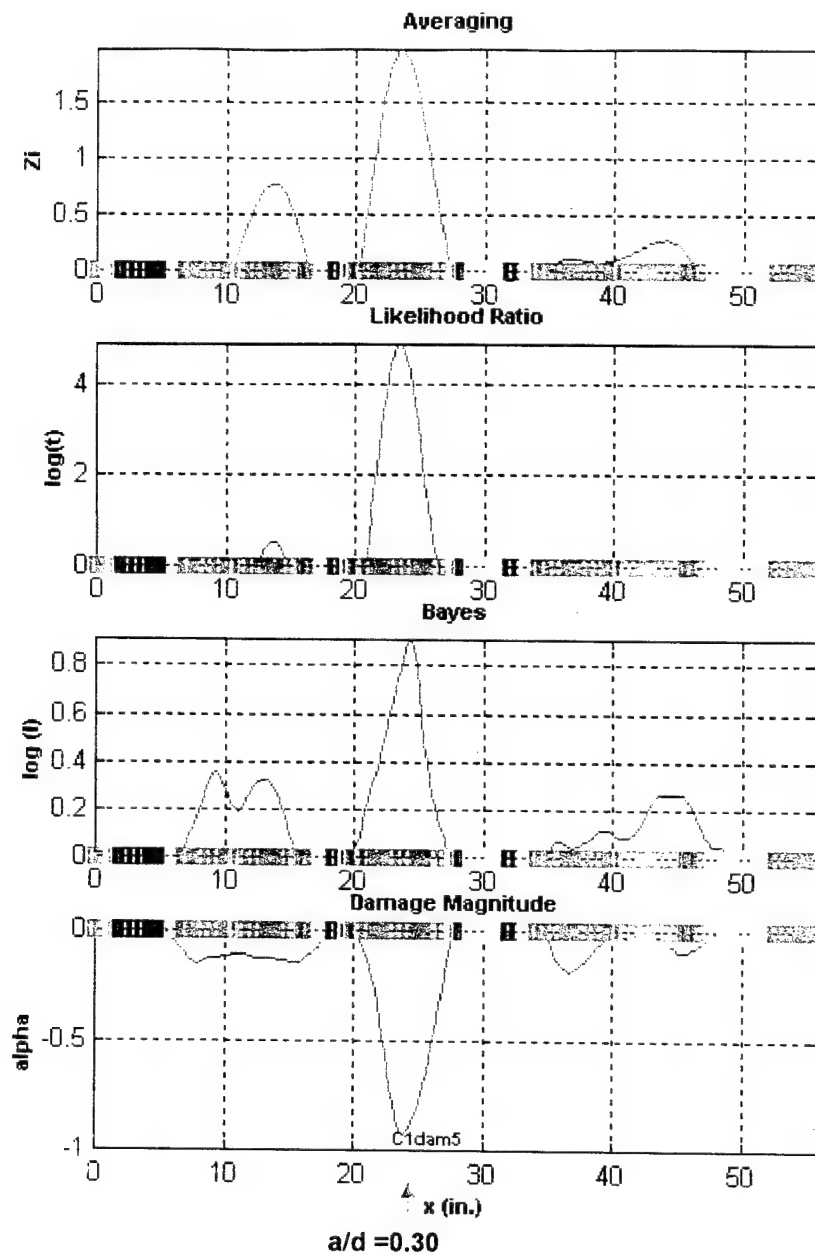


Figure 3.7. Fusion Results for C1dam5.

In order to further combine all the fusion methods and facilitate the damage assessment task, weights were given to each of the methods, the weights were subjective. *Evidential reasoning* is fundamental in the fusion process and was awarded the largest weight value, and in similar fashion the *average* method also has great relevance throughout the process, both provide the best results. Damage magnitude also represents indications of damage quite effectively and contributes to the damage assessing procedure, but is not as relevant as the methods previously discussed. The *likelihood* methodology had numerous indications of damage for those locations for which the ratio of the probability of damage to that of no damage is greater than one and *Bayes* fusion provided a large number of false indications; thus, lower weights were assigned to these two methods. The weights assigned to each method were: a) *averaging* – 25%, b) *likelihood ratio* – 10%, c) *Bayes fusion* – 17.5%, c) *damage magnitude* – 27.5% and d) *evidential reasoning* – 27.5 %.

The process is illustrated using the example of Figure 3.7 corresponding to case *C1dam5*. The first case and fifth damage magnitude inflicted on beam number 1. The actual damage location and magnitude is shown in the figure. Each graph is reviewed individually as follows:

- a) *Evidential reasoning*.- The color code plotted along the beam indicates support of evidence of damage in the ranges of : 11 – 14", 21 – 25" and 41 – 43". The evidential reasoning color code is graphed along the x-axis of each plot to simplify the damage detection and assessment. These three ranges are assigned a value of 1.
- b) *Averaging*.- The graph depicts 3 major peaks around the ranges of: 12 - 14", 22 – 24", and 44 – 45", all three within the ranges of evidential support. Thus, it suggests three damage locations. These three ranges are assigned a value of 1.
- c) *Likelihood ratios*.- This method suggests two damage locations at 12 – 14" and 22 – 24". The two ranges are assigned a value of 1.
- d) *Bayes fusion*.- Four peaks are present in the ranges of: 8 – 9", 12 – 14", 23 – 25", 37 – 39", and 44 – 45". However, the 8-9" range is outside the range of evidential support and is not further considered. Also note that the range of 44 to 45 inches is barely outside the supported range by the evidential reasoning approach. The ranges of 12-14" and 23-25" are assigned values of 1. The one for 44 - 45" is assigned a value of 0.5.
- e) *Damage magnitude*.- Five peaks are encountered throughout the graph but only the ranges of 15 – 17" and 22 – 24" are supported by the evidence. A value of 0.5 is assigned to the first interval and a 1 for the second interval.

**Table 3.3. Summary of Fusion Results for C1dam5.**

Range	Average	Likelihood	Bayes	Damage	E.I. Code	Decision	Percent Indicator	False Call
12 - 14.	1	1	1	0.5	1	damage	90.0%	
22 - 24	1	1	1	1	1	damage	100.0%	1
44 - 45	1	0	0.5	0	1	No damage	61.3%	

The results of the evaluation are summarized in Table 3.3. Only the ranges supported by evidential reasoning were considered. The values of the table are then multiplied by the corresponding weights and the results are added. This is illustrated as the percent indicator. A

threshold is then established to make a decision. For this set of experiments a value of 72.5% is chosen. If the percent of damage indication is greater than the threshold, then the location is damaged, otherwise, there is not enough evidence to conclude that it is damaged. Then the prediction results are compared to the actual damaged location. It is concluded that the actual damage was detected at the correct location and that a false positive (or false call) is at the range of 12-14 inches. A similar approach was followed for all the damage cases considered in this study.

The procedure described above was applied to each of the thirty damage scenarios comprising a total of 54 damage locations. Tables 3.4 and 3.5 list a summary of the results from the fusion techniques described above for Beams 1 and 2, respectively. By observing both tables, the single fusion technique that provided the best detectability was averaging (92.6%), followed by the evidential reasoning method (90.7%). When all fusion methods are combined 48 of the 54 damages were detected. Furthermore, averaging also provided the least localization error. The likelihood ratio method exhibited the poorest detectability (74.1%) because of its tendency to intensify large-magnitude damages.

The numbers presented in the two tables provide a general view of the performance of the methods to detect damage.

- 1) The damage detectability was 100% for Beam #2 and 83% for Beam 1; the detectability of the two beams combined was 88%.
- 2) The damages that were not detected typically consisted of a small magnitude accompanied with a large damage at another location.
- 3) The single fusion technique that provided the best detectability was averaging, followed by the Bayes fusion methods.
- 4) Averaging also provided the least localization error.
- 5) The likelihood ratio method exhibited the poorest detectability (74.1%) because of its tendency to intensify large-magnitude damages.
- 6) The Bayes fusion method proved extremely valuable in enhancing the detection for the small-magnitude damage, at the expense of producing more false calls than the other methods.
- 7) The number of false positives for the two beams combined was 20 locations out of a total of 54 damage locations.

**Table 3.4. Detectability Results for Damage Cases in Beam 1.**

Case		No. of Damages	Cut No.	Ave.	L.R.	Bayes	Dam. Mag.	Evid. Reas.	NFP	Decision
C1dam1	1	1	1	1	0	0	0.5	1	2	0
C1dam2	1	1	1	1	1	1	1	1	2	1
C1dam3	1	1	1	1	1	0.5	1	1	0	1
C1dam4	1	1	1	1	1	0.5	1	1	2	1
C1dam5	1	1	1	1	1	1	1	1	1	1
C1dam6	1	1	1	1	1	1	1	1	0	1
C2dam1	2	1	1	1	1	1	1	1	2	1
		2	1	0	1	0.5	1	1		1
C2dam2	2	1	1	1	1	1	1	1	0	1
		2	0	0	0	0	0	0		0
C2dam3	2	1	1	1	1	1	1	1	0	1
		2	0	0	1	0	0	0		0
C2dam4	2	1	1	1	1	1	1	1	0	1
		2	1	0	1	0.5	1	1		1
C2dam5	2	1	1	1	1	1	1	1	0	1
		2	1	0	1	0.5	1	1		1
C2dam6	2	1	1	0	0.5	1	1	1	1	1
		2	0	0	0.5	0.5	0	0		0
C3dam1	3	1	1	1	1	1	1	1	0	1
		2	1	1	1	1	1	1		1
		3	0	0	0	0	0	0		0
C3dam2	3	1	1	1	1	1	1	1	0	1
		2	1	1	1	1	1	1		1
		3	1	0	1	0.5	0	0		0
C3dam3	3	1	1	1	1	1	1	1	0	1
		2	1	1	1	0.5	1	1		1
		3	1	0	1	1	1	1		1
C3dam4	3	1	1	1	1	1	1	1	0	1
		2	1	1	1	1	1	1		1
		3	1	1	1	0.5	1	1		1
C3dam5	3	1	1	1	1	1	1	1	0	1
		2	1	1	1	0.5	1	1		1
		3	1	1	1	1	1	1		1
C3dam6	3	1	1	1	1	1	1	1	0	1
		2	1	1	1	1	1	1		1
		3	1	1	1	1	1	1		1
Totals		36		32	25	31	28.5	31	10	30
Detectability				89%	69%	86%	79%	86%		83%

**Table 3.5. Detectability Results for Damage Cases in Beam 2.**

Case	No. of Damages	Cut No.	Ave.	L.R.	Bayes	Dam. Mag.	Evid. Reas.	NFP	Decision
C4dam1	1	4	1	1	0.5	1	1	1	1
C4dam2	1	4	1	1	1	1	1	1	1
C4dam3	1	4	1	1	0.5	1	1	3	1
C4dam4	1	4	1	1	1	1	1	2	1
C4dam5	1	4	1	1	0.5	1	1	1	1
C4dam6	1	4	1	1	1	1	1	0	1
C5dam1	2	4	1	1	1	1	1	1	1
		5	1	0	1	1	1		1
C5dam2	2	4	1	1	1	1	1	1	1
		5	1	0	1	1	1		1
C5dam3	2	4	1	1	1	1	1	0	1
		5	1	0	0.5	1	1		1
C5dam4	2	4	1	1	1	1	1	0	1
		5	1	1	1	1	1		1
C5dam5	2	4	1	1	1	1	1	0	1
		5	1	1	1	1	1		1
C5dam6	2	4	1	1	1	1	1	0	1
		5	1	1	1	1	1		1
Totals	18		18	15	16	18	18	10	18
Detectability			100%	83%	89%	100%	100%	--	100%

### 3.9 Summary

The work summarized in this chapter was performed for the purpose of developing the vibrational damage evaluation techniques and to refine the fusion methods that are required to extract and combined the features from the modal strain energy differences from several modes. Of the methods considered, it is concluded that averaging, evidential reasoning and Bayes fusion are good methods to combine the information. This work also proved that damage detection is possible and viable to be applied to other types of structures. They seem to have a limitation on the size of defect they can detect. Obviously, the features on the global vibrational characteristics due to small defects may get obscured by the presence of noise and other forms of errors.

This work however served as the basis for the development of the techniques applied to more complicated structures.



## CHAPTER 4

### EXPERIMENTAL PROGRAM IN STIFFENED PLATE SPECIMEN

#### 4.1 Introduction

This Chapter describes the work performed to localize damage in a laboratory structure resembling aircraft construction using modal measurements and fusion techniques. The techniques considered were averaging, likelihood ratios and evidential reasoning.

The laboratory structure was a stiffened plate fabricated with aluminum sheet riveted to aluminum C-sections functioning as stringers and ribs. Two shakers were used at unsymmetrical points of the structure providing input force excitation. A laser Doppler Velocimeter (LDV) was used to sample the structure's response on the skin surface. The model was subjected to 22 different damage cases inflicted at eight different zones. The damage consisted of removal of bolts and cuts in the stiffening elements. Both forms of damage were caused at single and multiple locations. For each damage and baseline case, the FRF and Coherence functions with respect to two shakers were collected and processed to extract the vibrational characteristics. The modal assurance criterion (MAC) was used to correlate the mode shapes of the baseline to those of the damaged structure. The mode shapes were subjected to a curve-fit procedure to estimate modal bending and twisting curvatures of the front plate. These curvatures permitted the determination of the modal strain energies. The modal strain energy differences were determined for each mode and normalized using the standard norm. The damage indicators obtained from all available pairs of matching modes were combined by averaging the indicators. The results are presented in the form of damage maps.

The experimental data was also used to obtain damage detection using Likelihood Ratio and Evidential Reasoning. The only cases considered were cut damages in the stiffening elements. The statistical distribution of the normalized modal strain energy differences was approximated using the Kernel Density Estimator to obtain probabilities supporting damage and no-damage given the modal information. From these probabilities, damage likelihood ratios were obtained for all locations. The second process used techniques of evidential reasoning to determine belief and plausibility in support of damage given the evidence in the modal strain energy differences. The contents of this chapter are based on the work of Pereyra (1998) and Pereyra *et al.* (1999).

#### 4.2 Description of the Stiffened Plate Model

Figures 4.1 and 4.2 illustrate the front and rear views of the stiffened plate model, respectively. The stiffened plate was a  $\frac{1}{8}$ -inch thick aluminum sheet, 48 by 96 inches, with thirteen vertical ribs and two horizontal stringers. Aluminum channels of 1" x 1" x  $\frac{1}{8}$ " were used as the ribs and stringers. The ribs were separated 7.5 inches from each other; the two



horizontal stringers were spaced at 21 inches. The vertical ribs were 47 inches in length and were connected to the aluminum sheet by a line of 29 round head 10-32 x 1/2" aluminum bolts spaced at 1.5 inches. The rib's bolts were tightened to the sheet using aluminum washers at both sides of the plate and steel lock nuts. The two horizontal stringers were 95.5 inches long; these were fastened to the vertical ribs by one line of 13 bolts at 7.5 inches. The stringers were attached to the ribs using the same type of bolts and lock nuts as the ribs-sheet plate connection.

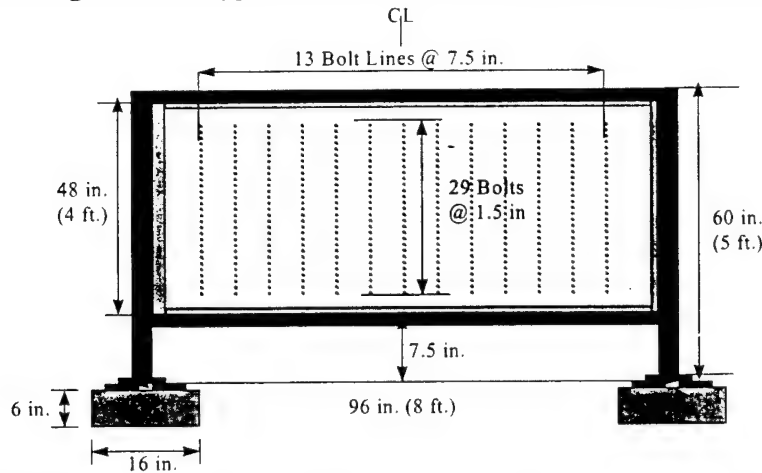


**Figure 4.1. Front View of Experimental Stiffened Plate Model.**

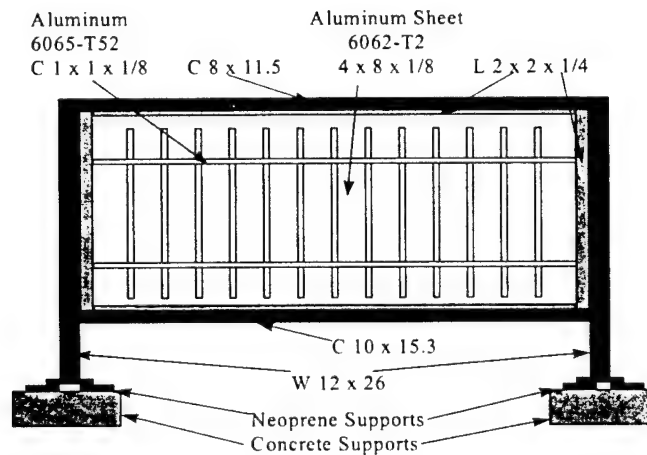


**Figure 4.2. Rear View of Experimental Stiffened Plate Model.**

### 4.3 Instrumentation and Experimental Procedure

The instrumentation for the experiments is illustrated in the diagram of Figure 4.3. The instrumentation was divided into two principal parts, body and central processing unit. The main component of the instrumentation's body was a multiple channel Zonic Analog to Digital (A/D) analyzer workstation. This workstation is a real time, Fast Fourier Transform computational analyzer and data acquisition system. Five input and four output channels of this system were used for the experiment. Four of the input channels extracted the signals read through the PCB Piezotronics ICD Signal Conditioner (SC) from two accelerometers and two force transducers

attached to the test article. The remaining input channel acquired the signals of the velocities sensed by the Ometron Scanning Laser Vibrometer (LDV) at different points of the stiffened-plate model. Two of the output channels of the Zonic system were used to generate signals through power amplifiers to control the electromagnetic shakers. The model shakers used were LDS brand, Model V411, capable of producing up to 44 lb of excitation and up to a frequency reaching 9 kHz. The remaining two output channels were connected to a Voltage Divider (VD) that controlled the movements of mirrors for targeting the laser beam of the LDV head. All the operations performed by the Zonic workstation were controlled and permanently stored by an HP computer that constituted the central processing unit of the instrumentation. The data was processed with the aid of an interface software. Such software was a Zonic A&D Engineering and Test Analysis (ZETA) and a user interface written specifically to be used with the laser vibrometer.

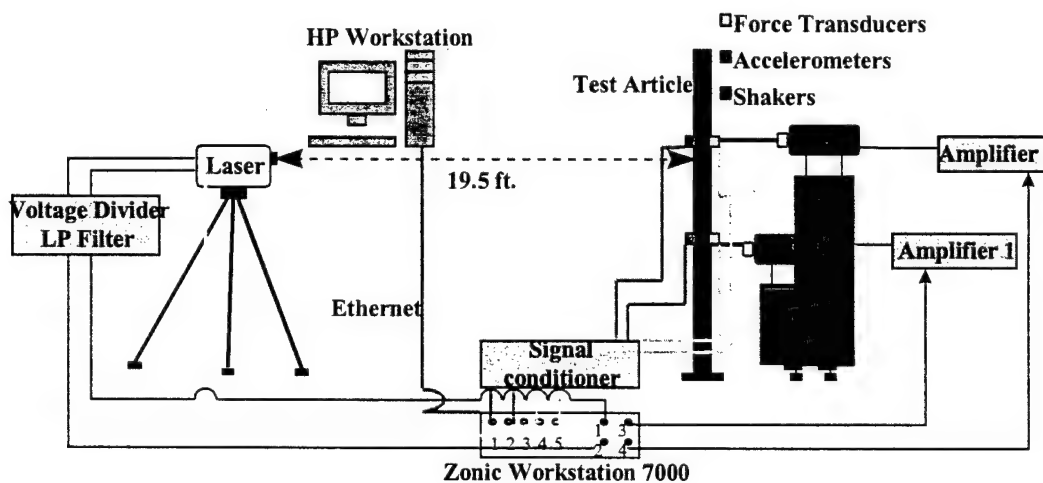


**Figure 4.3. Schematic Representation of Instrumentation.**

To provide the excitation force, the shakers were installed at unsymmetrical points of the structure providing force input in the direction normal to the plane of the test article. The shakers were driven by two different and uncorrelated signal generators. The output from these generators was passed through two different band-pass filters set from 0 to 300 Hz. Each shaker had a steel stinger and a force transducer glued to the stiffened plate using a hexagonal mounting stud. Accelerometers were placed at the front side of the stiffened plate at the same position where the force transducers were mounted. The sensitivity of those accelerometers was used to calibrate the velocity measured with the laser.

The shakers were placed at the positions shown in Figure 4.4. The shaker position was selected by choosing the points of maximum deflection for 20 mode shapes extracted from 0 to 200 Hz from a finite element model of the test article. The shakers excited the structure simultaneously at the chosen points to obtain smooth and clean mode shapes. The shakers were mounted on top of cylindrical steel bases that facilitated the placement of the shakers in any predefined location.

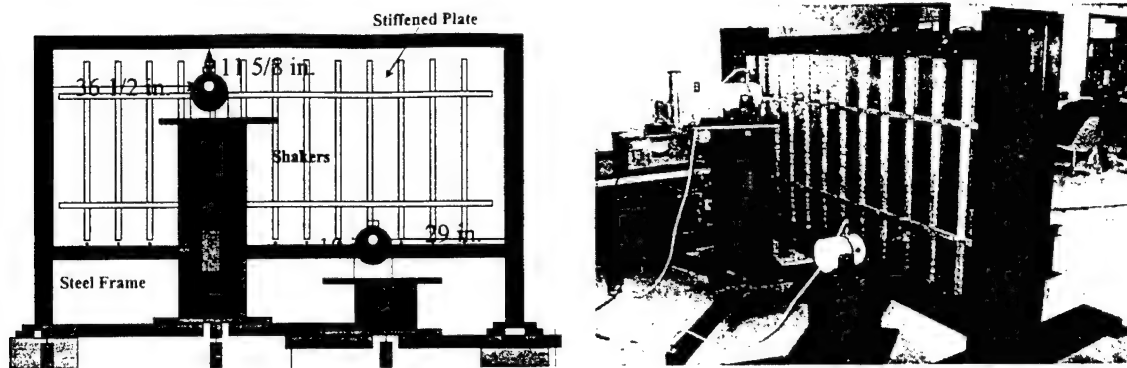


**Figure 4.4. Location of Shakers.**

The working distance of the laser was 19.5 feet from the stiffened plate as depicted in Figure 4.3. The LDV targeted a total of 239 points uniformly distributed within the testing structure. A total of 44 points were located along the supporting frame and the remaining points were distributed horizontally over the 13 lines of bolts fastening the vertical ribs and the stiffened plate. In the vertical direction, a measurement point was placed at a 3-inch spacing to complete 15 readings per line. Reflective tape having an area of one square inch was glued to each measurement point.

Prior to any formal testing, the laser beam was properly calibrated to acquire quality measurements. This was done by assuring that the laser was hitting the center of the reflective papers at each measurement point. Then, the coordinates of each measurement point were stored in the computer to be used in the subsequent experiments. Also, the excitation force Root-Mean-Square (RMS) level was selected to be 8.0 lb for both shakers. This force setting provided the best coherence and best reciprocity of the signals. However, the structure behaved non-linearly and exhibited poor reciprocity in the vicinity of some peaks and valleys in the FRFs as illustrated in Figure 4.5. This figure overlaps the FRF of a point A with respect to excitation force from the shaker 2 at B and the FRF of point B with respect to excitation force from shaker 1 at A. The FRFs coincide in almost all the frequency ranges indicating that there is a good reciprocity.

#### **4.4 Description of Damage Scenarios**

The model was subjected to 22 different damage cases inflicted at eight different zones. Figure 4.6 illustrates these zones. Two types of damage were introduced, the removal of bolts (Type A) and cut damage (Type B), and were caused at single and multiple locations. The removal of bolts (Type A) was inflicted by removing 1) adjacent bolts, 2) one every 2 bolts, and 3) 1 bolt every 3 bolts. Type A damage was inflicted to the connections between ribs-sheet plate and ribs-stringers in Zones 1 through 5. This damage type was introduced gradually starting by removing the least number of bolts to the maximum predefined. The description of the damage cases is shown in Table 4.1. This table also illustrates the sequence in which the baseline and

damaged cases were taken. Cut damage or Type B was inflicted in Zones 6 through 8 and consisted of a 1/16 in. thick cut over 33%, 50%, 66% and 100% of the cross section of the elements. This damage was introduced with a metal saw cutting through the member as shown in Figure 4.7. The zone locations where the damages were introduced are illustrated in Figure 4.6.

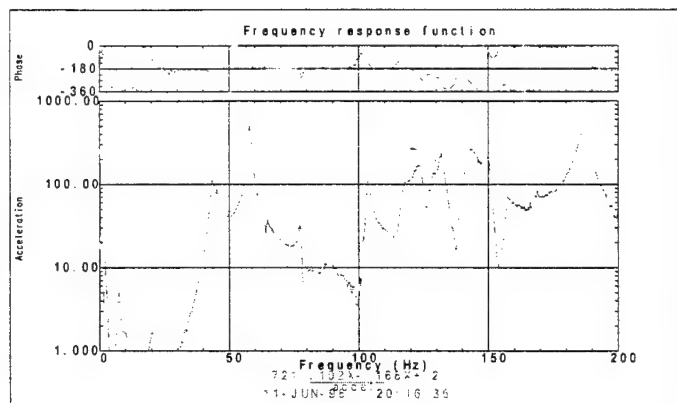


Figure 4.5. Frequency Response Functions for Reciprocity Test.



Figure 4.6. Location of Damage Cases.

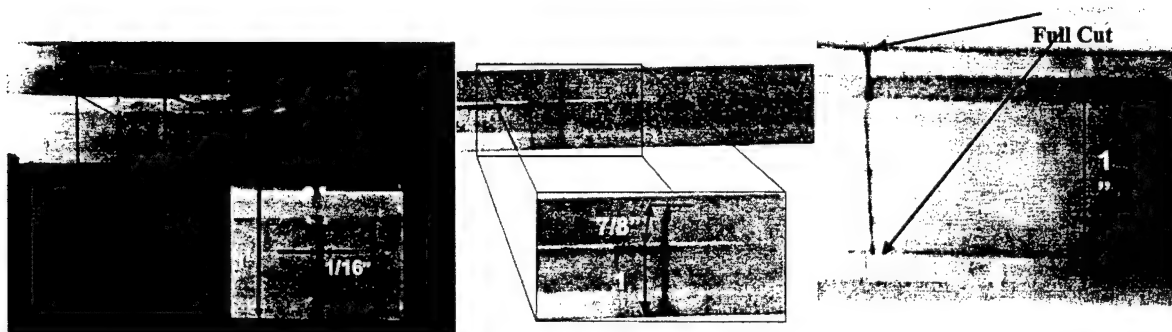


Figure 4.7. Examples of Cut Damage.

**Table 4.1 Description of Damage Cases.**

DAMAGE ZONES	DAMAGE CASES	DESCRIPTION
<b>Base 2</b>		
<b>1</b>	case 1a	Bolt 190L was completely removed
	case 1b	Bolts 190L and 190H were removed
	case 1c	Bolts 190L, 190H and 189L were removed
	case 1d	Bolts 190L, 190H, 189L, 189H and 188L were removed
	case 1e	Bolts 190L, 190H, 189L, 189H, 188L and 188H were removed
<b>Base 5</b>		
<b>2</b>	case 2a	Bolt 54LF completely removed
	case 2b	Bolt 54LF and 58LF completely removed
<b>3</b>	case 3a	Bolt 180H completely removed
	case 3b	Bolt 180H, 150H and 210H-LF completely removed
<b>Base 6</b>		
<b>4</b>	case 4a	Bolt 94H, 236H and 206H completely removed
	case 4b	Bolt 94H, 79H, 236L, 206L and 221L completely removed
<b>5</b>	case 5a	Bolt 140L completely removed
	case 5b	Bolt 140L, 141L and 142L completely removed
<b>Base 7</b>		
<b>6</b>	case 6a	Vertical 1" cut at 12 inches away from stringer's left end.
	case 6b	Vertical 1" and transverse 1/2" cuts at 12 inches away from stringer's left end.
	case 6c	Dam6_b and 1" cut at 49 inches from stringer's left end
<b>Base 8</b>		
<b>7</b>	case 7a	Transverse cut of 1" at 20 inches away from rib bottom end.
	case 7b	Transverse cut of 1 7/8" at 20 inches away from rib bottom end.
	case 7c	Dam7_b and transverse cut of 1" at 4 inches below rib's upper end.
<b>Base 9</b>		
<b>8</b>	case 8a	Transverse cut of 2" at 24 1/4" from stringer's right end.
	case 8b	Full transverse cut at 24 1/4" from stringer's right end.

The eight different damage zones of Figure 4.6 were selected to provide a spectrum of elements and plate zones that contain high, medium and low modal strain energy. Damage Type A and Type B were inflicted after taking the baseline corresponding to the predefined damage zone. When the tests corresponding to each zone were completed, the damage was repaired by replacing the bolts or the damaged element. The sequence followed in conducting the experimental tests with the corresponding baseline is summarized in Table 4.1

## 4.5 Summary of Acquired Data

For each of the damage cases and baselines listed in Table 4.1 the following data were acquired: (1) The FRF function of each measurement point with respect to shaker 1. (2) The FRF function of each measurement point with respect to shaker 2. (3) Multiple Coherence Function for each measuring point. (4) The FRF for the two accelerometers with respect to shakers 1 and 2. (5) The Force Spectrum of the Shakers. Items 1 through 3 served as the data to run multiple-degree-of-freedom curve-fitting algorithms to extract the vibrational characteristics of the stiffened plate model within the frequency range tested. Item 4 can be used to extract the modal mass of the structure. Item 5 was used to check that the force level sent to the shaker from test to test was the same.

The test measurements consisted of a series of Frequency Response Functions (FRFs); each corresponding to one of the target points of the stiffened-plate with respect to each of the two shakers. In all, there were 478 FRFs and 239 Coherence Functions (Multiple) for each of the 22 tests conducted. These functions were used for the extraction of the modal parameters presented in this chapter.

The resonant frequencies and damping ratios were extracted from the frequency response of the test article, before and after the infliction of damage, using a multiple degree of freedom polyreference curve fitting program. The number of modes extracted for each modal test (baseline and damaged cases) in the 0 to 200 Hz frequency range was from 18 to 27. Figure 4.8 depicts typical examples of experimental mode shapes extracted for a baseline case. Similar modes were obtained for the damage cases, with the exception that some of the mode shapes clearly depicted the location of damage as a spike in the graphs as depicted in Figure 4.9.

The modal assurance criterion (MAC) was used to quantify the correlation between the mode shapes of the undamaged test article and those of the damaged structure and to establish the mode pairing between the baseline and damaged data. The modes extracted for the stiffened plate were all real vectors.

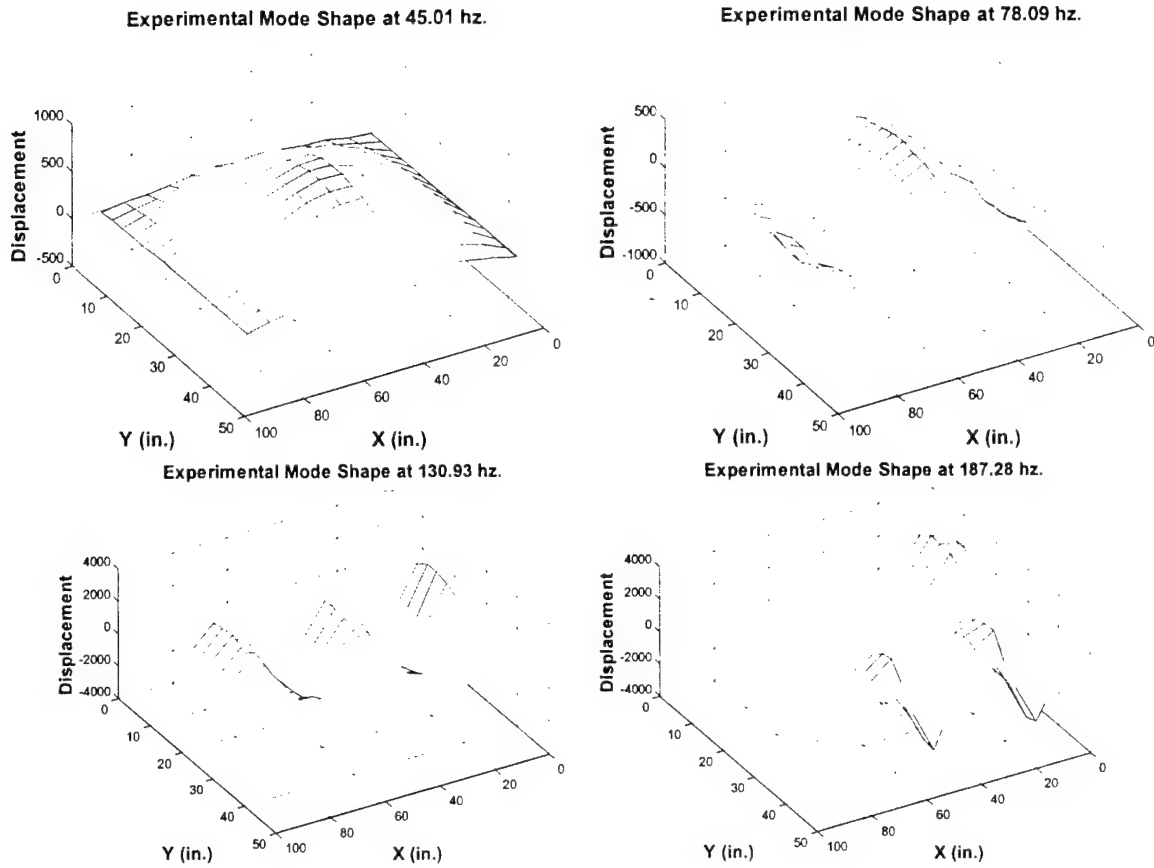


**Figure 4.8. Typical Mode Shapes.**

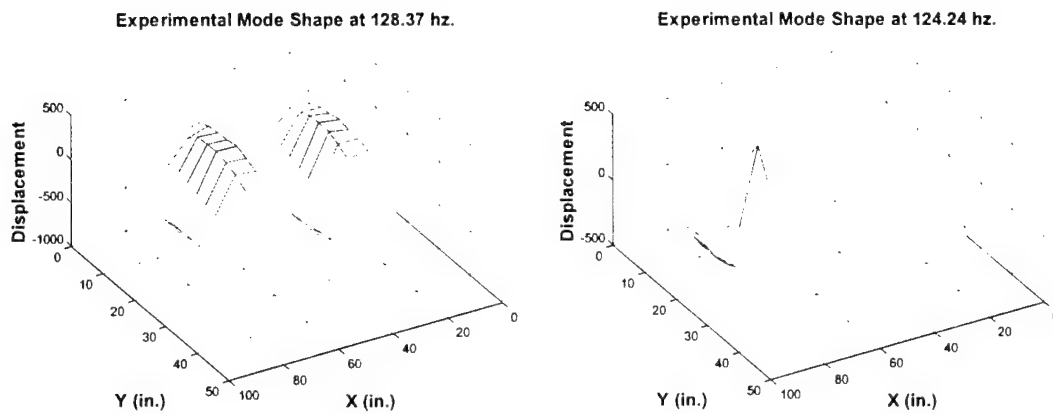


**Figure 4.9. Mode Shape Before and After Damage - Case 1e.**

#### 4.6 Description of Damage Localization Procedure

The method used for the localization of damage consisted on averaging the modal strain energy differences. The entire damage localization approach is illustrated in Figure 4.10. The process assumes that modal analysis data exist for the undamaged and damaged structure in the forms of FRFs and Coherence functions. The first step of the process is the extraction of the modal parameters from the FRFs to obtain the vibrational characteristics of the undamaged and damaged structure. The extraction procedure was carried out using the modal analysis tools in the SDRC I-DEAS software. Because the test article had two independent excitation points, the polyreference curve-fitting technique was used to extract the resonant frequencies, damping ratios and corresponding mode shapes. The mode shapes data of the two scenarios were exported to a universal file format. The second step was to obtain the modal bending and twisting curvatures for all the modes of the undamaged and damaged structures, using the iterative high-order curve-fit method described in Section A.2 of Appendix A. Values of the mode shapes, modal slopes and curvatures for a grid of 49 by 57 points were obtained. The third step was to compute the strain energy distributions of the modal shapes extracted from all scenarios. The strain energy distribution was computed first by using the bending curvature in x only, then the curvature in y, and finally the twisting curvature. This was done to improve the probability of detecting damage at any structural component of the test article by separating the components of the structure (ribs, stringers or plate). The fourth step in the damage detection process was to identify pairs of matching modes between the undamaged and damaged structures using the modal assurance criteria (MAC). The value used to filter MAC results was 0.9. The next step was to calculate modal strain energy differences between the pairs of mode shapes in the MAC lists. The strain energy differences were calculated using the energy distributions estimated with the bending and twisting curvatures. Then, the differences were estimated using each individual curvature. The modal strain energy differences for each mode were normalized using the average standard norm to provide indications of the location of damage (from Equation (2.12)). Finally, the damage indicators obtained from all available pairs of matching modes were combined by averaging the indicators. The average of the damage localization indicators was presented in the form of damage maps, representing the amplitude of the values for each of the 49 by 57 points. High values indicate the presence of damage. The damage maps represent the number of standard deviations deviating from the mean value of the strain energy differences for all points and modes. The scale that represents the magnitude of the damage index is the same for all the damage maps and is shown in Figure 4.11. Negative values of the damage index were graphed using the same color as for zero value. The possible damage zones are highlighted with the colors indicating values greater than 2 as shown in the figure.

#### 4.7 Summary and Discussion of Damage Localization Results

Figure 4.12 shows a summary of the best damage maps for Case 1. In these figures the location of the actual inflicted damage was marked with a red circle. As can be observed, the defect was first detected when two adjacent bolts were removed (Case 1b). However, the figure



corresponding to Case 1b is related to the changes in the modal strain energy due to bending stiffness in the x-direction. The actual damage induces predominant changes in the y-direction.

Thus, as a further thought, the detection for Case 1b is false positive and the actual damage was not detected. Therefore, the damage was conclusively detected in its proper location when five bolts were removed.

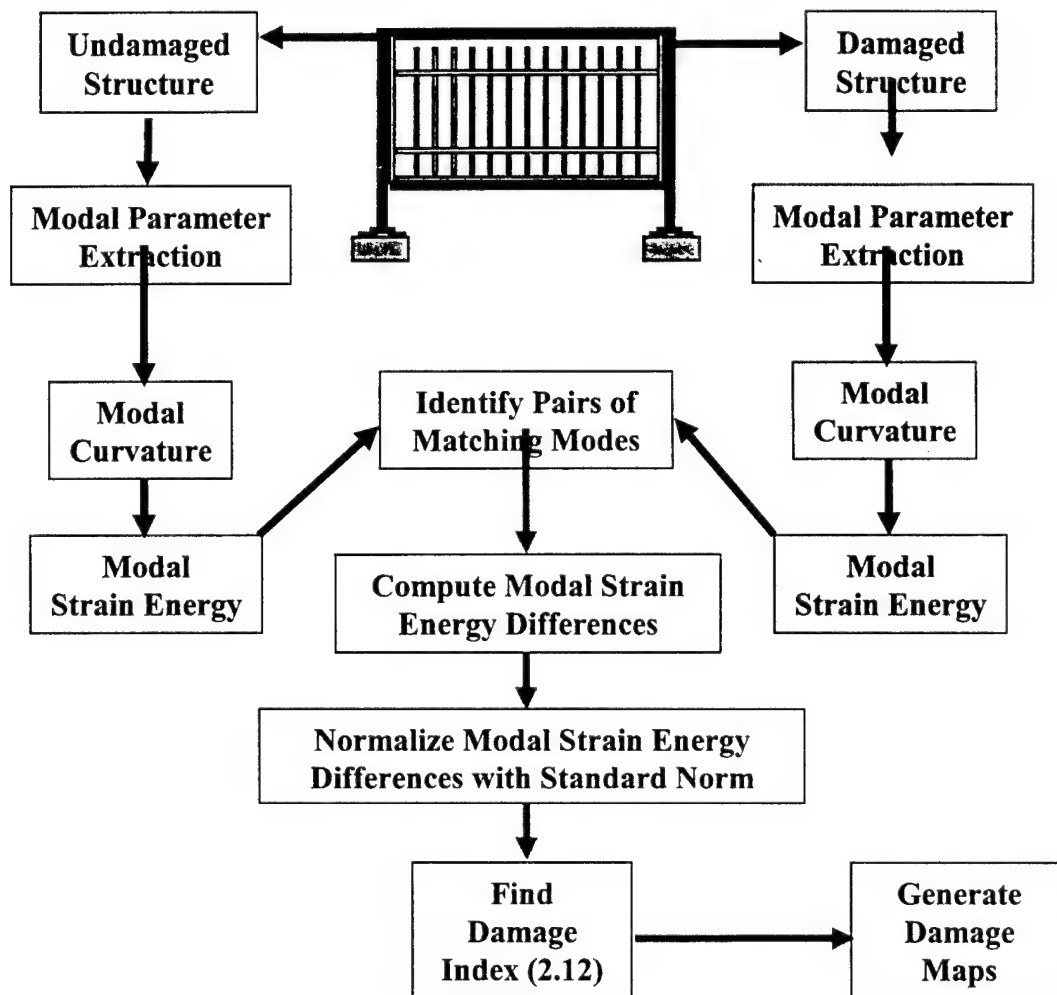
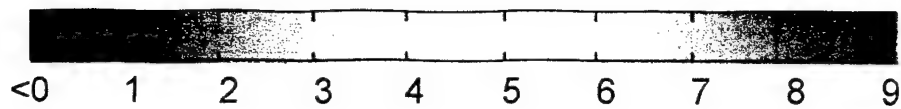
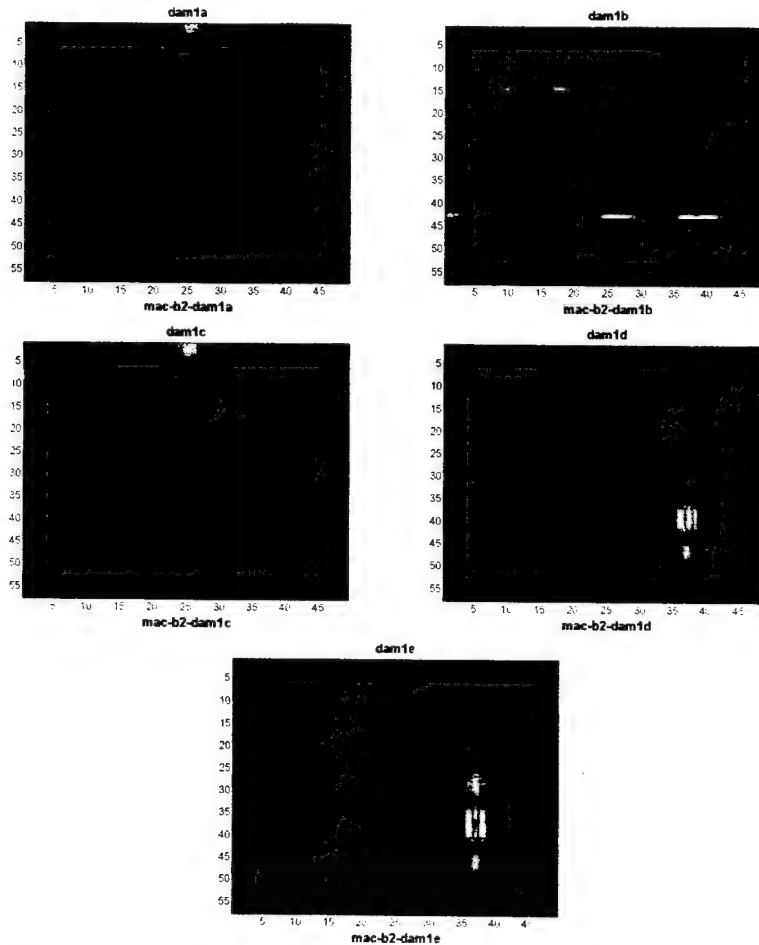


Figure 4.10. Damage Localization Process Flow Chart.

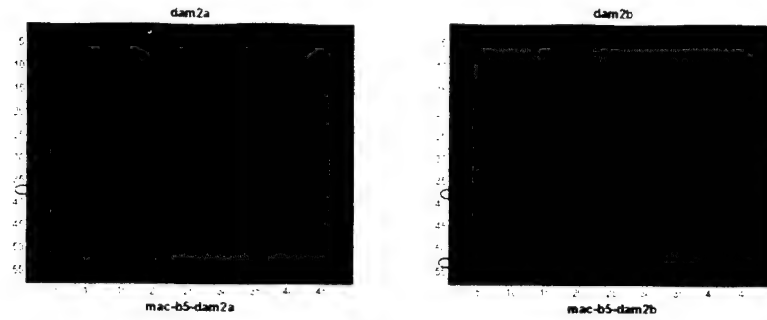


**Figure 4.11. Scale for Damage Index in Damage Maps.**

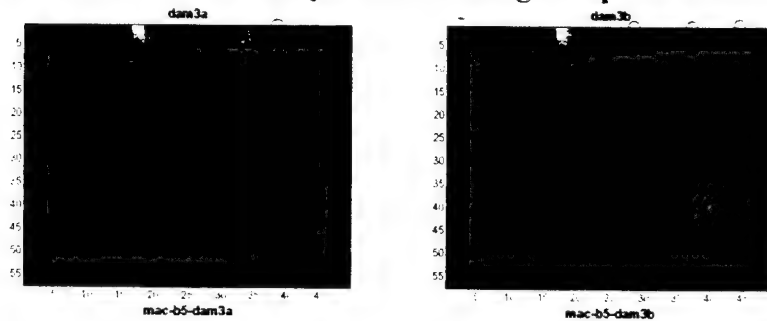


**Figure 4.12. Summary of Best Damage Maps for Case 1.**

Figures 4.13 and 4.14 summarize the results for Cases 2 and 3. The damages inflicted in these two cases were at locations of extremely high stiffness when compared to the rest of the stiffened plate test article. In addition, the particular bolts removed here provided clamping forces for the purpose of restraining the edge of the plate, in competition with several other bolts. The actual change in stiffness due to the removal of these bolts is suspected to be very small because of the neoprene pads in the clamping detail.

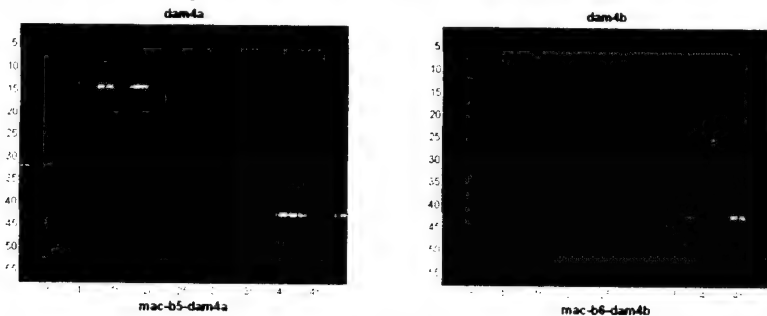


**Figure 4.13. Summary of Best Damage Maps for Case 2.**



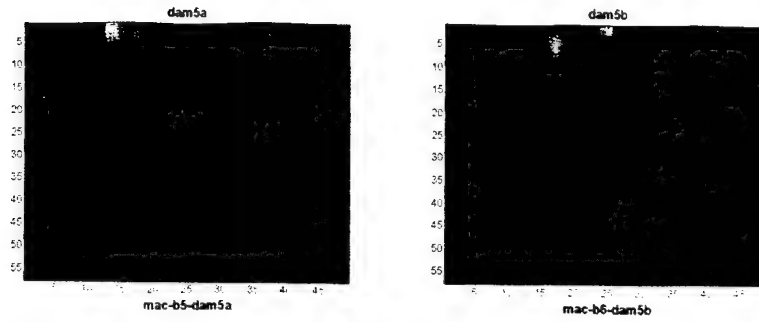
**Figure 4.14. Summary of Best Damage Maps for Case 3.**

Figure 4.15 show the best damage maps for Case 4. The damage localization was accurate and conclusive. In Case 4a, the prediction was at the exact location of the removed bolts. In Case 4b, the damage maps show the correct general location of the actual damage. However, they failed to accurately detect two of the five bolts removed.



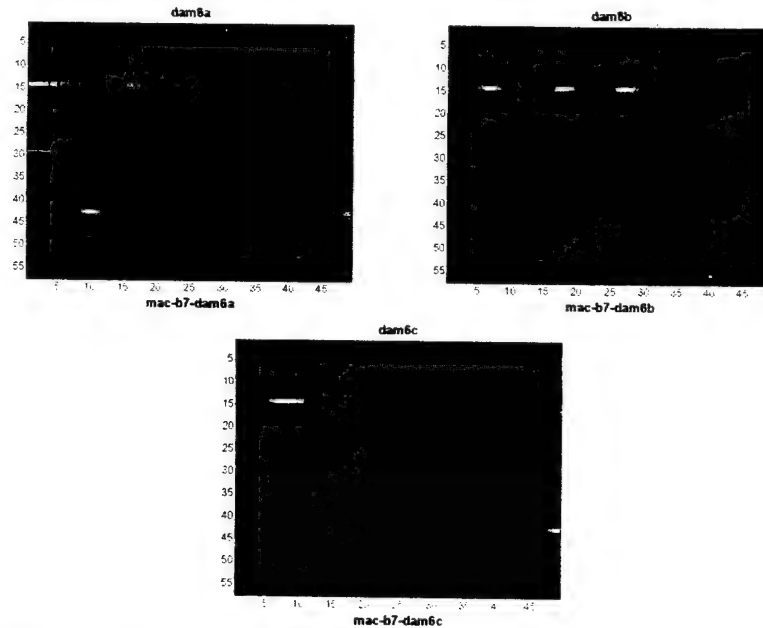
**Figure 4.15. Summary of Best Damage Maps for Case 4.**

Figure 4.16 clearly indicates that the damage locations corresponding to Case 5 were not detected at all. Two factors contributing to these results are: (1) The modes used in the experiments fail to have significant modal strain energy content in the center region of the plate. And (2) the inflicted damage consisted of removing one of every two bolts and the combined stiffness loss is significantly smaller than removing three adjacent bolts.



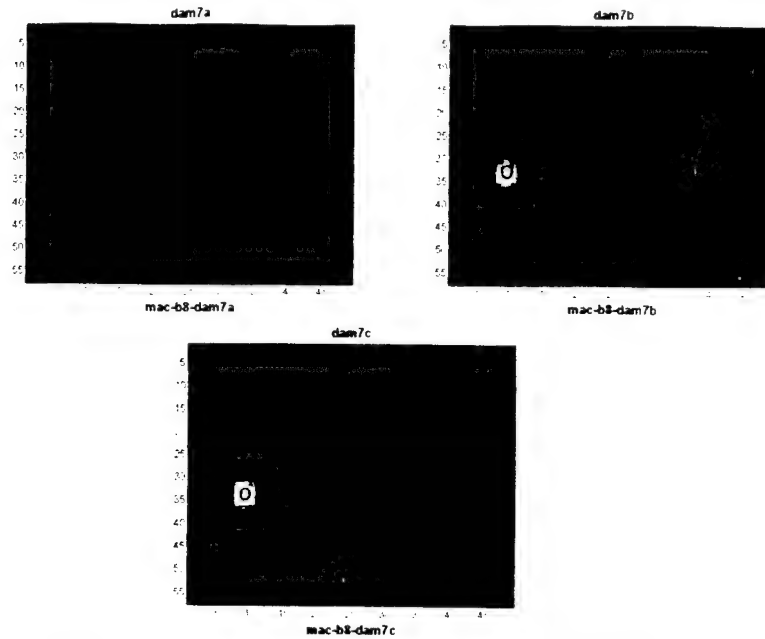
**Figure 4.16. Summary of Best Damage Maps for Case 5.**

Figure 4.17 depicts the summary of the damage maps obtained for Case 6 when cut damage was inflicted in the horizontal stringer. It can be seen that the locations of the cuts were accurately detected. However, there were some false positive detections in other points of the structure.



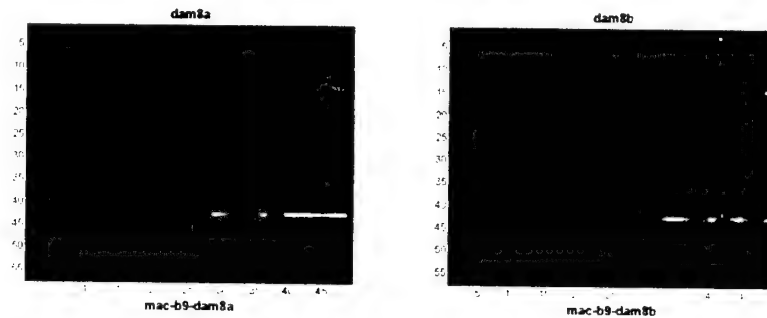
**Figure 4.17. Summary of Best Damage Maps for Case 6.**

Figure 4.18 shows the summary of the damage localization corresponding to Case 7. In these damage scenarios the vertical rib was cut in one and two locations. The small cut in Case 7a was not detected. The second cut in Case 7c was not detected either.



**Figure 4.18. Summary of Best Damage Maps for Case 7.**

Finally, Figure 4.19 illustrates the summary of the damage maps corresponding to Case 8. In this case the two damage scenarios consisted of a cut in the horizontal stringer of the test article. In both cases, the damage was correctly located.



**Figure 4.19. Summary of Best Damage Maps for Case 8.**

#### 4.8 Conclusions using Averaging

The following conclusions were obtained from the plates experiments when averaging was used to process the information:

1. The iterative curve fit procedure used to estimate the bending and twisting curvatures enhanced considerably the resolution of the damage detection.
2. Modal strain energy differences were proven effective in detecting the damage inflicted to the stiffened-plate.
3. The average damage indicators of several modes provided accurate and conclusive predictions for most of the cases studied.

4. Damage consisting in the removal of adjacent bolts was conclusively detected and located when five bolts were removed using the combined twisting and bending curvatures.
5. Damage in the stiff parts of the structure (at supports) was not detected. This is because there is hardly any measurable increase in the modal compliance.
6. Damage consisting of the removal of bolts of the inner members of the stiffened plate was detected and located using the bending curvature in the direction of the damaged member.
7. Damage in regions of low modal strain energy was not detected.
8. Damage consisting of a cut of the inner members was generally detected.
9. Damage was not detected when inflicted at the rigid support.
10. The type and number of mode shapes to use for the damage localization limit this damage detection method. The damage can only be detected with mode shapes that have significant energy content in the location of damage.

#### **4.9 Damage Detection Results Using Likelihood Ratio and Evidential Reasoning**

This section presents the damage detection results when data fusion techniques are used. The two data fusion techniques implemented were likelihood ratios and evidential reasoning as described in Section 2.4. The evidential results were obtained from computed values of belief and plausibility. The only cases considered here were Cases 6 through 8, where the damages were inflicted in the stiffening elements as depicted in Figure 4.6 and described in Table 4.1, for a total of 10 damage scenarios.

A similar approach to the one depicted in Figure 4.10 was used, with the exception that the damage was found using the likelihood ratio (Equations (2.17) and (2.18)) and the evidential reasoning method (Equations (2.23) through (2.26)) only. The statistical distribution of the normalized modal strain energy differences was approximated using the Kernel Density Estimator for the purpose of finding probabilities supporting damage and no-damage given the modal inspection events. From these probabilities, damage likelihood ratios were obtained for all locations given the modal inspection events. The product of the ratios coming from all modes accomplished one of the fusion processes. The second process consisted of using techniques of evidential reasoning to determine belief and plausibility in support of damage given the evidence in the modal strain energy differences.

Figure 4.20 shows these results. For each case, the map at the top corresponds to the evidential reasoning results and the one below to the fused damage likelihood ratio. The figures include circles indicating the actual location of the known inflicted damages. The shaded areas of the evidential reasoning results correspond to areas where the evidence strongly supports the possibility of damage. The areas not shaded correspond to places where the evidence suggests uncertainty or supports no-damage. For each case, detection results are available for the plate, the vertical stringers and the horizontal ribs. The one selected for Figure 4.20 is the one that contains the largest damage likelihood ratio.

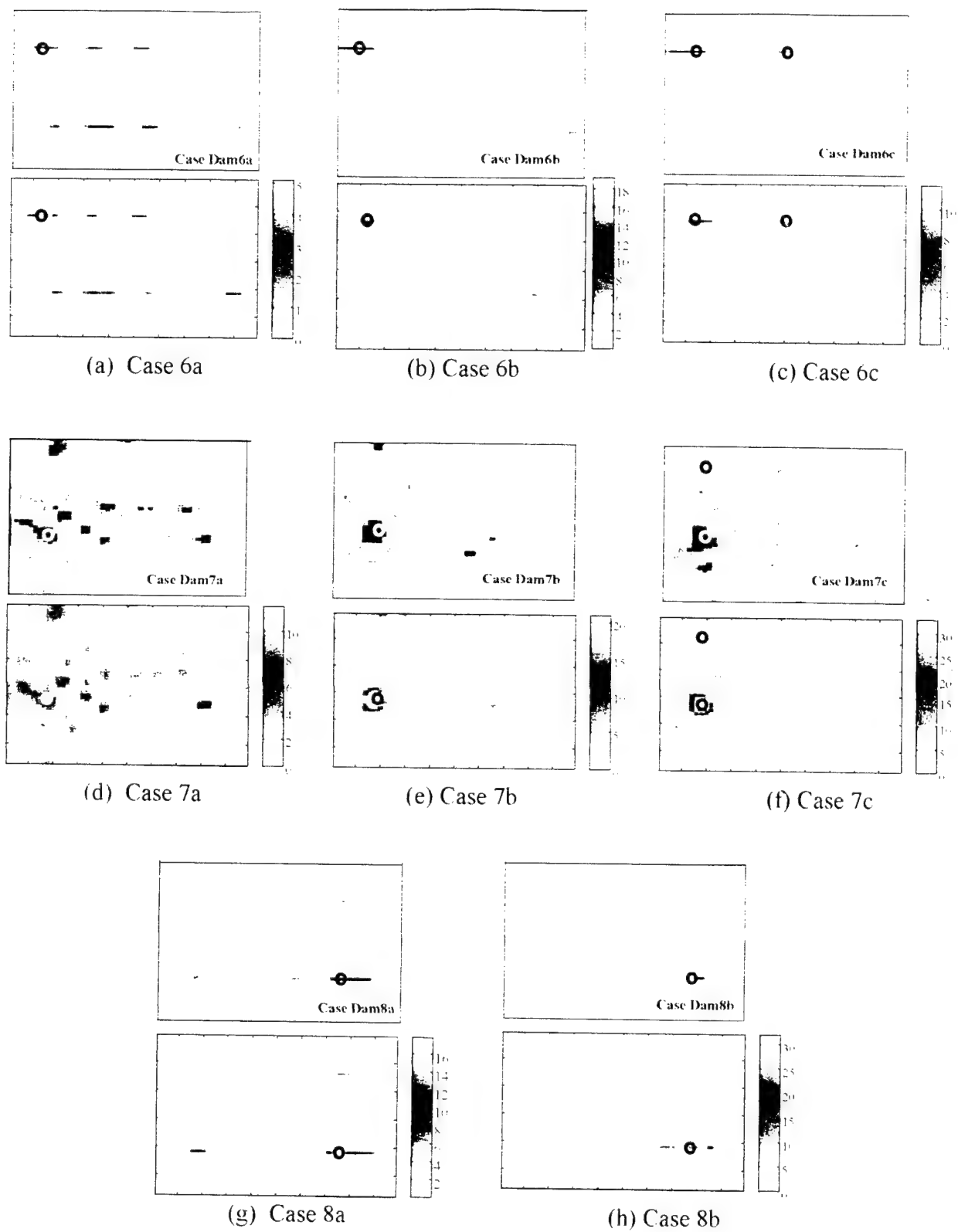


**Figure 4.20. Log of Damage Likelihood Ratio and Evidential Reasoning Results.**

Figure 4.20(a) illustrates the results corresponding to Case 6a. Although, difficult to observe in a gray scale, the largest value of the fused damage likelihood ratio is at the location where the cut was made. Notice that both the likelihood ratio and the evidential analysis yield similar results. Figure 4.20(b) illustrates the results when the damage was increased at the same location. With the larger damage, the location is very evident as the likelihood ratio significantly increased and the number of false calls is reduced. Figure 4.20(c) shows the results for Case 6(c) as a new damage was created in a different location. The second location is correctly located as suggested by the evidence and the damage likelihood ratio

Figures 4.20(d) through 4.20(f) illustrate the damage maps obtained for cases 7a, 7b and 7c. The figure illustrates the maps corresponding to the plate elements rather than those of the stiffening elements. The plate elements exhibited the largest likelihood ratios. The location of the damage in Cases 7a and 7b were correctly located. The smaller-magnitude damage in Case 7c was not detected. Notice that the damage maps reflect fewer false calls for larger magnitudes of damage.

The results for Cases 8a and 8b are illustrated in Figures 4.20(g) and 4.20(h). Notice that the correct location was detected in both cases.

#### **4.10 Conclusions using Fusion by Likelihood Ratio and Evidential Reasoning**

This previous section described the process to localize damage in a laboratory structure resembling aircraft construction using modal measurements and fusion techniques. The mode shapes were subjected to a curve-fit procedure to estimate modal bending and twisting curvatures of the front plate. These curvatures permitted the determination of the modal strain energies.

The following conclusions are stated:

1. The damage detection procedure was proven effective in detecting cut damage inflicted to the stiffening elements of the plate.
2. Out of 10 possible damage locations considered, 9 were correctly detected.
3. The damage that was not detected is of small magnitude in a case where a large damage was also present.
4. The number of false calls is larger for cases with small magnitude defects. However, the predictions narrowed the potential damage locations to a small portion of the structure.
5. The results of this work indicate that the detection of gross defects in certain stiffening elements of aircraft structures is possible using the techniques included in this report.





## **CHAPTER 5**

### **DAMAGE DETECTION TESTS IN VERTICAL STABILIZER STRUCTURE**

#### **5.1 Introduction**

This chapter presents a summary of the work reported by Andre (1999) on a prototype of the vertical stabilizer assembly of NASA's shuttle orbiter. The purpose of testing the VSA tests was to obtain a database that can help to develop damage identification techniques. The data obtained during testing consisted of frequency response functions (FRF) and coherence functions for all scenarios (damage and repaired configurations). As explained in the previous chapters, the data was used to extract the resonant frequencies and mode shapes. The measurements were taken with accelerometers and with the LDV. There were a total of eight damage cases involving reversible and irreparable damage. The first three cases were performed using accelerometer measurements only. The last five damage cases involved accelerometers and the LDV combined. The damages inflicted consisted of reversible and non-reversible scenarios with several levels of damage in each case. Damages inflicted on the Vertical Stabilizer Assembly (VSA) test article were located in several locations.

The mode-pairing between the baseline state and the damaged scenario was carried out through the modal assurance criterion (MAC). In addition, the mode pairs which exhibit significant change due to the inflicted damage were identified using a statistical analysis of the FRF data. This procedure is summarized in Appendix B. The effects of mode-pairing was also studied by repeating the damage detection process using mode-pairs (a) identified by the MAC analysis with values greater than 0.9, (b) identified by the MAC analysis with values greater than 0.5; and by further refining the mode-pairing in both (a) and (b) using the Z-function analysis. The estimation of the strain energy content of the structure due to the deflected modal shapes performed using the Finite Element approach described in Section A.4.

Four damage detection algorithms are considered in this chapter: (1) averaging, probability mass function method (PMF), (2) a weighted averaging method and (4) a weighted PMF method. Damage maps were obtained for all damage cases and damage levels using the four damage detection algorithms considered. The detectability was evaluated in terms of whether the correct location was detected as being damaged. The number of false positives was obtained by counting the number of regions with high levels of damage depicted by the orange-red colors of the contours of the damage maps. A performance index was evaluated in order to compare the efficacy of the detection methods as well as the mode-pairing approach.

#### **5.2 Description of Test Article**

The Vertical Stabilizer Assembly was a prototype of the upper section of an early version of a Shuttle Orbiter Vertical Stabilizer including the two upper Rudder/Speed Brakes (RSB) and two aluminum dummy actuators. The VSA was lacking the Thermal Protection System (TPS)

and the static load application pads. The structure was composed of five sections as illustrated in Figure 5.1.

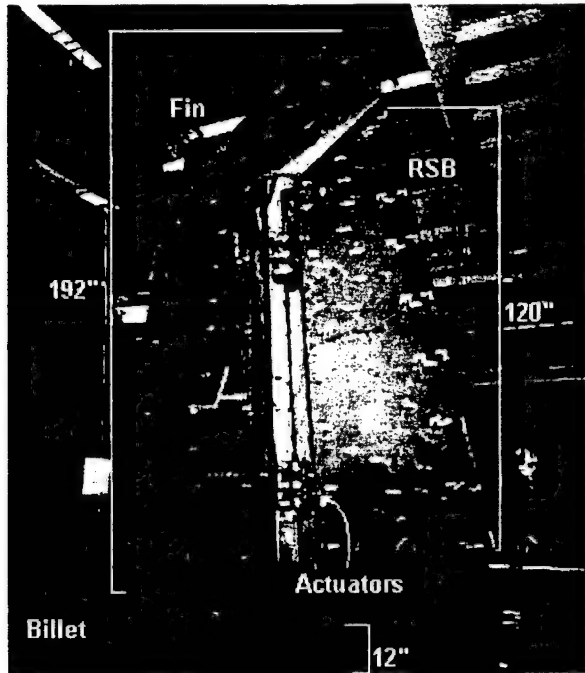


**Figure 5.1. Front View of Test Article.**

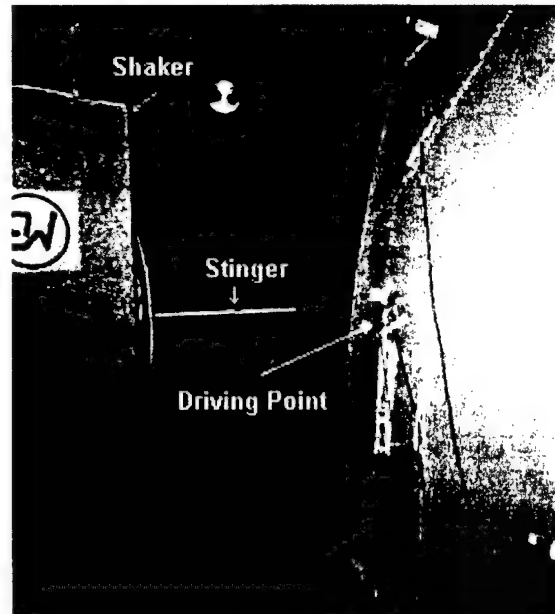


**Figure 5.2. Close-up View of Shaker Test Article Attachment**

The test setup is illustrated in Figures 5.1 through 5.4. The fin was anchored to the billet by means of attachment brackets. A 500-lb. electromagnetic shaker was suspended with steel cables from a beam located ten feet above the driving point (Figure 5.2). By suspending the shaker from cables, the main body of the shaker was isolated from the structure and prevented the transmission of any reaction forces to the structure. The shaker was connected to the driving point through a force transducer attached to a stinger.

A Laser Doppler Velocimeter (LDV), sitting on a tripod, was positioned 33 feet away from the structure. Fifty-six accelerometers were mounted to the structure using wax as a bonding agent. The accelerometers were placed on the structure according to the current Shuttle Modal Inspection System (SMIS) (West, 1987). Eighty-four pieces of reflective tape were also mounted on the side of the test article facing the LDV. Thirty-five of those pieces of reflective tape were placed on top of accelerometers. The remaining tapes were placed at mid distance between the accelerometers. Figure 5.3 illustrates a simple wire model of the test article that can be built by tracing lines between the sensor and reflective tape locations. Every intersection point in the figure was instrumented with the scanning LDV.

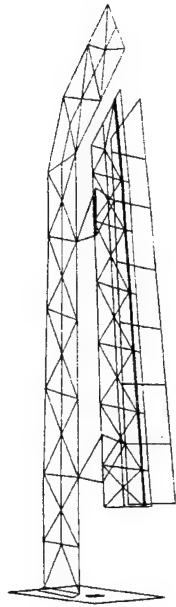


**Figure 5.3. Geometry of Sensor and Tape Locations.**

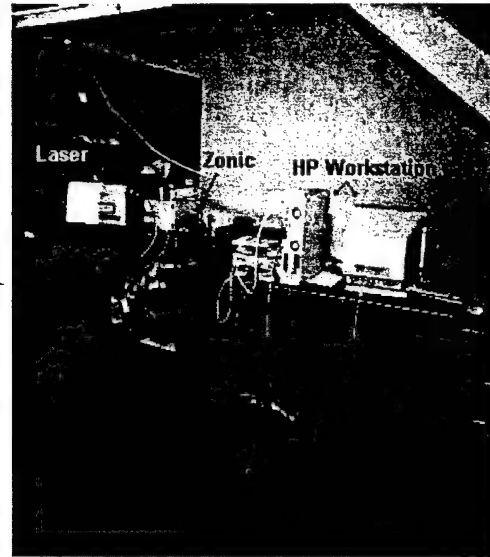


**Figure 5.4. Laser and Computer Set-up.**

A 16-channel Zonic A/D analyzer connected to a workstation was used to collect the data from the LDV and accelerometers. Two analog output channels and fourteen input channels of the analyzer were used. The two output channels were connected to the LP Voltage Divider, which is the controller for the mirrors of the LDV for targeting the laser beam onto the structure. The first analog input channel was used to acquire the velocities sensed by the LDV at different points of the Vertical Stabilizer Assembly. The second analog input channel was used to acquire the force signal from the driving point. The last twelve input channels were used to obtain data from the 56 accelerometers through the use of switch banks.

The instrumentation consisted of a Hewlett Packard Workstation that contained the modal testing software ZETA (Zonic A/D Engineering and Test Analysis). The workstation provided the control commands to the Analyzer for the processing of measurement functions, such as windowing, averaging, compute Fast Fourier Transforms (FFT) and controlled the signals to the shaker and LDV. The electromagnetic shaker was excited with continuous random excitations from 0 to 300 Hz and peak amplitude of 100 N. The signals were digitized using a block size of 1024 points. The FFT were obtained using 25 ensemble averages and Hanning windows for the input and output channels. The purpose of testing the VSA was to obtain a database that could help in developing damage identification techniques. The data obtained during testing consisted of frequency response functions (FRF), coherence functions for all scenarios (damage and repaired configurations) and time histories for two scenarios. For the purpose of this research, the data obtained was used to develop damage detection techniques applied to complex aerospace structures.

### 5.3 Description of Damage Test Program

Damages inflicted on the Vertical Stabilizer Assembly (VSA) test article were located in several locations. These selected locations were in actively inspected regions of the current Shuttle fleet. The damages inflicted consisted of reversible and non-reversible scenarios with several levels of damage in each case.

Two measuring techniques were used to modal test the VSA test article. The first one was a non-contact technique involving the LDV; the second one involved accelerometers mounted on the structure. The LDV was calibrated against one of the accelerometers used in the testing. A total of one hundred measuring points were defined on the structure. All acquired data were stored in SDRC associated data file format to facilitate analysis in IDEAS/TDAS software; the files were later converted to universal file format.

There were a total of eight damage cases involving reversible and irreparable damage. The first three cases were performed using accelerometer measurements only. These three cases were not considered in this research.

For the last five damage cases, FRF and Coherence functions were obtained from the LDV and accelerometer data using a continuous, pure random excitation signals with 25 ensembles, a band pass filter from 4 to 300 Hz and a block size of 1024. The excitation signal was continuous and pure random. A band pass filter from 4 to 300 Hz producing a 100-N peak force was used. All signals were processed with Hanning windows using 50% overlaps. The filtering and windowing were needed to reduce distortion due to leakage of energy into adjacent frequency lines.

The researchers were involved in five of eight damage cases inflicted on the VSA test article. All five controlled damage scenarios contained several levels of damage. After each level of damage, a modal test was conducted with the accelerometers only or with the accelerometers and the LDV techniques combined.

The first damage scenario was reversible and contained four levels of damage inflicted on the tip cap access panel of the VSA. Prior to the infliction of this series of progressive damage baseline modal measurements were taken, referred to as "Baseline 1". The levels of damage can be described making reference to Figure 5.5. The first level of damage consisted of removing the screws closest to the leading edge and at the top edge of the access panel; the access panel remained attached with additional screws. This case is referred to as "Case 4a". In the next level, the screws closest to the trailing edge and at bottom edge of the access panel were removed; the panel remained attached by the screws at the intermediate spars (see Figure 5.5). This case is indicated as "Case 4b". The third level of damage consisted of removing the remaining screws connecting the access panel to the spars and the panel was completely removed. This last case of this series is referred to as "Case 4c". Consult Figure 5.5 for an illustration of the three levels of damage in Case 4. After each level of damage was inflicted, modal measurements were obtained. The tip cap access panel was re-screwed into placed.

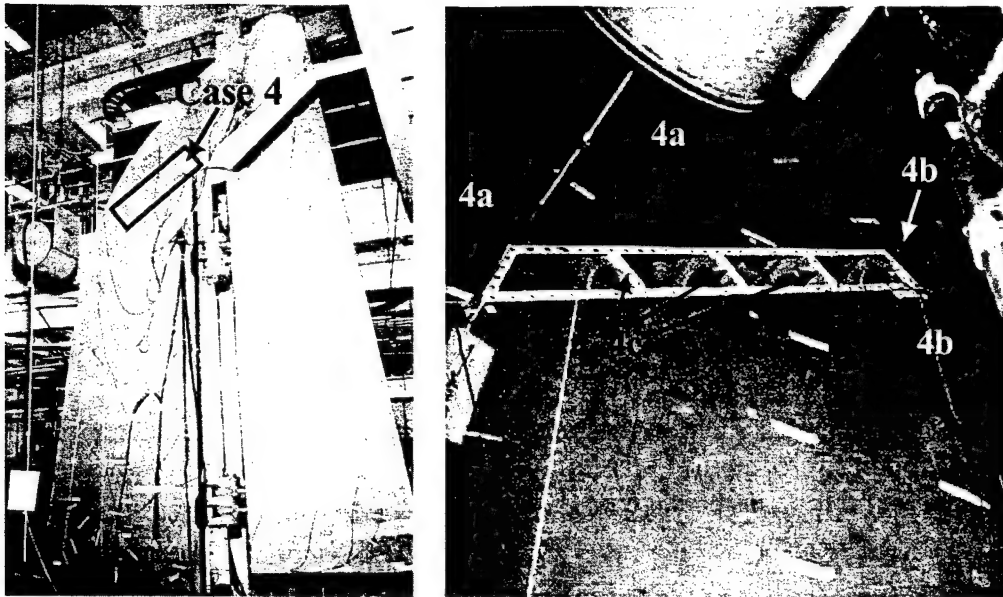


**Figure 5.5. Damage Inflicted in Case 4. (In Case 4a, the rows of screws indicated were removed. In Case 4b, two additional rows of screws were removed. In Case 4c, the remaining screws at the spars and the access panel were removed.)**

Figure 5.6 illustrates the general location of the inflicted damages in Case 5 at the tip cap of the VSA. There were ten damage levels, some of them partially reversible. Prior to the infliction of any damage in this case, baseline measurements were taken (Baseline 2). The damage levels were labeled from "Case 5a" to "Case 5j". LDV and accelerometer measurements were only taken in Cases 5a, 5b, 5c and 5h. These are the only four subcases considered in this work. The remaining cases corresponded to measurements taken with accelerometers only. In order to describe the actual state of damage at the cases considered it is necessary to describe all of them because some of them were irreversible.

The first four levels of damage in Case 5 involved the removal of rivets from both left and right sides of the tip cap. The rivets were drilled out and connected the skin panel to an interior rib called the "60% rib". The rib was a built-up I-shape with holes in the web. The holes are called "lightening holes". The chords of the rib (or flanges) connected directly to the skin panel with rivets. These were the rivets removed in Cases 5a through 5d. To illustrate these damage levels it is necessary to refer to Figure 5.7, which illustrates a close up of the left side of the VSA where the damage was inflicted. In Case 5a, the lowest two rivets on both left and right sides of the VSA were removed (a total of 4). This was done on the aft side of the rib as illustrated in Figure 5.7. The next level of damage (Case 5b) consisted of the removal of the next four lowest rivets on each side (left and right) in the same aft side (eight additional rivets for a total of 12). In damage Case 5c, the next seven lowest rivets were removed on each side in the aft side (fourteen additional rivets for a total of 26). In Case 5d, the lowest thirteen rivets in the fore side of the rib were removed from both sides (left and right), for 26 additional rivets and a

total of 52 rivets. To describe the next six levels of damage refer to Figure 5.8. Note the location of letter A in Figure 5.8 with respect to Figure 5.7. The additional level of damage for Case 5e consisted of the removal of the skin panel on the left side only, just aft of the lowest bay of the 60% rib as illustrated in Figure 5.8. The cutout of the skin panel was done in such a way that it could be riveted back in its position at eight locations. In Case 5f, two cuts were made in the web of the 60% rib, each extending from the one of the lightening holes to the exterior flanges. The cut from the lightening hole to the flange in the right side cannot be seen in Figure 5.8 but is indicated. Case 5g consisted of creating an additional cut between the two lightening holes. In Case 5h, the web of the second lowest bay of the 60% rib was cut between the two lightening holes. This cut is hidden in Figure 5.8 but its location is indicated. In Case 5i, all rivets except those associated with the cutout of the skin panel were replaced. And finally in Case 5j, the cutout of the skin panel was replaced by riveting at eight locations. Modal tests were conducted after each damage level described in the previous paragraphs. However, modal tests using the LDV and accelerometers combined were only performed after Cases 5a, 5b, 5c and 5h. These are the only cases of this series considered in this work.



**Figure 5.6. General Location of Inflicted Damages in Case 5.**



**Figure 5.7. Illustration of Rivets Removed in Cases 5a through 5d.**

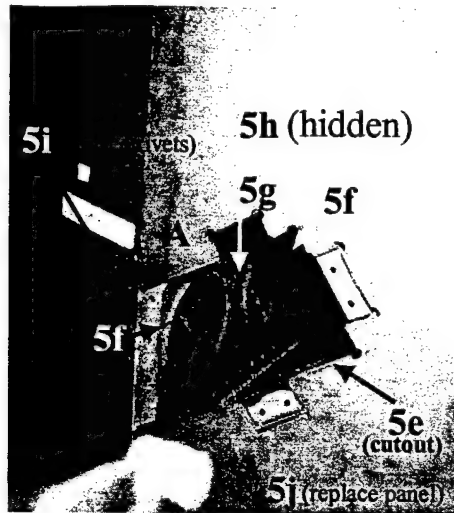


**Figure 5.8. Illustration of Damage Levels in Cases 5e through 5j.**

Figure 5.9 illustrates the location of the damages inflicted in Case 6. A new baseline modal test was conducted prior to the infliction of the damages in this case (Baseline 3). The form of damages inflicted was irreversible and consisted of three levels. LDV and accelerometer measurements combined were taken after the third damage level (Case 6c) only. In the first level, Case 6a, the skin forming the leading edge was cut perpendicularly between two horizontal ribs (see Figure 5.10). Notice this figure corresponds to a view from the right side. The second level of damage, Case 6b, consisted of removing all the rivets holding the skin panel and dislodging the cutout of the leading edge. The third level of damage, Case 6c, consisted of cutting the vertical front spar halfway through the right side as shown in Figure 5.10.



**Figure 5.9. General Location of Inflicted Damages in Case 6.**

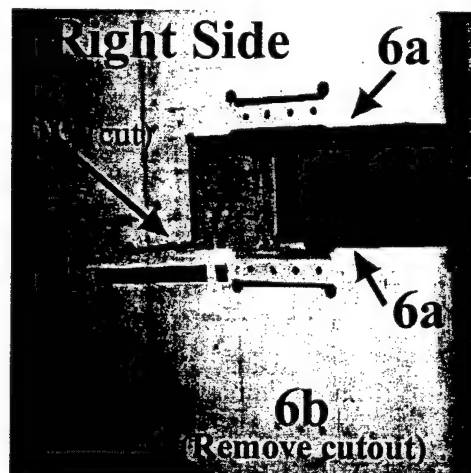


**Figure 5.10. Inflicted Damage Levels for Case 6.**





**Figure 5.11. General Location of Inflicted Damages in Case 7.**



**Figure 5.12. Inflicted Damages in Case 7.**

The damages created under Case 7 were located as shown in Figure 5.11. No baseline measurements were taken prior to this case. The damage location corresponds to the upper bead above one of the actuators and consisted of two levels of damage as shown in Figure 5.12. Case 7a consisted of cutting the left and right-hand sides of the upper bead in the bay. Notice that the cut in the right side is hidden in the picture of Figure 5.12. Case 7b consisted of cutting the lower side of the upper bead. Complete LDV and accelerometer measurements were taken after Case 7b.

The controlled damage scenarios of Case 8 were inflicted in the left Rudder Speed Brake (RSB) of the VSA at the location shown in Figure 5.13. The skin of the RSB is made with composite material panels. The damage consisted of six levels of damage. However, the modal testing procedure for this series of damage was performed on a high-density region consisting of 25 points defined at a 5 by 5 grid within the bay of the RSB where the damage was inflicted. This high-density region can be seen in Figure 5.14 defined by the location of the reflective tape markers on the surface of the RSB. Prior to the infliction of any damage, a new baseline set of measurements was only taken in the high-density region. This is referred to as Baseline 4. Also, after the last damage was inflicted under this series, a complete modal test of the VSA (fin and rudder) was additionally conducted.

The first level of damage consisted of a one-inch diameter hole drilled on the left RSB. This case is referred to as Case 8a. The next level of damage was caused with a knife, generating a one-half-inch disbond around the edge of the hole, for a total diameter of 2 inches of disbonded area. This damage level is defined as Case 8b. For Case 8c, an additional one-half-inch of disbond was similarly caused around the edge of the hole for a total disbond diameter of 3 inches. The additional damage introduced for Case 8d consisted of the removal of eight rivets in the upper horizontal spar of the bay tested. This damage can be observed in Figure 5.14. The next level of damage, Case 8e, consisted of the additional removal of four rivets in the lower

horizontal span of the bay tested. And in the last level of damage, Case 8f, four additional rivets were removed immediately below those removed in the prior case. After the last inflicted damage of Case 8f, a complete modal test of both fin and rudder of the VSA was performed using the combined accelerometer and LDV measurements similar to the other damage cases.



**Figure 5.13. General Location within the Right RSB of Inflicted Damages in Case 8.**

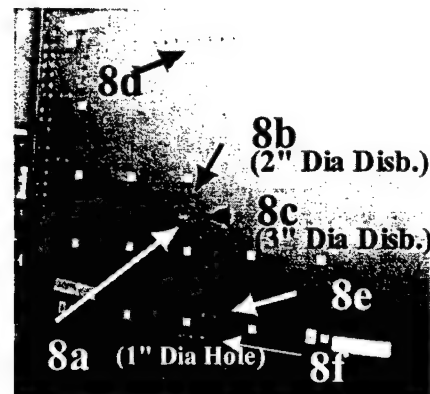


**Figure 5.14. Inflicted Damages in Case 8.**

#### **5.4 Baseline and Damaged Scenarios**

This section provides a list of the damage scenarios and, because some inflicted damages were irreversible, indicates which cases were utilized as the reference baselines for the purpose of damage detection. The baselines were selected as such as to have a single damage location. Table 5.1 provides such a list. For the damage levels under Case 4, the reference was Baseline 1. Baseline 2 corresponds to the reference used in the damage levels of Case 5. Baseline 3 was used as the reference for Case 6c. The baseline for Case 7b is the set of measurements obtained for Case 6c. And the reference for Case 8f is Case 7b. Cases 8a through 8f at the end of the table correspond to measurements taken at the high-density grid of 5 by 5 points around the defect location, and the corresponding reference is Baseline 4. These were not fully considered in this work.

**Table 5.1. Summary of Damage and Baseline Cases.**

Damage Case Set	Damage Case Level	Reference Baseline
4	Case 4a	Baseline 1
	Case 4b	
	Case 4c	
5	Case 5a	Baseline 2
	Case 5b	
	Case 5c	
	Case 5h	
6	Case 6c	Baseline 3
7	Case 7b	Case 6c
8	Case 8f	Case 7b
8	Case 8a	Baseline 4
	Case 8b	
	Case 8c	
	Case 8d	
	Case 8e	
	Case 8f	

### **5.5 Modal Parameter Extraction, MAC Analysis and Z-Function Analysis**

Two critical elements in the vibrational NDE methods described in Chapter 2 are the availability of the global mode shapes and the identification of pairs of matching modes between the undamaged and damaged states of the structure. The experimental sets of FRFs and coherence functions, obtained with the LDV, were subjected to a multiple-degree-of-freedom curve-fit algorithm available in a commercial software for the extraction of the resonant frequencies and modes. This analysis yielded a set of modes for the VSA in each of the baselines and damage levels considered in this work. Modal assurance criterion (MAC) analyses were performed between the modes of the baseline state and those of the damaged state to identify the pairs of matching modes. In addition, the mode pairs which exhibit significant change due to the inflicted damage were identified using a statistical analysis of the FRF data. This analysis is referred to as “The Z-Function Analysis” and is described in Appendix B of this report. In essence, this was an attempt to identify mode pairs that contain significant features to locate the inflicted damage.

The resonant frequencies were then compared to the frequency values where the Z-function analysis showed that the structure exhibited significant global changes.

The modal parameter extraction was performed with the software SRDC I-DEAS. A multiple-degree-of-freedom (MDOF) curve fitting technique was used to extract the mode shapes from FRFs. More specifically, the direct parameter method was used. The purpose of

the MDOF technique was to estimate the resonance frequency, damping and mode shapes. This technique allowed for the identification of closely coupled modes and heavily damped modes. The program used to extract the modes provided four MDOF techniques. The direct parameter technique was chosen since it used multiple response functions to obtain global estimates of modal parameters. This technique processed multiple response functions from a single excitation location and obtained global least squares estimates of the modal properties. Because it operated in the frequency domain, it inherently accounted for the effects of residual modes during the estimation process. The direct parameter technique was ideal for the analysis of the data since there where multiple response functions obtained for each case, and a single reference point existed.

The mode pairing was implemented with the modal assurance criterion (MAC) analysis between the sets of modes corresponding to the baseline and damage. The MAC analysis provides a scalar value between zero and one representing the correlation between two mode shapes. A value near one indicates a high degree of correlation or consistency between the two mode shapes. If a number near one is obtained, then it could be stated that both mode shapes represent a similar modal deformation. A value near zero indicates that the mode shapes are linearly independent and not correlated. In the proceeding analysis, if a number less than 0.5 was obtained in pairing mode shapes, then the correlation was considered to be too low to be of any significance for the purpose of detecting damage. The formula for the MAC analysis between two modes, one for the undamaged and the other for the damaged state, is given by:

$$MAC = \frac{\left( \sum_{k=1}^{nl} \phi_k \bar{\phi}_k^* \right)^2}{\left( \sum_{k=1}^{nl} \phi_k \phi_k^* \right) \left( \sum_{k=1}^{nl} \bar{\phi}_k \bar{\phi}_k^* \right)} \quad (5.1)$$

Where,  $\phi_k$  is the component of the mode-shape at location  $k$ ,  $nl$  represents the number of measurement locations, and the asterisk denotes the complex conjugate of the vector. For test article, all extracted mode shapes were real vectors

The resonant frequencies of the matching pairs of modes were compared to the frequency values where the structural response exhibited statistically significant changes as determined with the Z-function analysis. The pairs of mode shapes identified were used in the vibrational damage detection methods.

## 5.6 Damage Localization Procedure

The damage detection process used to identify inflicted damage in the Vertical Stabilizer Assembly (VSA) test article is described here. The methods used for the localization of the damage are based on modal strain energy difference using some of the approaches described in Section 2.4. The approaches include (a) averaging (ASN), (b) probability mass function formulations (PMF), (c) weighted averaging (WASN) and (d) weighted probability mass function (WPMF). Furthermore, the four approaches were followed considering two values for

the MAC, 0.5 and 0.9, and excluding and including the results of the Z-function analysis described in Appendix B. The Z-function analysis identifies mode-pairs with significant modal changes due to the inflicted damage. Nonetheless, in order to implement the damage detection methods a finite element model of the structure was required to estimate complete modes at the model's degrees-of-freedom from the experimental modes extracted at the sampled points. This approach is described in Section A.4 of Appendix A and consists of conducting a static analysis on the FE model, forcing the structure to displace according to experimental modes. In a sense, the FE results are equivalent to an interpolation. This was necessary because the model contained significantly more degrees of freedom than those instrumented with the LDV, the measured mode shapes are extrapolated to all degrees-of-freedom of the model. As explained in Section A.4, the FE approach also provided the modal strain energy content of the elements for each modal shape of the baseline and damaged structure. It should be pointed out that, for the analyses reported in this Chapter, the model was never updated with the irreparable damage. In other words the strain energy in the elements was always computed using a model of the "healthy" structure. For example, the baselines obtained for Case 6c corresponded to the damaged structure after Case 5h.

Figure 5.15 illustrates a flow chart of the complete procedure followed for implementing the detection of damage in the VSA test article. The first step of the process was the identification of frequencies with significant changes using the Z-function analysis of Appendix B conducted between the FRFs of the undamaged state to the FRFs of the damaged state. The second step was the extraction of the modal parameters from the FRFs to obtain the vibrational characteristics of the undamaged and damaged VSA test object. The modal analysis tools in SDRC I-DEAS software were used to extract the vibration characteristics. Once the mode shapes were extracted, they were exported to a file in universal format. The third step in the procedure was the static Finite Element Analysis to determine the complete modes at all degrees of freedom of the finite element model. The analysis yielded the complete mode shapes for all modes of the baseline and damage cases. From the mode shapes and the finite element description of the structures, the modal strain energy was also computed for all elements in the model for each mode of the baseline and damaged cases. The fourth step in the procedure for damage detection was to identify the pairs of matching modes between damaged and undamaged cases. The Modal Assurance Criteria (MAC) was used to identify these pairs. A value of 0.5 was the threshold established to filter the matching pairs. In addition, the results of the Z-function analysis were also used to identify the pairs of modes with resonant frequencies close to the frequencies identified as containing significant global changes from the FRFs. The fifth step in the process was to calculate the modal strain energy differences between undamaged and damaged states of the structure. The modal strain energy differences then served as the database for implementing the four damage detection algorithms described. Namely, the algorithms considered were the following: (1) the Average Standard Norm Method (ASN) or simply averaging, (2) the Probability Mass Function Method (PMF), (3) the Weighted Average Standard Norm Method (WASN) and (4) the Weighted Probability Mass Function Method (WPMF). These four methods were implemented in a MATLAB program, which generated output files listing the elements of the model and the corresponding damage detection results. The last step in the process was to generate damage maps to visualize the detection results.

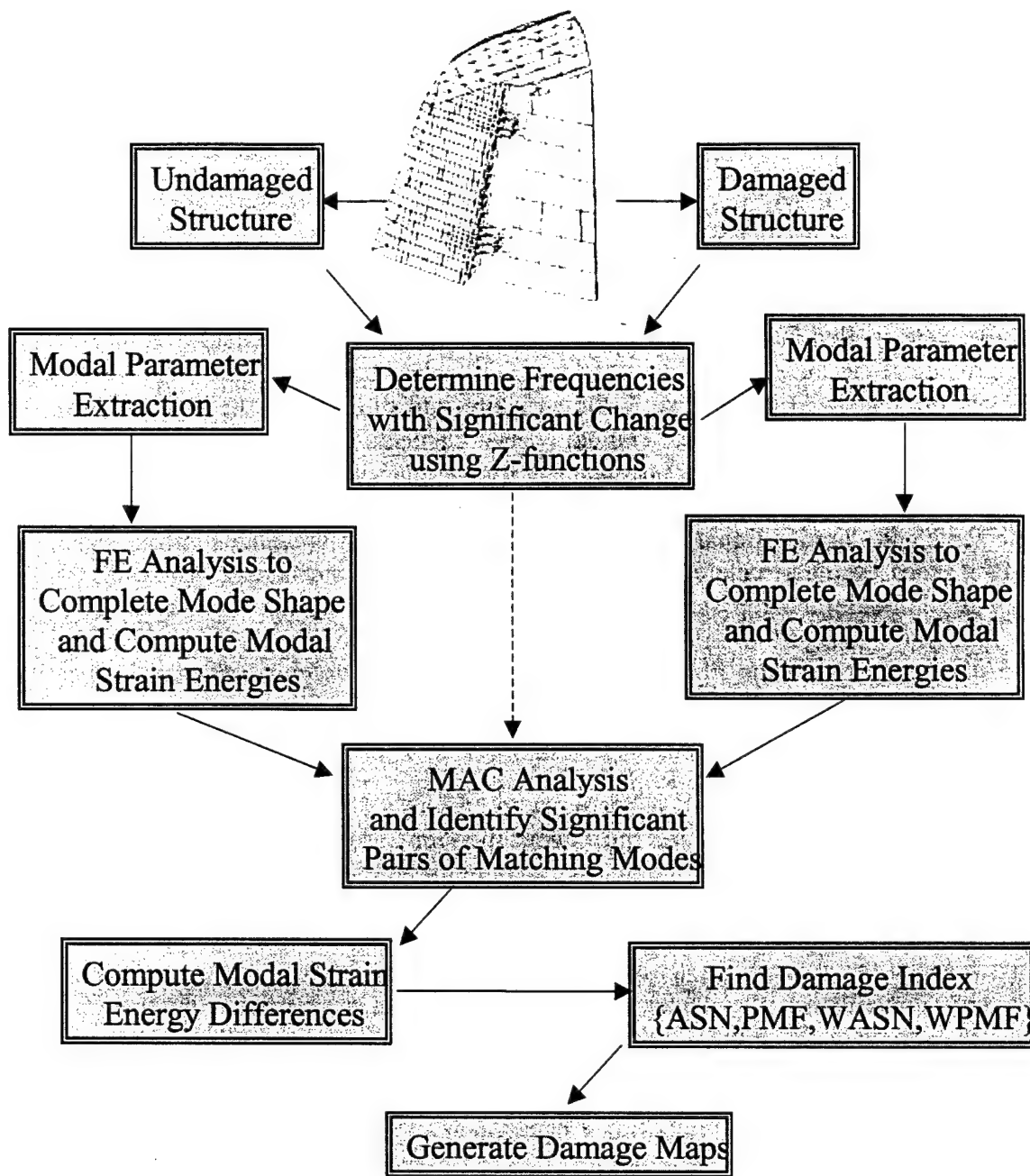


**Figure 5.15. Damage Localization Process Flow Chart.**

## 5.7 Damage Localization Results

This section includes the damage detection results obtained for the VSA. The weighted formulations (WASN and WPMF) were applied using modal weight functions defined at a threshold of 1% the maximum modal strain energy as defined in Section 2.5. In order to study the effects of the mode-pairing, four different mode-selection criteria were considered. (1) Mode-pairs with a MAC greater than 0.5 were included in the detection algorithms. (2) The

criterion was to include only the set of mode-pairs with MAC values greater than 0.9. (3) The third criterion included mode-pairs with a MAC greater than 0.5 and having found significant according to the Z-function analysis. And (4) the last criterion included mode-pairs with a MAC greater than 0.9 and having found significant according to the Z-function. The results are presented in the form of damage and summarized with tables listing detectability, number of false positives (NFP) and detection performance in terms of a performance index (PI). The efficacy of the methods and the mode-selection criteria were evaluated and compared as functions of the detectability, the NFP and the PI.

The final results of the damage detection procedure included the creation of damage maps. These were created in NASTRAN in order to visualize the damage detection results over the entire structure. Because the structure has the back surface and the middle elements hidden, they can only be visualized by separating the structure into three parts, the front surface, the middle structure and the back surface. The only set of elements that indicated damage was the one corresponding to the middle elements, which carry the majority of the stiffness. The reason for this pattern is that the lateral stiffness in the entire structure is provided primarily by the middle elements and the vibrational damage detection methods only evaluate stiffness changes between two states of the structure. For example in Case 4a, the damage consisted of the removal of the left-side and top screws of the access panel as illustrated in Figure 5.5. By removing the screws, part of the connection between the ribs and the panels is lost; reducing the composite stiffness between the ribs and the panels and thus it is only reflected in the ribs. Therefore all damage maps presented here correspond to the middle elements of the VSA structure only.

Before presenting the results it is necessary to present a discussion of the magnitudes in the damage maps. Figure 5.16 illustrates the damage map for Case 4a obtained with the Average Standard Norm Method (ASN). Notice that the maximum amplitude in the scale is about 15. This means that the location with the maximum value experienced an average increase in the modal strain energy 15 times the standard deviation of the mean value for all elements. In this method, however, if the index is greater than 2, then the location is potentially damaged. If this criterion were adopted, then the damage maps would contain a significant number of false positive damage predictions. Thus, for the purpose of this research, since all damage scenarios examined contained damage around a single location, damage is only reflected at the locations with the orange-red color levels. The same above discussion applies to the Weighted Average Standard Norm (WASN) Method. Figure 5.17 illustrates the damage maps for the same case obtained with the WASN method. Notice that in the WASN method, the maximum value is larger than the one obtained with the ASN methods. This is attributed to the utilization of the modal weight factors, eliminating regions of low modal strain energy using the threshold of 1% of the maximum modal strain energy. The values computed with the Probability Mass Functions (PMF) methods represent the relative probabilities of elements being damaged in relation to the rest of the elements. Figure 5.18 illustrates the damage map for Case 4a obtained with the PMF. The maximum amplitude in the scale is about 0.20. That is, the location is 20% more probable of being damaged than the rest of the elements. Thus, the damage maps obtained with the PMF indicate the locations that are more likely to be damaged. The same discussion applies to the Weighted Probability Mass Function (WPMF) Method.



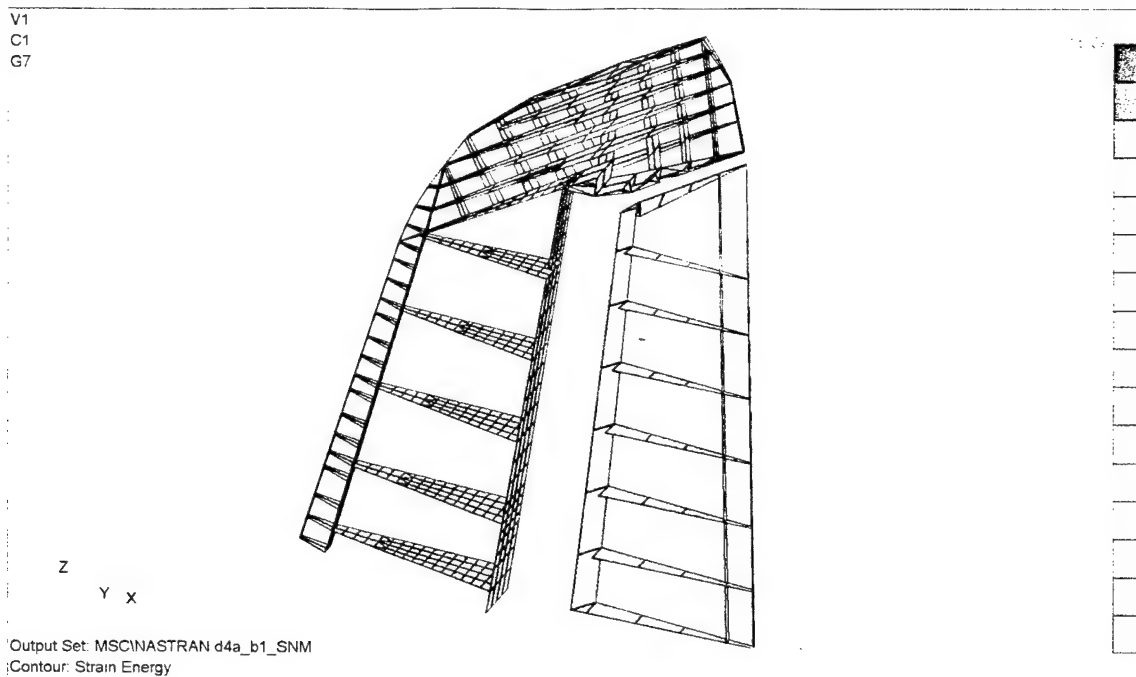


**Figure 5.16. Damage Map for Middle Elements for Case 4a - ASN Method.**

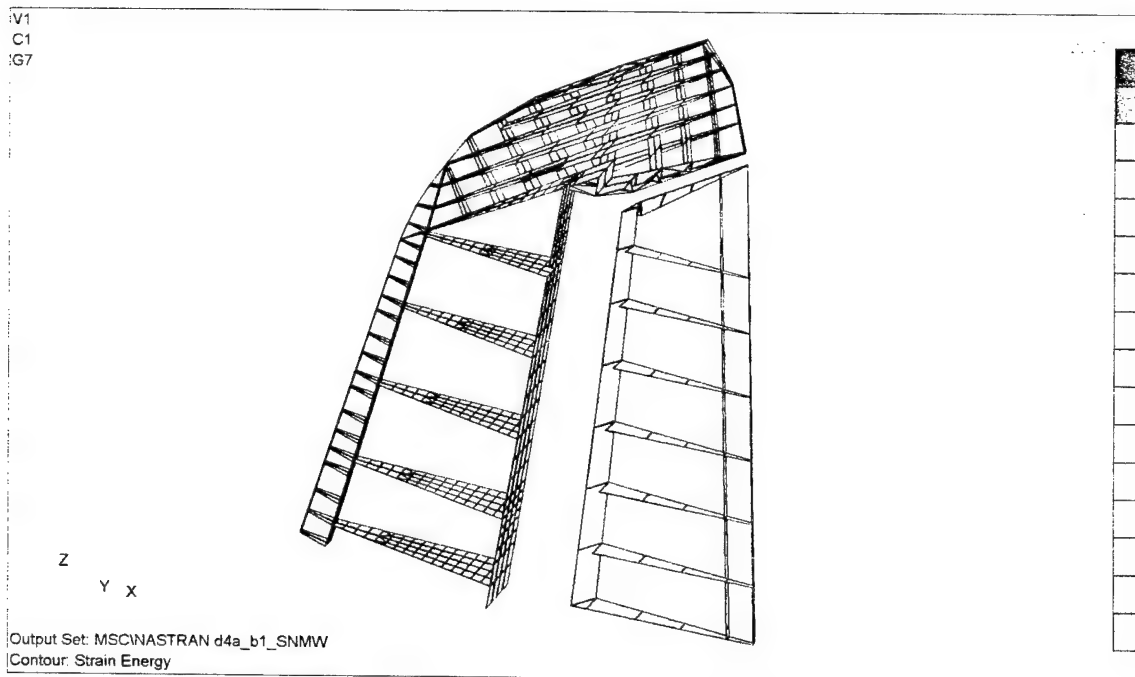


**Figure 5.17. Damage Map for Middle Elements for Case 4a - WASN Method.**



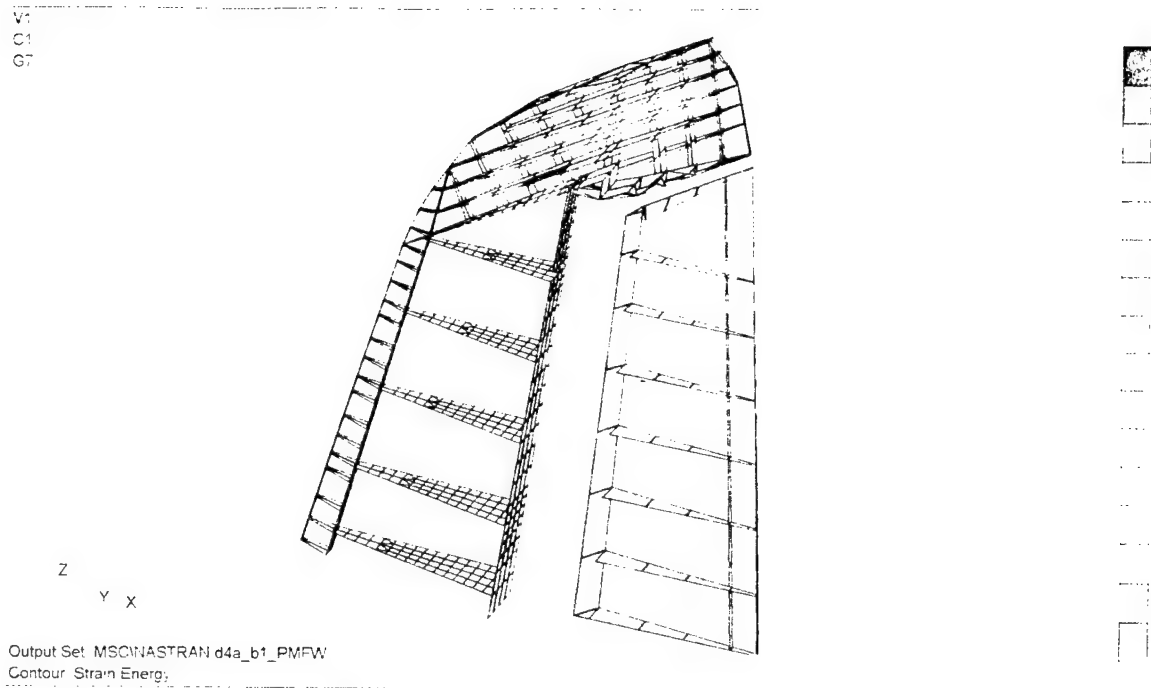


**Figure 5.18. Damage Map for Middle Elements for Case 4a - PMF Method.**

Damage maps, such as the ones depicted in the previous three figures, were obtained for all damage cases and damage levels using the four damage detection algorithms considered. In addition, the above task was repeated considering sets of modes chosen using four different mode-selection criteria as previously discussed. The damage maps were visually observed in a computer screen and information related to the detectability, the number of false positives (NFP) and the detection performance in terms of a performance index (PI) were collected. The detectability was simply evaluated in terms of whether the correct location was detected as being damaged. The number of false positives was obtained by counting the number of regions with high levels of damage depicted by the orange-red colors of the contours of the damage maps. Then, an indication was made for each damage map if the maximum damage index is located in the correct location. The performance index (PI) was intended to provide a measure of the abilities of the method to detect damage as a function of detectability, number of NFPs, and whether the maximum index is at the correct location. The PI was defined as follows:

If the damage is accurately located with no NFPs, then  $PI = 10$ . If the damage is located at the region of maximum damage magnitude but with false positives at other locations, then the PI was computed as  $(PI = 8 - NFP)$ . If the damage is detected but the maximum value in the damage map is not at the correct location, then the PI was computed with the expression  $(PI = 5 - NFP)$ . Finally, if the damage was not detected at the correct location at all, then  $PI = 0$ .

Table 5.2 summarizes the detection results obtained using the first mode-selection criterion of using the mode with MAC values greater than 0.5. The first column indicates the damage case. The second column lists the number of mode-pairs included in the set for damage detection. The third column indicates the damage detection method. The fourth column simply contains Y or N indicating whether the damage was detected in the damage map. The fifth column lists the number of false positives (NFP). The sixth column shows Y or N, to indicate if the maximum value in the damage map corresponded to the actual location of damage. The last column lists the PI value computed as previously described. Tables 5.3 through 5.5 summarize the damage detection results for the other three mode-selection criteria. The asterisk in the third column indicates that the damage maps are illustrated in the next section of this chapter.

It can be observed that none of the methods using any of the mode-selection criteria was able to locate the damage in Cases 5b, 6b and 7c. The reasons the damage in Case 5b was not detected were not known but it is puzzling that the damages in Cases 5a, 5c and 5h, in the same location, were detected. Perhaps, something wrong was performed during the modal extraction process for Case 5b. The Cases 6b and 7c were probably not detected because the regions of inflicted damage were of low modal strain energy.

**Table 5.2. Summary of Detection Results Using Mode-Pairs with MAC > 0.5.**

Case	Number of Modes	Method	Detection	NFP	Max at C. Loc.	P.I.
Case 4a	10	ASN	Y	0	Y	10
		PMF	Y	1	Y	7
		WASN	N	1	N	0
		WPMF	Y	1	Y	7
Case 4b	11	ASN *	Y	0	Y	10
		PMF	Y	1	N	4
		WASN	Y	1	N	4
		WPMF	Y	1	N	4
Case 4c	11	ASN	Y	0	Y	10
		PMF	Y	1	Y	7
		WASN	Y	1	Y	7
		WPMF	Y	1	N	4
Case 5a	14	ASN	N	2	N	0
		PMF	N	2	N	0
		WASN	N	1	N	0
		WPMF	N	3	N	0
Case 5b	14	ASN	N	2	N	0
		PMF	N	2	N	0
		WASN	N	4	N	0
		WPMF	N	2	N	0
Case 5c	13	ASN	N	2	N	0
		PMF	Y	1	N	4
		WASN	N	2	N	0
		WPMF	Y	1	N	4
Case 5h	14	ASN	Y	1	N	4
		PMF	Y	0	Y	10
		WASN	N	2	N	0
		WPMF	Y	0	Y	10
Case 6c	12	ASN	N	4	N	0
		PMF	N	1	N	0
		WASN	N	1	N	0
		WPMF	N	1	N	0
Case 7b	14	ASN	N	4	N	0
		PMF	N	1	N	0
		WASN	N	2	N	0
		WPMF	N	2	N	0
Case 8f	16	ASN	Y	0	Y	10
		PMF	Y	2	Y	6
		WASN	Y	0	Y	10
		WPMF	Y	2	N	3

**Table 5.3. Summary of Detection Results Using Mode-Pairs with MAC > 0.9.**

Case	Number of Modes	Method	Detection	NFP	Max at C. Loc.	P.I.
Case 4a	7	ASN	Y	2	Y	6
		PMF	Y	2	Y	6
		WASN	N	1	N	0
		WPMF	Y	1	Y	7
Case 4b	8	ASN	Y	1	Y	7
		PMF	Y	1	N	4
		WASN	Y	1	Y	7
		WPMF	Y	1	N	4
Case 4c	6	ASN	Y	1	N	4
		PMF	N	2	N	0
		WASN	N	1	N	0
		WPMF *	N	2	N	0
Case 5a	10	ASN	N	2	N	0
		PMF	Y	1	N	4
		WASN	N	1	N	0
		WPMF	Y	1	Y	7
Case 5b	8	ASN	N	1	N	0
		PMF	N	2	N	0
		WASN	N	2	N	0
		WPMF	N	1	N	0
Case 5c	8	ASN	N	1	N	0
		PMF	N	1	N	0
		WASN	N	2	N	0
		WPMF	N	1	N	0
Case 5h	10	ASN	Y	0	Y	10
		PMF	Y	1	Y	7
		WASN	Y	0	Y	10
		WPMF	Y	1	Y	7
Case 6c	9	ASN	N	2	N	0
		PMF	N	1	N	0
		WASN	N	3	N	0
		WPMF	N	1	N	0
Case 7b	10	ASN	N	2	N	0
		PMF	N	2	N	0
		WASN	N	2	N	0
		WPMF	N	2	N	0
Case 8f	12	ASN	Y	0	Y	10
		PMF	Y	1	Y	7
		WASN *	Y	0	Y	10
		WPMF	Y	1	Y	7

**Table 5.4. Summary of Detection Results Using Mode-Pairs with MAC > 0.5 and Indicated as Significant by the Z-Function Analysis.**

Case	Number of Modes	Method	Detection	NFP	Max at C. Loc.	P.I.
Case 4a	5	ASN	Y	0	Y	10
		PMF	Y	0	Y	10
		WASN	Y	0	Y	10
		WPMF *	Y	0	Y	10
Case 4b	5	ASN	Y	0	Y	10
		PMF	Y	0	Y	10
		WASN	Y	2	Y	6
		WPMF *	Y	0	Y	10
Case 4c	6	ASN	Y	1	N	4
		PMF	N	1	N	0
		WASN	N	1	N	0
		WPMF	N	1	N	0
Case 5a	9	ASN	Y	2	Y	6
		PMF	Y	1	N	4
		WASN	N	4	N	0
		WPMF	Y	3	Y	5
Case 5b	7	ASN	N	2	N	0
		PMF	N	1	N	0
		WASN	N	3	N	0
		WPMF *	N	1	N	0
Case 5c	6	ASN	Y	0	Y	10
		PMF	Y	0	Y	10
		WASN	N	1	N	0
		WPMF *	Y	0	Y	10
Case 5h	4	ASN	N	1	N	0
		PMF	Y	1	N	4
		WASN	N	1	N	0
		WPMF	Y	1	Y	7
Case 6c	5	ASN	N	2	N	0
		PMF	N	1	N	0
		WASN	N	2	N	0
		WPMF *	N	1	N	0
Case 7b	4	ASN	N	2	N	0
		PMF	N	1	N	0
		WASN	N	2	N	0
		WPMF *	N	2	N	0
Case 8f	6	ASN	N	2	N	0
		PMF	Y	1	N	4
		WASN	N	2	N	0
		WPMF	Y	1	Y	7

**Table 5.5. Summary of Detection Results Using Mode-Pairs with MAC > 0.9 and Indicated as Significant by the Z-Function Analysis.**

Case	Number of Modes	Method	Detection	NFP	Max at C. Loc.	P.I.
Case 4a	3	ASN	Y	0	Y	10
		PMF	Y	0	Y	10
		WASN	Y	0	Y	10
		WPMF	Y	0	Y	10
Case 4b	4	ASN	Y	2	N	3
		PMF	Y	0	Y	10
		WASN	Y	2	Y	6
		WPMF	Y	1	Y	7
Case 4c	3	ASN	Y	1	Y	7
		PMF	N	2	N	0
		WASN	N	1	N	0
		WPMF	N	2	N	0
Case 5a	5	ASN	N	1	N	0
		PMF	N	2	N	0
		WASN	N	1	N	0
		WPMF	N	2	N	0
Case 5b	6	ASN	N	2	N	0
		PMF	N	2	N	0
		WASN	N	3	N	0
		WPMF	N	1	N	0
Case 5c	4	ASN	N	2	N	0
		PMF	Y	1	Y	7
		WASN	N	1	N	0
		WPMF	Y	0	Y	10
Case 5h	3	ASN	N	1	N	0
		PMF	Y	2	Y	6
		WASN	N	1	N	0
		WPMF *	Y	0	Y	10
Case 6c	4	ASN	N	2	N	0
		PMF	N	2	N	0
		WASN	N	1	N	0
		WPMF	N	2	N	0
Case 7b	3	ASN	N	1	N	0
		PMF	N	2	N	0
		WASN	N	2	N	0
		WPMF	N	2	N	0
Case 8f	5	ASN	Y	3	N	2
		PMF	Y	2	Y	6
		WASN	N	3	N	0
		WPMF	Y	2	Y	6

## 5.8 Damage Detection Maps for All Cases

This section illustrates sample damage maps for all the cases considered. Figures 5.19, 5.20 and 5.21 illustrate the damage maps obtained for Cases 4a, 4b and 4c. Figure 5.19 also shows a picture of the test article indicating the actual location of the inflicted damages in this case series. It should be observed that the general location in the inflicted damage is detected. The specific mode-selection criteria corresponding to the figures can be obtained from the asterisks in Tables 5.2 through 5.5.

Figures 5.22 through 5.25 illustrate the damage maps obtained for Cases 5a, 5b, 5c and 5h, respectively. Figure 5.22 additionally includes a picture of the VSA showing the actual damage location of the Case 5 series. It should be observed that the only case where damage was not accurately detected is Case 5b of Figure 5.23. Also notice that in Case 5a, the damage detection includes a false positive location as indicated by the orange-red colors in the contours. In this case, however, the maximum value of the contour damage map corresponds to the actual general location of the damage.

Figures 5.26 and 5.27 correspond to Cases 6b and 7c. In these cases the damages were not detected. The accompanying photos indicate the actual location of the inflicted damages. Finally, Figure 5.28 illustrates the damage map corresponding to Case 8f. It should be noted that the damage was detected on the rib members of the rudder at the right of the actual damage location.

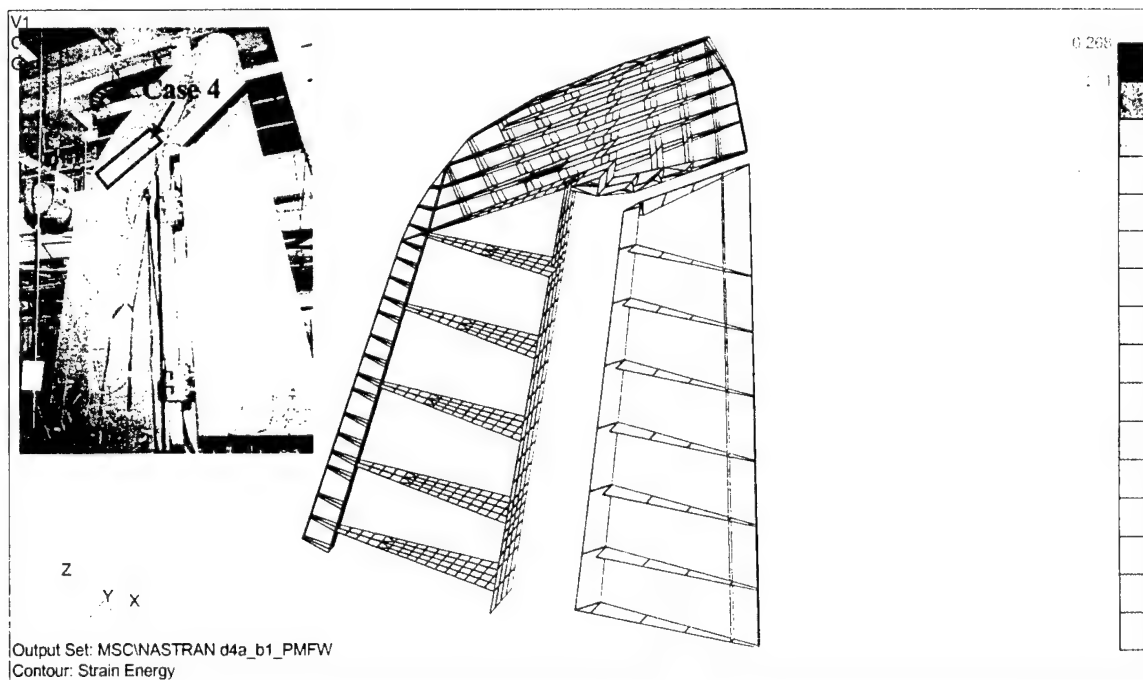


**Figure 5.19. Damage Maps for Case 4a Using WPMF Method.**

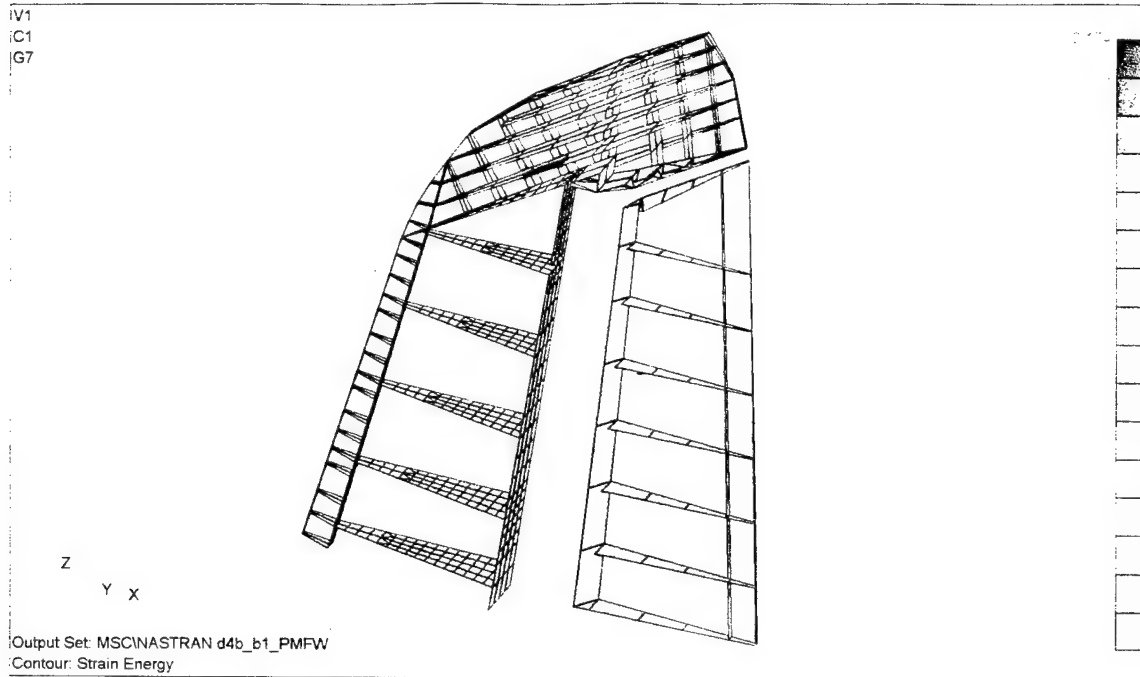


**Figure 5.20. Damage Maps for Case 4b Using WPMF Method.**

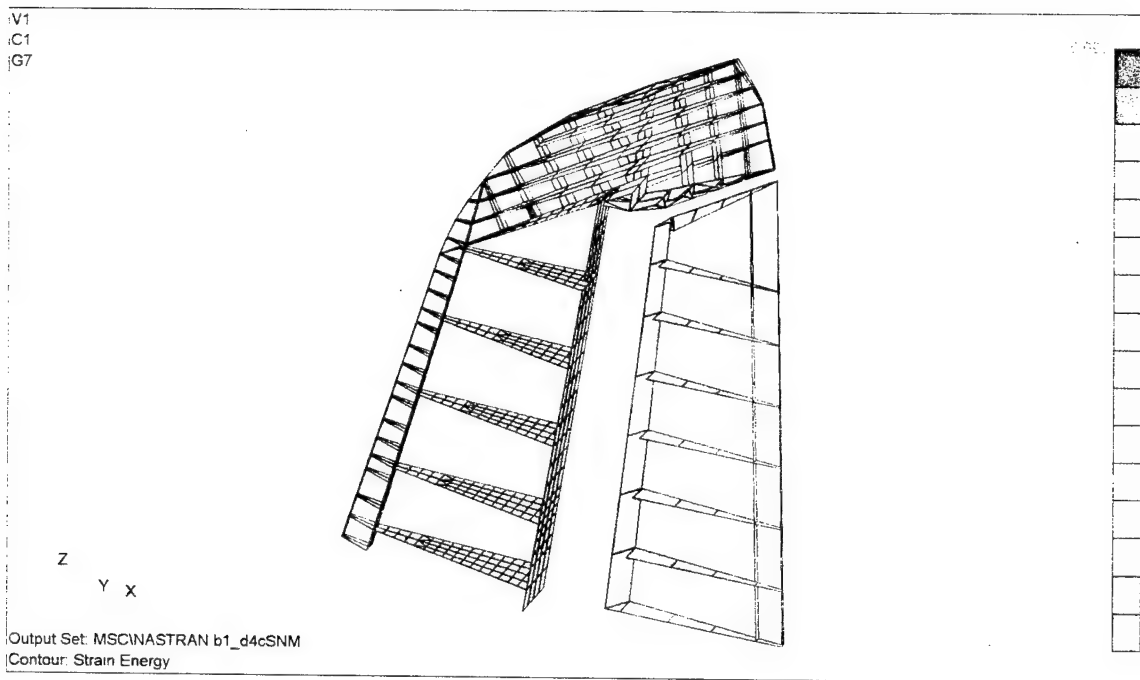


**Figure 5.21. Damage Maps for Case 4c Using ASN Method.**



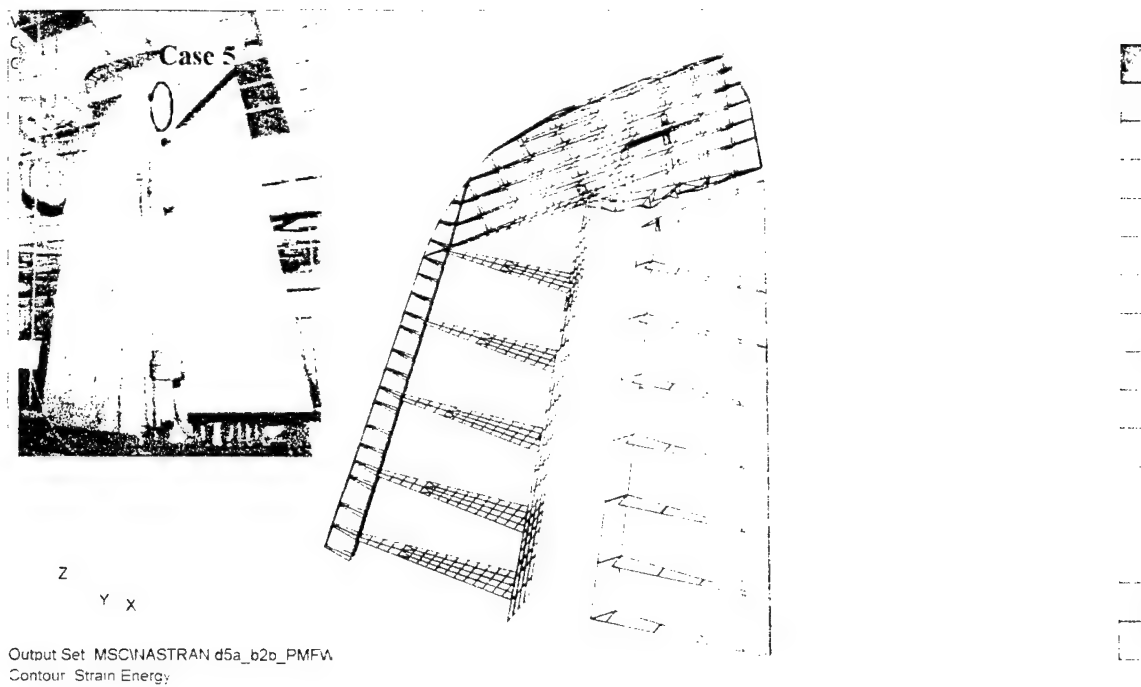


**Figure 5.22. Damage Maps for Case 5a Using WPMF Method.**

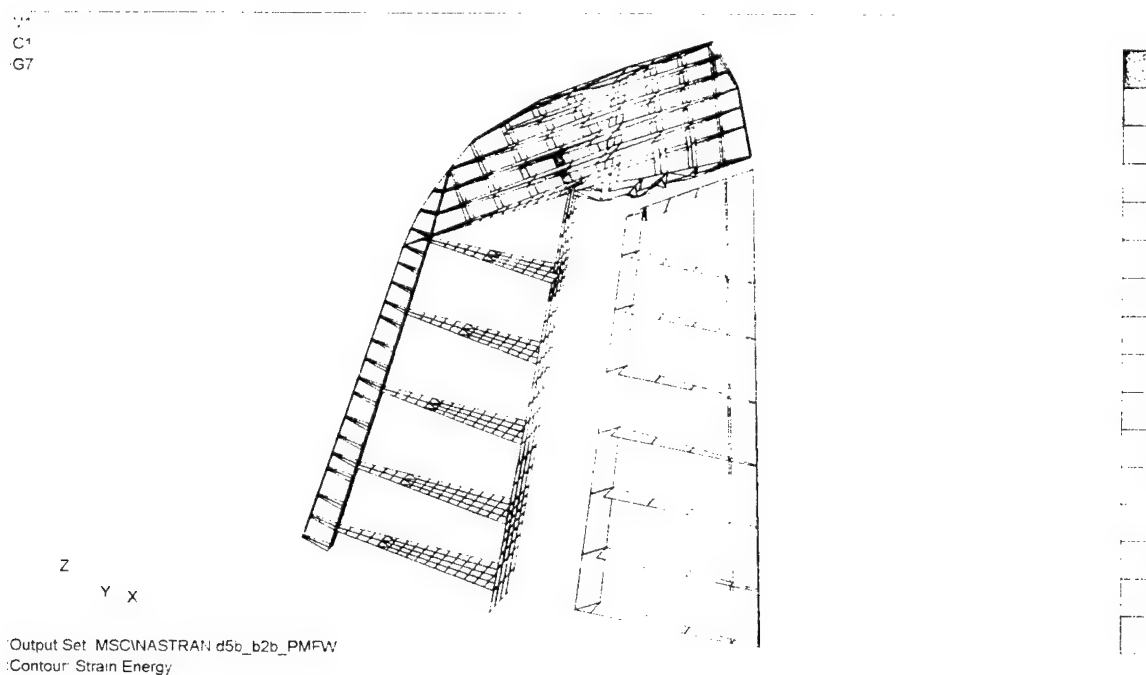


**Figure 5.23. Damage Maps for Case 5b Using WPMF Method.**

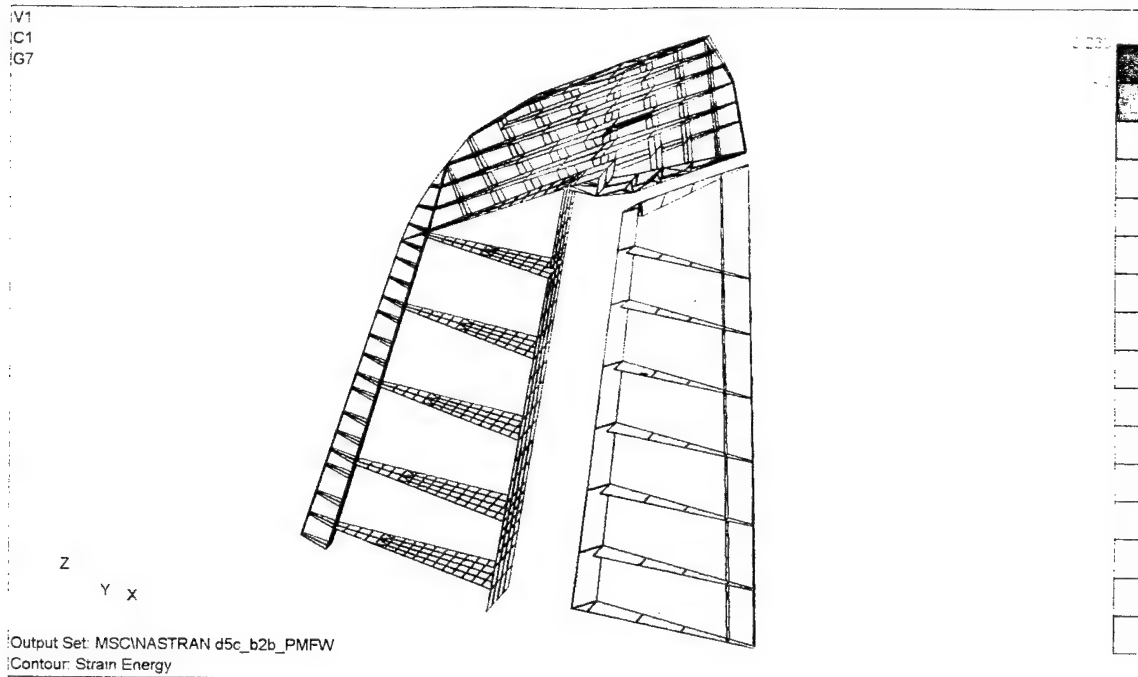


**Figure 5.24. Damage Maps for Case 5c Using WPMF Method.**

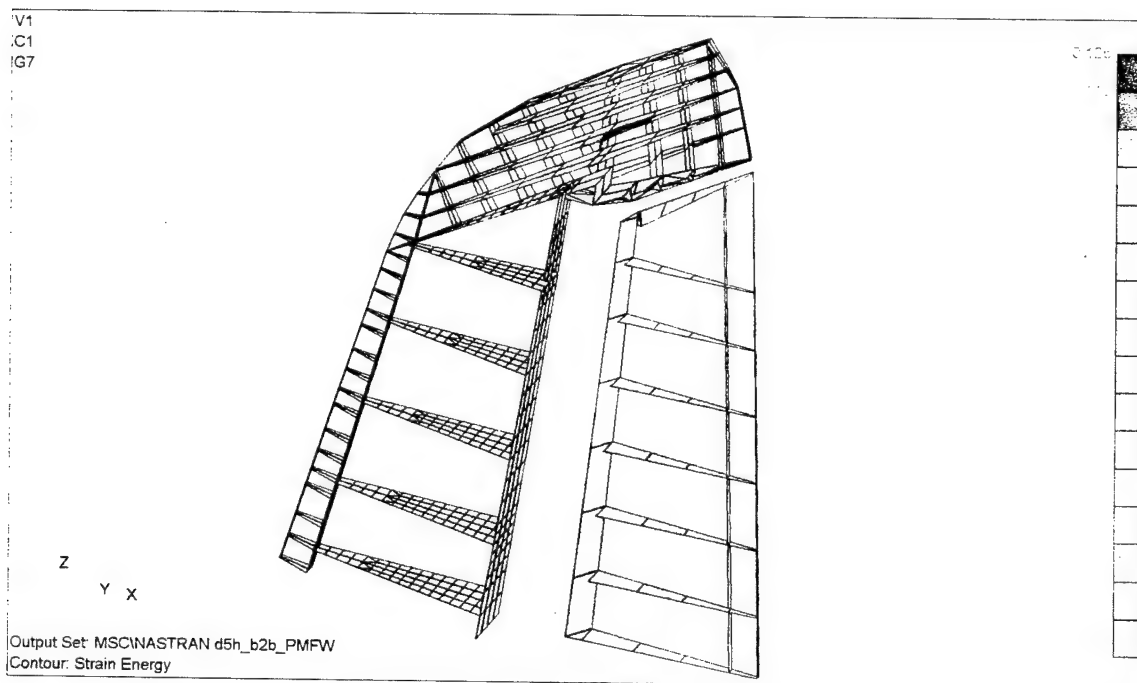


**Figure 5.25. Damage Maps for Case 5h Using WPMF Method.**

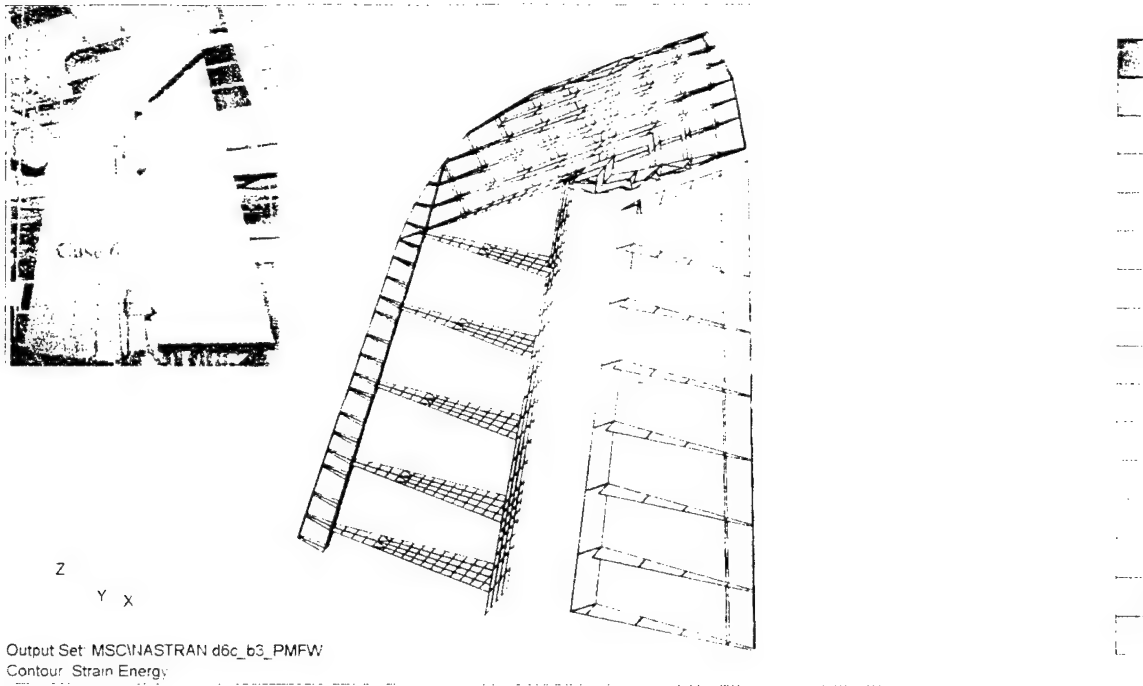


**Figure 5.26. Damage Maps for Case 6c Using WPMF Method.**

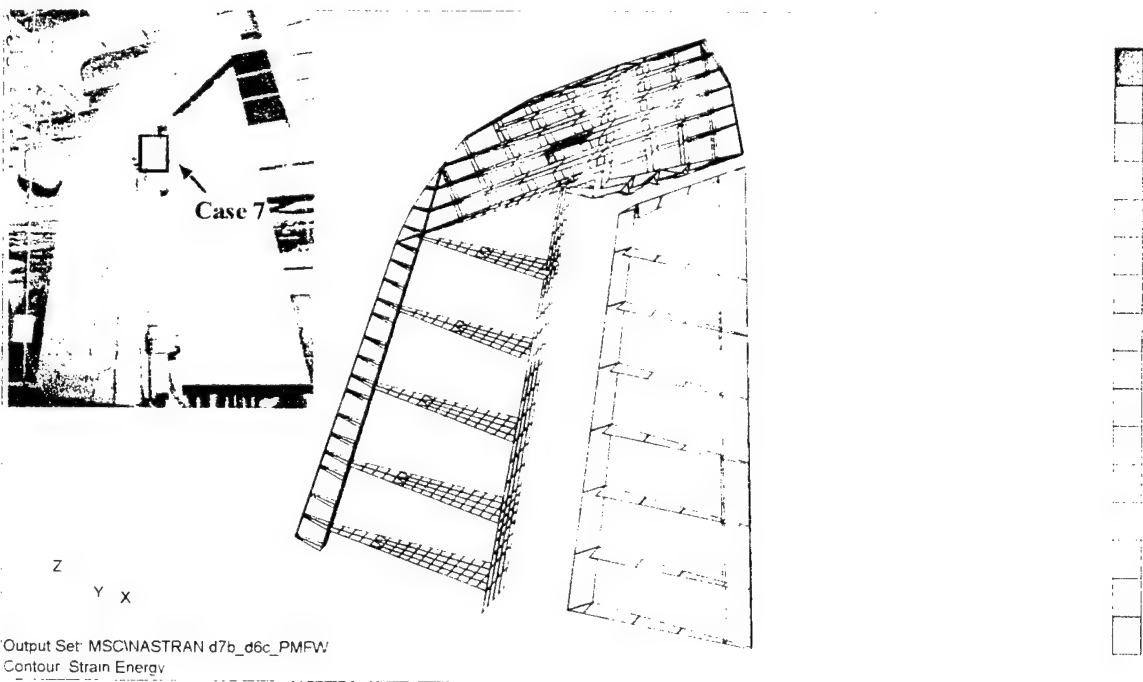


**Figure 5.27. Damage Maps for Case 7b Using WPMF Method.**

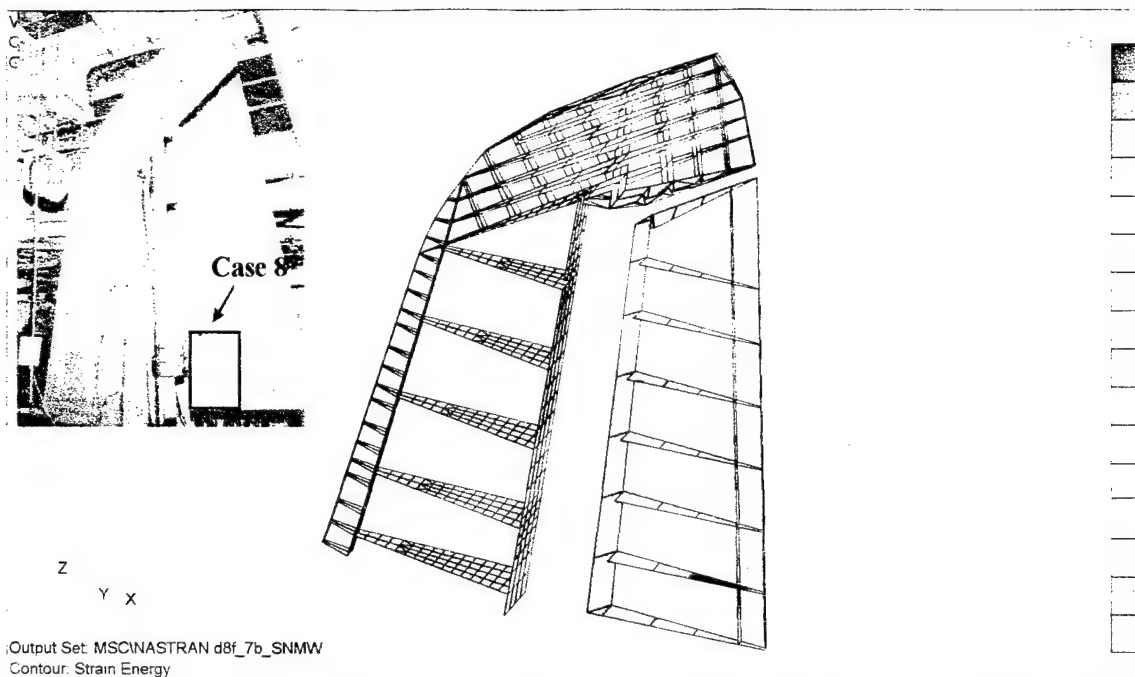


**Figure 5.28. Damage Maps for Case 8f Using WASN Method.**

## 5.9 Comparison of Performance of Damage Detection Algorithms

This section presents a comparison of the performance of the damage detection algorithms as a function of the four mode-selection criteria mentioned before. Table 5.6 lists a summary of the performance of the detection methods obtained from a further summary of Tables 5.2 through 5.5. The first column indicates the mode-selection criterion; the second, the average number of modes used in the detection for all cases; the third column lists the method. The fourth column lists the total number of successful damage detections. The fifth and sixth columns were similarly obtained by adding the number of false positives and the values of the performance index (PI), respectively. The last column is the addition of the PI values of column 5 for each mode-selection criterion. The interpretation of the numbers in this table leads to the following general conclusions:

- 1) Both the PMF and the WPMF methods, in general, provided better detectability regardless of the mode-selection criteria. The detectability here is defined as the number of correct detections divided by the number of cases.
- 2) The ASN Method yields the highest performance in locating damage, when the Z-function analysis described in Appendix B is not used. The obvious advantage of using the ASN method is the robustness of using all available modes without being selective on choosing the ones considered as significant.

**Table 5.6. Summary of Detection Methods' Performance According to Mode-Selection Criteria.**

<b>Selection Criteria</b>	<b>Ave. No. of Modes</b>	<b>Method</b>	<b>No. of Detections</b>	<b>Total NFP</b>	<b>PI</b>	<b>Total PL</b>
<b>MAC &gt;0.5</b>	12.9	ASN	5	15	44	135
		PMF	6	12	38	
		WASN	3	15	21	
		WPMF	6	14	32	
<b>MAC &gt;0.9</b>	8.8	ASN	5	12	37	130
		PMF	5	12	31	
		WASN	3	13	27	
		WPMF	5	11	35	
<b>MAC &gt;0.5 &amp; Z-Function</b>	5.7	ASN	5	12	40	147
		PMF	6	7	42	
		WASN	2	17	16	
		WPMF	6	10	49	
<b>MAC &gt;0.9 &amp; Z-Function</b>	4	ASN	4	15	22	120
		PMF	5	15	39	
		WASN	2	15	16	
		WPMF	5	10	43	

- 3) The WPMF yields the highest performance when the Z-function analysis is performed. This is of course at a cost of performing the Z-function analysis to identify the mode-pairs that contain significant global changes.
- 4) Higher detection performance is generally obtained by considering mode-pairs with MAC values of 0.5 between the undamaged and damaged states of the structure. This is the case with or without the use of the Z-function analysis results. The set of mode-pairs with MAC values greater than 0.9 provided a lower damage detection performance.
- 5) The combination of using the Z-function analysis to select significant mode-pairs with MAC values greater than 0.5 yielded the highest damage detection performance of all the methods and mode-selection criteria. It should be noticed with this mode-selection criterion, that the number of mode-pairs used in the damage detection is much lower than the one if the Z-function analysis is not used to screen out irrelevant mode-pairs.
- 6) The Weighted Average Standard Norm consistently yielded the lowest performance of all methods.

## CHAPTER 6

### FURTHER ANALYSES OF VSA TESTS

#### 6.1 Introduction

The work described in the previous chapter was extended by Macias (2000) to include additional fusion approaches as well as relying on an improved finite element model. The finite element model that was used to extract the complete modal information was modified to include all bar elements of the model. It turned out that the bar elements contributed significantly to the stiffness of the VSA structure and affected the distribution of the strain energy. In addition, the work described in the previous chapter only considered an undamaged finite element model. Finite element model updating due to the damage already present in some of the baselines was performed.

The damage detection results were obtained using the Averaging, Bayes fusion, and PMF methods described in Chapter 2. The methods only considered mode-pairs identified with a MAC value greater than 0.5. Two different mode-selection criteria were considered. First, mode-pairs with a MAC greater than 0.5 were included in the detection algorithms. Then, the second selection criterion included those mode-pairs identified to contain significant global changes from the Z-function analysis of Appendix B, and MAC values greater than 0.5. The results are presented in the form of damage and summarized in tables listing detectability, number of false positives (NFP) and detection performance in terms of a performance index (PI). The methods and the use of the Z-function were evaluated and compared as functions of detectability, the NFP and the PI.

#### 6.2 Finite Element Model Updating

In order to improve the damage detection results, the NASTRAN finite element model was updated. The permanent damages experienced by the structure were simulated on the model by erasing the elements that were damaged during the experiment. By doing this, the strain energy density of the elements surrounding the damaged elements increased. The model was updated starting with damage case 5h; this was the first case in which the structure had prior irreversible damage. Once the elements for this case were erased, a static analysis was performed to obtain the strain energy density. Then, for case 6c, the elements damaged in case 5h were erased and a new static analysis was performed. This process was repeated for cases 7b and 8f. That is, for the model representing case 7b, the damaged elements of cases 5h and 6c were erased; and for case 8f the damaged elements from cases 5h, 6c and 7b were removed. A static analysis was performed also for cases 7b and 8f.

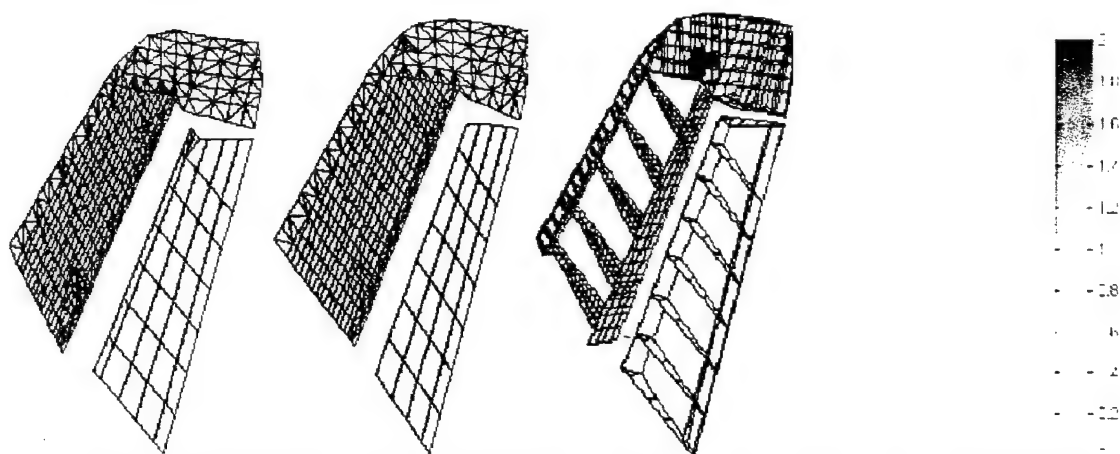
The idea behind the model updating was to use the strain energy density information of a damage case and use it as the baseline for the next case. For instance, the strain energy density results obtained from case 6c were compared to those results obtained from case 5h, which served as the baseline. Then, the results from case 6c served as the baseline for case 7b, and the results from case 7b for 8f.

### 6.3 Description of Damage Maps

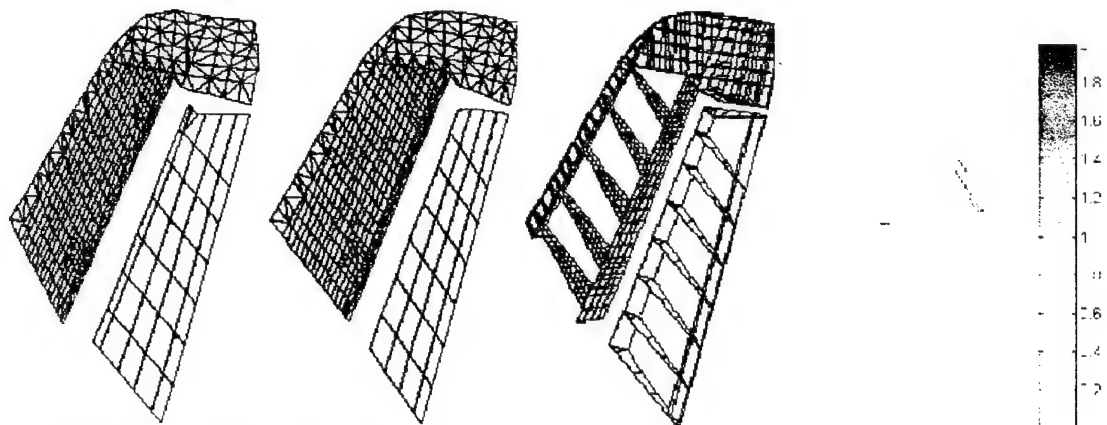
Figure 6.1(a) illustrates the damage detection results obtained for Case 4b by averaging using the mode-pairs matched with a MAC greater than 0.5 and through the Z-function analysis. The left graph illustrates the shell elements of the model on the left surface of the VSA. The second graph shows the similar elements but corresponding to the right surface. The third graph shows the hidden plate and shell elements. The fourth one illustrates the damage prediction results of the bar elements of the model (bars and beams). These bar elements were excluded from the analyses of Chapter 5. It is clearly seen, by comparing the red area of Figure 6.1(a) to the actual location of the damage shown in Figure 5.5 that the damage is correctly located with no false positives. Figure 6.1(b) shows the damage detection results for Case 5h, which was not detected by the averaging method. Figure 6.1(c) illustrates the damage maps obtained using the Bayes fusion method. This method correctly located the damage, with a better representation of the damage extent. Also note that it comes at a cost of false positives. Similar damage detection maps were obtained for all the cases, considering the two methods and the two mode-pairing and selection criteria. The damage maps for all cases were visually inspected in order to assess the damage detectability and the number of false positives.

Damage maps, such as the ones depicted in Figure 6.1 figures were obtained for all damage scenarios and using the three Damage Detection Methods discussed mentioned in the foregoing. In addition, the above maps considered those mode-pairs with a MAC greater than 0.5 with and without the use of the Z-function. The damages were visually inspected and the information related to detectability, number of false positives (NFP), and the detection performance in terms of the performance index (PI) was collected.

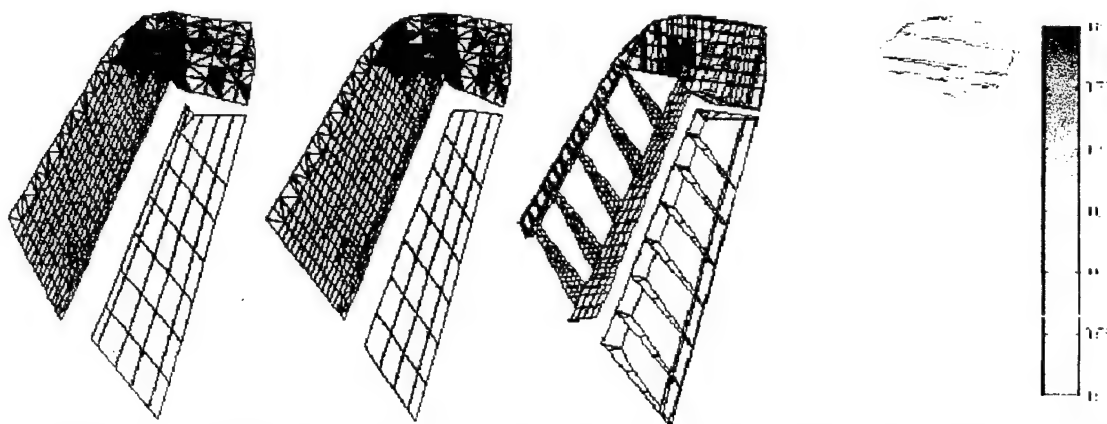
The evaluation of the detectability was based on whether the damage location is correct or not. The damage is said to be correctly located if the color at that region represents a value greater than zero on the contour bar, regardless of the magnitude. The number of false positives was obtained by counting the number of locations with the highest possible level of damage depicted by orange-red colors of the contours of the damage maps. Then, an indication was made for each damage map if the maximum damage index is located in the correct location. The performance index (PI) was intended to provide a measure of the abilities of the method to detect damage as a function of detectability, number of false positives (NFP), and whether the damage prediction reflected the correct location as a maximum. The PI was defined in Section 5.7 of this report.



(a) Damage Maps Results by Averaging, Case 4b, using Z-function. (Detection)



(b) Damage Maps Results by Averaging, Case 5h, using Z-function. (No Detection)



(c) Damage Maps Results by Bayes Fusion, Case 4b, using Z-function. (Detection)

**Figure 6.1 Sample Damage Maps, using Improved FE model.**



Table 6.1 summarizes the damage detection results obtained using the first criterion previously described above. The first column indicates the damage case. The second column lists the number of mode-pairs included in the set for damage detection. The third column indicates the damage detection method. The fourth column indicates with a Y or N if the damage was correctly located in the damage map. The fifth column indicates the number of false positives (NFP). The sixth column with a Y or N shows if the maximum value in the color map corresponded to the actual location of the damage. The last column lists the PI value computed as described previously in this section. Table 6.2 summarizes the results using the second criterion ( $MAC > 0.5$  with Z-function), and Table 6.3 presents the results obtained after the finite element model was updated and considering the second criterion.

It can be observed that none of the methods using any of the two mode-selection criteria was able to locate the damage in Case 6c. This was most probably because this is a region with very low sensitivity; that is, a region of very low strain energy. Therefore, whether there is a damage or not located in that region, the strain energy is low under any conditions (damaged or healthy). A modal strain energy analysis could be conducted to verify this hypothesis.

The damage maps for all the ten damage cases, considering the three detection methods, and the finite model update, are presented in Appendix C.

#### **6.4 Comparison of Performance of Damage Detection Methods**

The comparison was made from the information summarized in the previous tables and shown in Table 6.4. The first column indicates the mode selection criteria; the second, the average number of modes used in the detection for all cases; the third column lists the detection method. The fourth column lists the total number of damages detected correctly; this value was obtained by adding the number of detections per table for all ten cases as a function of the method. The fifth and sixth columns were obtained in a similar manner by adding the number of false positives (NFP) and the performance index (PI) respectively. The last column is the addition of all the PI values in column 5 for each selection criterion. By interpreting the values listed in this table, the following conclusions can be established:

- (1) Both the PMF method, in general, provided better detectability regardless of the mode-selection criteria and model update. That is, this method detected 9 out of 10 damages in every selection criteria.
- (2) The Averaging technique yielded the highest performance in locating damage, when the Z-function analysis described in Appendix B was used.
- (3) The PMF yields yielded the highest performance when the Z-function analysis was not used. Although averaging shows a greater performance value for this selection criterion, it only detected 7 damages correctly.
- (4) Higher detection performance was generally obtained considering mode-pairs "with significant global changes". That is, better results were obtained when the Z-function analysis was implemented in the mode-selection criteria.

**Table 6.1. Summary of Damage Detection Results Using Mode-Pairs with MAC >0.5.**

CASE	Number of Modes	Method	Detection	NFP	Max. at C. Loc.	P.I.
Case 4a	10	Averaging	Y	0	Y	10
		Bayes	Y	5	Y	3
		PMF	Y	2	Y	6
Case 4b	11	Averaging	Y	3	Y	5
		Bayes	Y	6	Y	2
		PMF	Y	5	Y	3
Case 4c	11	Averaging	Y	1	Y	7
		Bayes	Y	4	Y	4
		PMF	Y	1	Y	7
Case 5a	14	Averaging	Y	0	Y	10
		Bayes	Y	5	Y	3
		PMF	Y	4	Y	4
Case 5b	14	Averaging	Y	0	Y	10
		Bayes	Y	6	Y	2
		PMF	Y	4	Y	4
Case 5c	13	Averaging	N	0	N	0
		Bayes	Y	3	Y	5
		PMF	Y	2	Y	6
Case 5h	14	Averaging	N	0	N	0
		Bayes	Y	6	Y	2
		PMF	Y	4	Y	4
Case 6c	12	Averaging	N	1	N	0
		Bayes	N	5	N	0
		PMF	N	3	N	0
Case 7b	14	Averaging	Y	1	N	4
		Bayes	Y	5	Y	3
		PMF	Y	4	Y	4
Case 8f	16	Averaging	Y	0	Y	10
		Bayes	Y	5	Y	3
		PMF	Y	3	Y	5

**Table 6.2. Summary of Damage Detection Results Using Mode-Pairs with MAC > 0.5 and Indicated as Significant by the Z-Function Analysis.**

CASE	Number of Modes	Method	Detection	NFP	Max. at C. Loc.	P.I.
Case 4a	5	Averaging	Y	1	Y	7
		Bayes	Y	5	Y	3
		PMF	Y	4	Y	4
Case 4b	5	Averaging	Y	1	Y	7
		Bayes	Y	6	Y	2
		PMF	Y	0	Y	10
Case 4c	6	Averaging	Y	2	Y	6
		Bayes	Y	4	Y	4
		PMF	Y	2	Y	6
Case 5a	9	Averaging	Y	1	Y	7
		Bayes	Y	5	Y	3
		PMF	Y	2	Y	6
Case 5b	7	Averaging	Y	2	Y	6
		Bayes	Y	4	Y	4
		PMF	Y	2	Y	6
Case 5c	6	Averaging	Y	0	Y	10
		Bayes	Y	3	Y	5
		PMF	Y	1	Y	7
Case 5h	4	Averaging	Y	4	Y	4
		Bayes	Y	6	Y	2
		PMF	Y	3	Y	5
Case 6c	5	Averaging	N	3	N	0
		Bayes	N	5	N	0
		PMF	N	3	N	0
Case 7b	4	Averaging	Y	2	Y	6
		Bayes	Y	5	Y	3
		PMF	Y	2	Y	6
Case 8f	6	Averaging	Y	4	Y	4
		Bayes	Y	6	Y	2
		PMF	Y	3	Y	5

**Table 6.3. Summary of Damage Detection Results After FEM Updating, Using Mode-Pairs with MAC>0.5 and Indicated as Significant by the Z-Function Analysis**

CASE	Number of Modes	Method	Detection	NFP	Max. at C. Loc.	P.I.
Case 4a	5	Averaging	Y	1	Y	7
		Bayes	Y	5	Y	3
		PMF	Y	4	Y	4
Case 4b	5	Averaging	Y	1	Y	7
		Bayes	Y	6	Y	2
		PMF	Y	0	Y	10
Case 4c	6	Averaging	Y	2	Y	6
		Bayes	Y	4	Y	4
		PMF	Y	2	Y	6
Case 5a	9	Averaging	Y	1	Y	7
		Bayes	Y	5	Y	3
		PMF	Y	2	Y	6
Case 5b	7	Averaging	Y	2	Y	6
		Bayes	Y	4	Y	4
		PMF	Y	2	Y	6
Case 5c	6	Averaging	Y	0	Y	10
		Bayes	Y	3	Y	5
		PMF	Y	1	Y	7
Case 5h	4	Averaging	Y	2	Y	6
		Bayes	Y	4	Y	4
		PMF	Y	4	Y	4
Case 6c	5	Averaging	N	4	N	0
		Bayes	N	5	N	0
		PMF	N	4	N	0
Case 7b	4	Averaging	N	2	N	0
		Bayes	N	3	N	0
		PMF	Y	5	Y	3
Case 8f	6	Averaging	Y	2	N	3
		Bayes	Y	4	Y	4
		PMF	Y	5	Y	3

**Table 6.4. Summary of Detection Method's Performance According to Mode-Selection Criteria.**

Selection Criteria	Ave. No. of Modes	Method	No. of Detections	Total NFP	PI	Total PI
<b>MAC &gt; 0.5</b>	12.9	Averaging	7	6	56	126
		Bayes	9	50	27	
		PMF	9	32	43	
<b>MAC &gt; 0.5 &amp; D-Function</b>	5.7	Averaging	9	20	57	140
		Bayes	9	49	28	
		PMF	9	22	55	
<b>MAC &gt; 0.5 &amp; D-Function FEM Updated</b>	5.7	Averaging	8	17	52	130
		Bayes	8	43	29	
		PMF	9	29	49	

- (5) The use of the Z-function to select the mode-pairs yielded the highest damage detection performance of all the methods and mode-selection criteria. It should be noted that with this selection criteria, the number of mode-pairs used in the damage detection is much lower than the case where the Z-function is not used to cut out irrelevant mode-pairs.
- (6) In general, Bayesian fusion yielded the lowest performance of all the damage detection techniques.

## 6.5 Conclusions

From the damage detection results and the comparisons of the performance of the damage detection algorithms as functions of mode-selection criteria, the following conclusions are stated:

1. Health monitoring of complex aerospace structures such as that of the VSA can be achieved using vibrational NDE techniques based on modal strain energy density differences.
2. The inflicted damage was successfully detected in 9 of the 10 cases considered in this work using the detection methods and mode-pairing criteria described before.
3. Damage detection using the three techniques, individually, correctly detected 9 of the 10 cases considered.
4. In particular, the Averaging method yielded the best performance overall. This was achieved when the Z-Function analysis described in Appendix B was used.
5. Higher performance was obtained for the three methods when using the Z-Function analysis.
6. Bayes Fusion, in general, yielded the worst performance of the three methods. The reason is that the number of false positives was high when compared to the other two methods.

## **CHAPTER 7**

### **DAMAGE EVALUATION IN CURVED SHELL TEST ARTICLE**

#### **7.1 Introduction**

Castillo (2001) performed vibration tests in a stiffened shell resembling an aircraft fuselage at damaged and undamaged states. The vibrational signatures of the structure were analyzed by applying the averaging method combined with the Z-function. Nine cases were studied involving a total of 28 reversible damage scenarios. Damage cases were selected so that regions of both, low and high strain energy content were affected.

The test object was fabricated with an aluminum plate riveted to longitudinal stringers and curved ribs. The test object was mounted on a supporting steel frame. Modal testing was conducted with the use of the LDV targeting at 112 reflective points on the curved plate. Mode shapes were obtained for all baseline and damage scenarios. The modal assurance criterion (MAC) was then used to match pairs of modes between the undamaged and damaged structure for all 28 damage scenarios. Furthermore, the Z-function analysis of Appendix B was implemented to identify mode-pairs of significant change. Damage maps were created to identify the location of damage.

#### **7.2 Description of Test Object**

The test object for this set of experiments was a curved aluminum-stiffened shell resembling a fuselage from an aircraft. The test object was tested using a Laser Doppler Velocimeter (LDV) in a similar way as the plates specimen considered in Chapter 4. The shell was fabricated with an 8 x 4 ft by 1/32 in. Aluminum sheet stiffened with seven Al 2024-T351 horizontal hat beams (stringers) with dimensions of 1 in. x 1 in. x 1/16 in. and 92 inches in length. These were evenly spaced seven inches apart and attached to the aluminum sheet with 47 aluminum rivets per stringer evenly spaced at 2 inches apart. Five Al 2024-T351, 1 by 1 in. by 1/16 in. Z-section beams (ribs) with a length of 46 inches and a radius of curvature of 75 inches were attached to the stringers with a total of 14 aluminum rivets per rib or 2 rivets per rib/stringer connection. A total of 399 rivets were used throughout the structure. Figures 7.1 and 7.2 illustrate a front and a rear view schematic of the test article, respectively.

The supporting frame consisted of steel channels, angles and plates. Two C12X10.6 channels 5 ft. in length were used as columns one at each side of the curved plate and 2 ½ inches away from each side of the plate. Each column was welded to a 4 ft. leg that consisted of C5X6.7 channels. Two L3X3X1/4 angles 8 ft. in length were used to support the top and bottom edges of the curved plate to the frame. Each support consisted of a PL 2.5 in. by 1/8 in. that ran the horizontal length of the angle support and joined the curved plate in the middle. This attachment was connected with 32 bolts evenly spaced at 3 inches. A 4 ft. length channel of dimensions C6X8.2 was welded at each end of the top and bottom edge supports in order to allow a bolt connection to the columns. The frame structure rested on two concrete blocks (6 in. by 6 in. by

16 in.) on each side joined by neoprene supports between the concrete block and the steel frame. Figure 7.3 illustrates a front and a side view of the supporting steel frame and the curved plate. Figure 7.4 shows the end attachments details.

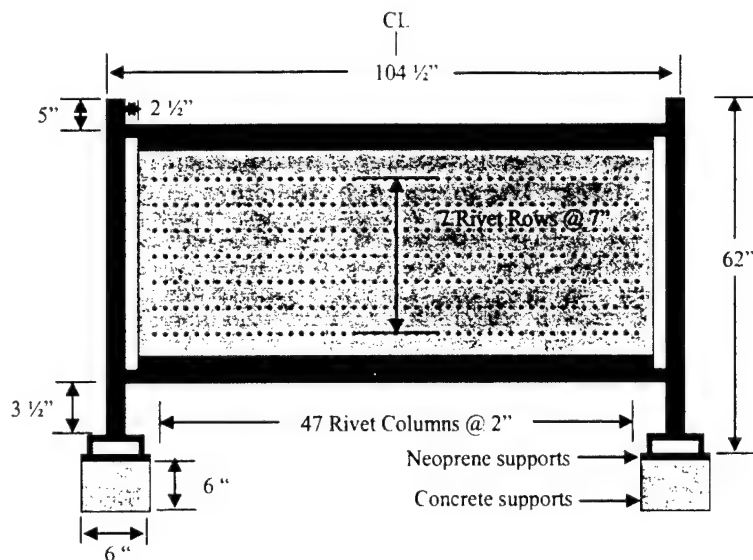


**Figure 7.1. Front View of Stiffened Curved Plate Model.**

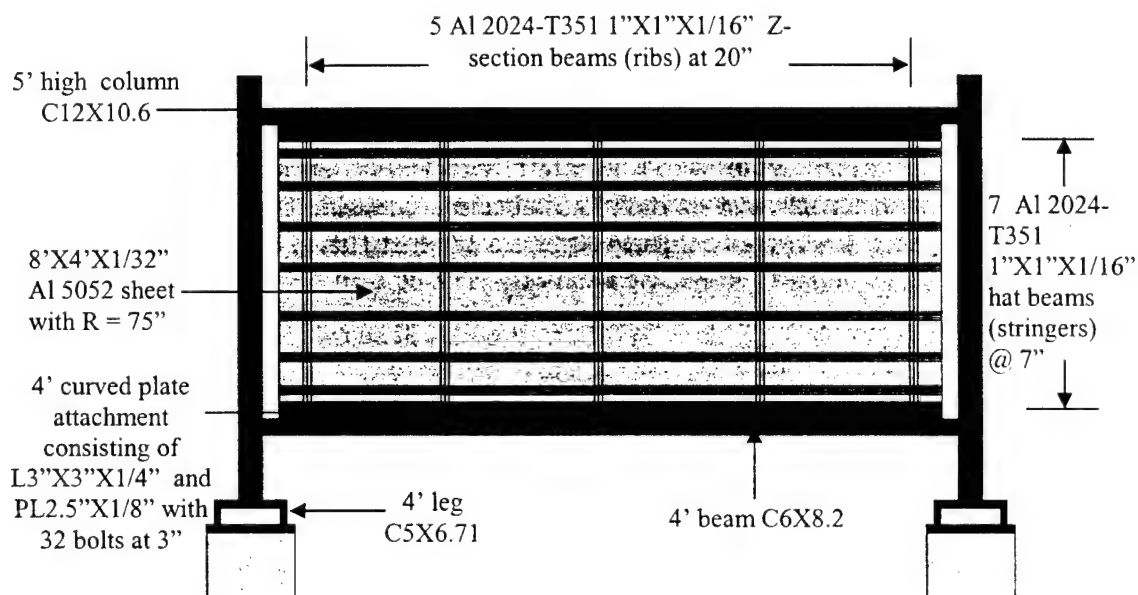


**Figure 7.2. Rear View of Stiffened Curved Plate Model.**

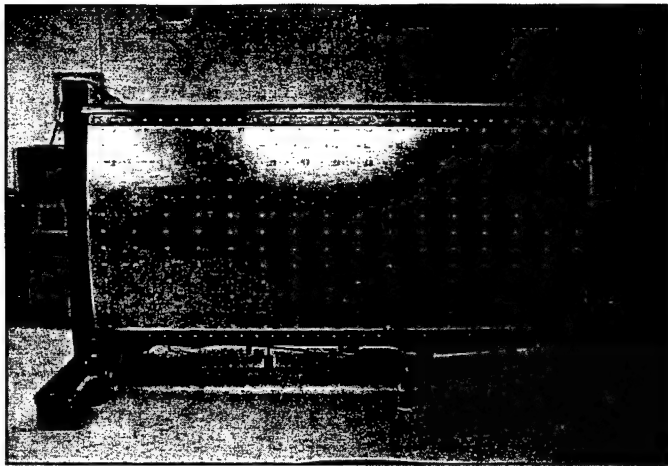


**Figure 7.3. Front and Side Views of Shell Specimen.**

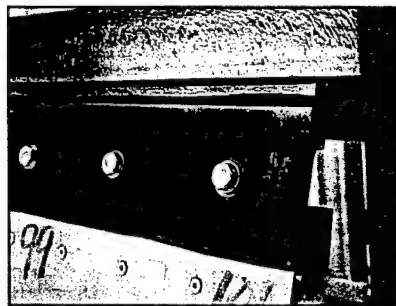


**Figure 7.4. Top (Left) and Bottom (Right) End Attachments.**

### **7.3 Instrumentation and Test Set-up**

The data acquisition system consisted of a Hewlett Packard Workstation (central processing unit) that includes the ZETA (Zonic A&D Engineering and Test Analysis) software that was used to process measurement functions (Fast Fourier Transforms (FFT), averaging, etc.) and control signals to the Zonic Analog to Digital (A/D) analyzer and the Ometron LDV. Five input and four output channels of the analyzer were used for the experiment. The input channels were used to extract the signals read from a Signal Conditioner (SC) from the two accelerometers (1 V/g sensitivity) and the two force transducers that were attached to the back of the test article. The velocity signals sensed by the LDV were acquired through the remaining input channel. Two electromagnetic shakers (Model V411) were driven through power amplifiers and were connected to dual channel filters (Model SR650). The filters were connected to two output channels of the Zonic system. The remaining output channels were



connected to the LDV in order to control the galvanometer driven mirrors that were used for laser targeting . Figure 7.5 depicts the instrumentation used in the experimental tests.

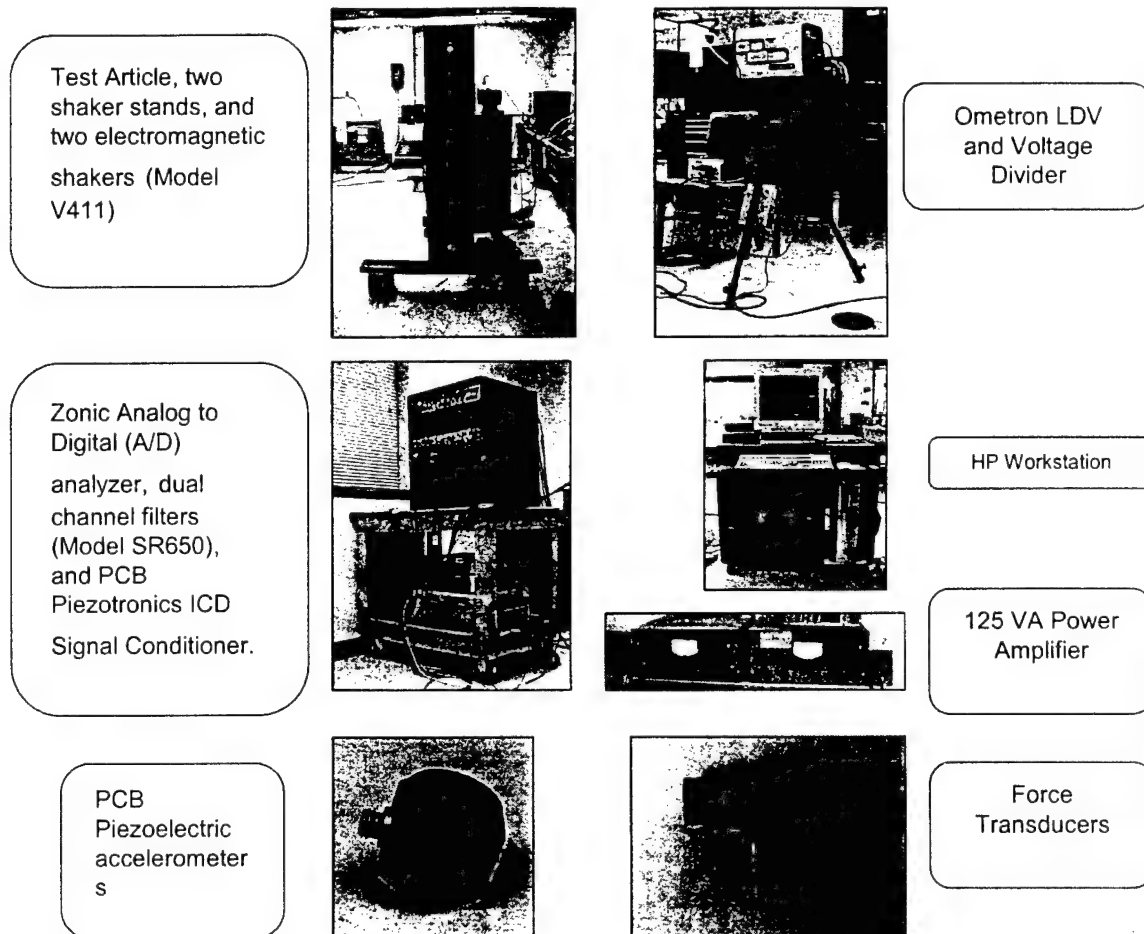


**Figure 7.5. Instrumentation**

The LDV was placed 12 feet away from the curved plate and was used to target 112 points distributed throughout the plate in order to obtain velocity readings that were induced by the excitation caused by two shakers. Each measurement point consisted of a  $\frac{1}{4}$  square in. reflective tape uniformly spaced at 6 inches in the horizontal and 7 inches in the vertical direction of the plate. Two measurement points were located directly in front of the excitation points. Figure 7.6 shows a schematic representation of the test set-up.

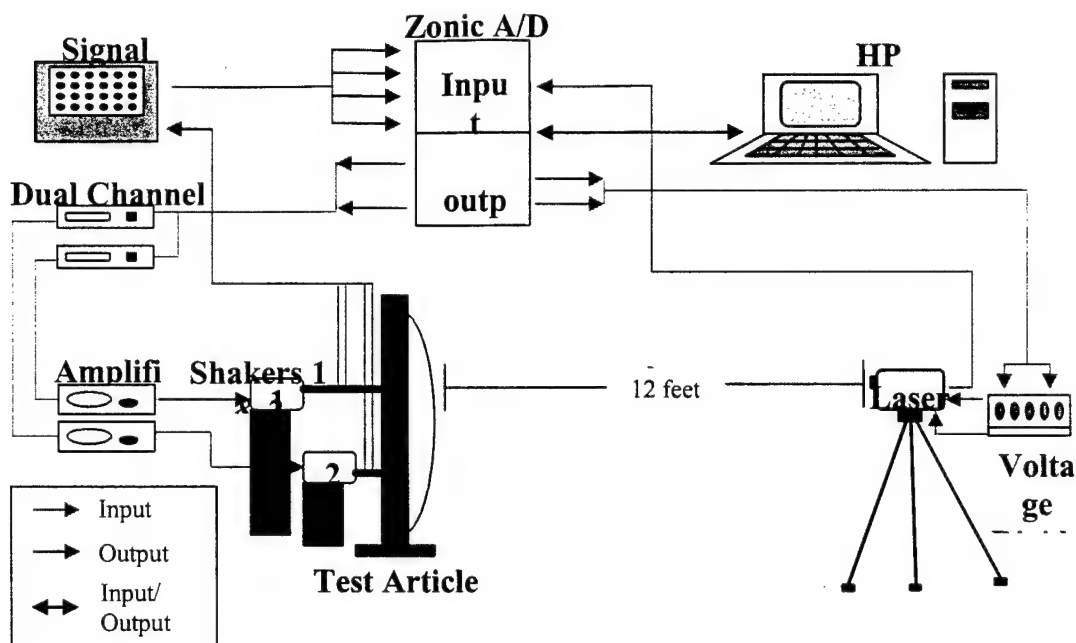


Figure 7.6. Schematic of Instrumentation Set-up.

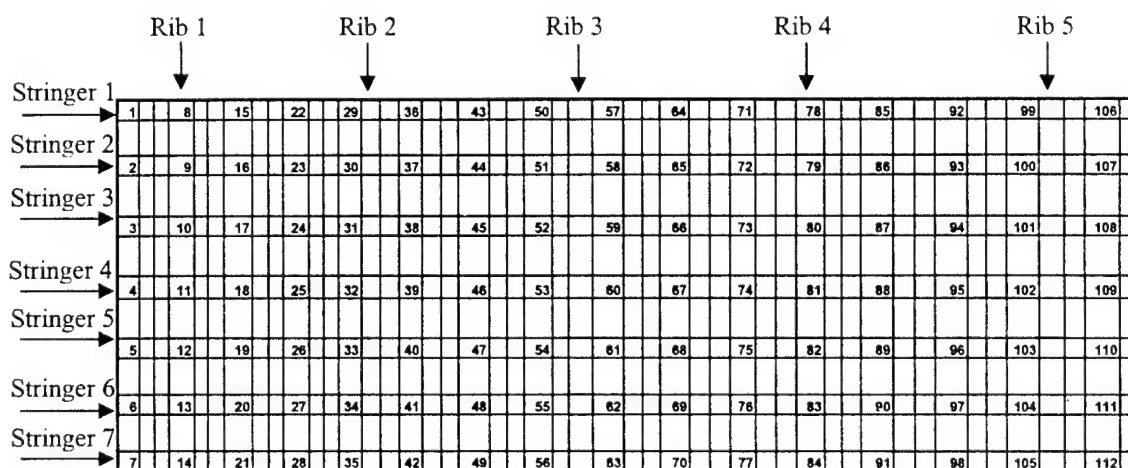
#### 7.4 Description of Damage Test Program in Shell Specimen

The curved aluminum plate was inflicted with reversible damage at several locations. Damage consisted of the removal of one to several rivets as well as cuts made to the stiffening members. The locations of inflicted damage were selected to cover areas of high and low modal strain energy content in the modes studied. When a stiffening element was cut, the member was replaced in order to reverse the damage.

Modal testing was conducted with the use of the LDV targeting at 112 reflective points on the curved plate (a grid of 7 by 16 points). The LDV along with the accelerometers and force transducers were calibrated prior to initiating modal testing of the test article. The coordinates of the measuring points were then stored in the computer and were used for laser targeting. Each shaker was configured to produce an excitation force Root-Mean-Square (RMS) level of 4.0 lb. at a frequency range from 0-600 Hz. Data acquisition was configured to use a Hanning window using 50% overlap, 12 averages, and a block size of 2048. The data acquired consisted of FRFs and coherences for both baselines and damage scenarios. Prior to beginning a test on the physical model, the coherence and the reciprocity were checked.

The experimental model was inflicted with 28 damage scenarios that comprised a total of 9 cases. The damage consisted of the removal of rivets and cut damage at single and multiple locations. The removal of rivets ranged from one to five adjacent rivets and cut damages through 1/6, 1/3, 2/3 and 100% the full depth of the rib. Each damage case was repaired by replacing the removed rivets or by replacing the members before conducting further tests on a different zone. The damages were categorized according to the type of damage inflicted. The

In order to facilitate identifying the rivets that were removed for each case, as well as the ribs and stringers, a numbering convention was assigned. Three rivets were assigned to each numbered location in front of the curved plate. The numbers ranged from 1 to 112 (same as the numbers targeted by the LDV). The rivet located to the left of each target location was assigned a letter L, the one located to the right was labeled with an R, and the rivet that corresponded with the numbered location was assigned the letter M. The five ribs were assigned a value in sequence from 1 to 5. For example, Rib1 corresponds to the rib located at the left and Rib5 corresponds to the last rib (located at the right) if viewing the test article from the front. Likewise, the seven stringers were assigned values from 1 to 7. From a front view of the test article and beginning at the top, Stringer 1 would be first and Stringer 7 the last one (bottom). The diagram on Figure 7.7 shows an illustration of this numbering scheme.



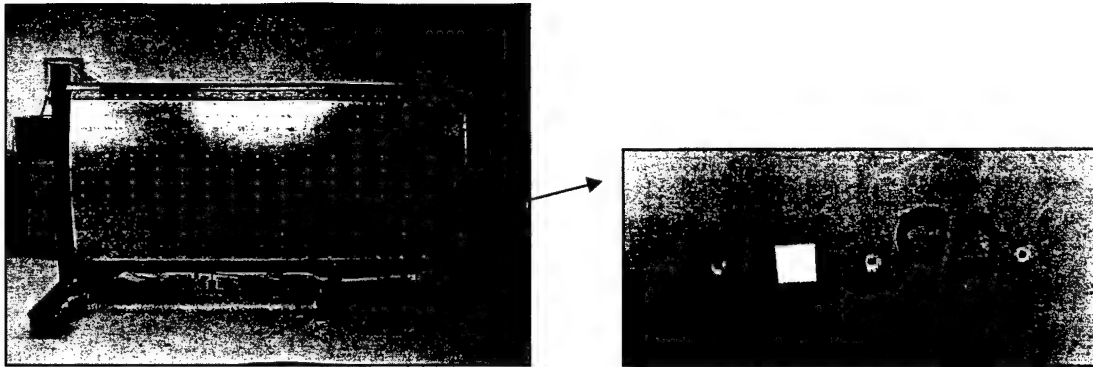


**Figure 7.8. Damage Location for Case 1.**

### **Case 2**

This damage case consisted of damage at a single location. The following adjacent rivets were removed: 33L, 33M and 33R. These were located in the left section of the curved plate (plate to Stringer 5 connection, see Figure 7.9).

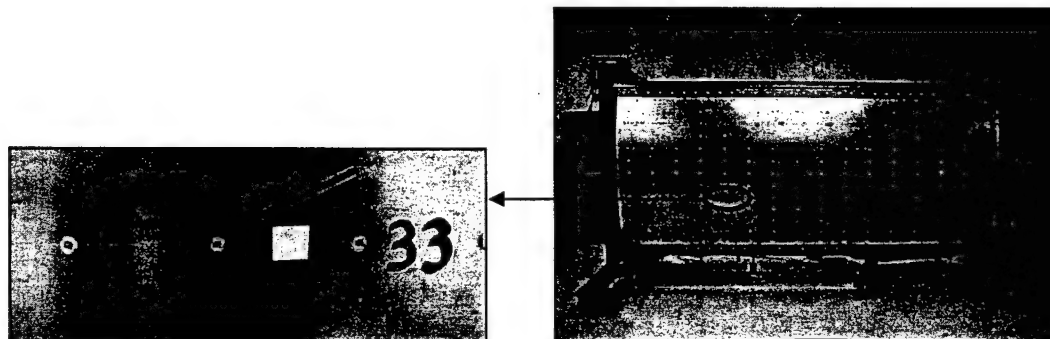


**Figure 7.9. Damage Location for Case 2.**

### **Case 3**

Three damages at a single location were performed for this case as shown in Figure 7.10. The first damage (Case 3a) consisted of removing four adjacent rivets (53L, 53R, 60L and 60M). Rivet 60R was additionally removed corresponding to Case 3b. Finally, a sixth rivet (53L) was removed corresponding to Case 3c. The damaged rivets connect the center region of the plate with the middle of Stringer 4. In addition, the center of Rib 3 is located directly behind the damaged location.

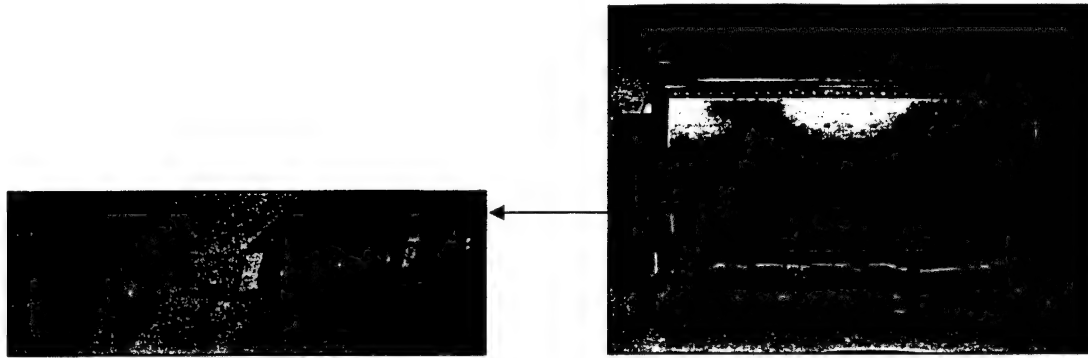


**Figure 7.10. Damage Location for Case 3.**

#### **Case 4**

Case 4 consisted of multiple damage of rivets located in the upper right and lower left region of the curved plate. Five damage scenarios were involved in this case. Two rivets (100R and 13L) were removed for the first damage (Case 4a) and two additional adjacent rivets were removed thereafter for each subsequent damage scenario. The following rivets were removed for the final damage (Case 4e) in this case: 93R, 100L, 100M, 100R, 107L, 13L, 13M, 13R, 20L and 20M. The top region of damage connects the plate to Stringer 2 and is located in front of Rib 5. The lower region of the curved plate connecting the plate to Stringer 6 was the other damaged area. This damage was located in front of Rib 1 (See Figure 7.11).

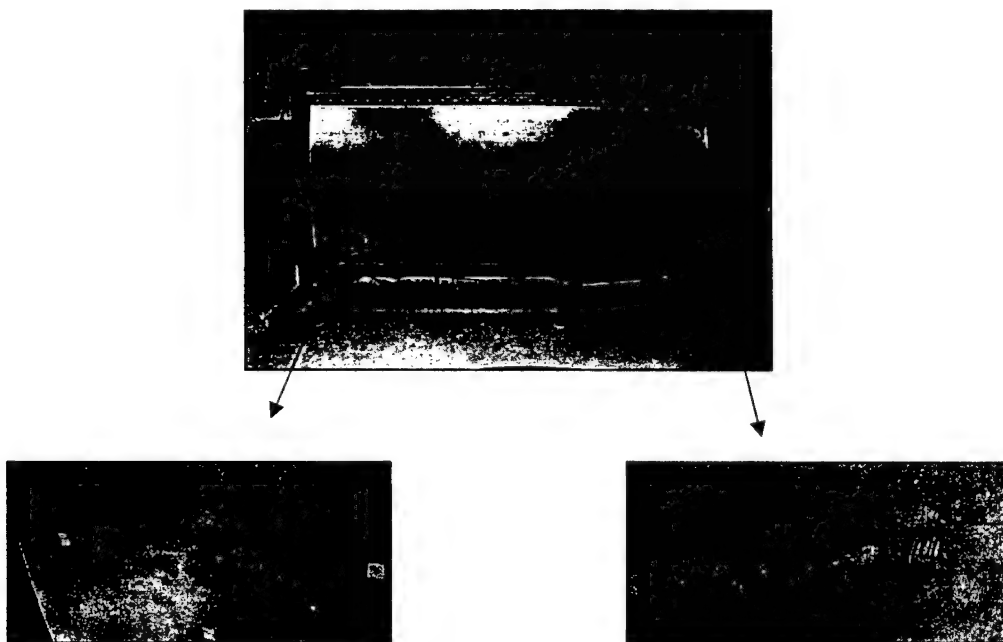


**Figure 7.11. Location of Damage for Case 4.**

### **Case 5**

Four damages at a single location were performed for this case. The first damage (Case 5a) consisted of removing rivet 24M. An additional adjacent rivet was removed for each subsequent damage case. The following four rivets were removed for the final damage (Case 5d) of this case: 24L, 24M, 24R and 31L. These damages were located on the left part of the curved plate on Rib 3 (See Figure 7.12)

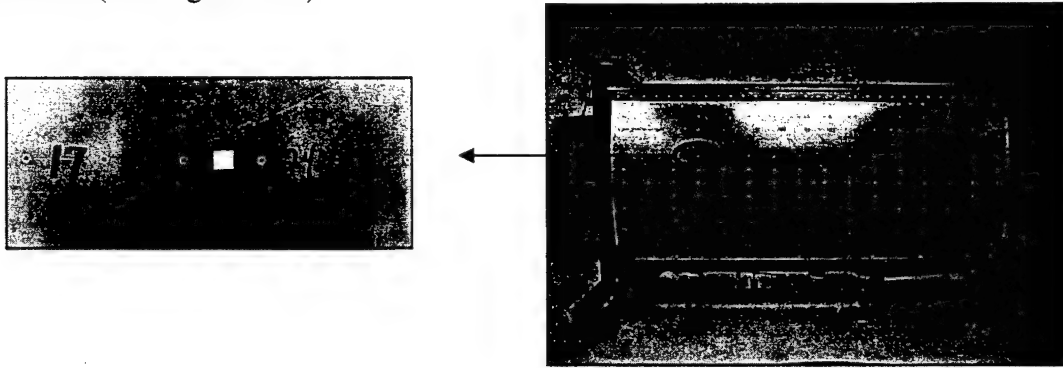


**Figure 7.12. Location of Damage for Case 5.**

### **Case 6**

The series of damage from Case 6 consisted of rivet removal at a single location from the rear of the curved plate, specifically from the rib to stringer connection. The fifth rivet from the top of Rib 1 connecting to Stringer 2 was removed for the first damage (Case 6a). The second damage (Case 6b) for this case consisted of removing the rivet below the previous damage. The area affected by this was located directly above and below 31R of the rear of the test article for the first and second damage, respectively. Figure 7.13 shows the location of damage for this case.

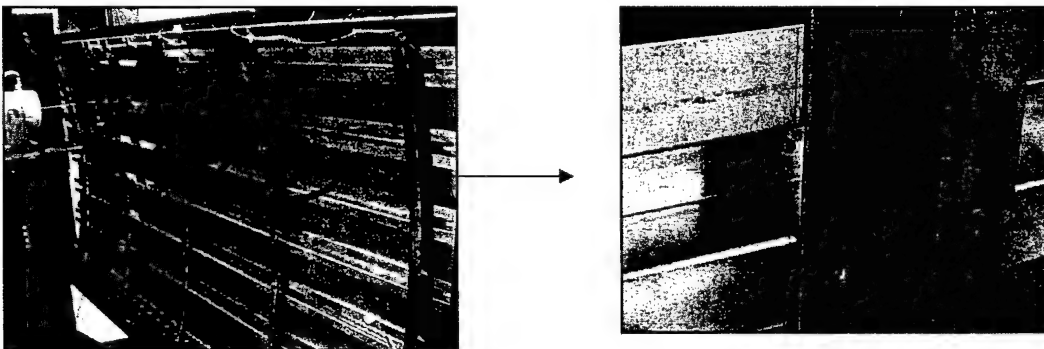


**Figure 7.13. Location of Damage for Case 6.**

### **Case 7**

Two damage scenarios consisting of multiple locations of damage were selected for this case. The third rivet from Rib 1 connecting to Stringer 2 and the eleventh rivet from Rib 3

connecting to Stringer 6 were simultaneously removed for the first damage (Case 7a). The locations for this damage were above 9M and 62L. One rivet below each location of the previous damage was removed for the second damage (Case 7b). The map locations for the second damage were below 9M and 62L (see Figure 7.14)

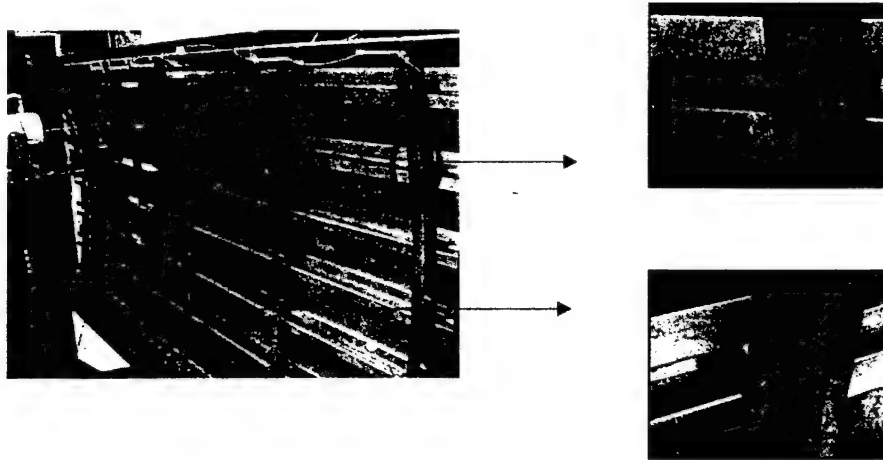


**Figure 7.14. Location of Damage for Case 7.**

#### **Case 8**

A series of five single and multiple transverse cuts were made on Rib 5 for this case. The first, second and third damage (Case 8a, 8b and 8c, respectively) consisted in cutting Rib 5 on a single location directly behind 101R (16" from the top) at 33, 66 and 100% the depth of the rib, respectively. Additional transverse cuts (multiple locations) were performed between 12M and 13M, 33" from the top of Rib 5. These cuts penetrated at 33 and 66% of the rib and they constituted the fourth and fifth damages, respectively (see Figure 7.15)

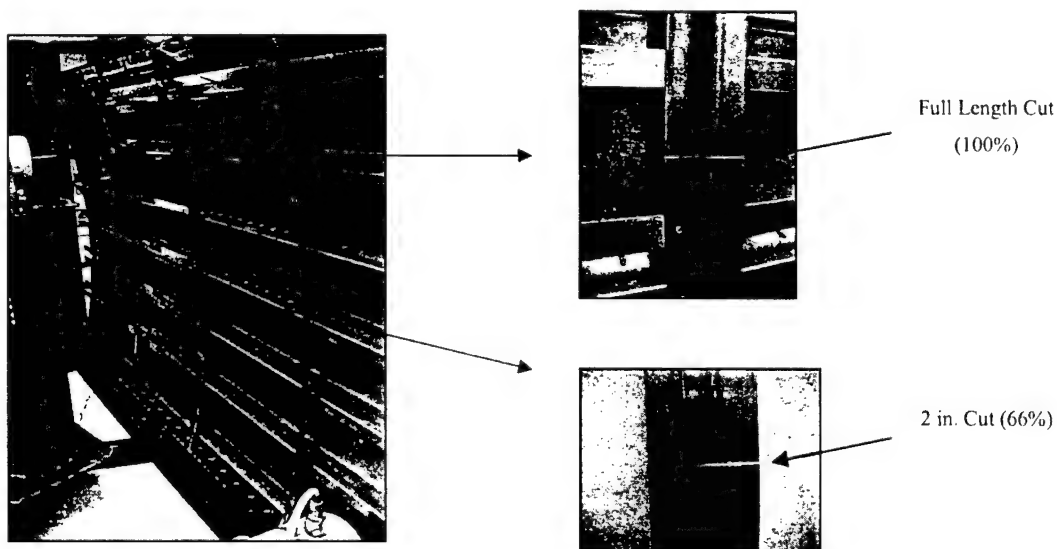


**Figure 7.15. Location of Damage for Case 8.**

### **Case 9**

Five single and multiple locations of damage on two ribs were performed for this case as illustrated in Figure 7.16. The first 3 damages consisting of cutting Rib 1 at a single location between 12M and 13M (33" from the top of the rib). The cuts were made in sequence beginning with 16, 33 and 66% the transverse section of the rib for the first (Case 9a), second (Case 9b) and third damages (Case 9c), respectively. The fourth and fifth damages (Case 9d and 9e, respectively) consisted of multiple damage locations. Rib 3 was inflicted with a series of two cuts in addition to the damage from Rib 1. The first transverse cut on Rib3 was made at a depth of 33% at a location between 61L and 62L. A full transverse cut was made to Rib 3 for the final damage in this case.

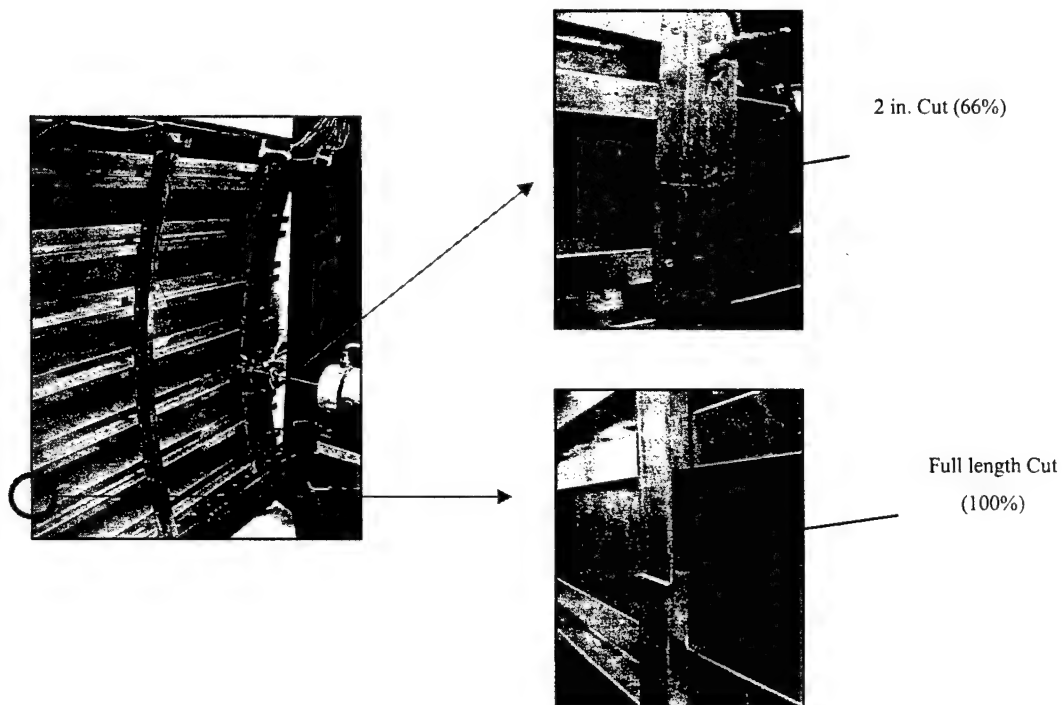


**Figure 7.16. Location of Damage for Case 9.**

The sequence in the experimental testing and a description of the damages inflicted to the test article are shown in Table 7.1. In addition, the corresponding reference baseline applied to each case and the damage type for each damage case is also presented.

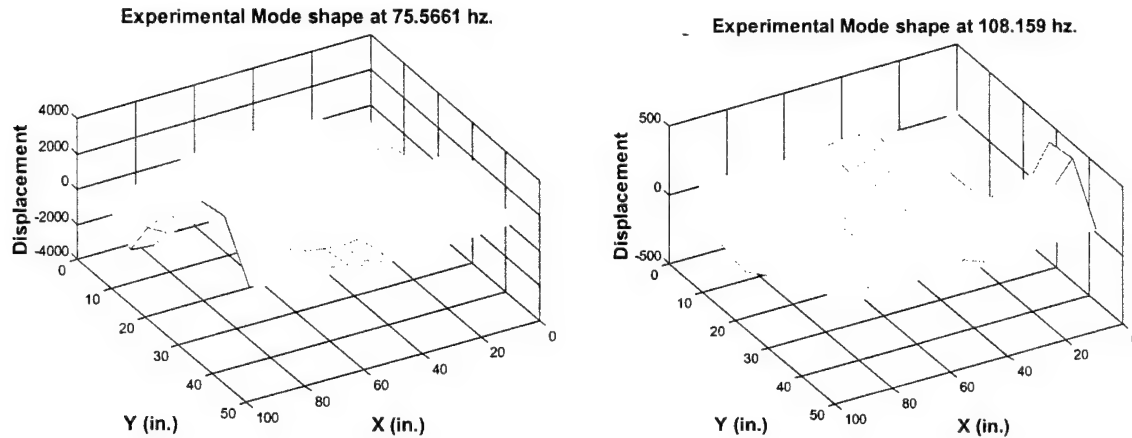


**Table 7.1. Case Description with Corresponding Baseline.**

Reference Baseline	Damage Case	Damage Type	Description
base 1	case 1a	A1	Rivets 90M, 90R and 97L removed
base 2	case 2a	A1	Rivets 33L, 33M and 33R removed
base 3	case 3a	A1	Rivets 53M, 53R, 60L and 60M removed
	case 3b	A1	Rivets 53M, 53R, 60L, 60M and 60R removed
	case 3c	A1	Rivets 53L, 53M, 53R, 60L, 60M and 60R removed
base 4	case 4a	A2	Rivets 100R and 13L removed
	case 4b	A2	Rivets 100M, 100R, 13L and 13M removed
	case 4c	A2	Rivets 100M, 100R, 107L, 13L, 13M and 13R removed
	case 4d	A2	Rivets 100L, 100M, 100R, 107L, 13L, 13M, 13R and 20L removed
	case 4e	A2	Rivets 93R, 100L, 100M, 100R, 107L, 13L, 13M, 13R, 20L and 20M removed
base 5	case 5a	A1	Rivet 24M removed
	case 5b	A1	Rivets 24M and 24R removed
	case 5c	A1	Rivets 24L, 24M and 24R removed
	case 5d	A1	Rivets 24L, 24M, 24R and 31L removed
base 6	case 6a	B1	5th rivet from the top of Rib 2 connecting to Stringer 3 located above 31R
	case 6b	B1	5th and 6th rivet from the top of Rib 2 connecting to Stringer 3 located above and below 31R
base 7	case 7a	B2	3rd rivet from the top of Rib 1 connecting to Stringer 2 located above 9M and 11th rivet from the top of Rib 3 connecting to Stringer 6 located above 62L
	case 7b	B2	3rd and 4th rivet from the top of Rib 1 connecting to Stringer 2 located above and below 9M and 11th and 12th rivet from the top of Rib 3 connecting to Stringer 6 located above and below 62L
base 8	case 8a	C1	1" transverse cut 16" from the top of Rib 5 located at 101R.
	case 8b	C1	2" transverse cut 16" from the top of Rib 5 located at 101R.
	case 8c	C1	Full transverse cut (3") 16" from the top of Rib 5 located at 101R.
	case 8d	C2	Full transverse cut (3") 16" from the top of Rib 5 located at 101R plus a 1" transverse cut 33" from the top of Rib 5 located at 103R and 104R.
	case 8e	C2	Full transverse cut (3") 16" from the top of Rib 5 located at 101R plus a 2" transverse cut 33" from the top of Rib 5 located at 103R and 104R.
base 9	case 9a	C1	1/2" transverse cut 33" from the top of Rib 1 located between 12M and 13M
	case 9b	C1	1" transverse cut 33" from the top of Rib 1 located between 12M and 13M
	case 9c	C1	2" transverse cut 33" from the top of Rib 1 located between 12M and 13M
	case 9d	C2	2" transverse cut 33" from the top of Rib 1 located between 12M and 13M plus a 1" transverse cut 33" from the top of Rib 3 located at 61L and 62L
	case 9e	C2	2" transverse cut 33" from the top of Rib 1 located between 12M and 13M plus a full transverse cut (3") 33" from the top of Rib 3 located at 61L and 62L

## 7.5 Damage Localization Results

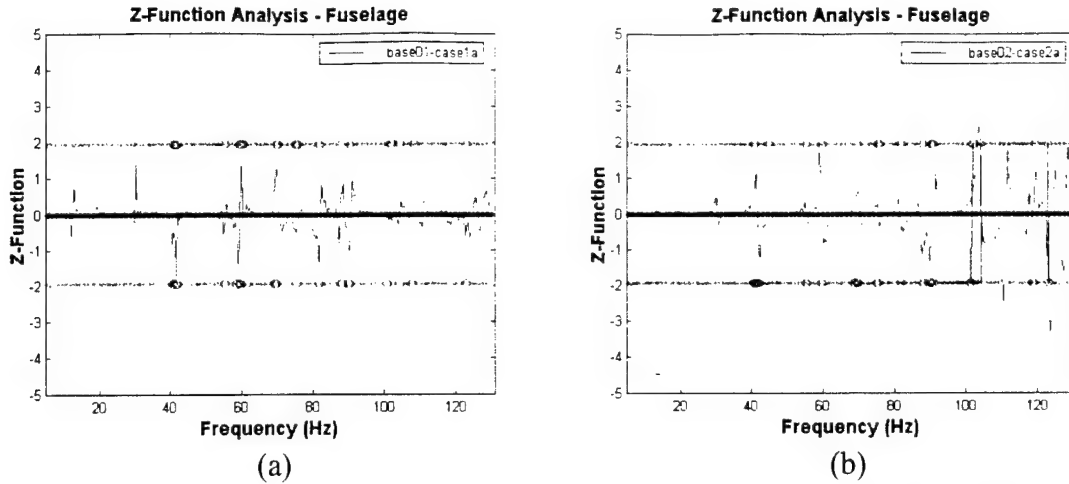
The first step in the process involved the extraction of vibrational characteristics for all the baseline and damage scenarios using the software SRDC I-DEAS. A total of up to 11 different mode shape types were identified in the range of 40 – 130 Hz. Figure 7.17 illustrates two of the 11 modes that were obtained. Mode shapes such as those depicted in the figure were obtained for all baseline and damage scenarios.



**Figure 7.17. Typical Modes for the Curved Shell Test Object**

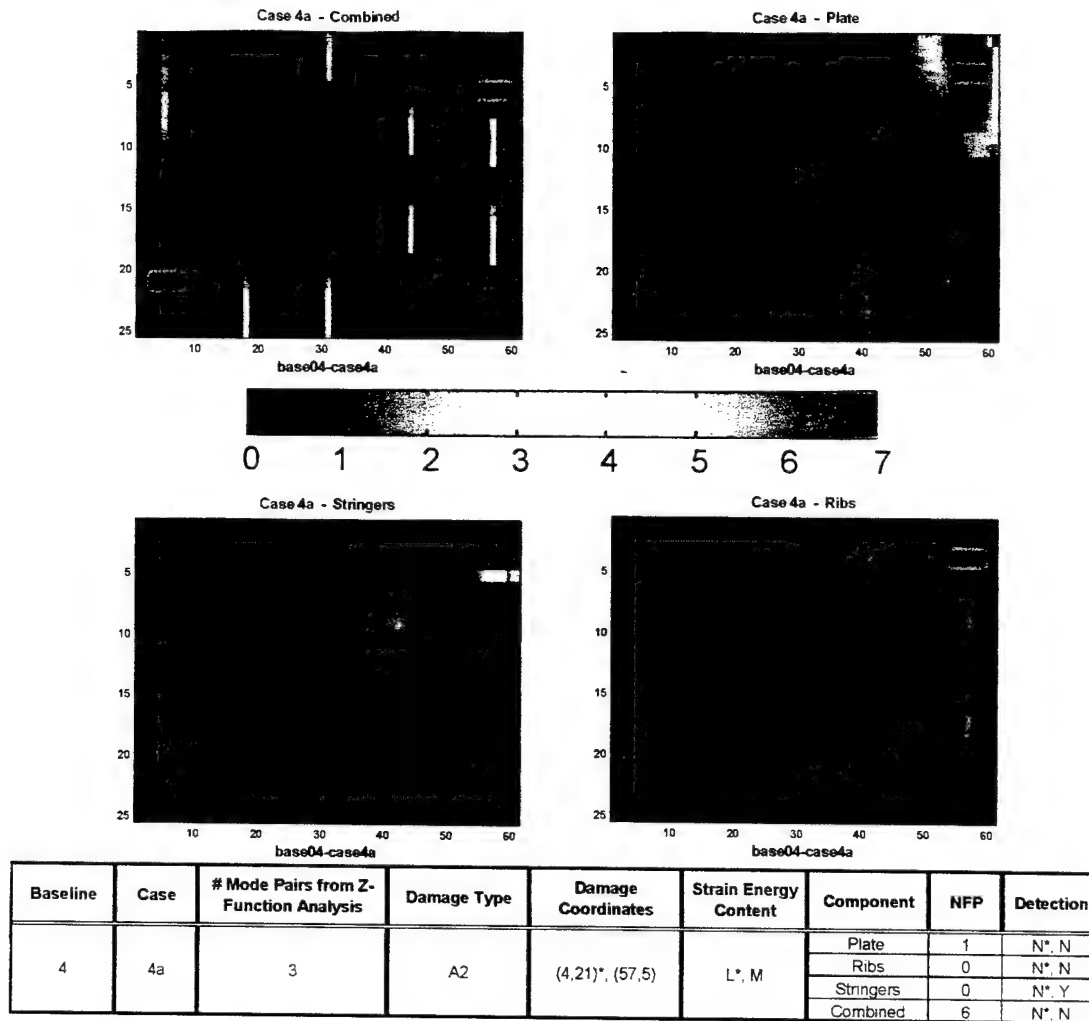
After extracting the modal shapes the second derivatives of the shapes were numerically extracted using the curve-fitting procedure of Appendix A. This was necessary in order to compute the modal strain energy from equations (2.10) and (2.11). Implied here is that the effect of the shell's curvature is negligible and the behavior of the out-of-plane vibrations is like a plate. The modal assurance criterion (MAC) was then used to match pairs of modes between the undamaged and damaged structure for all 28 damage scenarios. Furthermore, the Z-Function analysis of Appendix B was implemented to identify the mode shapes of significant change.

Figure 7.18 illustrate typical results obtain from the Z-function analysis. A threshold value of 1.96 (upper and lower bound) was used for each case. This represents a confidence interval of 95%. The circles located within the upper and lower bound limits represent a mode-pair identified with the MAC analysis.



**Figure 7.18. Z-Function Results for (a) Base01-Case1a and (b) Base02-Case2a.**

The averaging method described in Chapter 2, was applied using the pairs of matching modes identified by the Z-function analysis. Damage maps were created to identify the location of damage. Appendix D includes the damage maps for all damage scenarios considered in this work. Figure 7.19 illustrates a sample of damage maps. For each case, the location of the actual damage is indicated. This example is used for discussion. (A) The map of the upper left corner was obtained by combining the damage indicators of all the elements, which included the plate, the stringers and the ribs. (B) The map in the upper right shows the damage indicators by only considering the plate stiffness. (C) The map of the lower left corner only considers the damage indicators only considering the longitudinal stringers. And (D) the map of the lower left corner only considers the rib elements. The superposition obtained by combining all the elements did not give a good indicator of the damage. The problem is that the rib elements are much stiffer and sampled at fewer points than the rest of the elements. Therefore, errors in the measurements tend to create the effect that the ribs are damaged. Thus, the damage maps in the lower left corner have little value in detecting the correct flaw location.



**Figure 7.19. Damage Map Results for Case 4a with Baseline 4.**

A table for each damage scenario is found below the damage maps. This table gives a summary of the number of false positives (NFP) for each component of the damage maps, whether detection was identified (Y=yes or N=no), the type of damage that was inflicted, the strain energy content of the region (L-low, M-medium, H-high), the coordinates of the actual damage, the number of pairs of modes (from Z-function analysis) used, and the corresponding reference baseline for each damage case. In cases of damage at multiple locations, an asterisk was used to identify the NFP and the detection at those particular coordinates of damage.

In general, damage detectability in areas of higher strain energy content was higher than in those of lower strain energy content. The larger the magnitude of damage, the better the detectability. Damage Case 1a was the only one that showed no detectability. The rest of the cases show detectability in one or several of the components (plate, ribs, stringers or a combination of all). For damages inflicted on the front of the structure the damage maps corresponding to the plate, stringer and combined damage maps are the ones that show the higher

damage content, as expected. Likewise, the damage maps for the ribs and the combined components are more susceptible to damage on the rear of the structure. Table 7.2 includes a list of the damage maps that showed the highest level of detection for each case. The cuts that were made to the ribs showed a high level of detection for most of the damage maps. The main reason for this is that the ribs contain a higher level of strain energy content than the plate or stringers. It is also important to note that damage on the ribs was detected on cuts that penetrated at 66% or higher of the transverse length. The damage consisting of cuts on the rear of the shell at multiple locations ( i.e.: Case 8) was not detected conclusively. Detectability on both damage locations for Case 4 was also inconclusive. For the two cases previously mentioned, damage was located in the region that contained the higher strain energy content.

**Table 7.2. List of damage maps that showed the highest level of detection.**

Case	Damage Type	Strain Energy Content	Component	Detection
1a	A1	L	Any	N
2a	A1	M	Stringers	Y
3c	A1	M	Plate	Y
			Stringers	Y
			Combined	Y
4b	A2	L*,M	Stringers	N*,Y
			Plate	N*,Y
			Stringers	N*,Y
			Combined	N*,Y
5d	A1	M	Stringers	Y
			Combined	Y
6b	B1	H	Combined	Y
7b	B2	H*,M	Ribs	Y
			Stringers	Y
			Combined	Y
8c	C1	H	Plate	Y
			Ribs	Y
			Combined	Y
8d	C2	H*,M	Plate	Y*,N
			Ribs	Y*,N
			Combined	Y*,Y
9c	C1	H	Combined	Y
9e	C2	H*,M	Combined	Y*,Y

## 7.6 Conclusions from the Shell Tests

The following conclusions can be made about the results obtained from this work:

1. Damage maps obtained from the bending curvatures ( $x$  and  $y$ ) were found to be sensitive to detect damage. The reason for this is that stiffening members have a high stiffness value. This leads to a high degree of strain energy content especially for the damage map for the  $y$  curvature (Ribs).
2. The number of modes had no significant effect on the damage detection results.
3. In general, the higher the strain energy content in the damaged location, the higher the probability of detection.
4. At least one damage map from each case detected the damage location with the exception of Case 1. This case had no significant global change in the Z-functions analysis.
5. All cases that detected damage in at least one damage map had false positives.
6. The damage maps for Case 8e contained the least number of false positives.
7. For the multiple damage location of Case 7, the damage was only located in the region of higher strain energy content.
8. For Damage Type A, the least number of rivets needed to be removed for damage detection was 3 (Case 2a).
9. For Damage Type B, the least number of rivets needed to be removed for damage detection was 2 (Case 6b).
10. For Damage Type C, the shortest depth of cut for damage detection was 1 in. (Case 9b).



## CHAPTER 8

### SUMMARY AND CONCLUSIONS

#### 8.1 Summary

The objective of this report was to document the research work on the development of vibrational NDE methods to infer damage over a large area of aircraft structures using laser Doppler Velocimeter (LDV) accompanied with data fusion techniques to process the modal information before and after damage.

The theoretical developments of the vibrational NDE method and data fusion methodologies were presented in Chapter 2. Vibrational NDE for damage detection and assessment are based on experimental modal analysis testing to obtain the response characteristics. Since all forms of damage may cause changes in the structural stiffness, the damage is reflected in changes in the vibrational characteristics that can be measured. Since the dynamic characteristics of a structure are altered by the damage, then changes in frequencies, mode shapes and damping ratios or any value that derives from these changes can be used to detect damage. The vibrational NDE methods considered in this work are based on quantifying modal strain energy differences between the structure in a damaged state and a healthy state. From structural mechanics relationships, the differences in the strain energy can be evaluated using the measured modal shapes. From the static shapes of the modes, the strain energy distribution within the structure is computed by curvefitting or using finite element models. Since experimental modes are only obtained at the sampling points, curve-fitting and/or finite element techniques are required to complete the missing components of the modes. The energy differences of equally scaled modes before and after damage are normalized. This is necessary in order to combine information from multiple modes. Damage in an element causes changes in the modal shapes in the vicinity of or at the location of damage. The damage location is indicated as an apparent strain energy increase. The damage detection formulation relies on the features of the differences of modal strain energy when the modes are equally normalized giving collection sets of modal strain energy differences for the available modes. The distribution of the normalized strain energy differences also provide the mechanism to extract probabilities in support of damage and no damage at each location of the structure given the information in each mode. Information from modal pairs was then combined using data fusion techniques.

The Vibrational NDE and fusion methodologies were first developed and refined considering experiments on simple beams as described in Chapter 3. Modal vibration testing was conducted on beams to obtain their dynamic characteristics including, resonant frequencies, damping ratios and mode shapes. The tests were conducted using accelerometers evenly spaced and one force transducer while the excitation force was provided by an electro-magnetic shaker. Two aluminum beams were subjected to 54 damage scenarios at different magnitudes and included damage at single and multiple locations. The different damage magnitudes helped test the ability and sensitivity of the methods to detect small defects (flaws or cuts) on the system. For each baseline and damage scenario, sets of FRFs and Coherence functions were obtained to



extract the modal parameters of the first five bending modes. Graphical representations of the damage evaluation results were provided.

The methods were applied to a large Aluminum stiffened plate laboratory structure which resembles aircraft construction as described in Chapter 4. The purpose of this work was to localize inflicted damage over a large area when the modal measurements are obtained with a scanning laser Doppler velocimetry (LDV). The data was processed using the methodologies and fusion techniques described in Chapter 2. The laboratory structure was a stiffened plate fabricated with aluminum sheet riveted to aluminum C-sections functioning as stringers and ribs. Two shakers were used at unsymmetrical points of the structure providing input force excitations. The LDV was used to sample the structure's response on the skin surface. The model was subjected to 22 different damage cases inflicted at eight different zones. The damage consisted of removal of bolts and cuts in the stiffening elements. Both forms of damage were caused at single and multiple locations. For each damage and baseline case, the FRF and Coherence functions with respect to the two shakers were collected and processed to extract the vibrational characteristics. The modal assurance criterion (MAC) was used to correlate the mode shapes of the baseline to those of the damaged structure. The mode shapes were subjected to a curve-fit procedure to estimate modal bending and twisting curvatures of the front plate. These curvatures permitted the determination of the modal strain energies. The modal strain energy differences were determined for each mode and normalized using the standard norm. The damage indicators obtained from all available pairs of matching modes were combined by averaging the indicators. The results were presented in the form of damage maps. The experimental data was also used to obtain damage detection using likelihood ratio and evidential reasoning. The cases considered for the likelihood ratio and evidential reasoning methods were the cut damages in the stiffening elements. The statistical distribution of the normalized modal strain energy differences was approximated using the Kernel density estimator to obtain probabilities supporting damage and no-damage. From these probabilities, damage likelihood ratios were obtained for all locations given the modal inspection events. The second process consisted of using techniques of evidential reasoning to determine belief and plausibility in support of damage given the evidence in the modal strain energy differences.

Chapter 5 described the research performed on a prototype of the vertical stabilizer assembly (VSA) of NASA's shuttle orbiter. This is an example how the large area inspection techniques could be implemented for aircraft structures. The purpose of the tests was to obtain a database that helped developed damage identification techniques. The data obtained during testing consisted of frequency response functions (FRF) and coherence functions for all scenarios (damage and repaired configurations). The data was used to extract the resonant frequencies and mode shapes. The measurements were taken with accelerometers and with the LDV. There were a total of eight damage cases. The first three cases were performed using accelerometer measurements only. The last five damage cases involved accelerometers and the LDV combined. The damages inflicted consisted of reversible and non-reversible scenarios with several levels of damage in each case. Damages inflicted on the VSA test article were at several locations. The mode-pairing between the baseline state and the damaged scenario was carried out through the modal assurance criterion (MAC). In addition, the mode pairs which exhibit significant changes due to the inflicted damage were identified using a statistical analysis of the FRF data. This procedure was summarized in Appendix B. The effects of mode-pairing was

also studied by repeating the damage detection process using mode-pairs (a) identified by the MAC analysis with values greater than 0.9, (b) identified by the MAC analysis with values greater than 0.5; and by further refining the mode-pairing in both (a) and (b) using the Z-function analysis. The estimation of the strain energy content of the structure, due to the deflected modal shapes, was performed using the finite element approach described in Section A.4. Four damage detection algorithms were considered: (1) averaging, (2) probability mass function method (PMF), (3) a weighted averaging method and (4) a weighted PMF method. Damage maps were obtained for all damage cases and damage levels using the four algorithms. The detectability was evaluated in terms of whether the correct location was detected. The number of false positives was obtained by counting the number of regions with high levels of potential damage depicted by the orange-red colors of the contours of the damage maps. A performance index was also evaluated in order to compare the efficacy of the detection methods as well as the mode-pairing approaches.

Chapter 6 included an extension of the VSA work where additional fusion approaches were applied to the VSA test structure while considering an improved finite element model. The finite element model to extract the complete modal information was modified to include additional bar elements of the model. The bar elements contributed significantly to the stiffness of the structure and affected the distribution of the strain energy. Prior work assumed the model to be at an undamaged state and no updating was performed when the inflicted damage was irreversible. The work presented in Chapter 6 utilized model-updating due to the damage already present in some of the baselines. The damage detection results were then obtained using the Averaging, Bayes fusion, and PMF methods. The methods were only applied considering mode-pairs identified with a MAC with and without the Z-function results. The results were presented in the form of damage maps and summarized in tables listing detectability, number of false positives (NFP) and detection performance in terms of a performance index (PI). The methods and the use of the Z-function were evaluated and compared as functions of detectability, the NFP and the PI.

Chapter 7 documented the work performed in a laboratory shell structure that resembles a fuselage structure. Vibration tests were performed in a stiffened plate at damaged and undamaged states. The vibrational signatures of the structure were analyzed by applying the averaging method combined with the Z-function. Nine cases were studied involving a total of 28 reversible damage scenarios. Damage cases were selected so that regions of both, low and high strain energy content were affected.

## 8.2 Conclusions

From the beam experiments the following conclusions were obtained. The single fusion technique that provided the best detectability was averaging, followed by the Bayes fusion methods. Averaging provided the least damage localization error. The likelihood ratio method exhibited the poorest detectability (74.1%); this was because of its tendency to intensify large-magnitude damages. The Bayes fusion method proved extremely valuable in enhancing the detection for the small-magnitude damage, at the expense of producing more false positives than other methods. The damage detectability for Beam 2 was 100 percent and that for Beam 1 was

83%; the detectability of the two beams combined was 88 percent. The damages that were not detected typically consisted of small magnitude accompanied with a large damage at another location. The number of false positives for the two beams combined was 20 locations out of a total of 54 damage locations.

The averaging technique when applied to the plate experiments was proven effective in detecting the damage inflicted to the stiffened-plate. Damage consisting in the removal of adjacent bolts was conclusively detected and located when five bolts were removed using the combined twisting and bending curvatures. Damage in the stiff parts of the structure (at supports) was not detected. This was primarily because of the low levels of vibrations compared to other parts of the plate; during the experiments the sensitivity of the laser was adjusted to the maximum level of vibrations. Damage consisting of the removal of bolts of the inner members of the stiffened plate was detected and located using the bending curvature in the direction of the damaged member. Damages in regions of low modal strain energy were not detected. Damage consisting of a cut of the inner stiffening members was detected. Damage was not detected when inflicted at the rigid support.

When the plate test data corresponding to the damage scenarios of the stiffening elements was processed using the likelihood ratio method and the evidential reasoning approaches, nine of ten cut damage locations were correctly detected. The one that was not detected was a damage of small magnitude accompanied with large magnitude damage at a different location. The number of false calls was larger for cases with small magnitude defects.

The major conclusions that can be stated for the tests conducted in the VSA prototype are as follows. The averaging method yielded the highest performance in locating damage when the Z-function analysis of Appendix B was not used. The weighted probability mass function method yielded the highest performance when the Z-function analysis was performed. Higher detection performance was generally obtained by considering mode-pairs matched with MAC values of 0.5 between the undamaged and damaged states of the structure. This was the case with or without the use of the Z-function analysis. The detections, considering the set of mode-pairs with MAC values greater than 0.9, provided a lower detection performance. The combination of using the Z-function analysis and MAC values greater than 0.5 yielded the highest damage detection performance of all the methods and mode-selection criteria.

The additional analyses on the VSA tests considering the averaging, Bayes fusion, and probability mass function (PMF) methods and the improved finite element model yielded the following conclusions. The inflicted damage was successfully detected in 9 of the 10 cases. The damages were correctly detected in 9 of the 10 cases by all three methods, individually. The averaging method yielded the best performance when the Z-Function analysis was used. Higher performance was obtained for the three methods when using the Z-Function analysis. Bayes Fusion, in general, yielded the worst performance of the three methods. This is due to a large number of false positives when compared to the other two methods.

From the work performed on the shell test articles, the following conclusions are stated. At least one damage map from each case detected the correct location with the exception of one case. This case had no significant global change according to the Z-functions analysis to indicate

that the monitored modes were not sensitive to or affected by the inflicted damage. The damage maps obtained using the bending curvatures  $x$  and  $y$  were found to be the most likely to correctly display the damage. This was because of large strain energy content in the stiffening elements. In general, the higher the strain energy content in the damaged location, the higher the probability of detection. All cases that correctly detected damage had at least a false positive damage. In general, the number of modes had no effect on the damage detection results.

The work on vibrational NDE methods reported in this document provides encouraging evidence that global NDE methods may be feasible for large area inspection of aircraft structures, in particular for detecting flaws in members located deep inside the aircraft which contribute significantly to the structure's stiffness. It is also clear that the methods described here can not be used to find small sized defects such as cracks in rivet holes. The methods also required careful processing of the modal test data using carefully tailored models. Further tools are needed to automate the process in order for implementation to be possible. Also, the refinement of the finite element models may limit the application of the methods.



## REFERENCES

- Andre, G. (1999), "Comparison of Vibrational Damage Detection Methods in an Aerospace Vertical Stabilizer Structure", M.S. Thesis, Civil Engineering, The University of Texas at El Paso, El Paso, TX, May 1999.
- Ang, A. H. and Tang, W. H. (1975), "*Probability Concepts in Engineering Planning and Design*", Vol. 1, Wiley Pub., New York.
- Carrasco, C. J. , Osegueda, R. A. , Ferregut, C. M. and Grygier, M. (1997), "*Damage Localization In A Space Truss Model Using Modal Strain Energy Distribution*", Proc. of IMAC XV, Vol. II, Orlando Florida, pp. 1786-1792.
- Carrasco, C. J., Osegueda, R. A., and Ferregut, C. M., (1996), "Modal Tests of a Space Truss Model and Damage Localization Using Modal Strain Energy", Technical Report No. 96-01, FAST Center for Structural Integrity of Aerospace Systems, University of Texas at El Paso, July.
- Castillo, S. (2001), "Vibration-Based Damage Detection on a Curved, Aluminum-Stiffened Plate Resembling an Aircraft Fuselage", M.S. Thesis, Civil Engineering. The University of Texas at El Paso, El Paso, TX, July 2001.
- Gros, X. E. (1997), "*NDT Data Fusion*", J. Ewiley Pub., New York 1997.
- Lawry, M. H. (1996), "*SDRC / IDEAS Master Series*", Structural Dynamics Research Corporation, Milford, Ohio.
- Lopez, H. M. (2000), "Fusion of Strain Energy Differences For Damage Localization", M.S. Thesis, Civil Engineering, The University of Texas at El Paso, El Paso, TX, December 2000.
- Macias, M. (2000), "Health Monitoring of Aircraft Structures by Fusion of Modal Strain Energy Density", Civil Engineering, The University of Texas at El Paso, El Paso, TX, December 2000.
- Meza, R. (1996), "Modal Tests of Composite Honeycomb Panels Using Laser Doppler Velocimetry for Damage Assessment", M.S. Thesis, Civil Engineering, The University of Texas at El Paso, El Paso, TX, July 1996.
- Osegueda, R. A., Revilla, A., Pereyra L, and Moguel, O. (1999), "*Fusion of Modal Strain Energy Differences for Damage Localization*", Proc. of SPIE, Vol. 3586, pp. 189-199, Newport Beach, California.
- Osegueda, R. A., Lopez, H., Pereyra, L., and Ferregut, C. (2000a), "*Localization of Damage Using Fusion of Modal Strain Energy Differences*", Vol. I, pp. 695-701, IMAC XVIII, San Antonio, Texas, Feb. 2000.
- Osegueda, R. A., Macias, M., Andre, G, Ferregut, C., and Carrasco, C. (2000b), "*Fusion of Modal Strain Energy for Health Monitoring of Aircraft Structures*", Proceedings of SPIE Vol. 3994 pp. 117-127, Newport Beach, California, March 2000
- Osegueda, R. A., Carrasco, C. J. and Meza, Jr. R, (1997), "*A Modal Strain Energy Distribution Method to Localize and Quantify Damage*," IMAC XV, pp. 1298-1304, 1997.

- Pereyra, L. R. , Osegueda, R. A., Carrasco, C. and Ferregut, C., (2000), " Detection of Damage in a Stiffened Plate from Fusion of Modal Strain Energy Differences." Proc. of International Modal Analysis Conference XVIII. SEM. Vol. II. San Antonio, TX, Feb. 7-10, 2000, pp. 1556-1562.
- Pereyra, L. R., Osegueda, R. A., Carrasco, C. and Ferregut, C., (1999), "Damage Detection in a Stiffened-Plate Using Modal Strain Energy Differences", in Nondestructive Evaluation of Aging Aircraft, Airports and Aerospace Hardware III, Ed. A. K., Mal, Proceedings of SPIE, Vol. 3586, Paper 3586-29.
- Pereyra, L. R. (1998), "Structural Damage Localization in a Stiffened-Plate Using Modal Analysis, Laser Velocimetry and a High-Order Curve Fit Method", M.S. Thesis, Civil Engineering, The University of Texas at El Paso, El Paso, TX, December 1998.
- Silverman, (1994), "*Density Estimation for Statistics and Data Analysis*", Chapman and Hall Pub., New York.
- Tappert, P. M., Snyder, T. D. and Robertshaw, H. H., (1995), "*Attacking the Damage Identification Problem*", Proceedings of SPIE, Vol. 2443 pp. 286-294, 1995.
- West, W., (1987) "Revised Plan for the Implementing Operational Orbiter Control Surface Inspection Via Modal Test/Analysis Processes," JSC-REV. No 22164, NASA-JSC, Houston, TX.

## APPENDIX A

### EXTRACTION OF MODAL SHAPES AND STRAIN ENERGY FROM DISCRETE MEASUREMENTS

#### A.1 Introduction

One of the problems that exists in vibrational non-destructive evaluation is that modal analysis provides modal shapes defined only at a discrete number of measurement points. The techniques developed under this research rely on modal strain energy differences between the healthy and damaged states of the structure. If the structure is continuous, estimates of the curvature of the modal shapes need to be estimated from the modal shapes. This is equivalent to extracting the second spatial derivatives utilizing numerical methods. Otherwise, if the structure is complex or irregular in shape, then the extraction of complete modal shapes from a discrete number of measurement points can be obtained via finite element techniques. This Appendix cover in details the numerical procedures to obtain complete modal shapes by either curve-fitting the modal shapes, if the structure is uniform, or by finite elements if the structure is complex. The techniques covered here were developed by Pereyra (1998), Lopez (2000) and Andre (2000).

#### A.2 Curve-Fit Approach for Beam-like Structures

Consider a beam-like structure that is vibrating at one of its resonant frequencies and its corresponding mode shape  $\phi(x)$  is extracted. Let the mode shape be defined as a set of values equally spaced along the direction of the beam. Thus,

$$w(x_i) = [w_0(x_0), w_1(x_1), w_2(x_2), \dots, w_n(x_n)] . \quad (\text{A.1})$$

Then, the mode shape is represented as a collection of points as illustrated in Figure A.1. These points correspond to an actual mode shape measured for a beam with overhangs at its ends. Then, the slope or first derivative of the function can be estimated by means of finite differences. For the first and last points, a forward and backward differences are taken, respectively; and for the intermediate points the central difference theorem is used. This leads to a set of estimated values for the slope given by:

$$\hat{\theta}(x_i) = [\hat{\theta}_0(x_0), \hat{\theta}_1(x_1), \hat{\theta}_2(x_2), \dots, \hat{\theta}_n(x_n)] . \quad (\text{A.2})$$

Where,

$$\hat{\theta}_0(x_0) = \frac{w_1(x_1) - w_0(x_0)}{x_1 - x_0} , \quad (\text{A.3a})$$

$$\hat{\theta}_i(x_i) = \frac{w_{i+1}(x_{i+1}) - w_{i-1}(x_{i-1})}{2(x_{i+1} - x_{i-1})} , \text{ and} \quad (\text{A.3b})$$



$$\hat{\theta}_n(x_n) = \frac{w_n(x_n) - w_{n-1}(x_{n-1})}{x_n - x_{n-1}}. \quad (\text{A.3c})$$

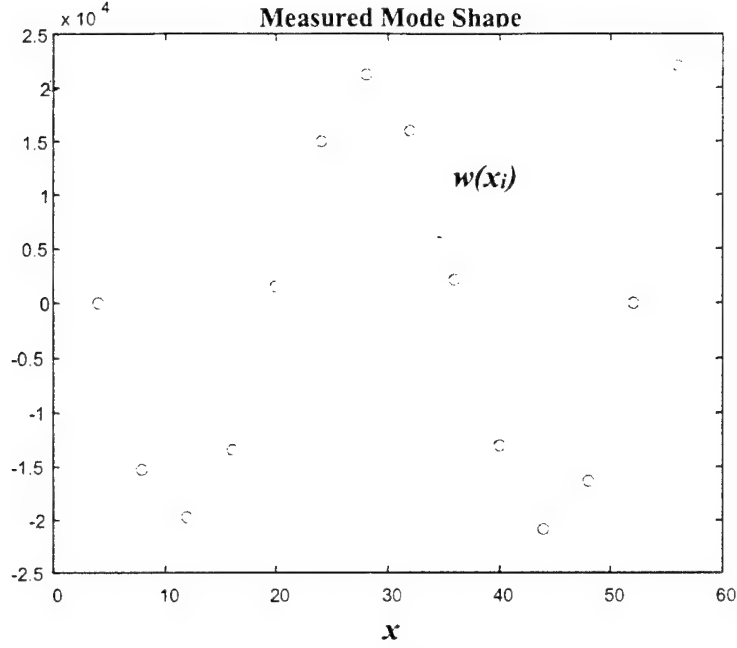


**Figure A.1 Example Measured Mode Shape for a Beam.**

The hatch notation is used in the previous expressions to indicate that the parameters are estimates. Also notice that if the slopes were to be known at the ends, then these conditions could be readily applied just by setting the slope condition to its proper value (i.e.: zero for a clamp support). Estimates of the modal curvature  $\hat{\psi}(x_i)$  can be similarly obtained by differentiating the slope estimates  $\hat{\theta}(x_i)$  in the same fashion. This gives,

$$\hat{\psi}(x_i) = \frac{\partial \hat{\theta}(x_i)}{\partial x} = \frac{\partial^2 w}{\partial x^2} = [\hat{\psi}_0(x_0), \hat{\psi}_1(x_1), \hat{\psi}_2(x_2), \dots, \hat{\psi}_n(x_n)] \quad (\text{A.4})$$

This time, the finite difference equations are

$$\hat{\psi}_0(x_0) = \frac{\hat{\theta}_1(x_1) - \hat{\theta}_0(x_0)}{x_1 - x_0}, \quad (\text{A.4a})$$

$$\hat{\psi}_i(x_i) = \frac{\hat{\theta}_{i+1}(x_{i+1}) - \hat{\theta}_{i-1}(x_{i-1})}{2(x_{i+1} - x_{i-1})}, \quad (\text{A.4b})$$

and

$$\hat{\psi}_n(x_n) = \frac{\hat{\theta}_n(x_n) - \hat{\theta}_{n-1}(x_{n-1})}{x_n - x_{n-1}}. \quad (\text{A.4c})$$

Boundary conditions, such as a free end, can be readily applied by setting the curvature at the corresponding end equal to zero.

The set of values  $\hat{\Psi}(x_i)$  of Equation (A.4) can be curve-fitted using cubic splines to obtain interpolated values between the original experimental measurement points. Furthermore, if the data is suspected of being contaminated with errors, then the type of splines applied could be smoothing splines. Let the cubic splines (or smoothing splines) interpolating  $\hat{\Psi}(x_i)$  be defined as  $\hat{\Psi}(x)$ . Figure A.2 illustrates the estimated values of modal curvature at the measuring points along with its interpolating function  $\hat{\Psi}(x)$ .

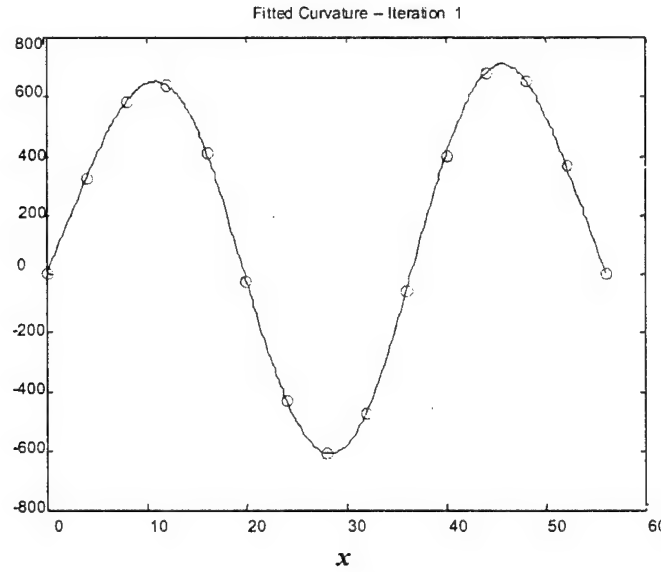


**Figure A.2 Fitted Curvature (First Iteration).**

The curvature function of Figure A.2 is only an estimate and it is expected to be in error. Because the only known values are the mode shape values represented in  $w(x_i)$ , the error can only be quantified by comparing the measured modal shape values to the second integral of  $\hat{\Psi}(x)$ . This is done using an iteration procedure to determine the "best" modal curvature that matches with the modal shape values. To estimate the error, the estimated curvature function is integrated twice to determine an estimate of the mode shape, as follows:

$$\hat{w}_1(x) = \int \left( \int \hat{\Psi}_1(x) dx \right) dx + c_1 x + c_2 \quad (\text{A.5})$$

The integrals in (A.5) can be evaluated using a cumulative trapezoidal numerical integration. The constants  $c_1$  and  $c_2$  can be determined by a least square linear fit of the difference of  $\left\{ w(x_i) - \int \left( \int \hat{\Psi}_1(x_i) dx \right) dx \right\}$ , where  $w(x_i)$  corresponds to the actual mode shape values. The error between the actual measured mode shape values and the estimated value obtained through Equation (A.5) can be defined as,

$$E_1(x_i) = w(x_i) - \hat{w}_1(x_i).$$

This subscript 1 indicates that this is for the first iteration. For any  $j^{\text{th}}$  iteration, we can generalize the error expression as:

$$E_j(x_i) = w(x_i) - \hat{w}_j(x_i). \quad (\text{A.6})$$

The mean square error between the actual values and the estimated values can be evaluated as,

$$MSE_j = \sqrt{\sum (w(x_i) - \hat{w}_j(x_i))^2} \quad (\text{A.7})$$

The error in Equation (A.6) serves as the basis for an iteration procedure applicable for any mode shape. First, the deflected shape of the mode is considered. Then the initial estimates of the mode and the modal curvature are set equal to zero. The initial function whose second derivative is to be estimated and curve-fitted is set equal to measured values. The slope and curvature of this function are obtained by means of finite differences using analogous expressions to those of Equations (A.2) and (A.4), and then the curvature is curve-fitted using smoothing cubic splines. This process results in an estimate of the curvature of the mode considered,  $f_j(x_i)$ . The curvature function is double integrated using Equation (A.5) and results in an estimate the mode  $f_j(x_i)$ . The estimates of the curvature and of the mode shape values are then added to the results of the previous iteration. The mean square error (MSE) with respect to the actual mode shape values is then computed by means of Equation (A.7). A decision is then made whether the iteration procedure converges. If the MSE is a minimum, then the final values for the curve-fitted mode shape and the modal curvature are obtained. If the MSE is not a minimum, the error obtained at the  $j^{\text{th}}$  iteration with respect to the original mode shapes is set equal to the function to be considered in the next iteration. Steps E through I are repeated until the MSE is minimized. Figure A.3 illustrates the original mode shape data and the final curve-fitted mode shape function after eight iterations. Notice that values of the mode shapes can be obtained between the measuring points or sensor locations. It should be observed that the fit of the points is very good. Figure A.4 illustrates the final fitted modal curvature (second derivative) compared to the estimated curvature obtained by finite differences in the first iteration. Notice that the final modal curvature is continuous and seems to follow the natural sinusoidal-type shape. Note that the modal strain energy is proportional to the square of the curvature.

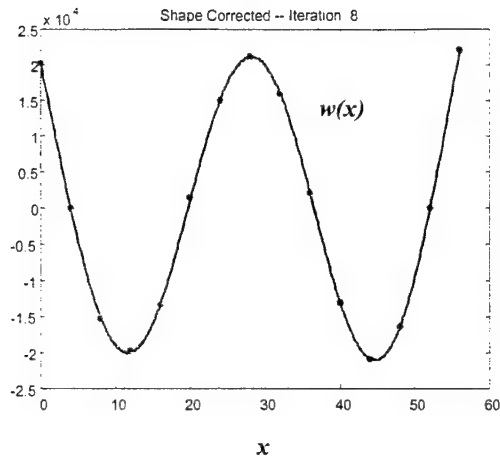


**Figure A.3 Final Fitted Mode Shape after Eight Iterations**

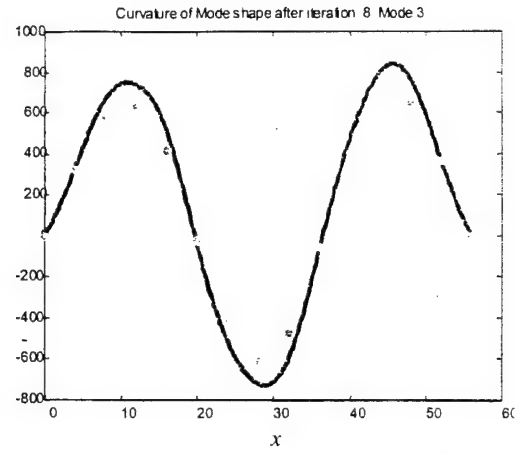


**Figure A.4 Fitted Modal Curvature after Eight Iterations.**

### A.3 Mode Curve-Fit Algorithm for Plate-like Structures

The iterative curve-fit algorithm used to estimate curvatures for plate-like structures is similar to the one discussed in the previous section. However, the three-dimensional case (plate-like structures) is more involved because it requires the evaluation of slopes and curvatures over a surface area dealing with partial derivatives. In other words, computations need to be performed simultaneously in the longitudinal and transverse axes of the surface to calculate two slopes and bending and twisting curvatures,  $\left( \frac{\partial w}{\partial x}, \frac{\partial w}{\partial y}, \frac{\partial^2 w}{\partial x^2}, \frac{\partial^2 w}{\partial y^2}, \text{and } \frac{\partial^2 w}{\partial x \partial y} \right)$ . Furthermore, the

numerical double integration needed to back-calculate the shape corresponding to the fitted curvatures requires the evaluation of functions of two variables and constants. This section describes the curve-fitting algorithm for plate like structures.

Consider a plate-like structure that is vibrating at one of its resonant frequencies and its corresponding mode shape  $\phi(x, y)$  is extracted. Let the mode shape measurements obtained in a closed, bounded and rectangular region be defined as:

$$w_{i,j}(x_i, y_j) = \begin{bmatrix} w_{00}(x_0, y_0) & w_{01}(x_0, y_1) & w_{02}(x_0, y_2) & \cdots & w_{0m}(x_0, y_m) \\ w_{10}(x_1, y_0) & w_{11}(x_1, y_1) & w_{12}(x_1, y_2) & \cdots & w_{1m}(x_1, y_m) \\ w_{20}(x_2, y_0) & w_{21}(x_2, y_1) & w_{22}(x_2, y_2) & \cdots & w_{2m}(x_2, y_m) \\ \vdots & \vdots & \vdots & \ddots & \vdots \\ w_{n0}(x_n, y_0) & w_{n1}(x_n, y_1) & w_{n2}(x_n, y_2) & \cdots & w_{nm}(x_n, y_m) \end{bmatrix}. \quad (\text{A.8})$$

Where  $n$  and  $m$  are the number of intervals along the  $x$  and  $y$  axes, respectively. For example, Figure A.5 illustrates a typical mode shape. The mode shape was measured over a rectangular area using 12 intervals in  $x$  ( $n=12$ ) and 14 in  $y$  ( $m=14$ ). Thus, the curvatures  $\left( \frac{\partial^2 w}{\partial x^2}, \frac{\partial^2 w}{\partial y^2}, \text{and } \frac{\partial^2 w}{\partial x \partial y} \right)$  need to be estimated from the set of grid measurements. This can be accomplished using the finite difference and numerical integration concepts introduced in the previous section. First the slopes  $\theta_x = \frac{\partial w}{\partial x}$  and  $\theta_y = \frac{\partial w}{\partial y}$  are directly estimated from finite differences. Then the curvatures  $\left( \frac{\partial^2 w}{\partial x^2}, \frac{\partial^2 w}{\partial y^2}, \text{and } \frac{\partial^2 w}{\partial x \partial y} \right)$  follow by applying the finite difference to the slopes.

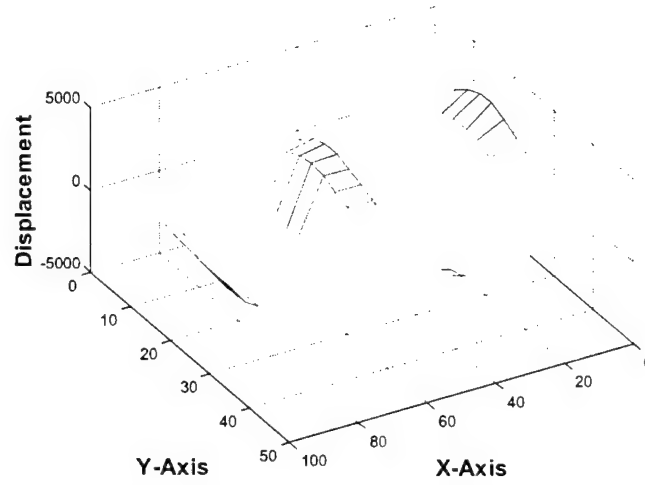


**Figure A.5 Typical Measured Mode Shape Over a Rectangular Area.**

The slope  $\theta_x = \frac{\partial w}{\partial x}$  can be estimated from the previous equation by finite differences, leading to the following expression:

$$\hat{\theta}_{x i, j}(x_i, y_j) = \begin{bmatrix} \hat{\theta}_{x00}(x_0, y_0) & \hat{\theta}_{x01}(x_0, y_1) & \hat{\theta}_{x02}(x_0, y_2) & \cdots & \hat{\theta}_{x0m}(x_0, y_m) \\ \hat{\theta}_{x10}(x_1, y_0) & \hat{\theta}_{x11}(x_1, y_1) & \hat{\theta}_{x12}(x_1, y_2) & \cdots & \hat{\theta}_{x1m}(x_1, y_m) \\ \hat{\theta}_{x20}(x_2, y_0) & \hat{\theta}_{x21}(x_2, y_1) & \hat{\theta}_{x22}(x_2, y_2) & \cdots & \hat{\theta}_{x2m}(x_2, y_m) \\ \vdots & \vdots & \vdots & \ddots & \vdots \\ \hat{\theta}_{xn0}(x_n, y_0) & \hat{\theta}_{xn1}(x_n, y_1) & \hat{\theta}_{xn2}(x_n, y_2) & \cdots & \hat{\theta}_{xnm}(x_n, y_m) \end{bmatrix} \quad (\text{A.9})$$

The values along the edges at  $x=x_0$  and at  $x=x_n$  are obtained by forward and backward difference expressions, respectively.

$$\hat{\theta}_{x_{0j}}(x_0, y_j) = \frac{w_{1j}(x_1, y_j) - w_{0j}(x_0, y_j)}{x_1 - x_0}, \quad (\text{A.10a})$$

$$\hat{\theta}_{x_{nj}}(x_n, y_j) = \frac{w_{nj}(x_n, y_j) - w_{n-1j}(x_{n-1}, y_j)}{x_n - x_{n-1}} \quad (\text{A.10b})$$

For all other points, the central difference theorem is used.

$$\hat{\theta}_{x_{ij}}(x_i, y_j) = \frac{w_{i+1j}(x_{i+1}, y_j) - w_{i-1j}(x_{i-1}, y_j)}{2(x_{i+1} - x_{i-1})} \quad (\text{A.10c})$$

If any edge at  $y = y_o$  or  $y = y_m$  are simply- or fixed-supported then the slope  $x$  along the edges can be set equal to zero.

The slope  $\theta_y = \frac{\partial w}{\partial y}$  can be similarly estimated leading to:

$$\hat{\theta}_{y_{i,j}}(x_i, y_j) = \begin{bmatrix} \hat{\theta}_{y_{00}}(x_0, y_0) & \hat{\theta}_{y_{01}}(x_0, y_1) & \hat{\theta}_{y_{02}}(x_0, y_2) & \cdots & \hat{\theta}_{y_{0m}}(x_0, y_m) \\ \hat{\theta}_{y_{10}}(x_1, y_0) & \hat{\theta}_{y_{11}}(x_1, y_1) & \hat{\theta}_{y_{12}}(x_1, y_2) & \cdots & \hat{\theta}_{y_{1m}}(x_1, y_m) \\ \hat{\theta}_{y_{20}}(x_2, y_0) & \hat{\theta}_{y_{21}}(x_2, y_1) & \hat{\theta}_{y_{22}}(x_2, y_2) & \cdots & \hat{\theta}_{y_{2m}}(x_2, y_m) \\ \vdots & \vdots & \vdots & \ddots & \vdots \\ \hat{\theta}_{y_{n0}}(x_n, y_0) & \hat{\theta}_{y_{n1}}(x_n, y_1) & \hat{\theta}_{y_{n2}}(x_n, y_2) & \cdots & \hat{\theta}_{y_{nm}}(x_n, y_m) \end{bmatrix} \quad (\text{A.11})$$

This time however, the slope  $y$  values along the edges at  $y=y_o$  and at  $y=y_m$  are obtained by:

$$\hat{\theta}_{y_{io}}(x_i, y_o) = \frac{w_{i1}(x_i, y_1) - w_{i0}(x_i, y_0)}{y_1 - y_0}, \quad (\text{A.12a})$$

$$\hat{\theta}_{y_{in}}(x_i, y_n) = \frac{w_{in}(x_i, y_n) - w_{in-1}(x_i, y_{n-1})}{y_{n-1} - y_n} \quad (\text{A.12b})$$

For all other points, the central difference theorem is used.

$$\hat{\theta}_{y_{ij}}(x_i, y_j) = \frac{w_{ij+1}(x_i, y_{j+1}) - w_{ij-1}(x_i, y_{j-1})}{2(y_{j+1} - y_{j-1})} \quad (\text{A.12c})$$

If any edge at  $x = x_o$  or  $x = x_n$  is simply- or fixed-supported, then the slope  $y$  along the edges can be set equal to zero.

To obtain the curvature  $\left(\frac{\partial^2 w}{\partial x^2} = \frac{\partial \theta_x}{\partial x}\right)$ , the values obtained in expression (A.9) are subject to the finite difference treatment explained for  $\hat{\theta}_x$ . Like wise, the curvature  $\left(\frac{\partial^2 w}{\partial y^2} = \frac{\partial \theta_y}{\partial y}\right)$  is obtained by applying the finite theorem to the values obtained in expression (A.11).

The above leads to the following expressions:

$$\hat{\kappa}_{x_{i,j}}(x_i, y_j) = \frac{\partial^2 w(x_i, y_j)}{\partial x^2} = \begin{bmatrix} \hat{\kappa}_{x00} & \hat{\kappa}_{x01} & \hat{\kappa}_{x02} & \cdots & \hat{\kappa}_{x0m} \\ \hat{\kappa}_{x10} & \hat{\kappa}_{x11} & \hat{\kappa}_{x12} & \cdots & \hat{\kappa}_{x1m} \\ \hat{\kappa}_{x20} & \hat{\kappa}_{x21} & \hat{\kappa}_{x22} & \cdots & \hat{\kappa}_{x2m} \\ \vdots & \vdots & \vdots & \ddots & \vdots \\ \hat{\kappa}_{xn0} & \hat{\kappa}_{xn1} & \hat{\kappa}_{xn2} & \cdots & \hat{\kappa}_{xnm} \end{bmatrix}, \quad (\text{A.13})$$

and,

$$\hat{\kappa}_{y_{i,j}}(x_i, y_j) = \frac{\partial^2 w(x_i, y_j)}{\partial y^2} = \begin{bmatrix} \hat{\kappa}_{y00} & \hat{\kappa}_{y01} & \hat{\kappa}_{y02} & \cdots & \hat{\kappa}_{y0m} \\ \hat{\kappa}_{y10} & \hat{\kappa}_{y11} & \hat{\kappa}_{y12} & \cdots & \hat{\kappa}_{y1m} \\ \hat{\kappa}_{y20} & \hat{\kappa}_{y21} & \hat{\kappa}_{y22} & \cdots & \hat{\kappa}_{y2m} \\ \vdots & \vdots & \vdots & \ddots & \vdots \\ \hat{\kappa}_{yn0} & \hat{\kappa}_{yn1} & \hat{\kappa}_{yn2} & \cdots & \hat{\kappa}_{ynm} \end{bmatrix}. \quad (\text{A.14})$$

Where,

$$\hat{\kappa}_{x0j} = \hat{\kappa}_{x0j}(x_0, y_j) = \frac{\hat{\theta}_{x1j}(x_1, y_j) - \hat{\theta}_{x0j}(x_0, y_j)}{x_1 - x_0}, \quad (\text{A.15a})$$

$$\hat{\kappa}_{xnj} = \hat{\kappa}_{xnj}(x_n, y_j) = \frac{\hat{\theta}_{xnj}(x_n, y_j) - \hat{\theta}_{xn-1j}(x_{n-1}, y_j)}{x_n - x_{n-1}} \quad (\text{A.15b})$$

$$\hat{\kappa}_{xij} = \hat{\kappa}_{xij}(x_i, y_j) = \frac{\theta_{xi+1j}(x_{i+1}, y_j) - \theta_{xi-1j}(x_{i-1}, y_j)}{2(x_{i+1} - x_{i-1})} \quad (\text{A.15c})$$

$$\hat{\kappa}_{yio} = \hat{\kappa}_{yio}(x_i, y_o) = \frac{\hat{\theta}_{yi1}(x_i, y_1) - \hat{\theta}_{yi0}(x_i, y_0)}{y_1 - y_0}, \quad (\text{A.15d})$$

$$\hat{\kappa}_{yin} = \hat{\kappa}_{yin}(x_i, y_n) = \frac{\hat{\theta}_{yin}(x_i, y_n) - \hat{\theta}_{yin-1}(x_i, y_{n-1})}{y_{n-1} - y_n} \quad (\text{A.15e})$$

$$\hat{\kappa}_{yij} = \hat{\kappa}_{yij}(x_i, y_j) = \frac{\hat{\theta}_{yij+1}(x_i, y_{j+1}) - \hat{\theta}_{yij-1}(x_i, y_{j-1})}{2(y_{j+1} - y_{j-1})} \quad (\text{A.15f})$$

If any edge at  $y = y_o$  or  $y = y_m$  is simply- or fixed-supported then the curvature  $x$  along the edge can be set equal to zero. Likewise, for the edge at  $x = x_o$  or  $x = x_n$  the curvature  $y$  along the edge can be set equal to zero. Furthermore, if the edge along  $x = x_o$  or  $x = x_n$  are free, then the curvature  $x$  can also be set equal to zero. Likewise, if the edge at  $y = y_o$  or  $y = y_m$  is free, then the curvature  $y$  is set to zero.

The determination of the twisting curvature  $\kappa_{xy} = \frac{\partial^2 w}{\partial x \partial y}$  can be done in two ways, one is differentiating the slope  $x$  with respect to  $y$ ,  $\frac{\partial \hat{\theta}_x}{\partial y}$ , and the other differentiating the slope  $y$  with respect to  $x$ ,  $\frac{\partial \hat{\theta}_y}{\partial x}$ . Either way, the finite difference results provide the same values, to give:

$$\hat{\kappa}_{xy_{i,j}}(x_i, y_j) = \frac{\partial^2 w(x_i, y_j)}{\partial x \partial y} = \begin{bmatrix} \hat{\kappa}_{xy_{00}} & \hat{\kappa}_{xy_{01}} & \hat{\kappa}_{xy_{02}} & \cdots & \hat{\kappa}_{xy_{0m}} \\ \hat{\kappa}_{xy_{10}} & \hat{\kappa}_{xy_{11}} & \hat{\kappa}_{xy_{12}} & \cdots & \hat{\kappa}_{xy_{1m}} \\ \hat{\kappa}_{xy_{20}} & \hat{\kappa}_{xy_{21}} & \hat{\kappa}_{xy_{22}} & \cdots & \hat{\kappa}_{xy_{2m}} \\ \vdots & \vdots & \vdots & \ddots & \vdots \\ \hat{\kappa}_{xy_{n0}} & \hat{\kappa}_{xy_{n1}} & \hat{\kappa}_{xy_{n2}} & \cdots & \hat{\kappa}_{xy_{nm}} \end{bmatrix}. \quad (\text{A.16})$$

Where,

$$\hat{\kappa}_{xy_{io}} = \hat{\kappa}_{xy_{io}}(x_i, y_o) = \frac{\hat{\theta}_{x1j}(x_i, y_1) - \hat{\theta}_{xi0}(x_i, y_0)}{y_2 - y_1}, \quad (\text{A.17a})$$

$$\hat{\kappa}_{xy_{in}} = \hat{\kappa}_{xy_{in}}(x_i, y_n) = \frac{\hat{\theta}_{xin}(x_i, y_n) - \hat{\theta}_{xin-1}(x_i, y_{n-1})}{y_{n-1} - y_n} \quad (\text{A.17b})$$

$$\hat{\kappa}_{xy_{ij}} = \hat{\kappa}_{xy_{ij}}(x_i, y_j) = \frac{\hat{\theta}_{xij+1}(x_i, y_{j+1}) - \hat{\theta}_{xij-1}(x_i, y_{j-1})}{2(y_{j-1} - y_j)} \quad (\text{A.17c})$$

The appropriate twisting curvature boundary conditions at the appropriate edges can be applied.

The set of values for the plate bending and twisting curvatures  $\hat{\kappa}_{x_{i,j}}(x_i, y_j)$ ,  $\hat{\kappa}_{y_{i,j}}(x_i, y_j)$  and  $\hat{\kappa}_{xy_{i,j}}(x_i, y_j)$  of Equations (A.13), (A.14) and (A.16), respectively, can be curve-fitted using bivariate cubic splines to obtain interpolated values between the measurement points and a denser grid. If the data is suspected of being contaminated with errors, then the type of splines applied could be smoothing splines. The bivariate cubic splines (or smoothing splines) interpolating the plate bending and twisting curvatures can be defined as curvatures  $\hat{\kappa}_x(x, y)$ ,  $\hat{\kappa}_y(x, y)$  and  $\hat{\kappa}_{xy}(x, y)$ . Figure A.6 illustrates the plate bending and twisting curvatures obtained for the mode shape of Figure A.5 by curve-fitting the estimated values through the finite difference equations. The curvature functions of Figure A.6 are only estimates and, like in the two-dimensional case, are expected to be in error. Because the only known true values are the mode shape grid values represented in  $w(x_i, y_j)$ , the errors can only be quantified by comparing the measured modal shape values to the second integrals of curvatures  $\hat{\kappa}_x(x, y)$ ,  $\hat{\kappa}_y(x, y)$  and  $\hat{\kappa}_{xy}(x, y)$ . Notice that double integrating the curvatures lead to the same deflection function.

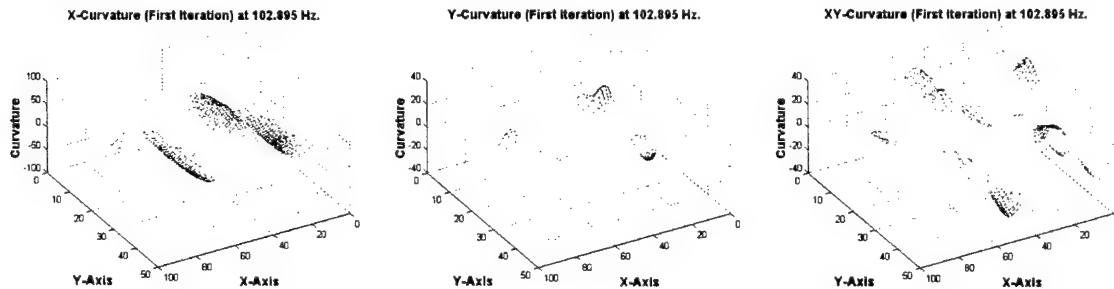


**Figure A.6 Example of Plate Bending and Twisting Curvatures Obtained by Curvefitting.**



To estimate the error, each of the estimated curvature functions is integrated twice to determine an estimate of the mode shape. This leads to three different mode shape equations, one from each curvature, as follows:

$$\hat{w}_a(x, y) = \int \left( \int \hat{\kappa}_x(x, y) dx \right) dy + c_1 x + c_2 + f_1(y) \quad (\text{A.18})$$

$$\hat{w}_b(x, y) = \int \left( \int \hat{\kappa}_y(x, y) dy \right) dx + c_3 y + c_4 + f_2(x) \quad (\text{A.19})$$

$$\hat{w}_c(x, y) = \int \left( \int \hat{\kappa}_{xy}(x, y) dx \right) dy + c_5 y + f_3(y) + f_4(x) \quad (\text{A.20})$$

The integrals in (A.18) through (A.20) can be evaluated using a double cumulative trapezoidal numerical integration. The constants  $c_1$  through  $c_5$  and the functions  $f_1$  through  $f_4$  in these equations can be determined by least square fits of the difference of,

$$\begin{aligned} & \left\{ w(x_i, y_j) - \int \left( \int \hat{\kappa}_x(x_i, y_j) dx \right) dy \right\} \\ & \left\{ w(x_i, y_j) - \int \left( \int \hat{\kappa}_y(x_i, y_j) dy \right) dx \right\} \\ & \left\{ w(x_i, y_j) - \int \left( \int \hat{\kappa}_{xy}(x_i, y_j) dx \right) dy \right\} \end{aligned}$$

Where,  $w(x_i, y_j)$  corresponds to the actual mode shape values. Once the constants and functions are determined, then the estimate of the mode shape functions can be computed by averaging the results from the three double integrals. This gives:

$$\hat{w}_1(x, y) = \frac{\hat{w}_a(x, y) + \hat{w}_b(x, y) + \hat{w}_c(x, y)}{3} \quad (\text{A.21})$$

The subscript 1 in the equation above indicates the results for the first iteration. These results of the first iteration serve as the basis for an iterative procedure similar to that described for the two dimensional case (beam).

Figure A.7 illustrates the final fitted modal curvatures (bending and twisting). It should be observed that the final modal curvature is continuous and seems to follow the natural sinusoidal-type shape. It should also be observed that the mode is dominated by the bending curvature in the x direction.

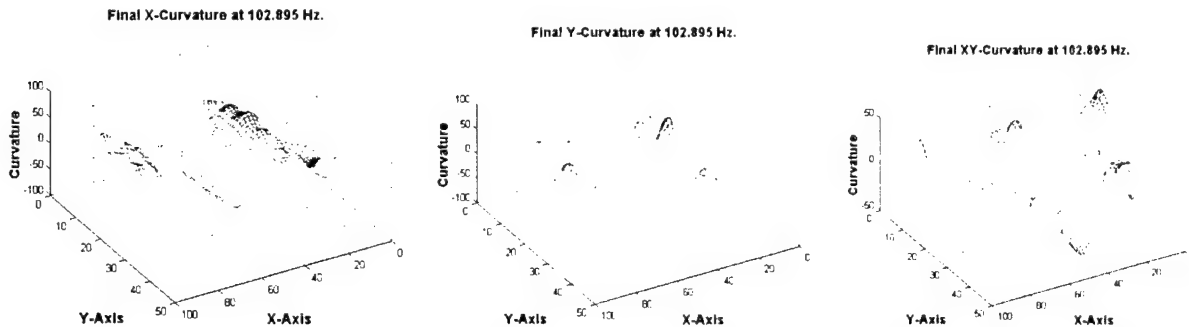


### **Figure A.7 Final Bending and Twisting Curvatures.**

The damage detection process used to identify inflicted damage in the Vertical Stabilizer Assembly (VSA) test article is described in this chapter. The methods used for the localization of the damage are based on modal strain energy difference approaches. The process assumes that modal analysis data exists for the undamaged and damaged structure in the form of paired resonant frequencies and mode shapes. In order to implement the damage detection methods a finite element model of the structure was required and is described here. Also, because the model contains significantly more degrees of freedom than those instrumented with the LDV, the measured mode shapes are extrapolated to all degrees-of-freedom of the model. The extrapolation technique is based on a static finite element analysis and is briefly described here.

#### **A.4 Finite Element Approach for Complex Structures**

Both of the curvefitting approaches described in the previous two sections are applicable if the structure is regular. In the case of aerospace structures, the structures are complex involving skins, spars, ribs and other forms of elements. The challenge here is to determine the distribution of modal strain energy from modal measurements obtained at the exterior surface of the structure. The approach adopted employs the use of finite element model. For example a drawing of the finite element mesh for the Vertical stabilizer assembly of the space shuttle is illustrated in Figure A.8. What is visible in the figure are the outer plate elements forming the skin of the VSA. Internally, there exists numerous elements that form the stringers and ribs, which provide the primary stiffness of the structure. The tests that UTEP students conducted resulted in modal shapes from measurements at 84 exterior points. This particular model contained more than 4,000 elements, and the challenge is to estimate the internal strain energy from the modal shape measurements at the 84 locations. In other words, the mode shapes measured only correspond to 84 locations taken normal to the central plane of the structure. In order to determine the modal strain energy in all elements, the mode shapes are required in all degrees of freedom of the model.

In order to estimate the complete mode shapes of the model, a static analysis was conducted by forcing the model to displace as the modal shapes. A neutral file containing the new model was exported because it was easier to manipulate since it was in a text format. The 84 points in which readings were taken were identified in the finite element model. At each of the measuring location, there was a node in the model. The set of experimental mode shapes for the baseline and damage cases were exported into universal format files. These files were then imported into the NASTRAN model of the test article as deflections applied at the corresponding nodes in the direction normal to the central plane of the test article. A new model file was created for each damage and baseline case to facilitate handling of the files. Once the neutral file contained the modes as deflections, the file was imported into NASTRAN. A static analysis was then performed with NASTRAN to obtain the complete deformations at all degrees of freedom of the model. These complete deformations corresponded to the estimated global mode shapes extracted from the experimental values. Armed with the complete modes at all degrees of

freedom of the model, then the calculations of the strain energy due to all the mode shapes were easily carried out. The strain energy expressions are inherently built into NASTRAN. Therefore, with each static analysis, the strain energy of the elements was additionally computed. A file containing the list of elements and the corresponding strain energy was generated for each mode of the baseline and damaged cases. These files were later used to calculate the strain energy differences and to perform the algorithms of damage detection.

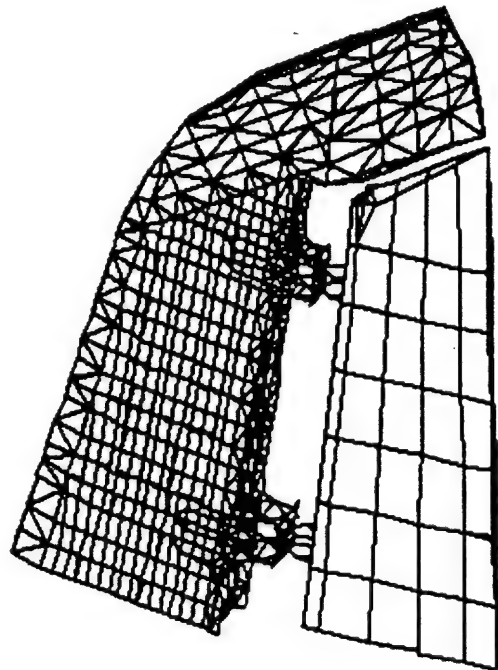


**Figure A.8 Original Finite Element Model (left) and Modified Model (right).**

## APPENDIX B

### PROCEDURE TO DETERMINE MODE WITH SIGNIFICANT CHANGE BETWEEN DAMAGED AND UNDAMAGED SCENARIOS

#### B.1. Introduction

A statistical procedure to compare the FRFs obtained for the undamaged and damaged test article is presented. The analysis is applied between measurements taken with the same sensors at the same points between the undamaged and damaged states of the structure. The advantage of such analysis is that it reveals frequency ranges where the structure's vibrational characteristics have changed. However, in order to visualize the global changes, it is necessary to combine the information obtained from all points of the structure. This section presents a procedure to compare the FRFs of the undamaged and damaged structure that reveals not only the frequency ranges where the structural response changed due to damage but also indicates the significance of the changes.

#### B.2. Approach for Comparison

The statistical comparison between the FRFs of the damaged and undamaged scenarios can be made using the frequency response functions obtained from measuring points of the undamaged and damaged structure. A null hypothesis and alternative hypothesis are formulated that the difference in the FRFs is zero and non-zero, respectively, at all measuring locations.

$$H_o : \sum_{i=1}^n (|H_{di}(\omega)| - |H_{ui}(\omega)|) = 0 \quad (B.1)$$

$$H_a : \begin{aligned} &\sum_{i=1}^n (|H_{di}(\omega)| - |H_{ui}(\omega)|) > 0 \\ &\sum_{i=1}^n (|H_{di}(\omega)| - |H_{ui}(\omega)|) < 0 \\ &\sum_{i=1}^n (|H_{di}(\omega)| - |H_{ui}(\omega)|) \neq 0 \end{aligned} \quad (B.2)$$

Where,  $i$  is the location number,  $n$  was the number of measuring locations, the subscripts  $u$  and  $d$  were used to indicate the appropriate FRFs for the undamaged and damaged states of the structure, respectively, and the absolute sign indicates the magnitude of the FRF computed by:

$$|H_i(\omega)| = \sqrt{H_{ri}^2(\omega) + H_{ii}^2(\omega)} \quad (B.3)$$

An estimate of the standard deviation on the FRF difference is given by the expression:

$$\sigma_i(\omega) = \frac{\sqrt{1 - \gamma_i^2(\omega)}}{\gamma_i(\omega)\sqrt{2n_d}} |H_i(\omega)| \quad i = 1 \dots n_{loc} \quad (B.4)$$

Where  $\gamma_i(\omega)$  is the coherence function at location  $i$  and  $n_d$  is the number of averages while collecting the FRFs in the experiments.

A two-tailed test is also chosen for the 95% confidence intervals as defined by the alternative hypothesis. Thus the equations corresponding to the bounds of the difference of the FRFs are:

$$\begin{aligned} \rho_i^u(\omega) &= |H_{di}(\omega)| - |H_{ui}(\omega)| \pm t_{\frac{\alpha}{2}} S_{pi} \sqrt{\frac{1}{n_d^u} + \frac{1}{n_d^d}} \\ \rho_i^l(\omega) &= |H_{di}(\omega)| - |H_{ui}(\omega)| \pm t_{\frac{\alpha}{2}} S_{pi} \sqrt{\frac{1}{n_d^u} + \frac{1}{n_d^d}} \end{aligned} \quad (B.5)$$

Where  $\rho$  is used here to indicate the difference in the means of the FRFs between the undamaged and damaged state for location  $i$ . The superscripts  $u$  and  $l$  are used to indicate upper and lower bounds, respectively. Equation (B.5) is normalized at each location with respect to the mean and standard deviation of the FRF differences at the discrete frequencies. These means and standard deviations were computed by the expressions:

$$\mu_{\rho u_i} = \frac{\sum_{j=1}^{n_f} \rho_i^u(\omega_j)}{n_f} \quad \mu_{\rho l_i} = \frac{\sum_{j=1}^{n_f} \rho_i^l(\omega_j)}{n_f} \quad (B.6)$$

$$\sigma_{\rho u_i} = \sqrt{\frac{(\rho_i^u(\omega_j) - \mu_{\rho u_i})^2}{n_f - 1}} \quad \sigma_{\rho l_i} = \sqrt{\frac{(\rho_i^l(\omega_j) - \mu_{\rho l_i})^2}{n_f - 1}} \quad (B.7)$$

Where,  $\mu_{\rho u_i}$  and  $\mu_{\rho l_i}$  are the mean of the upper and lower bounds, respectively, of the differences between the FRFs of the undamaged and damaged states at location  $i$  of the structure;  $n_f$  is the number of frequency lines in the FRFs; and  $\sigma_{\rho u_i}$  and  $\sigma_{\rho l_i}$  are the corresponding standard deviations. Thus, the expressions of Equations (B.5) were transformed using the standard norm of Equations (B.6) and (B.7) to give:

$$Z_i^u(\omega) = \frac{\rho_i^u(\omega) - \mu_{\rho u_i}}{\sigma_{\rho u_i}} \quad (B.8)$$

$$Z_i^l(\omega) = \frac{\rho_i^l(\omega) - \mu_{\rho l_i}}{\sigma_{\rho l_i}} \quad (B.9)$$

There corresponds a pair of Z functions, as in Equation (B.9) for each measurement locations. In order to obtain an indication of the FRF changes for all locations combined, the average value can be taken. This gives:

$$Z^u(\omega) = \frac{\sum_{i=1}^n Z_i^u(\omega)}{n} \quad \text{and} \quad Z^l(\omega) = \frac{\sum_{i=1}^n Z_i^l(\omega)}{n} \quad (\text{B.10})$$

These Z-functions behave as indicators identifying frequency values where changes in the modal response of the structure occur between the undamaged and damaged states. The Z-function measures how many standard deviations away from the mean are the differences between the mean damaged and undamaged responses. The mean value is given by:

$$Z(\omega) = \frac{Z^u(\omega) + Z^l(\omega)}{2} \quad (\text{B.11})$$

Consequently, if the absolute value of  $Z(\omega)$  is greater than 1.96, then the null hypothesis can be rejected with a 95% confidence. Therefore, the indicator function  $Z(\omega)$  identifies the frequency ranges where the response has statistically changed considering all measurement locations.

### B.3. Typical Results of Z-Function Analysis

The Z-functions are calculated for all pairs of baseline and damaged cases. Figure B.1 illustrates a typical set of results obtained for the Z-function of (B.11) through the use of Equations (B.3) through (B.10). These calculations involved the FRFs and Coherence functions of the measurements of the undamaged and damaged states of the test article at all points. This particular graph corresponds to the experiments conducted on the VSA test article. The significance of these results is discussed in the next section.

An overlay of the resonant frequencies of the structure in the two states with a graph of the Z-function assists in identifying the nature of the changes in the dynamic response as well as mode pairs with significant global changes. Figure B.1 also shows horizontal lines with dots corresponding to the resonant frequencies of the damaged and healthy states of the structure. MAC analysis results are also illustrated with dashed lines connecting the associated frequencies with MAC values greater than 0.8. One positive peak adjacent to a negative peak, or vice versa, is indicative of frequency shifts. If the amplitude of one peak is larger than the other one, then it is also indicative of increases or decreases of modal amplitudes. Also note that the figure also suggests the presence of new modes by peaks with a dot with no adjacent peaks. More important, if peaks identified though the MAC exceed a threshold, then the mode pairs may have been sensitive to the inflicted damage, and thus may have higher probability of detecting it using the strain energy-based methods. For example, see the mode pairs corresponding to the circled dots; these modes were affected by the inflicted damage and are more likely to contain features that can potential detect the inflicted damage.

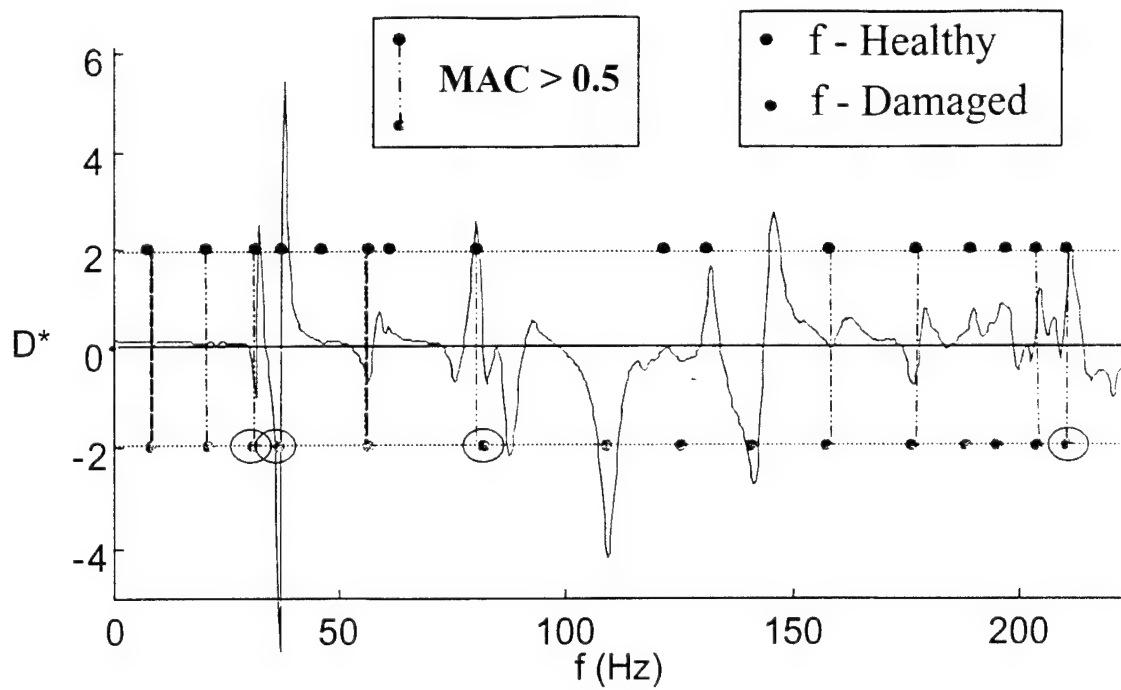


**Figure B.1** Average of Normalized FRF Magnitude Differences of All 84 Measured Points in VSA Test Article for One Case.

**APPENDIX C**

**DAMAGE MAPS OBTAINED FOR THE VSA TEST OBJECT USING  
IMPROVED FE MODEL**



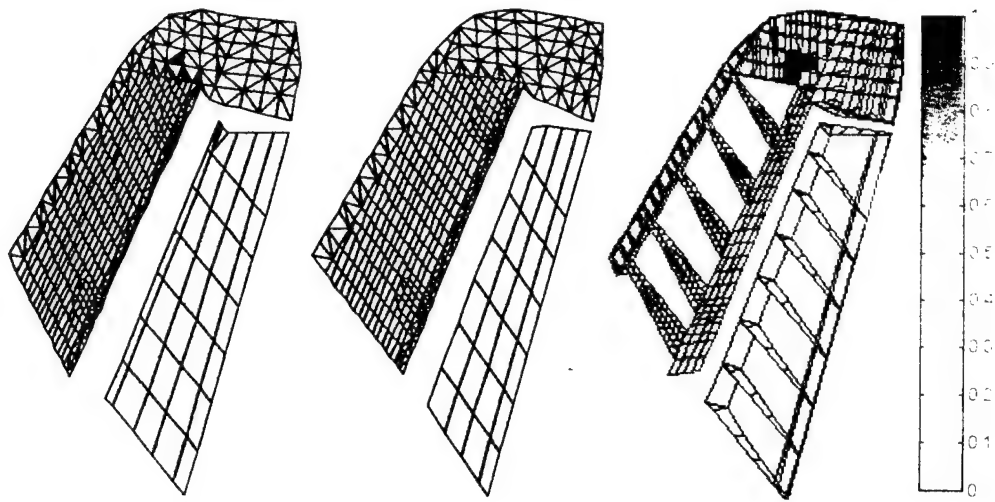


Figure C.1.1 Results by averaging for Case 4a, using Z-function (Detected).

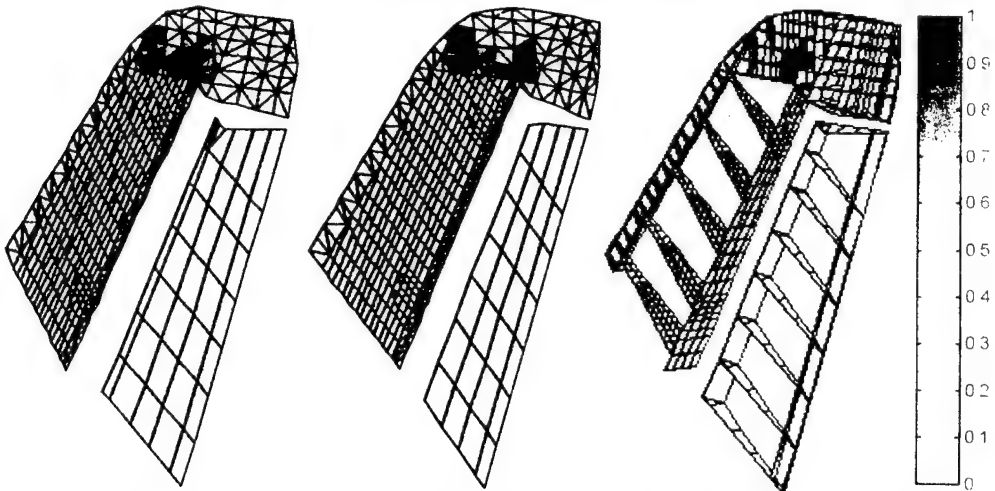


Figure C.1.2 Results by averaging for Case 4b, using Z-function (Detected).

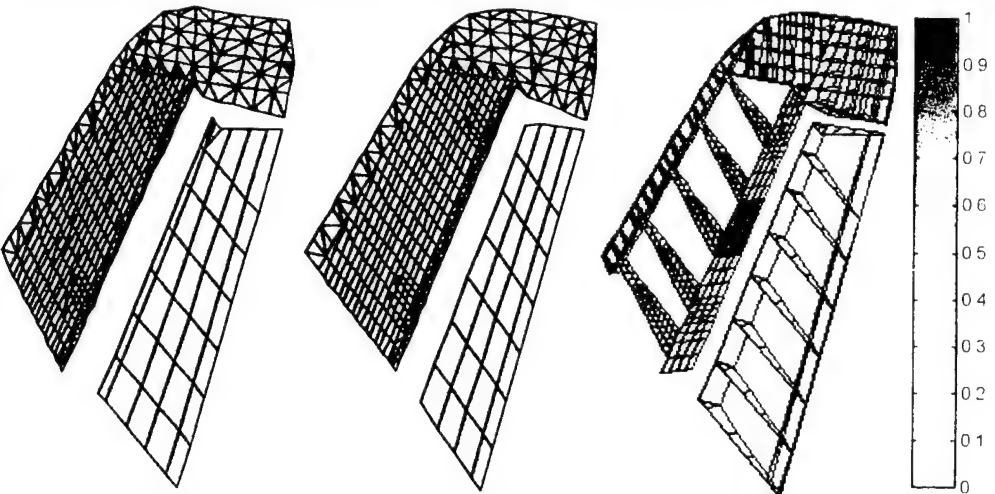


Figure C.1.3 Results by averaging for Case 4c, using Z-function (Detected).

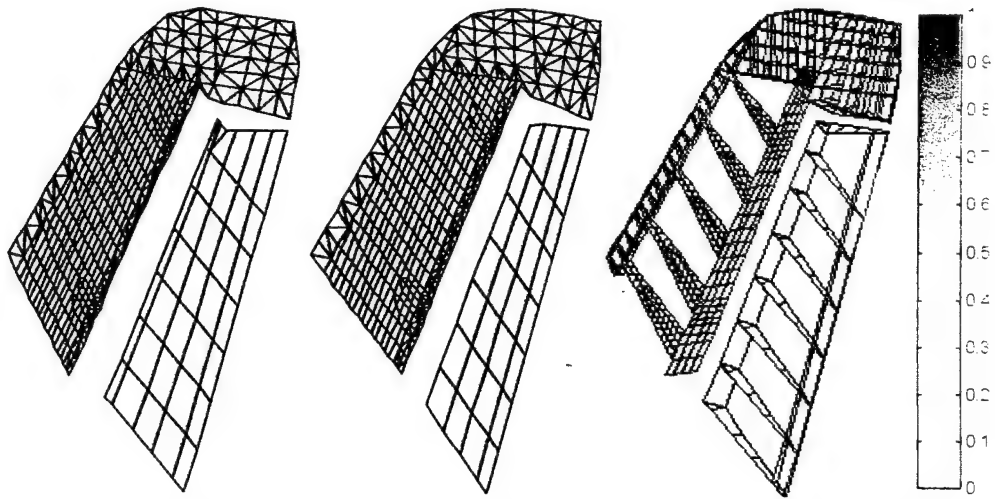


Figure C.1.4 Results by averaging for Case 5a, using Z-function (Detected).

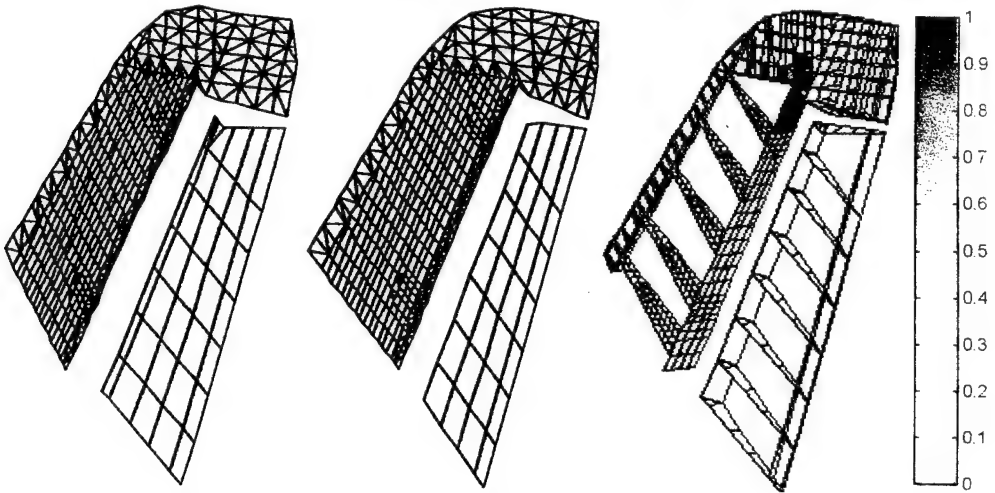


Figure C.1.5 Results by averaging for Case 5b, using Z-function (Detected).

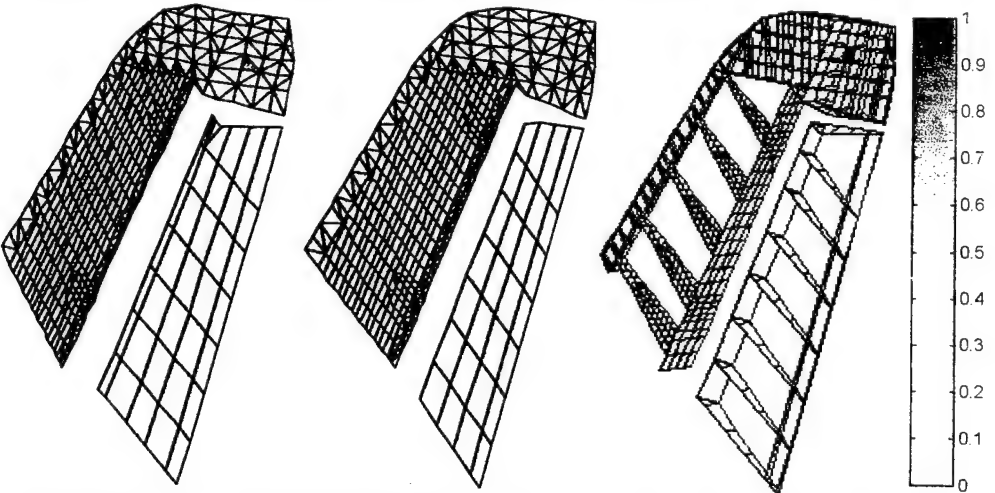


Figure C.1.6 Results by averaging for Case 5c, using Z-function (Detected).

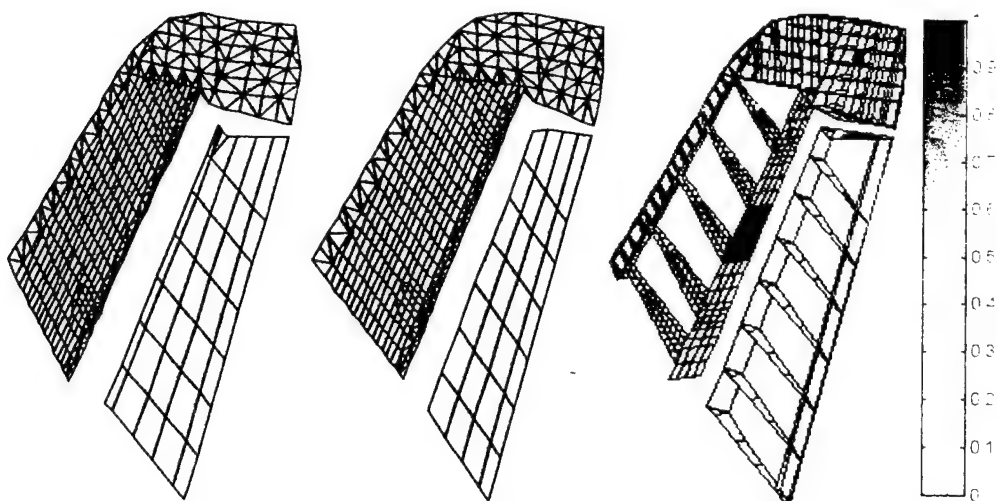


Figure C.1.7 Results by averaging for Case 5h, using Z-function (Detected).

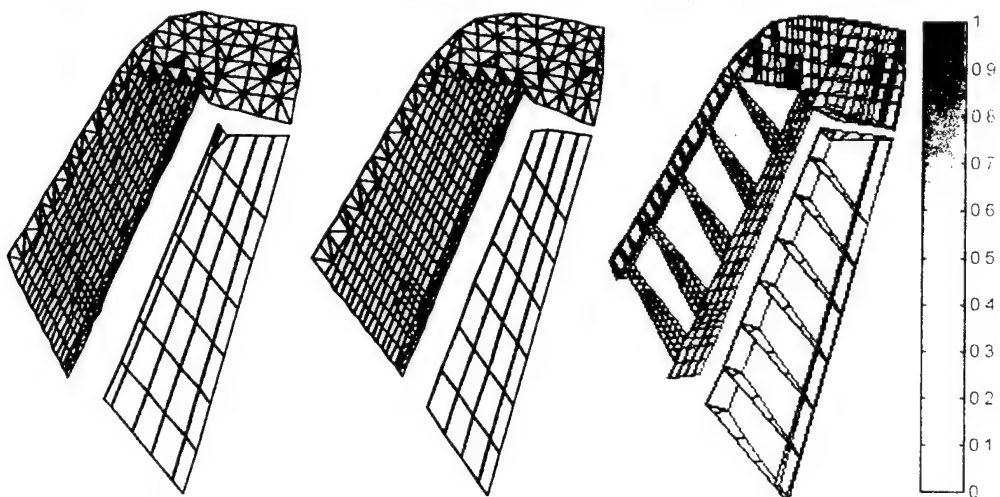


Figure C.1.8 Results by averaging for Case 6c, using Z-function (Not Detected).

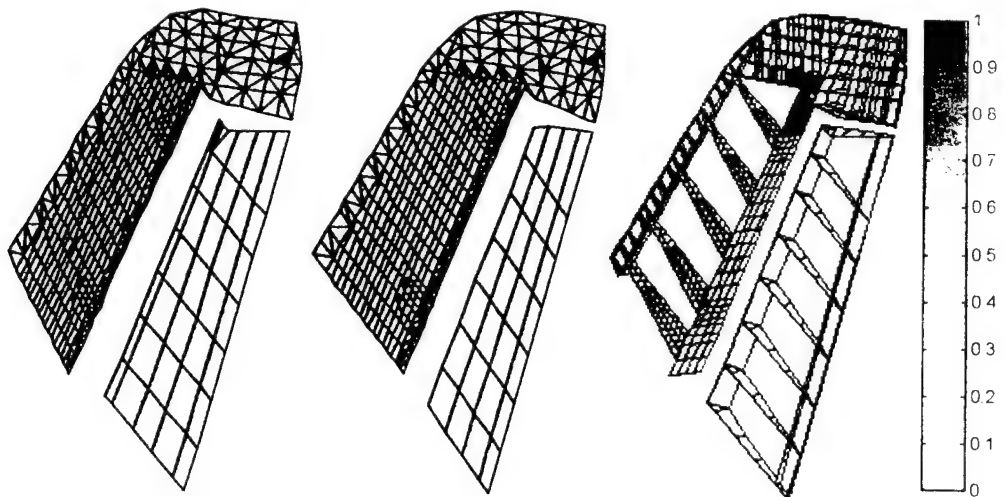


Figure C.1.9 Results by averaging for Case 7b, using Z-function (Detected)

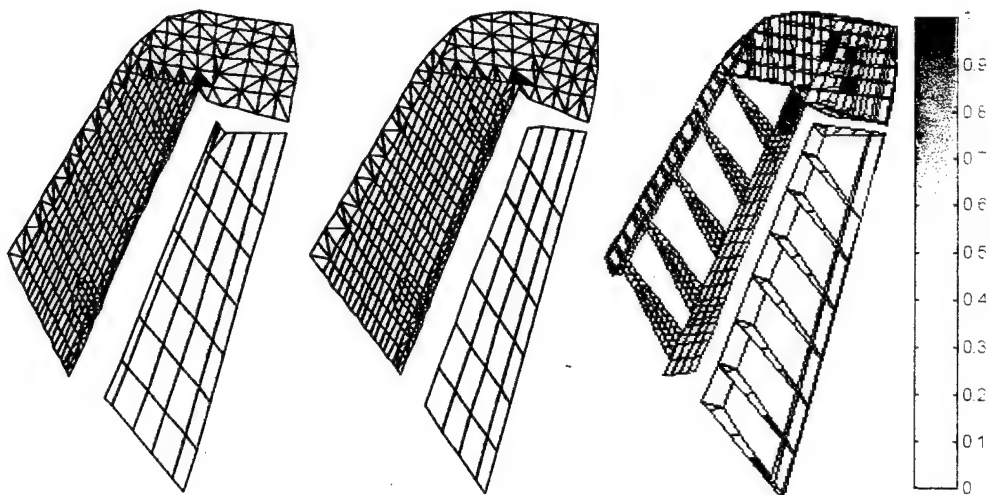


Figure C.1.10 Results by averaging for Case 8f, using Z-function (Detected).

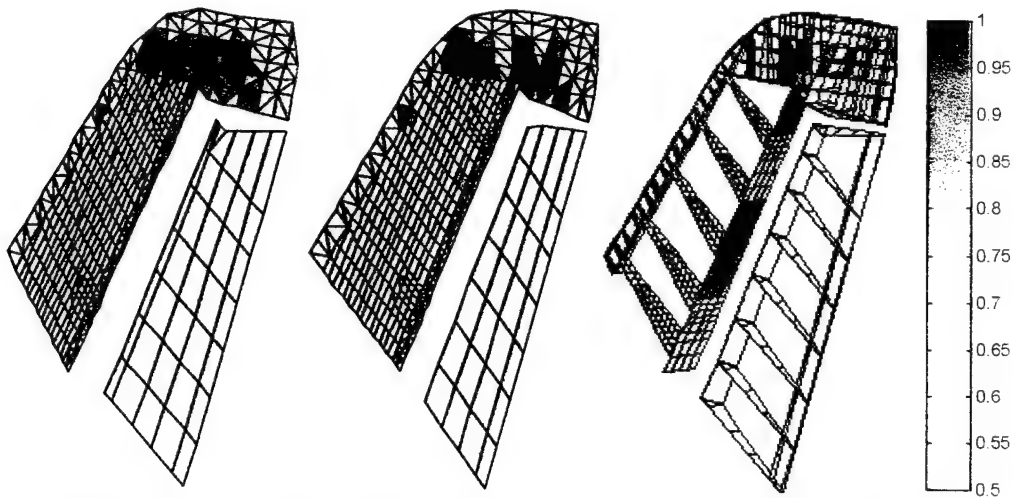


Figure C.2.1 Results by Bayes for Case 4a, using Z-function (Detected).

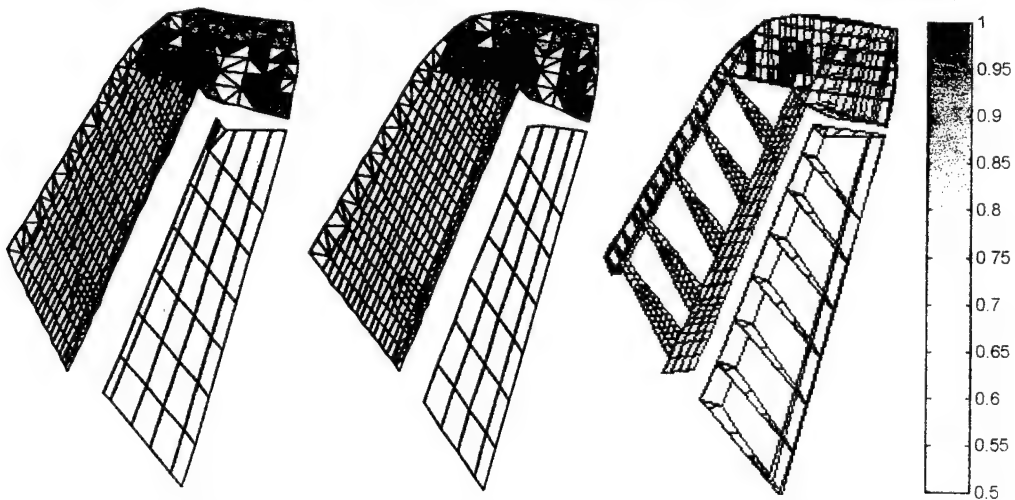


Figure C.2.2 Results by Bayes for Case 4b, using Z-function (Detected).

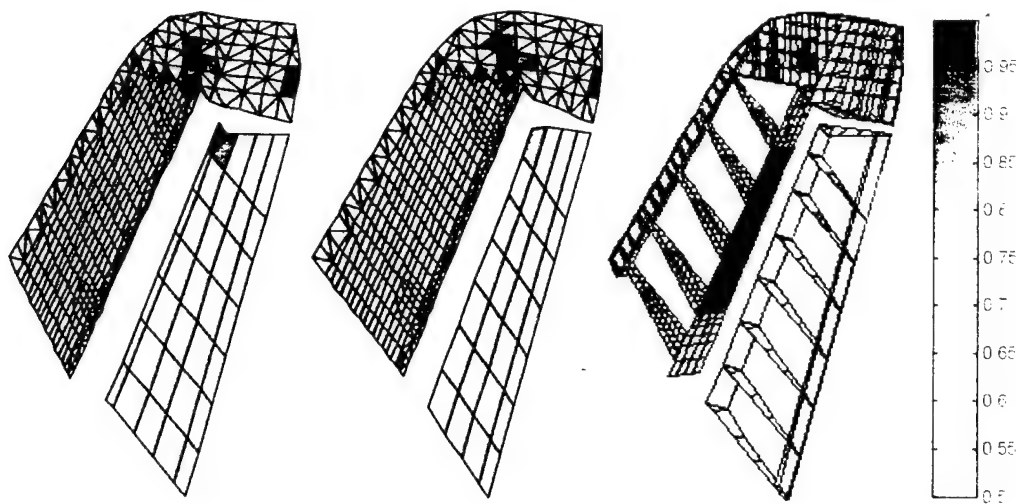


Figure C.2.3 Results by Bayes for Case 4c. using Z-function (Detected).

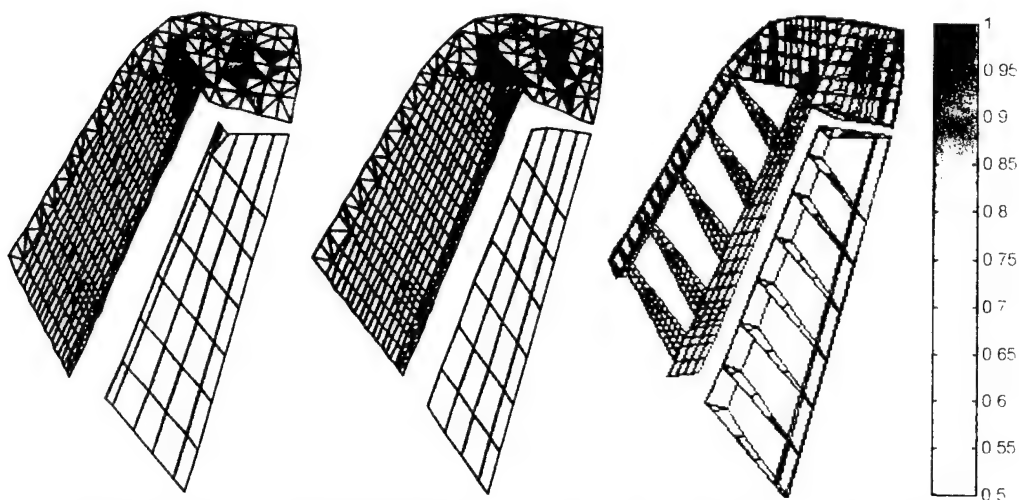


Figure C.2.4 Results by Bayes for Case 5a. using Z-function (Detected).

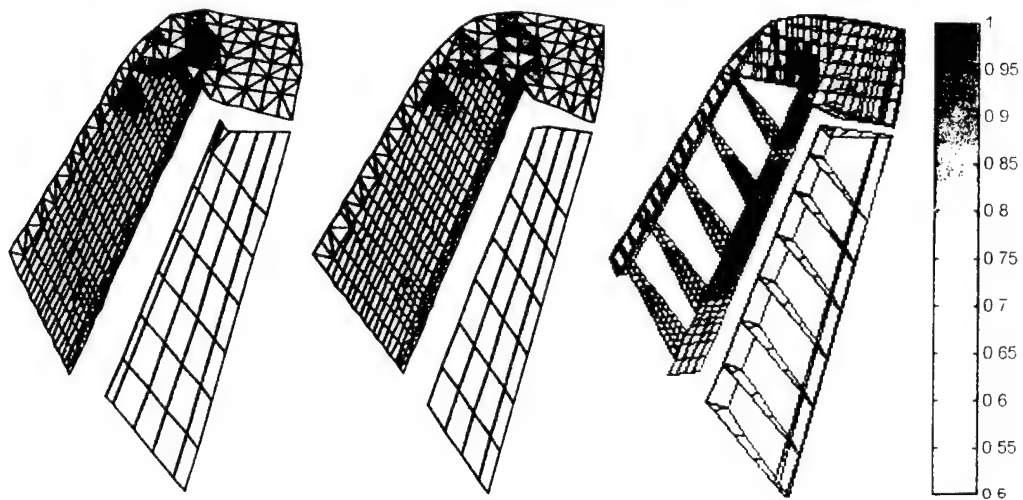


Figure C.2.5 Results by Bayes for Case 5b. using Z-function (Detected).

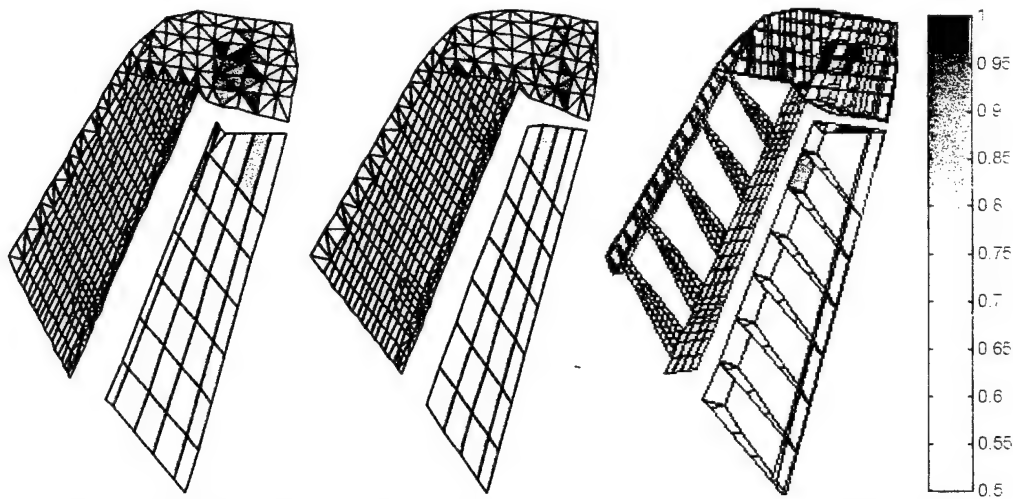


Figure C.2.6 Results by Bayes for Case 5c, using Z-function (Detected).

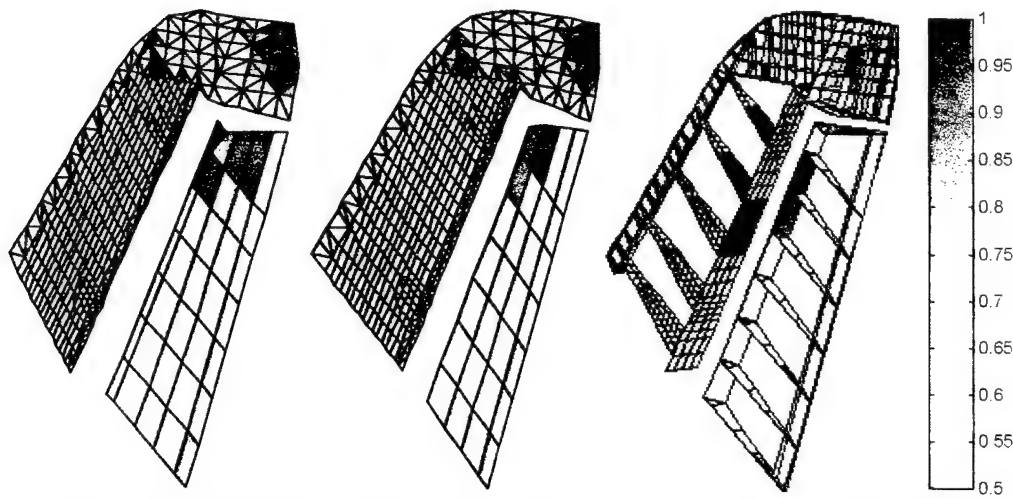


Figure C.2.7 Results by Bayes for Case 5h, using Z-function (Detected).

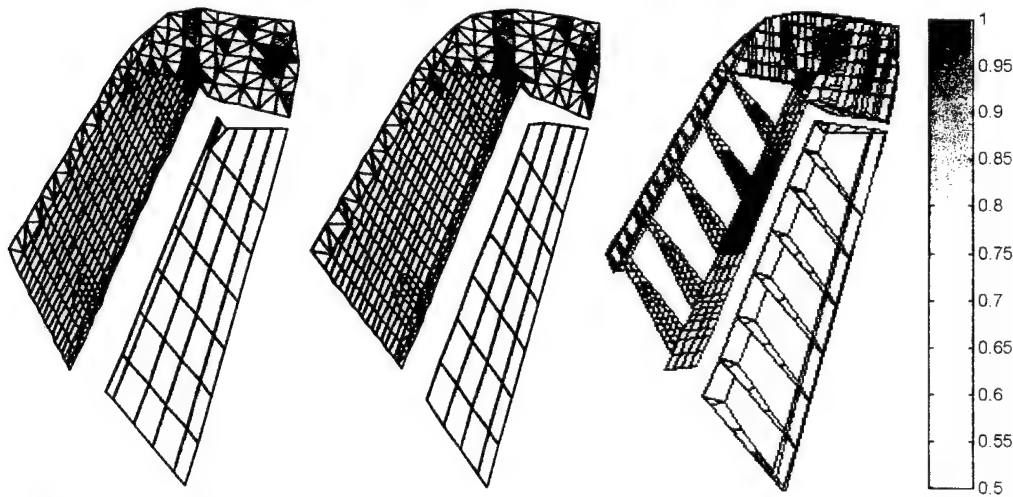


Figure C.2.8 Results by Bayes for Case 6c, using Z-function (Not Detected).

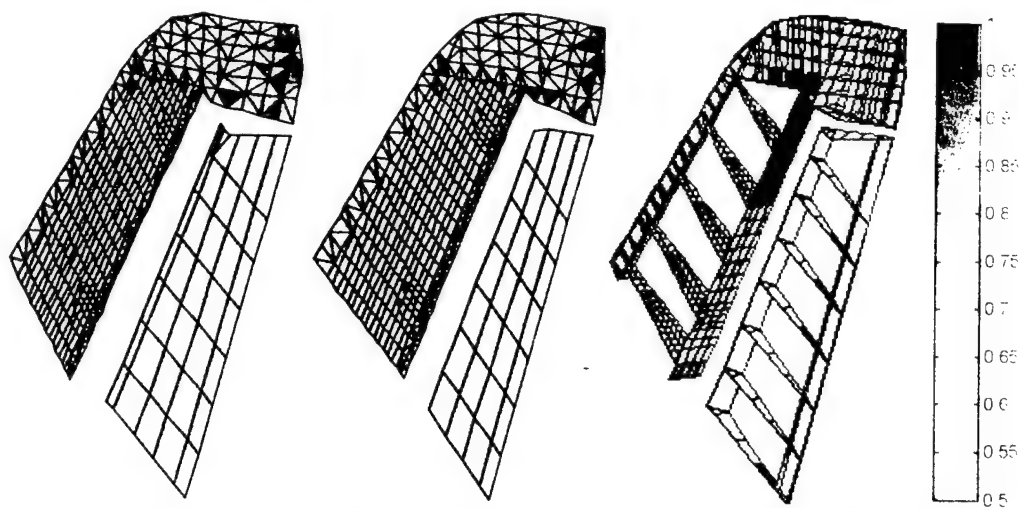


Figure C.2.9 Results by Bayes for Case 7b, using Z-function (Detected).

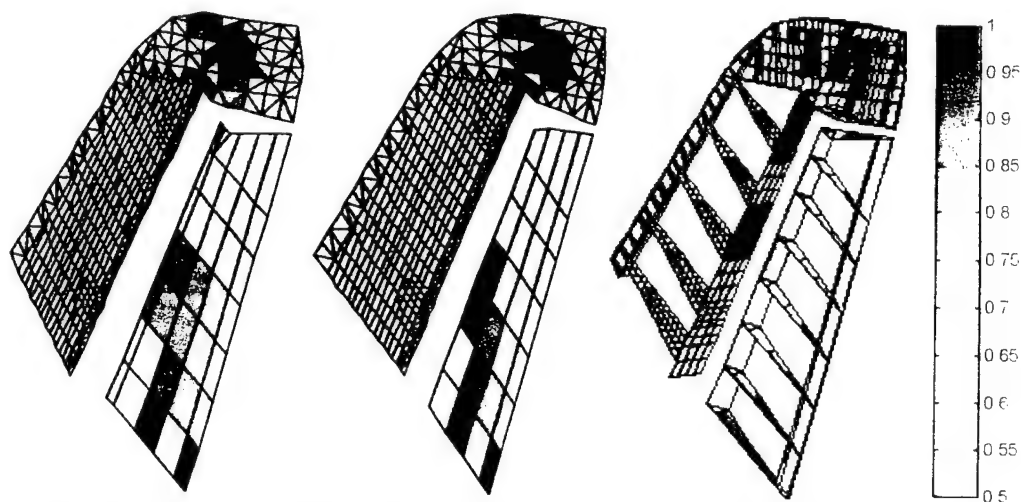


Figure C.2.10 Results by Bayes for Case 8f, using Z-function (Detected).

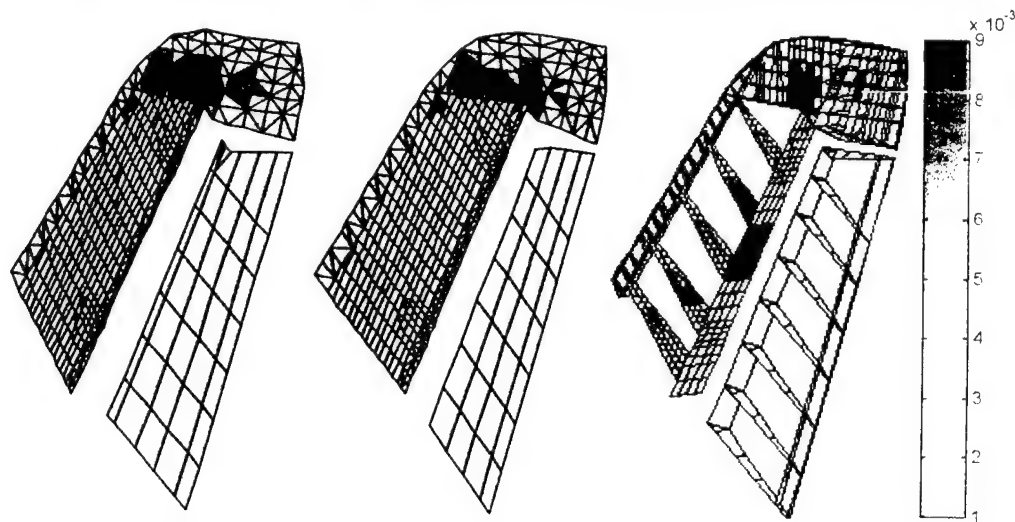


Figure C.3.1 Results by PMF for Case 4a, using Z-function (Detected).



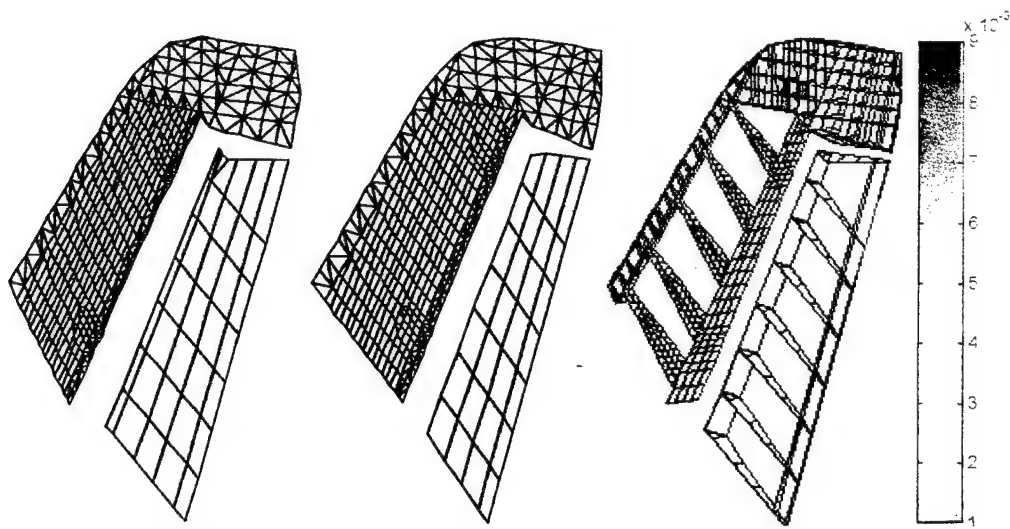


Figure C.3.2 Results by PMF for Case 4b, using Z-function (Detected).

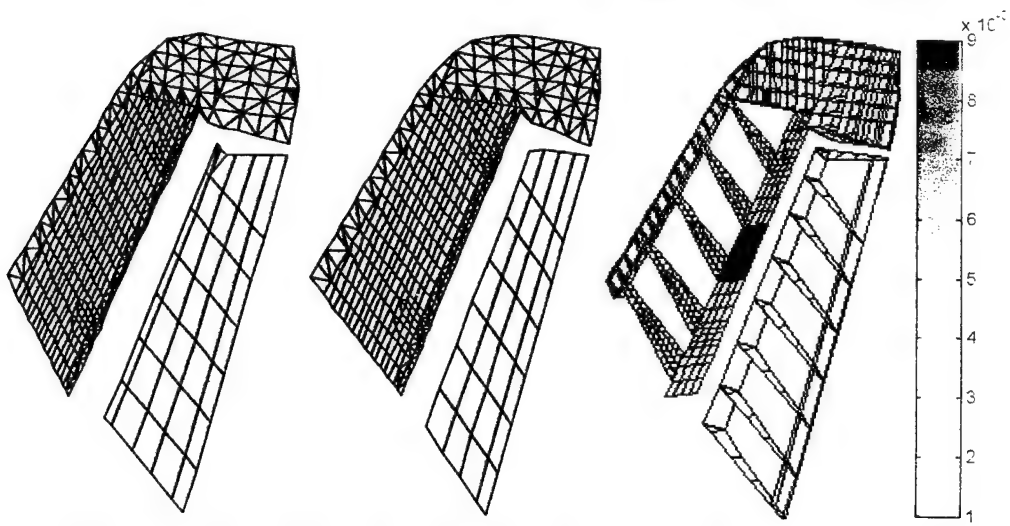


Figure C.3.3 Results by PMF for Case 4c, using Z-function (Detected).

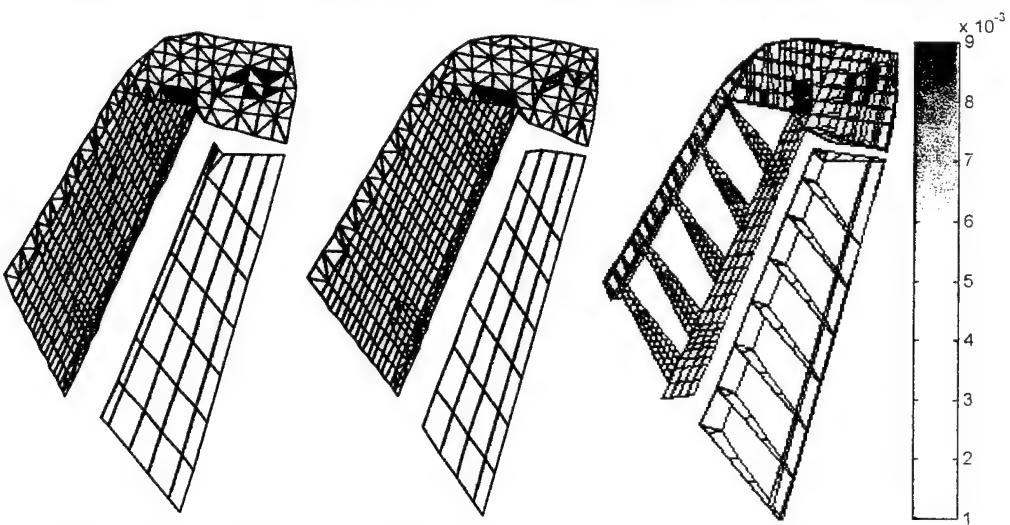


Figure C.3.4 Results by PMF for Case 5a, using Z-function (Detected).



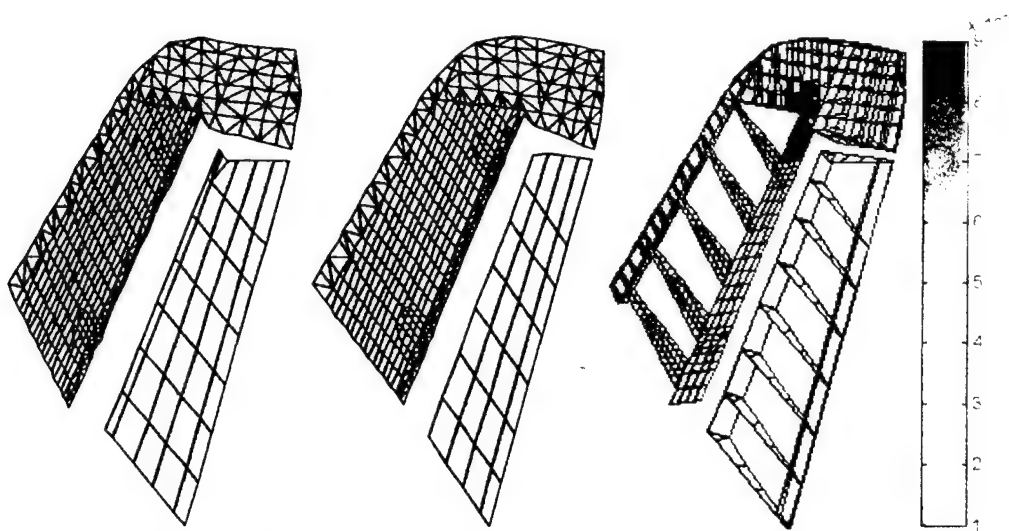


Figure C.3.5 Results by PMF for Case 5b, using Z-function (Detected).

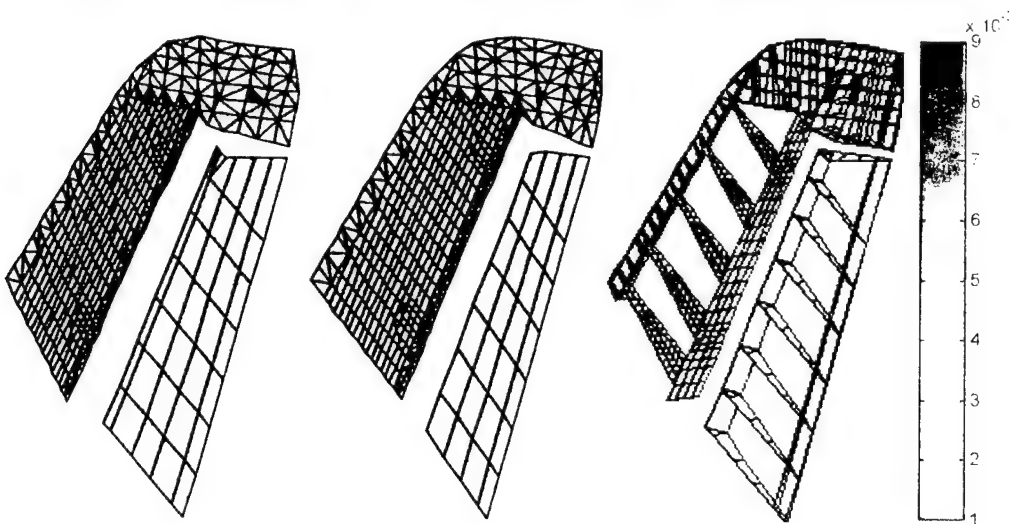


Figure C.3.6 Results by PMF for Case 5c, using Z-function (Detected).

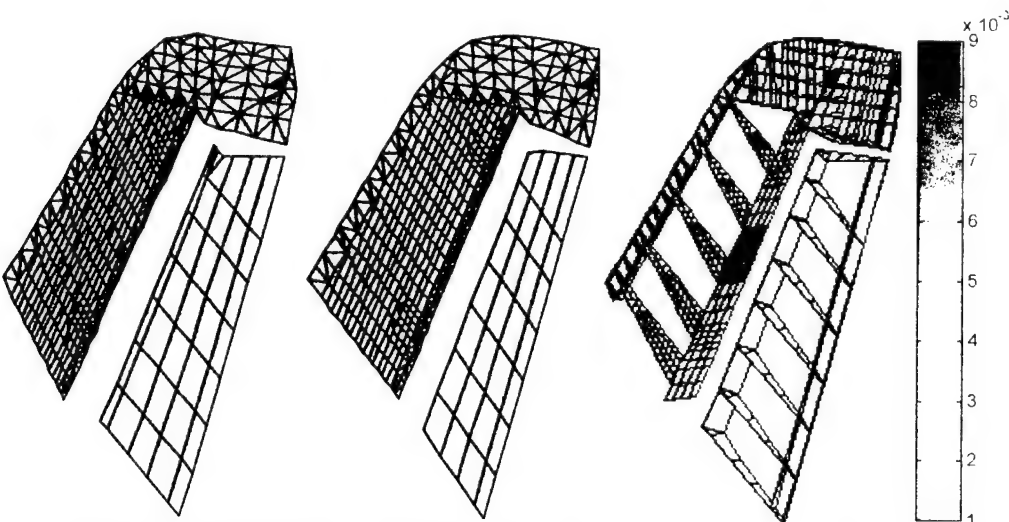


Figure C.3.7 Results by PMF for Case 5h, using Z-function (Detected).

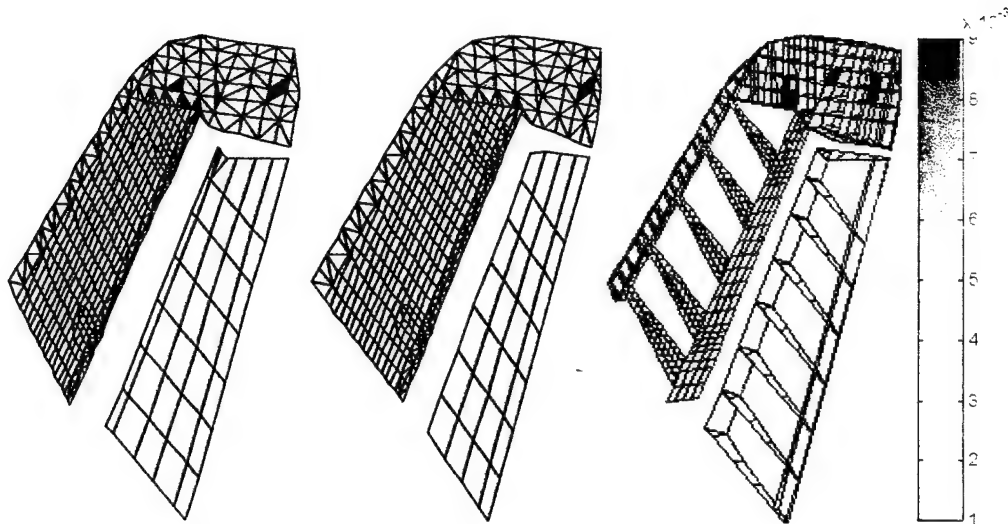


Figure C.3.8 Results by PMF for Case 6c, using Z-function (Not Detected).

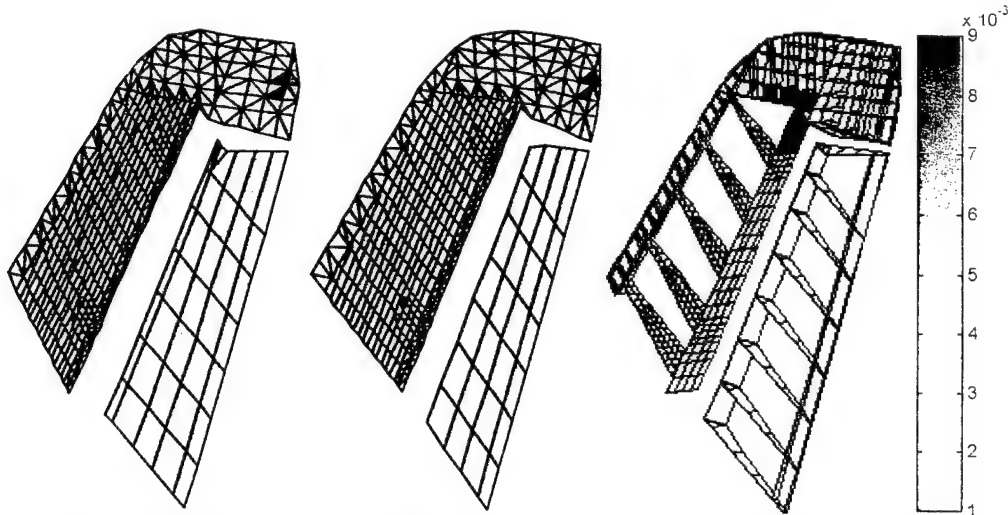


Figure C.3.9 Results by PMF for Case 7b, using Z-function (Detected).

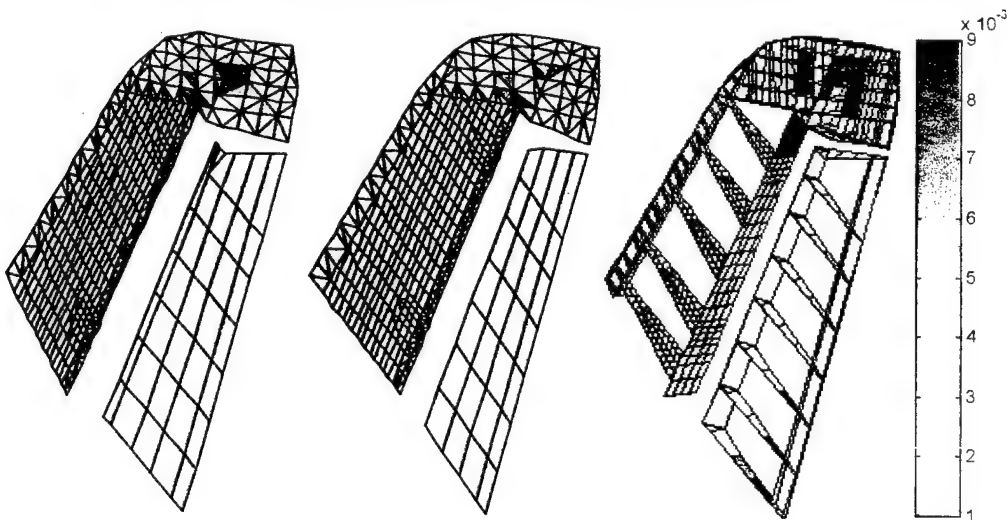


Figure C.3.10 Results by PMF for Case 8f, using Z-function (Detected).

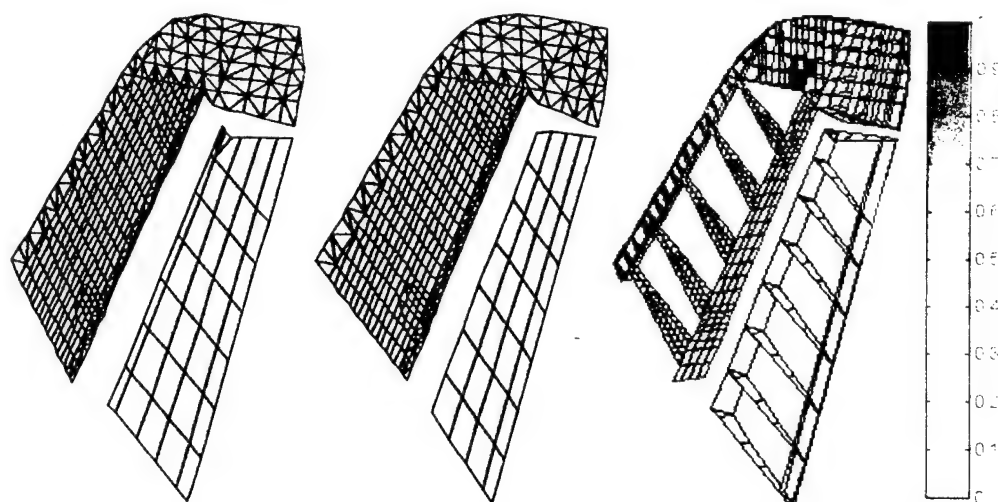


Figure C.4.1 Results by averaging for Case 4a, not using Z-function (Detected).

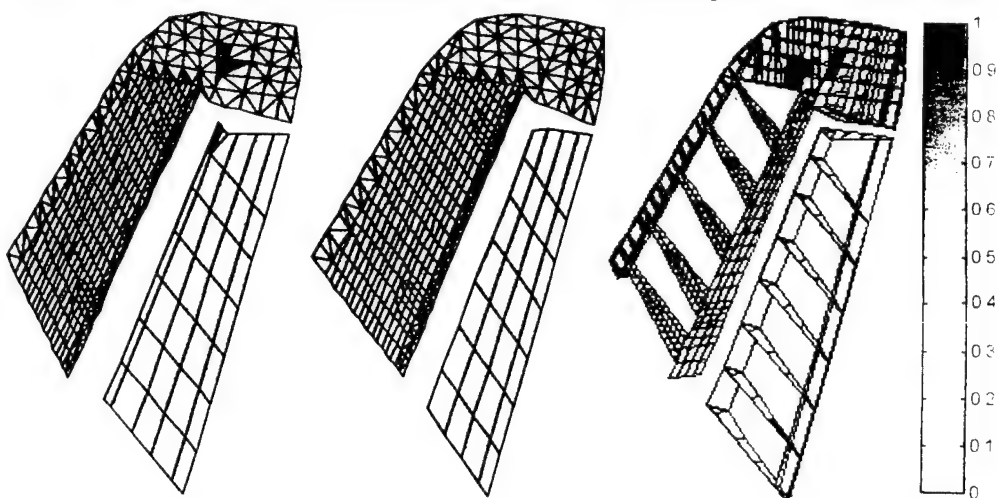


Figure C.4.2 Results by averaging for Case 4b, not using Z-function (Detected).

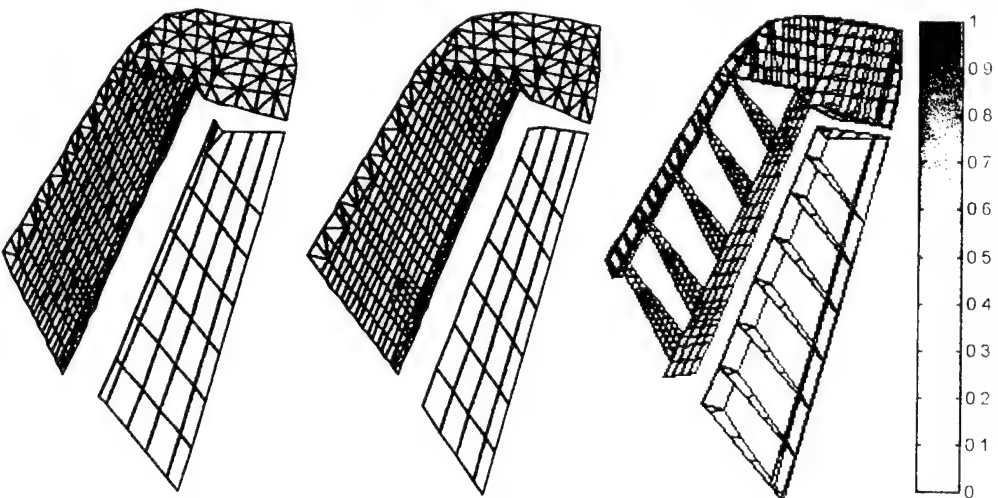


Figure C.4.3 Results by averaging for Case 4c, not using Z-function (Detected).

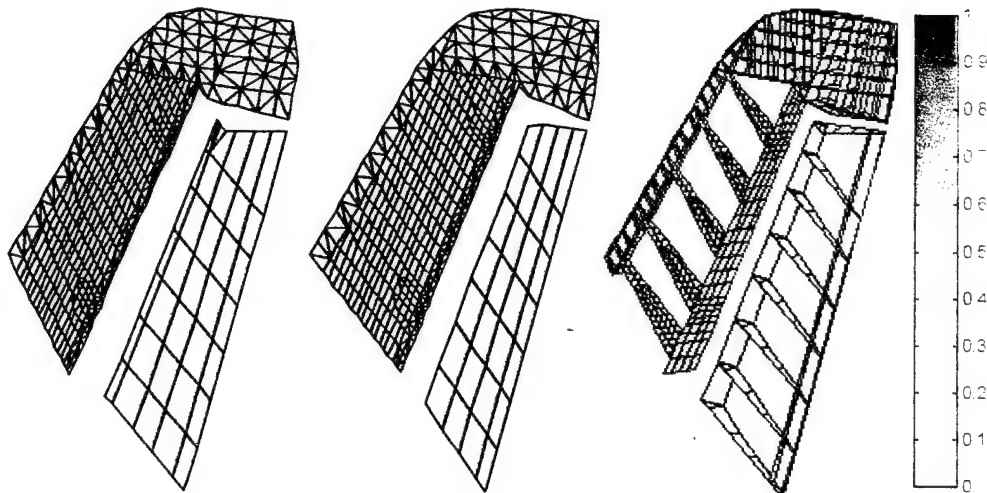


Figure C.4.4 Results by averaging for Case 5a, not using Z-function (Detected).

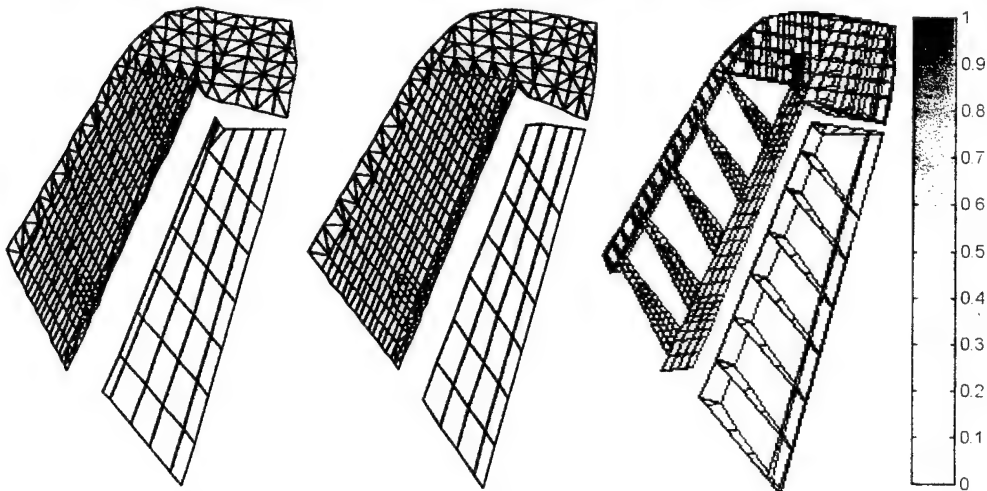


Figure C.4.5 Results by averaging for Case 5b, not using Z-function (Detected).

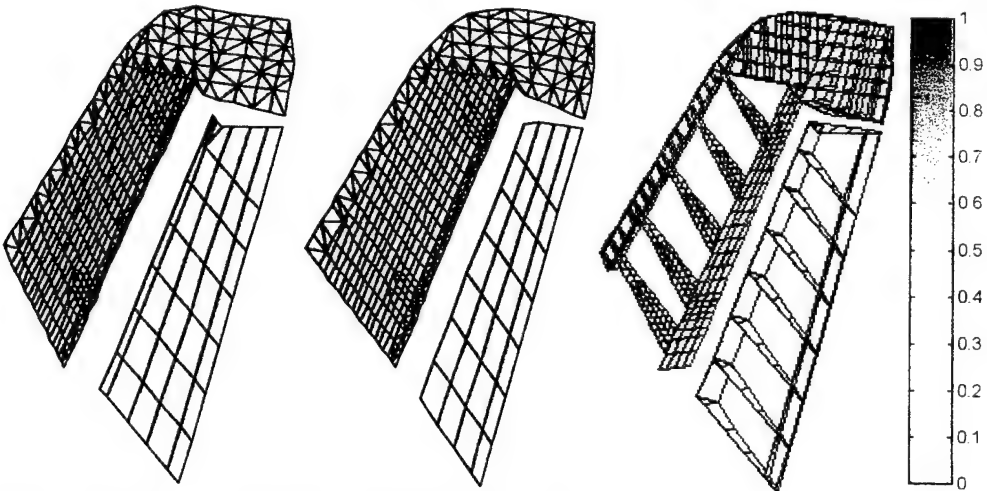


Figure C.4.6 Results by averaging for Case 5c, not using Z-function (Detected).

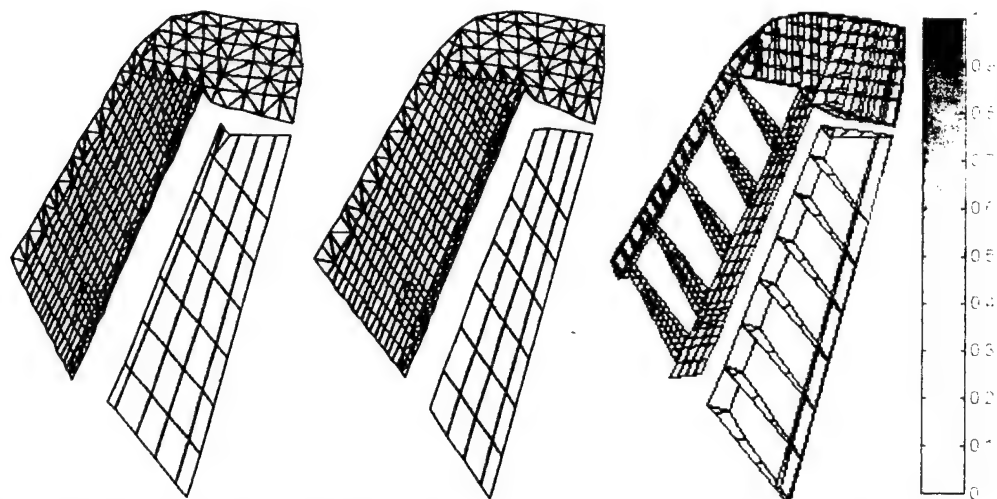


Figure C.4.7 Results by averaging for Case 5h, not using Z-function (Not Detected).

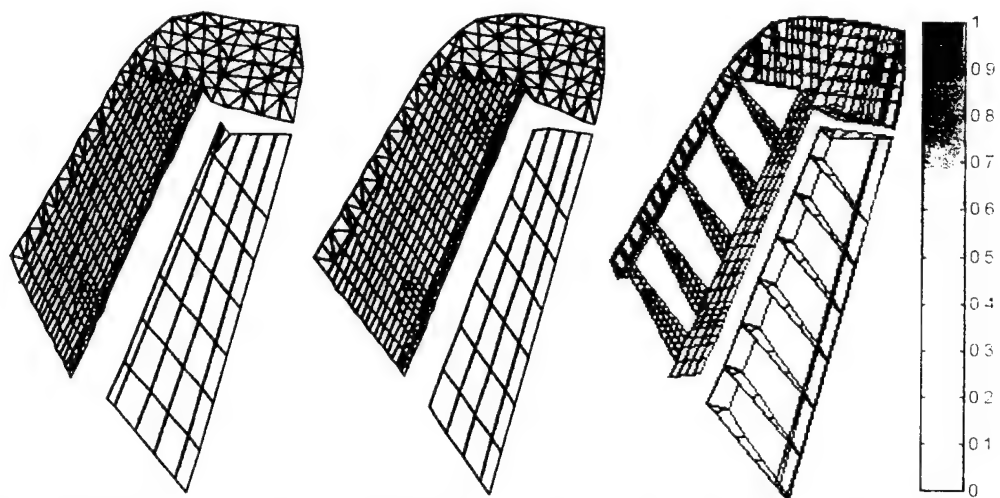


Figure C.4.8 Results by averaging for Case 6c, not using Z-function (Not Detected).

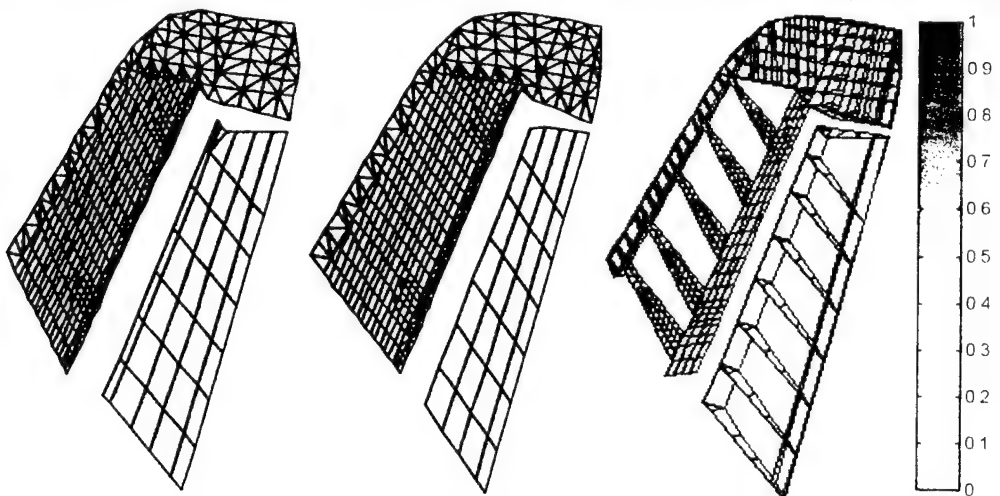


Figure C.4.9 Results by averaging for Case 7b, not using Z-function (Not Detected).

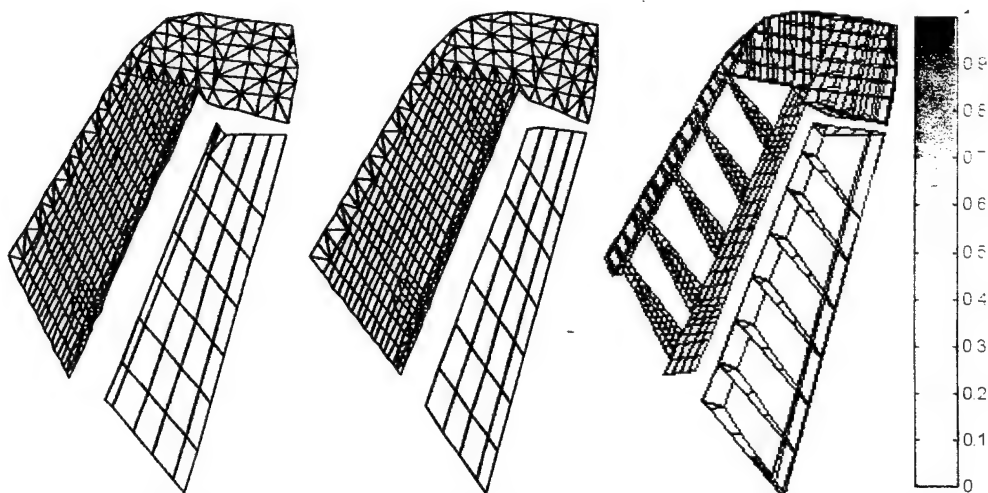


Figure C.4.10 Results by averaging for Case 8f, not using Z-function (Detected).

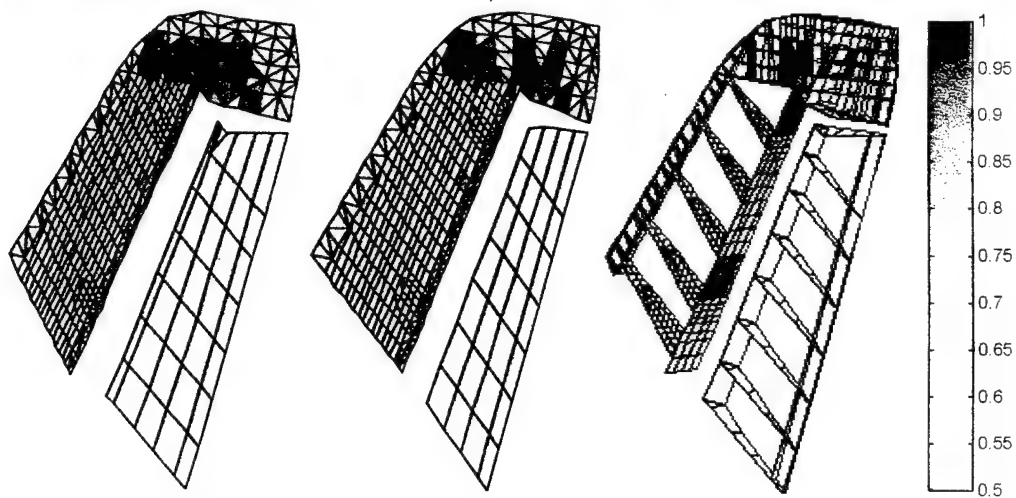


Figure C.5.1 Results by Bayes for Case 4a, not using Z-function (Detected).

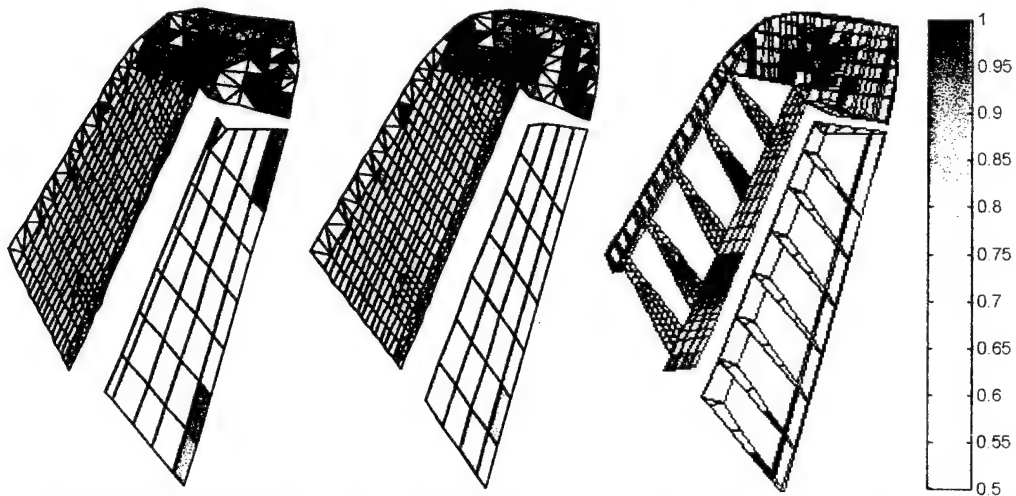


Figure C.5.2 Results by Bayes for Case 4b, not using Z-function (Detected).



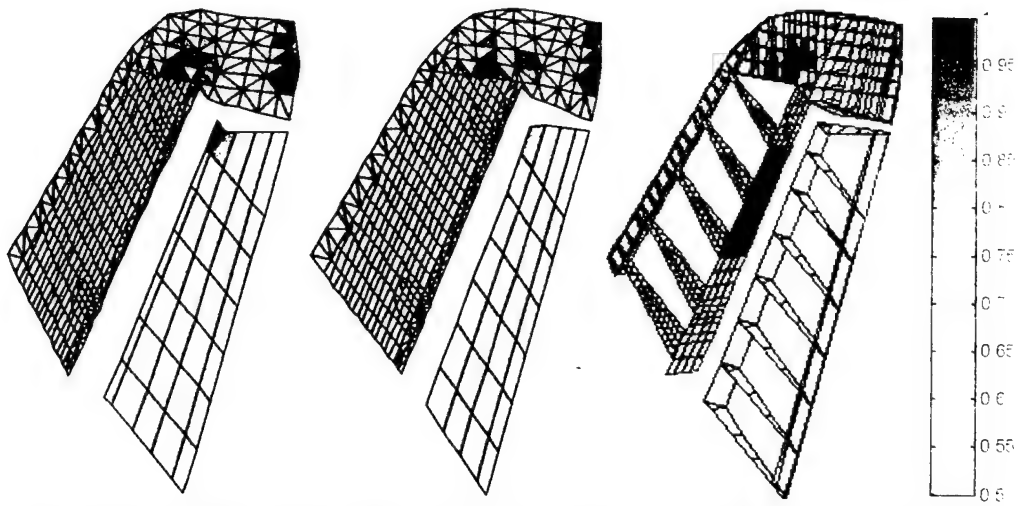


Figure C.5.3 Results by Bayes for Case 4c, not using Z-function (Detected).

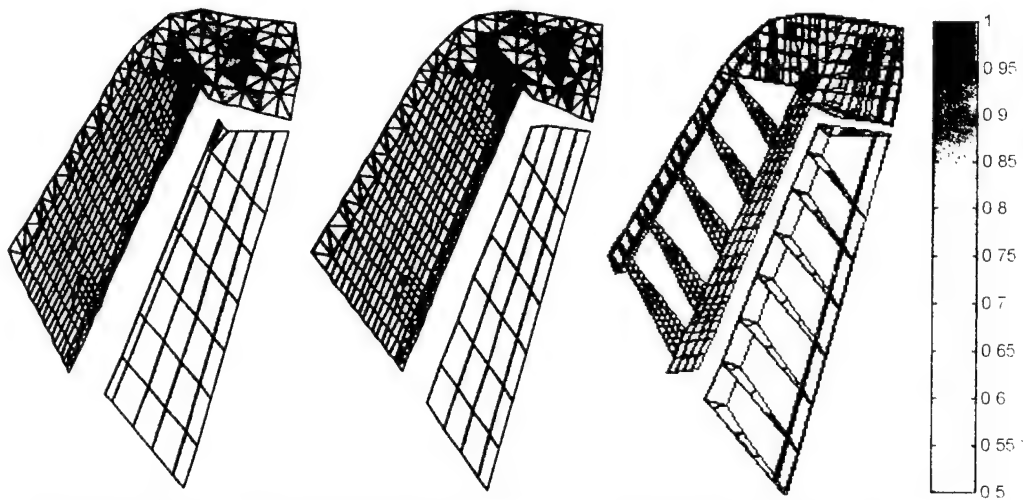


Figure C.5.4 Results by Bayes for Case 5a, not using Z-function (Detected).

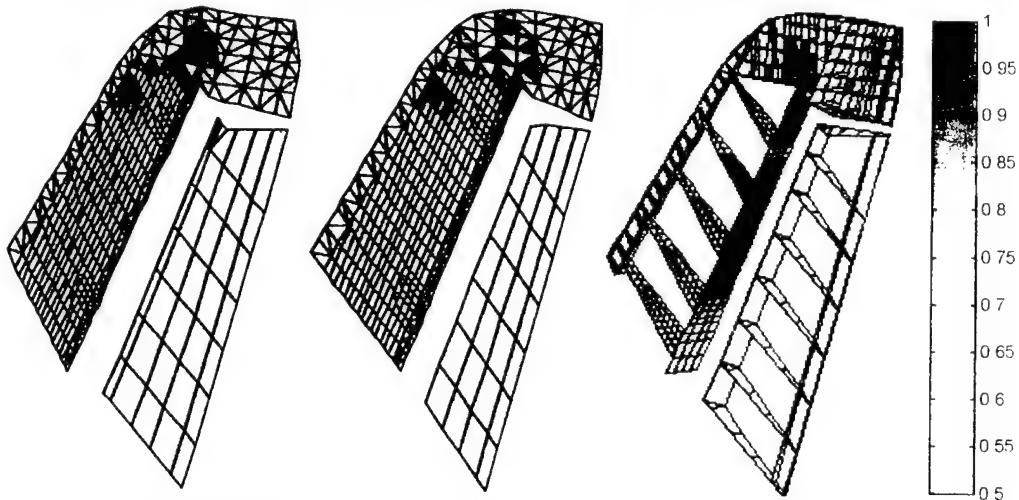


Figure C.5.5 Results by Bayes for Case 5b, not using Z-function (Detected).

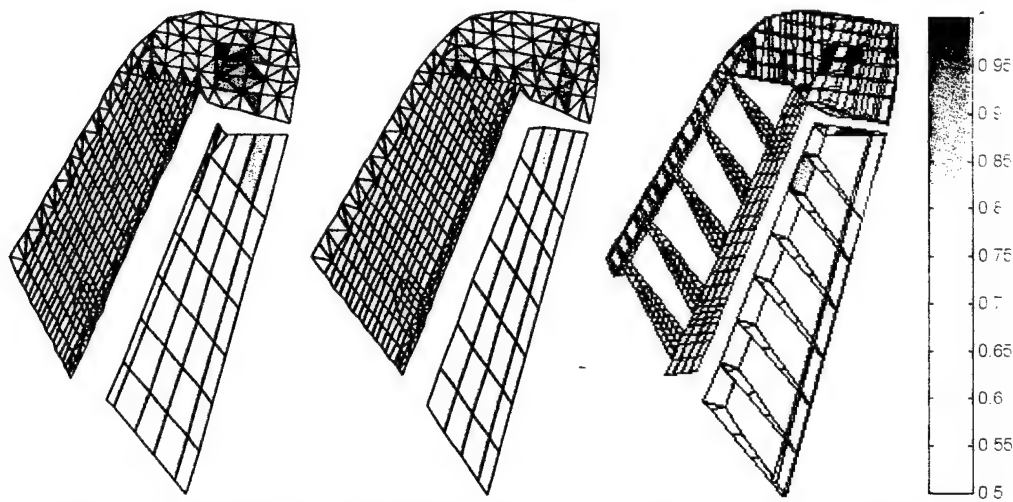


Figure C.5.6 Results by Bayes for Case 5c, not using Z-function (Detected).

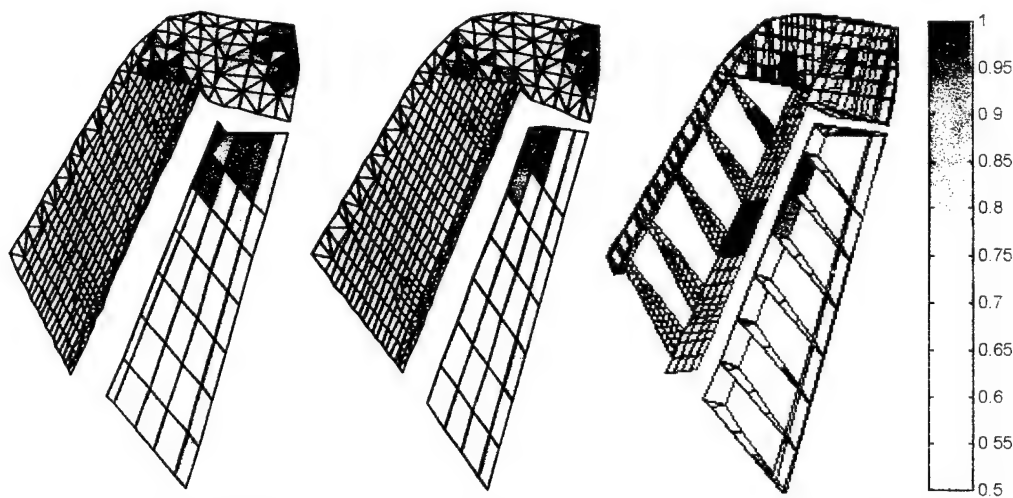


Figure C.5.7 Results by Bayes for Case 5h, not using Z-function (Detected).

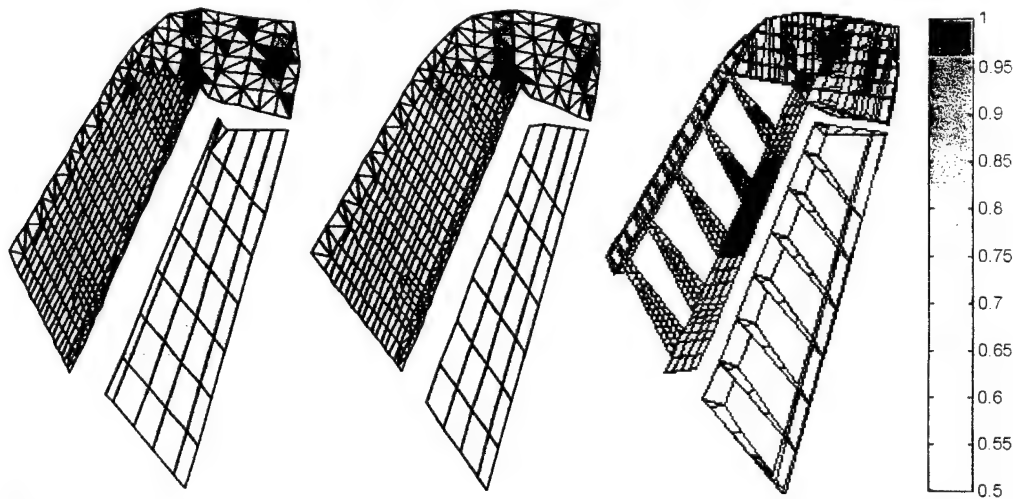


Figure C.5.8 Results by Bayes for Case 6c, not using Z-function (Not Detected).



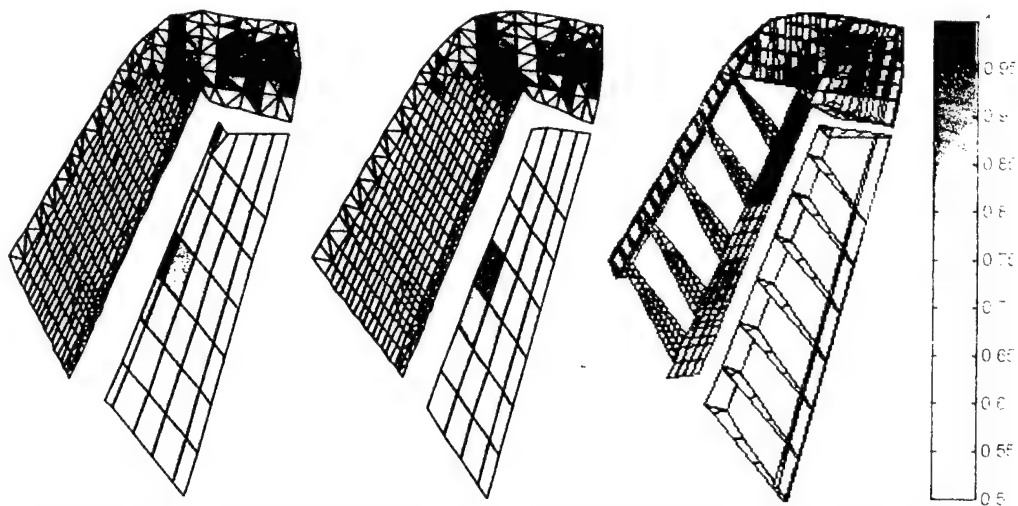


Figure C.5.9 Results by Bayes for Case 7b, not using Z-function (Detected).

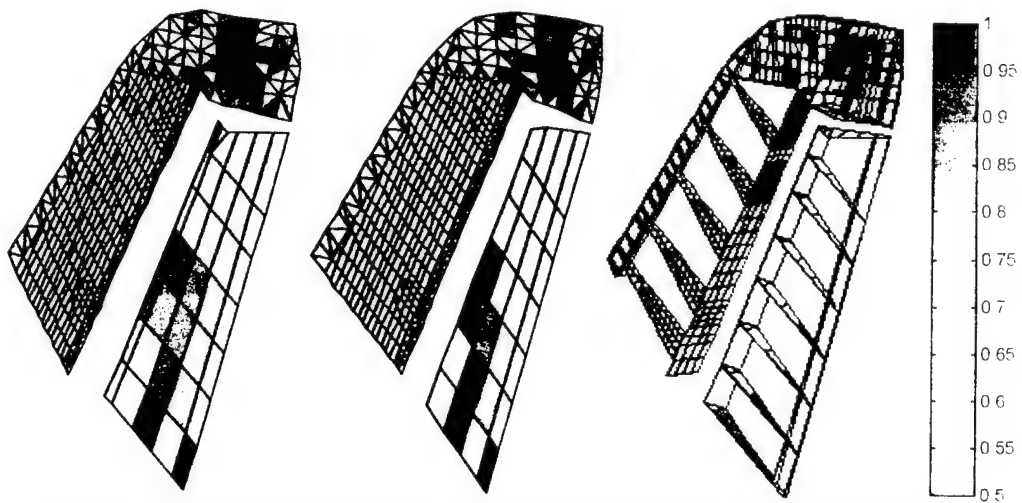


Figure C.5.10 Results by Bayes for Case 8f, not using Z-function (Detected).

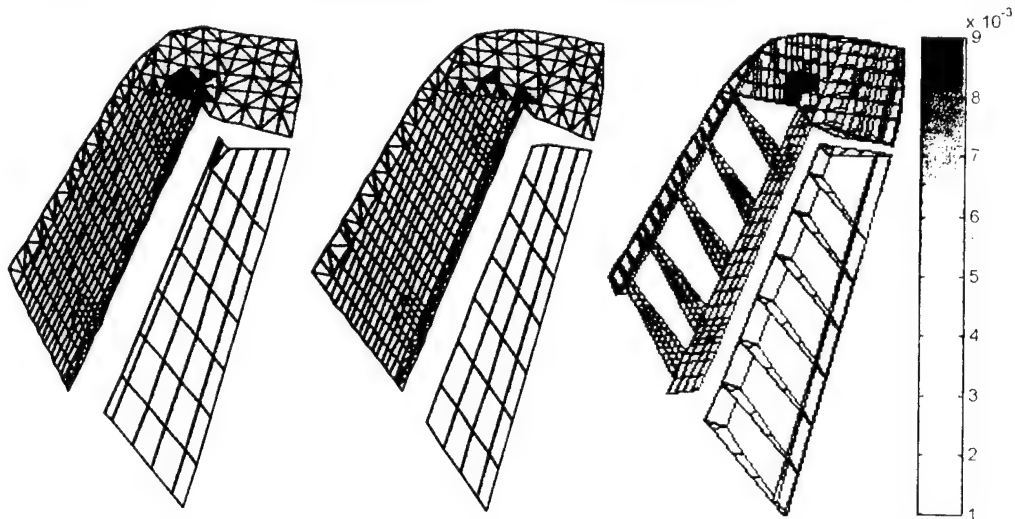


Figure C.6.1 Results by PMF for Case 4a, not using Z-function (Detected).

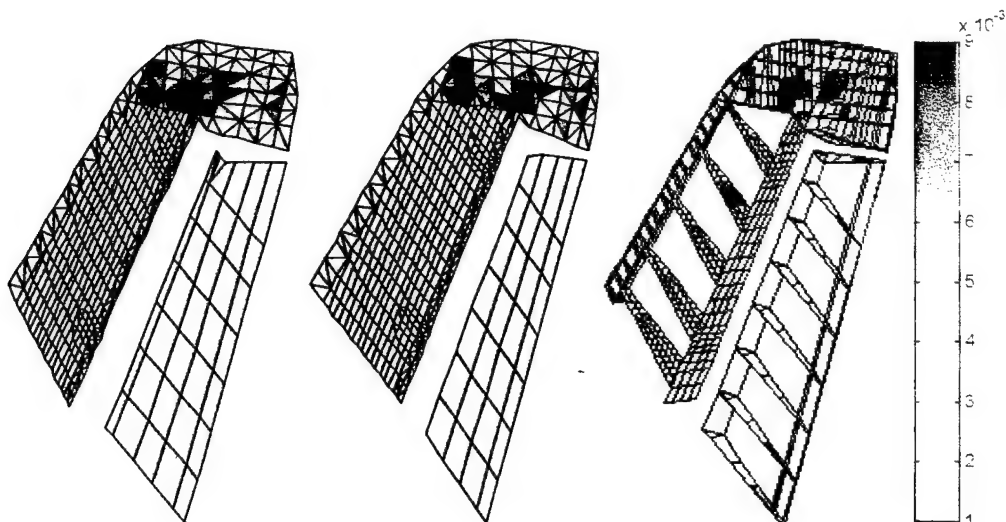


Figure C.6.2 Results by PMF for Case 4b, not using Z-function (Detected).

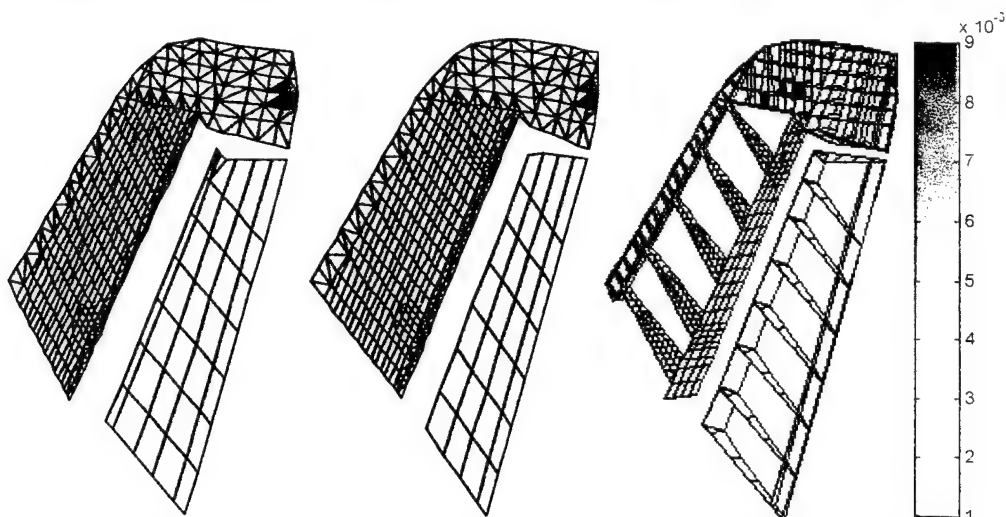


Figure C.6.3 Results by PMF for Case 4c, not using Z-function (Detected).

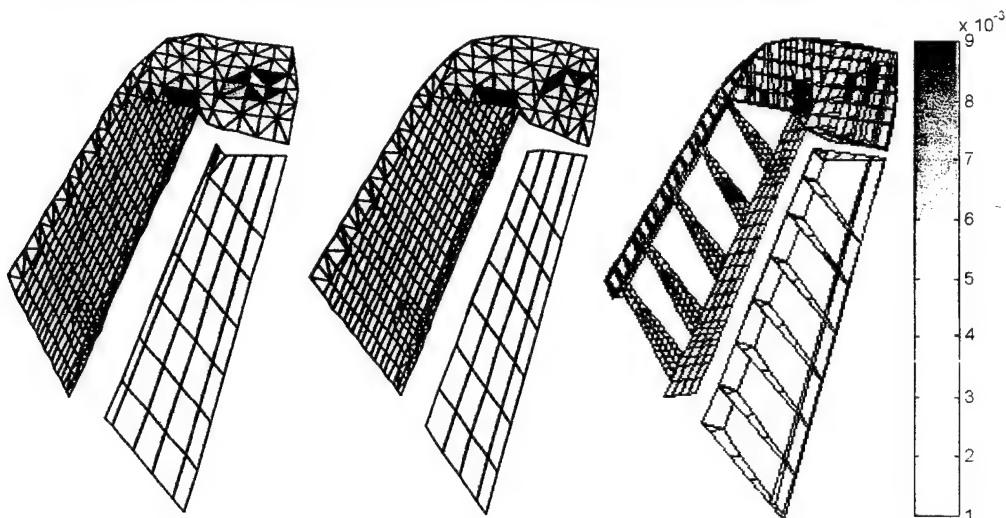


Figure C.6.4 Results by PMF for Case 5a, not using Z-function (Detected).

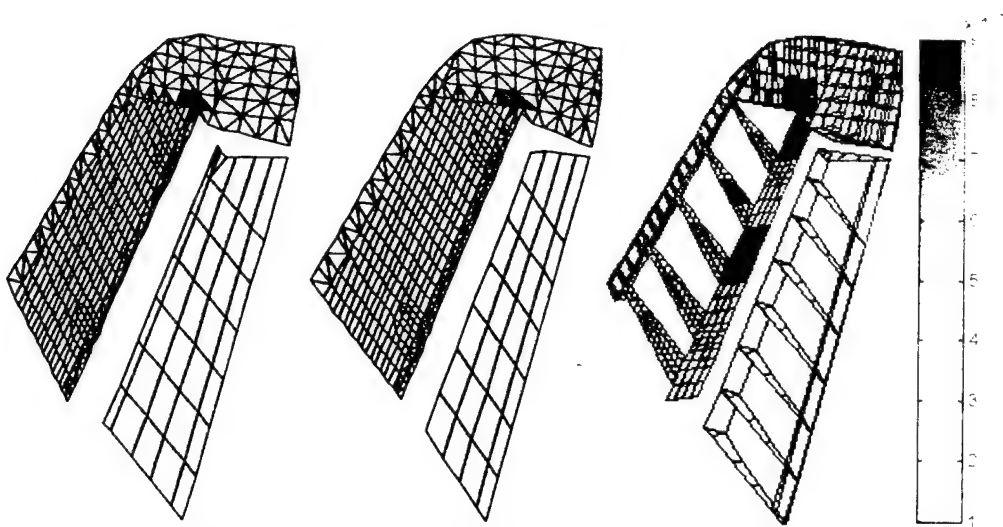


Figure C.6.5 Results by PMF for Case 5b. not using Z-function (Detected).

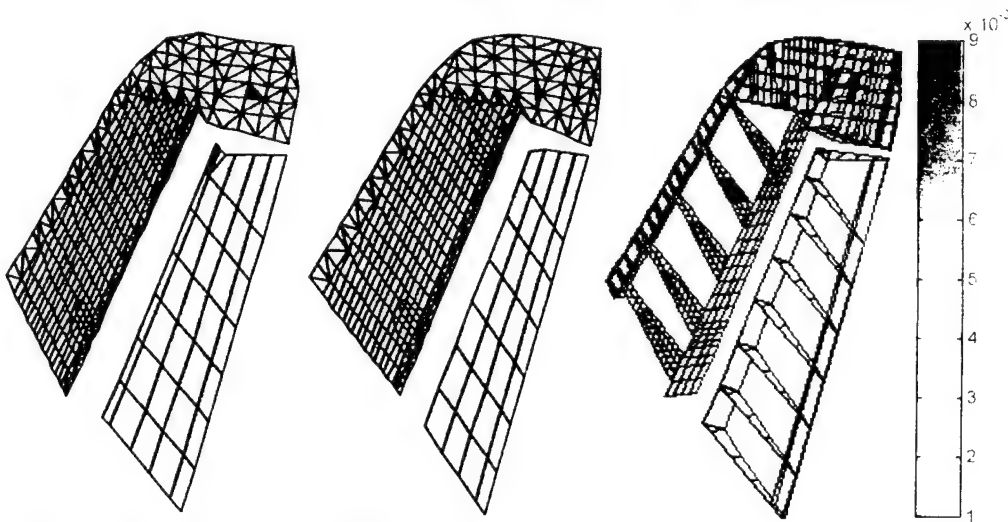


Figure C.6.6 Results by PMF for Case 5c. not using Z-function (Detected).

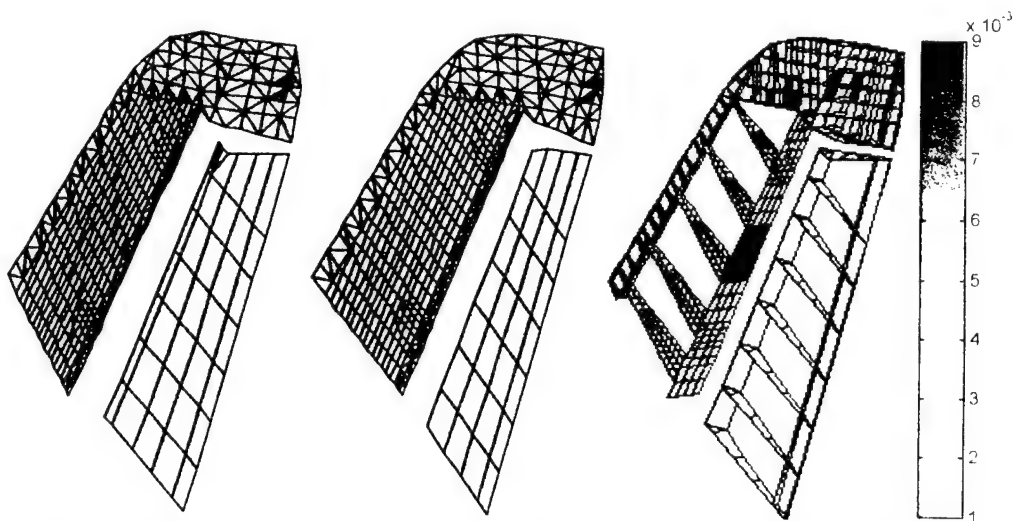


Figure C.6.7 Results by PMF for Case 5h. not using Z-function (Detected).

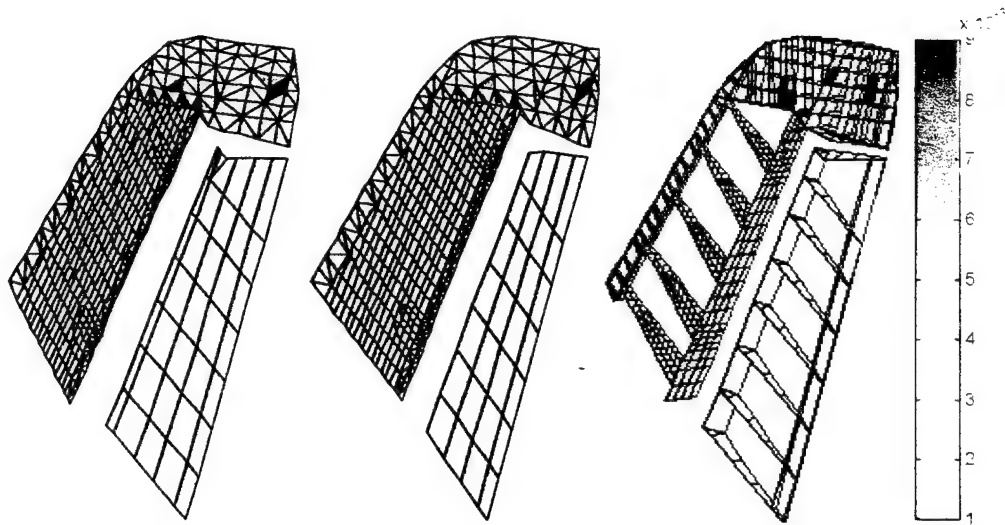


Figure C.6.8 Results by PMF for Case 6c, not using Z-function (Not Detected).

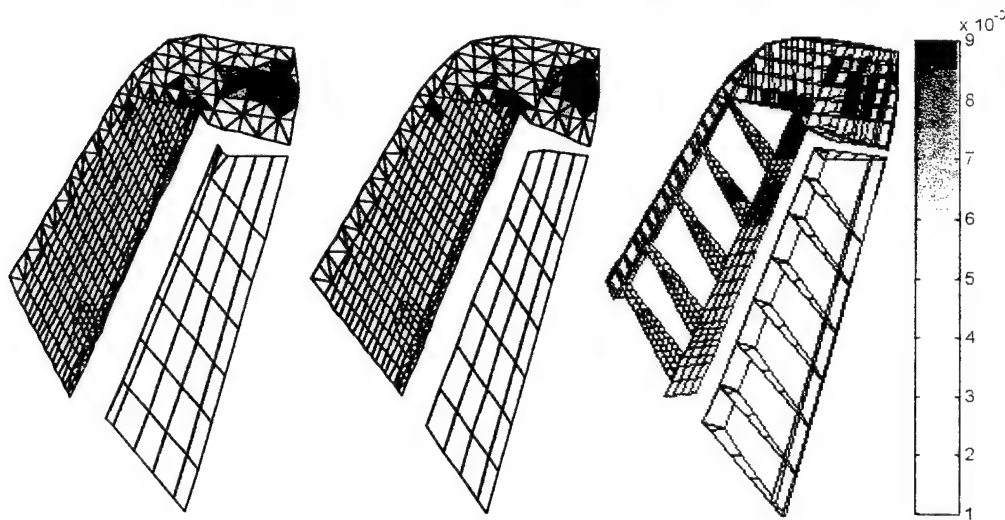


Figure C.6.9 Results by PMF for Case 7b, not using Z-function (Detected).

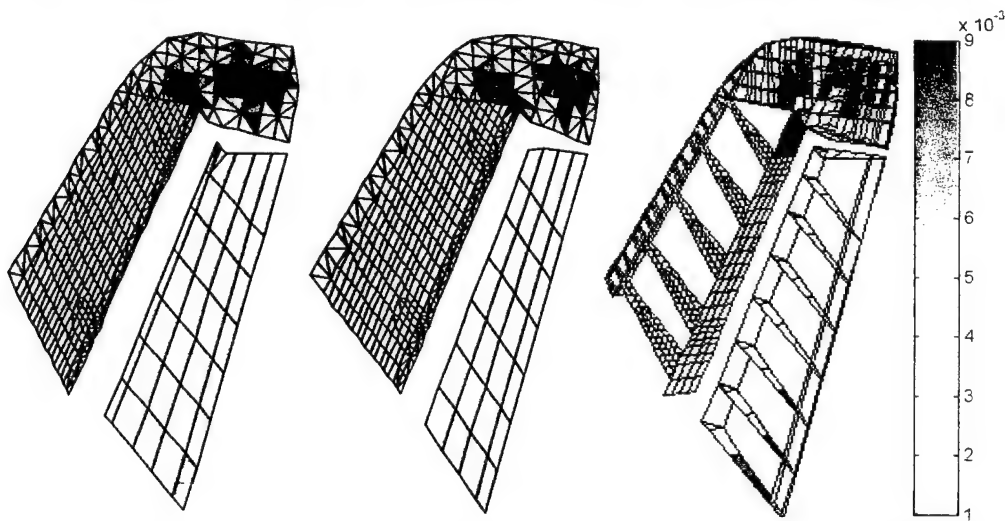


Figure C.6.10 Results by PMF for Case 8f, not using Z-function (Detected).

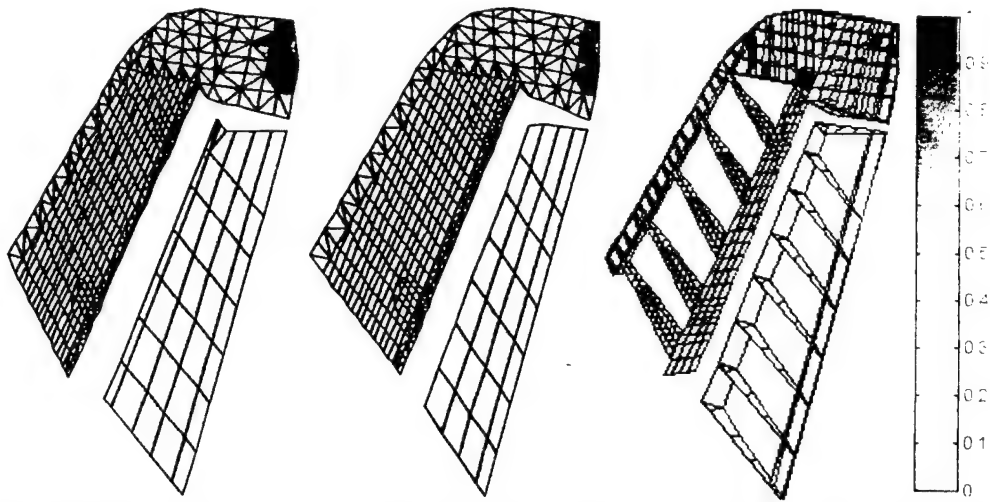


Figure C.7.1 Results by averaging for Case 5h. using Z-function and FEM updated (Detected).

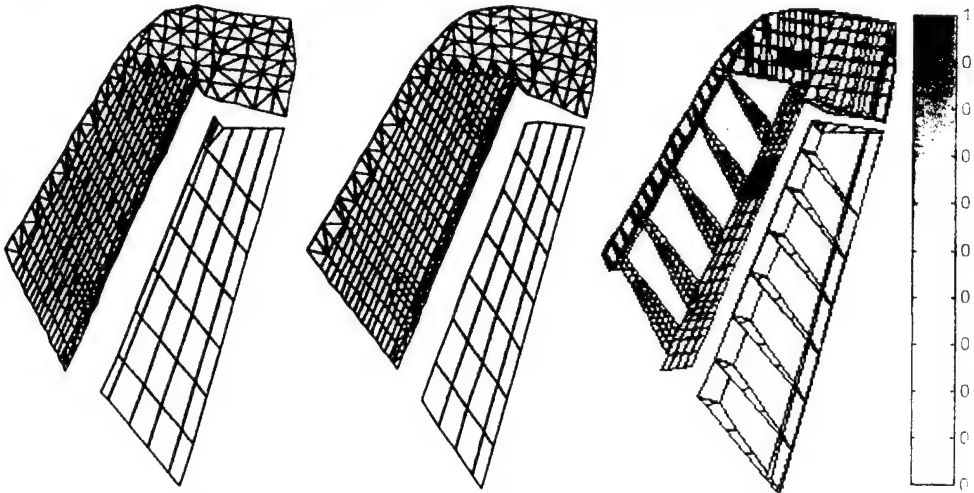


Figure C.7.2 Results by averaging for Case 6c. using Z-function and FEM updated (Not Detected).

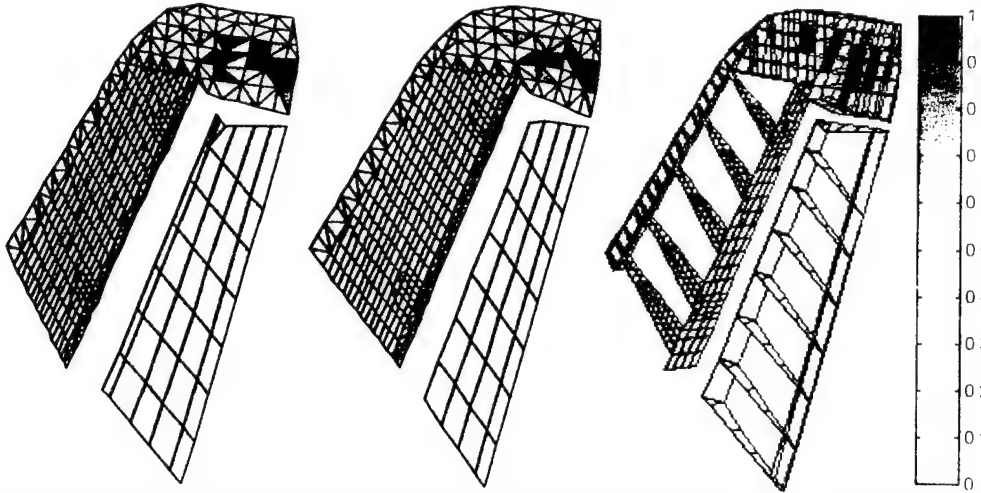


Figure C.7.3 Results by averaging for Case 7b. using Z-function and FEM updated (Not Detected).

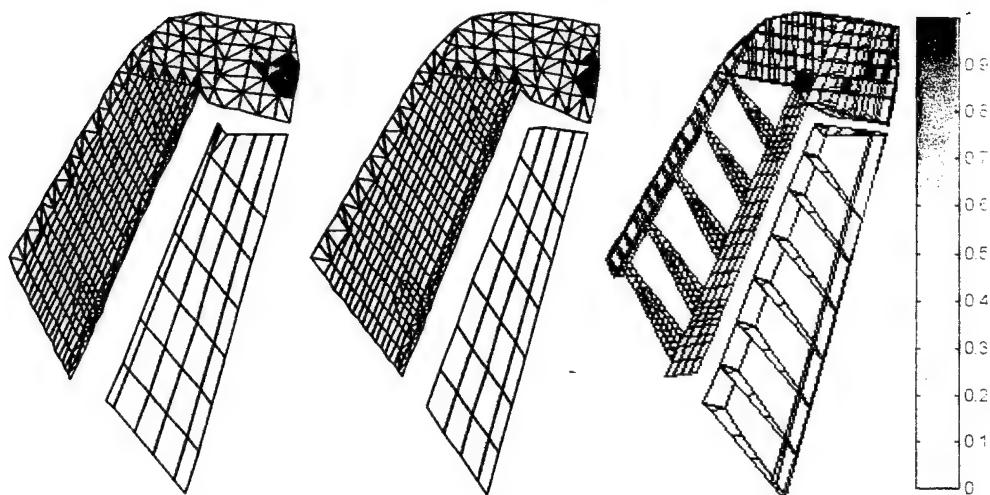


Figure C.7.4 Results by averaging for Case 8f, using Z-function and FEM updated (Detected).

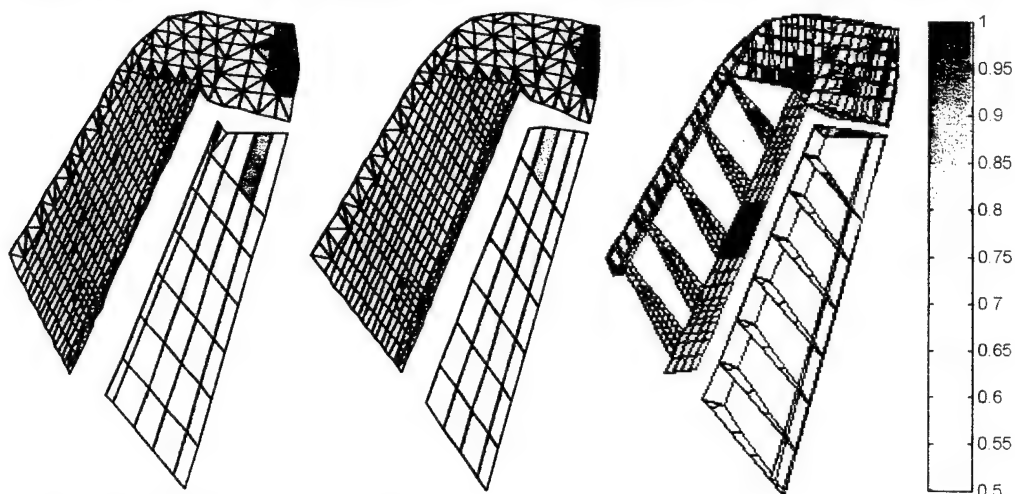


Figure C.8.1 Results by Bayes for Case 5h, using Z-function and FEM updated (Detected).

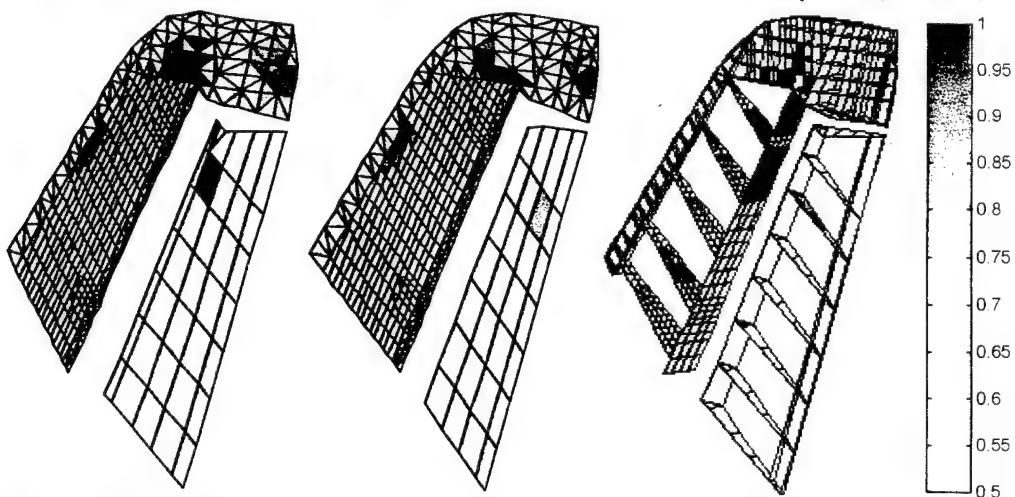


Figure C.8.2 Results by Bayes for Case 6c, using Z-function and FEM updated (Not Detected).

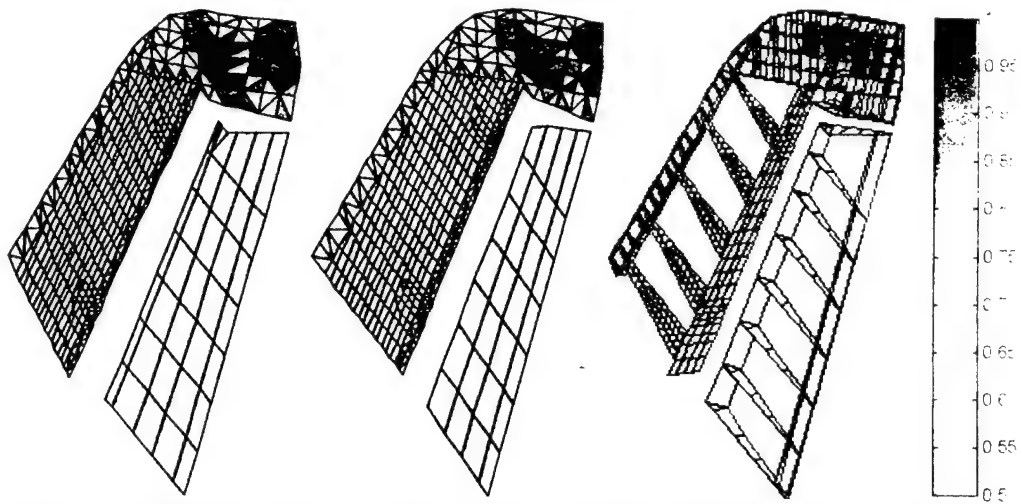


Figure C.8.3 Results by Bayes for Case 7b. using Z-function and FEM updated (Not Detected).

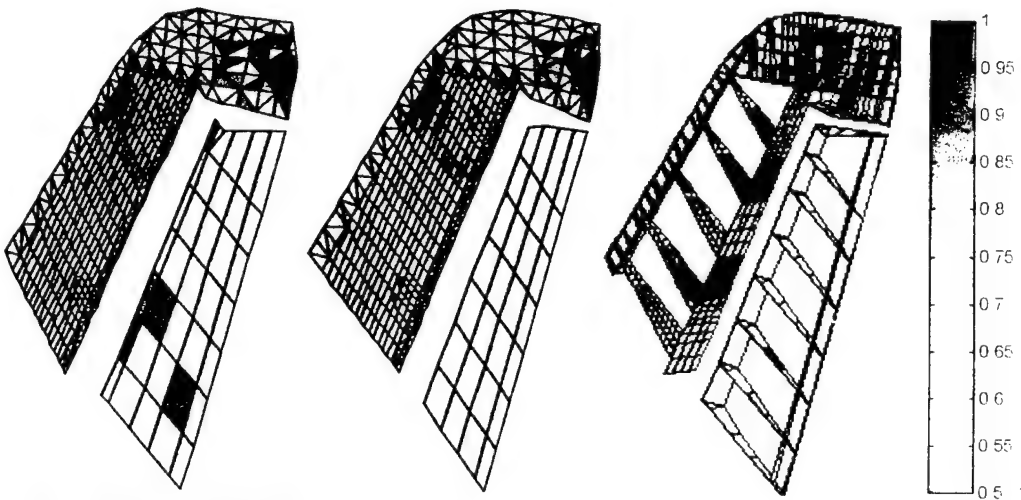


Figure C.8.4 Results by Bayes for Case 8f. using Z-function and FEM updated (Detected).

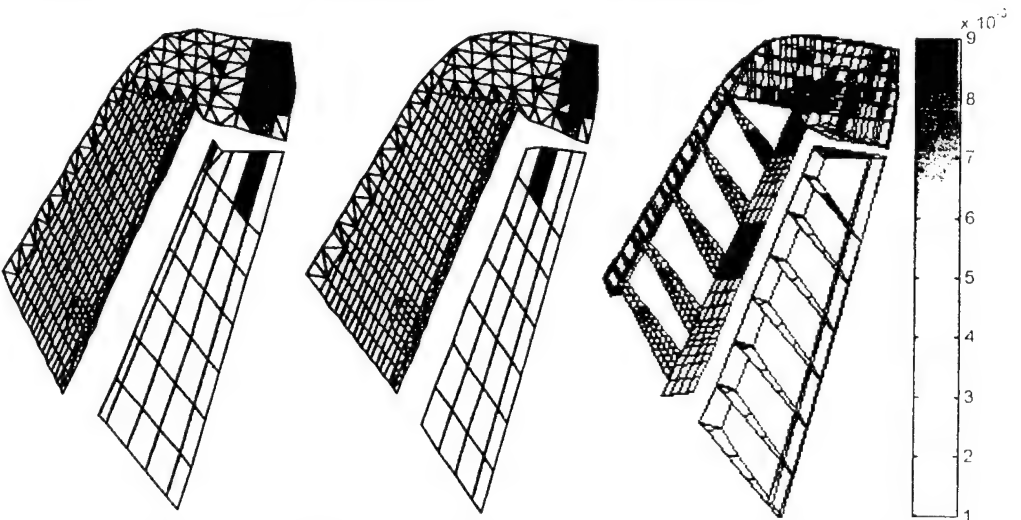


Figure C.9.1 Results by PMF for Case 5h. using Z-function and FEM updated (Detected).



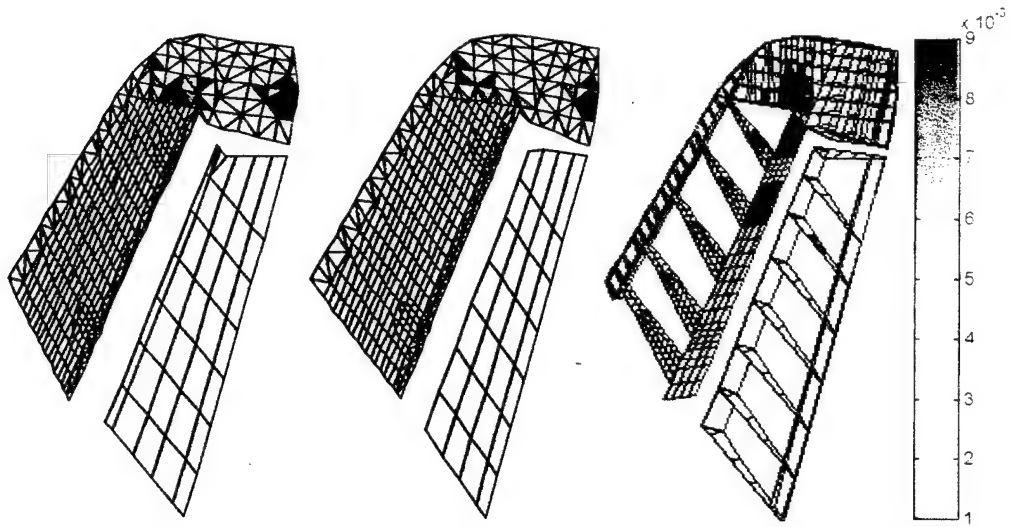


Figure C.9.2 Results by PMF for Case 6c. using Z-function and FEM updated (Not Detected).

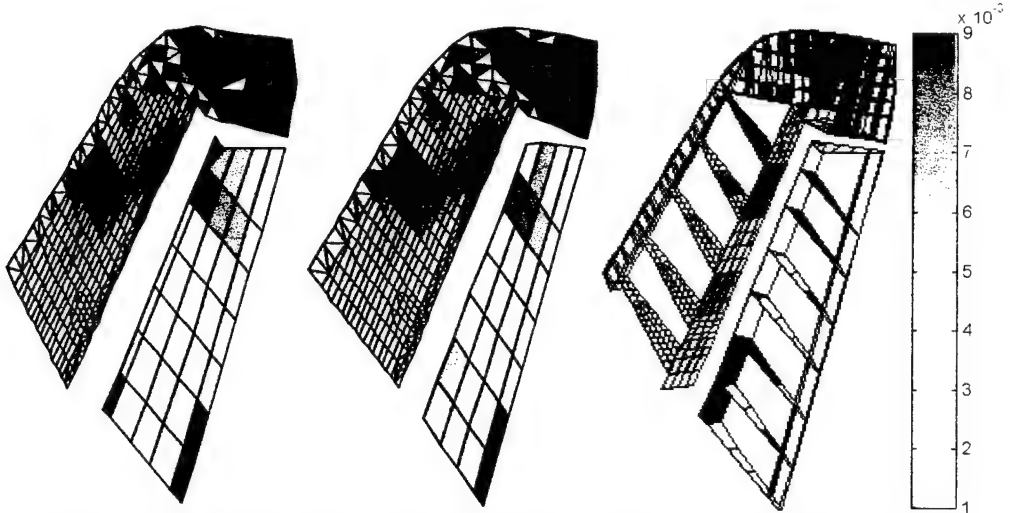


Figure C.9.3 Results by PMF for Case 7b. using Z-function and FEM updated (Detected).

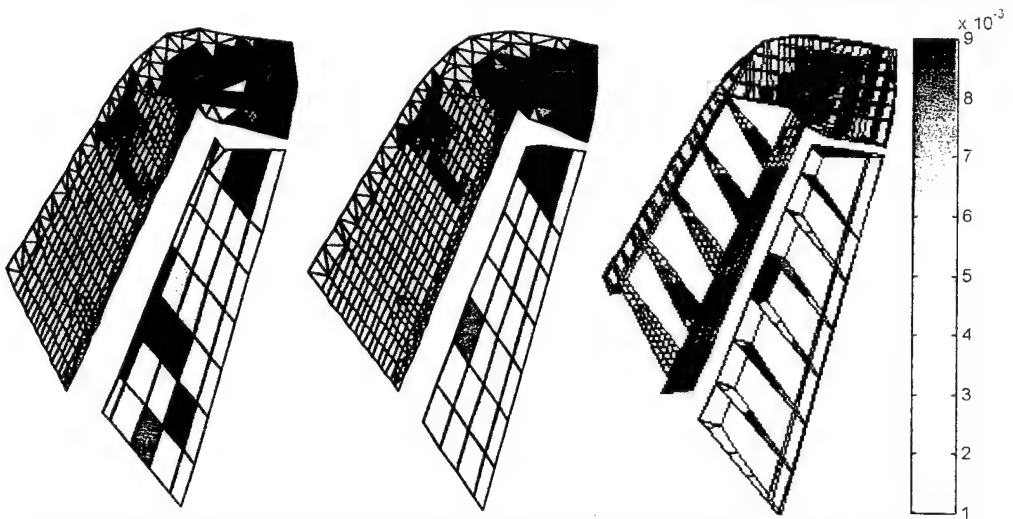


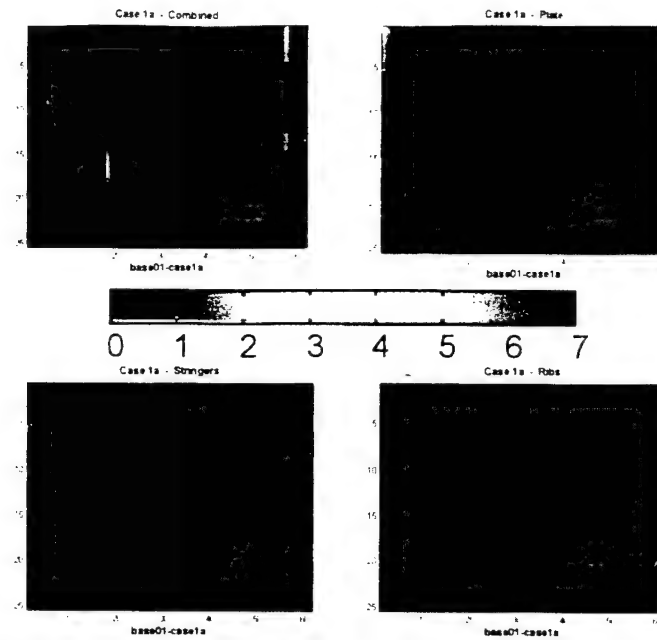
Figure C.9.4 Results by PMF for Case 8f. using Z-function and FEM updated (Detected).





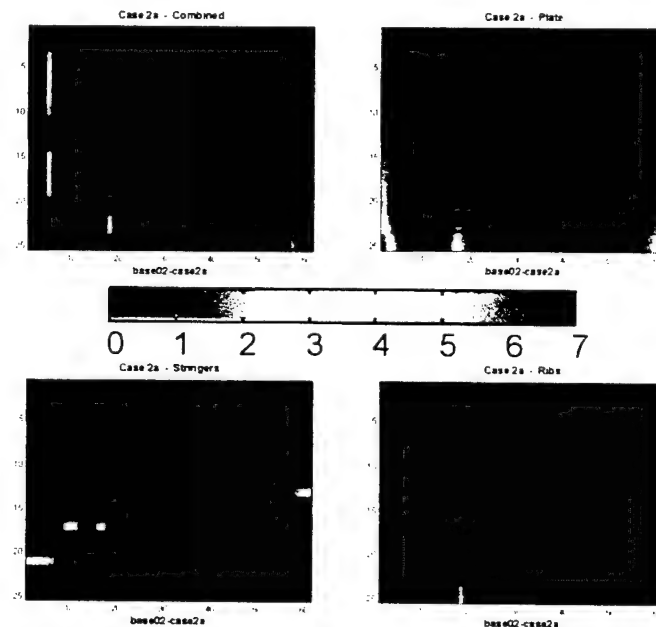
**APPENDIX D**

**DAMAGE PREDICTION MAPS FOR SHELL SPECIMENS**



Baseline	Case	# Mode Pairs from Z-Function Analysis	Damage Type	Damage Coordinates	Strain Energy Content	Component	NFP	Detection
1	1a	0	A1	(48-51,21)	L	Plate	2	N
						Ribs	0	N/A
						Stringers	0	N
						Combined	2	N

**Figure D.1 Damage Map Results for Case 1a with Baseline 1.**



Baseline	Case	# Mode Pairs from Z-Function Analysis	Damage Type	Damage Coordinates	Strain Energy Content	Component	NFP	Detection
2	2a	5	A1	(16-18,17)	M	Plate	3	N
						Ribs	1	N
						Stringers	3	Y
						Combined	3	N

**Figure D.2 Damage Map Results for Case 2a with Baseline 2.**

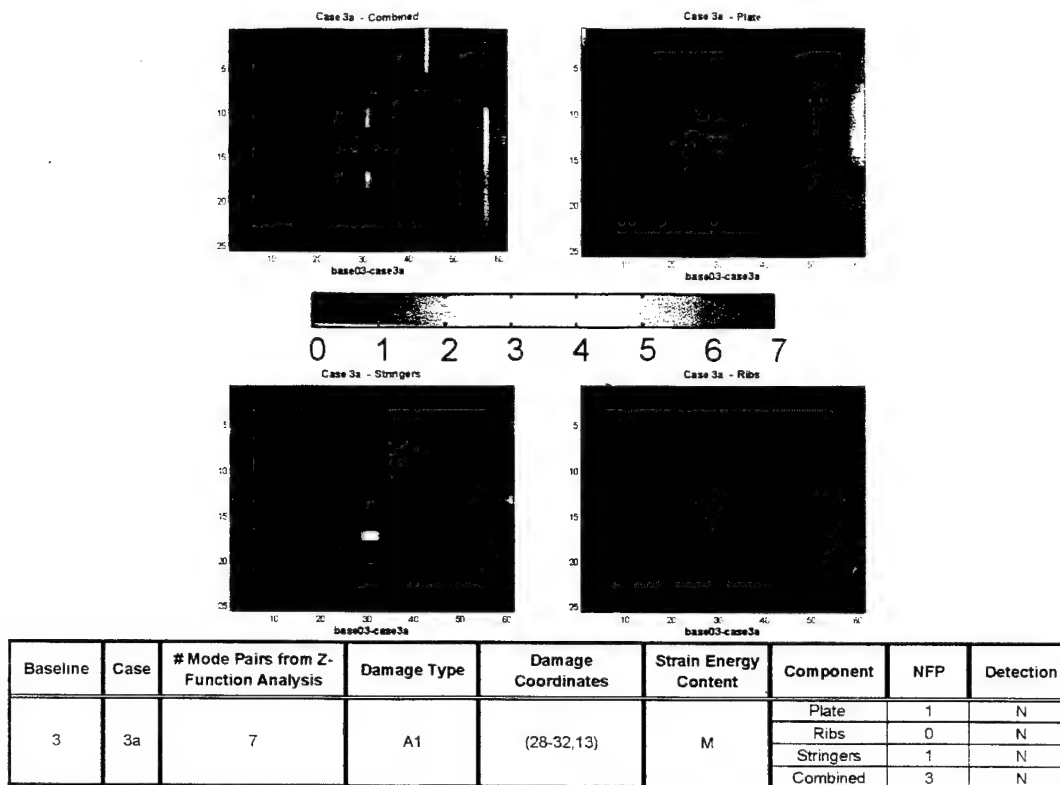


**Figure D.3 Damage Map Results for Case 3a with Baseline 3.**

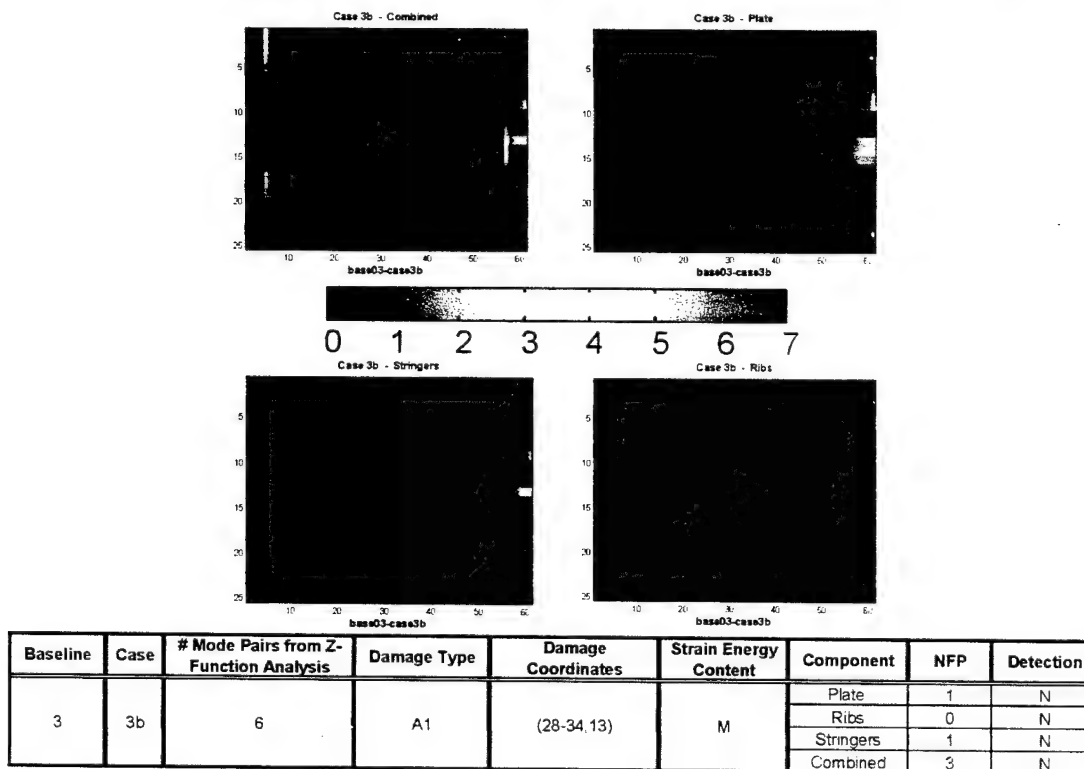


**Figure D.4 Damage Map Results for Case 3b with Baseline 3.**

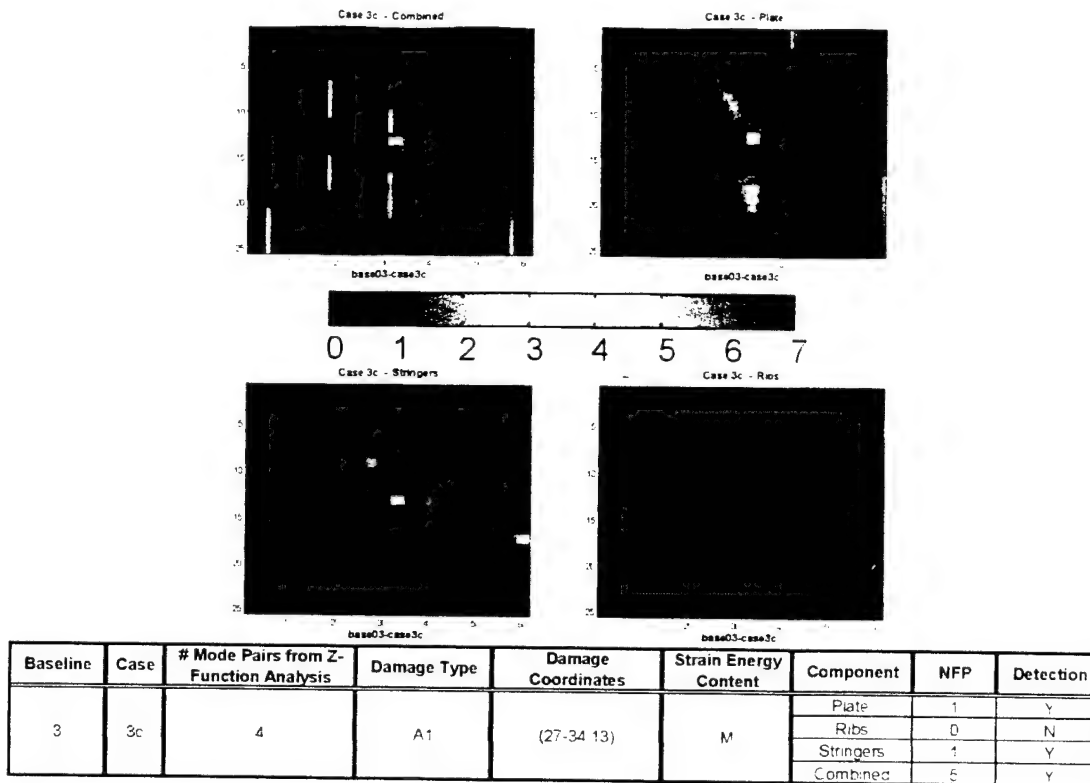


**Figure D.5 Damage Map Results for Case 3c with Baseline 3.**

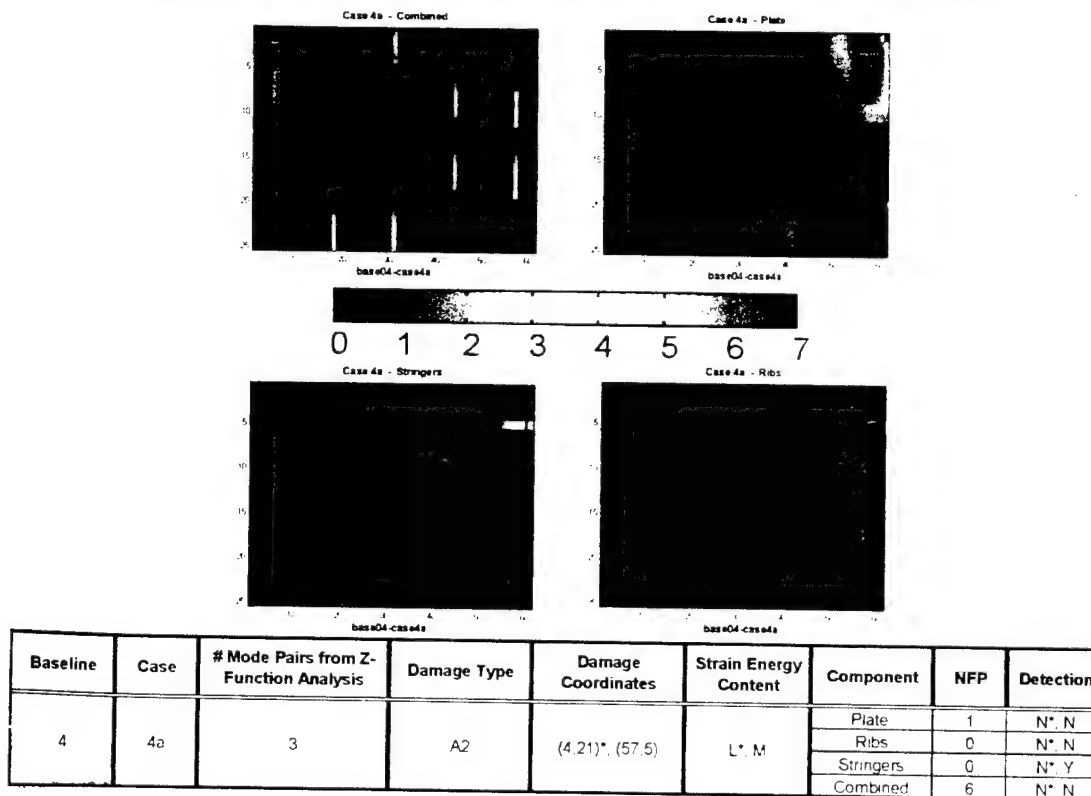


**Figure D.6 Damage Map Results for Case 4a with Baseline 4.**

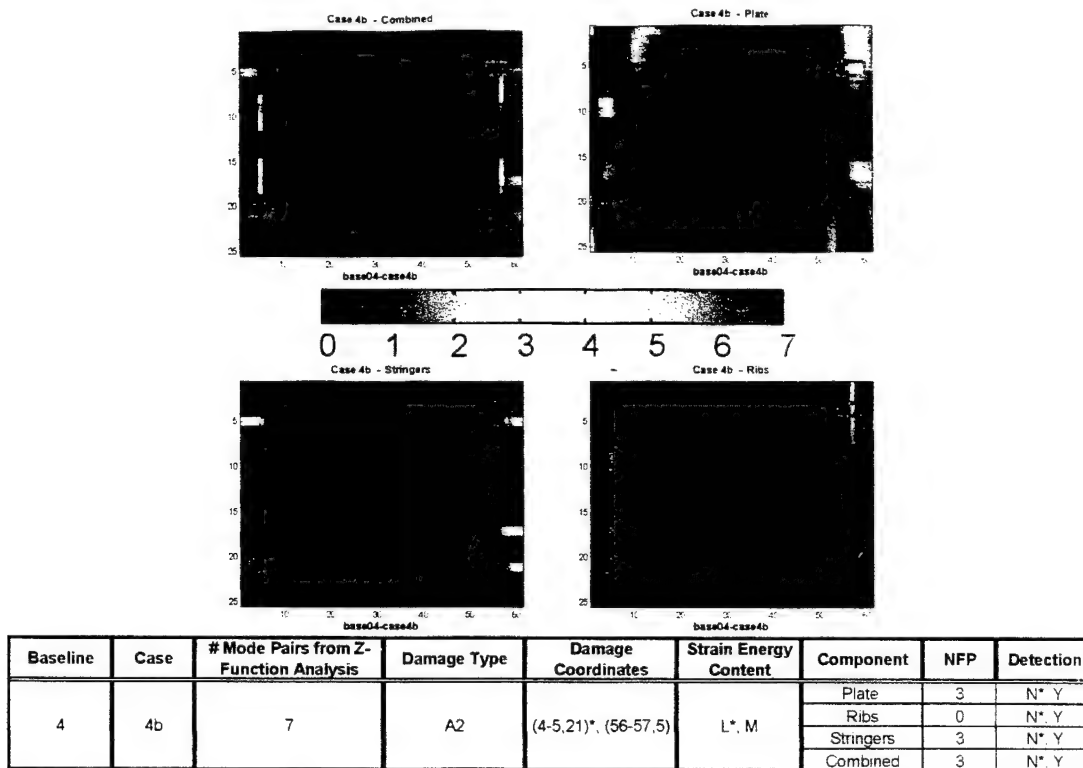


**Figure D.7 Damage Map Results for Case 4b with Baseline 4.**

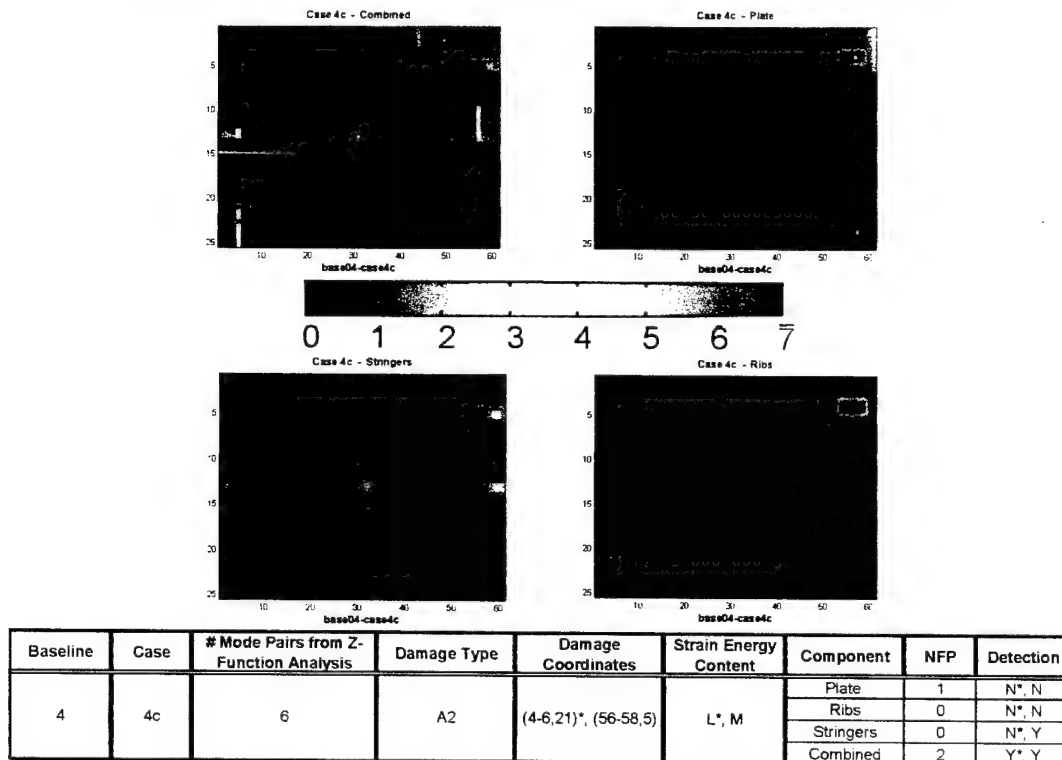


**Figure D.8 Damage Map Results for Case 4c with Baseline 4.**

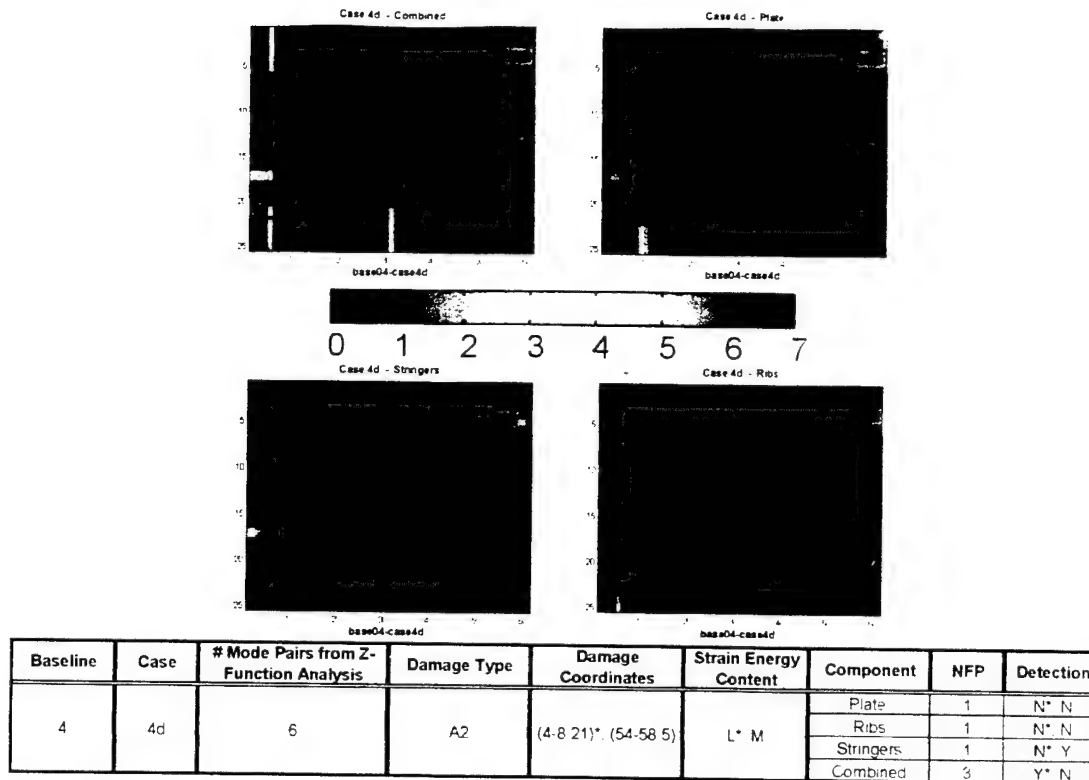


Figure D.9 Damage Map Results for Case 4d with Baseline 4.

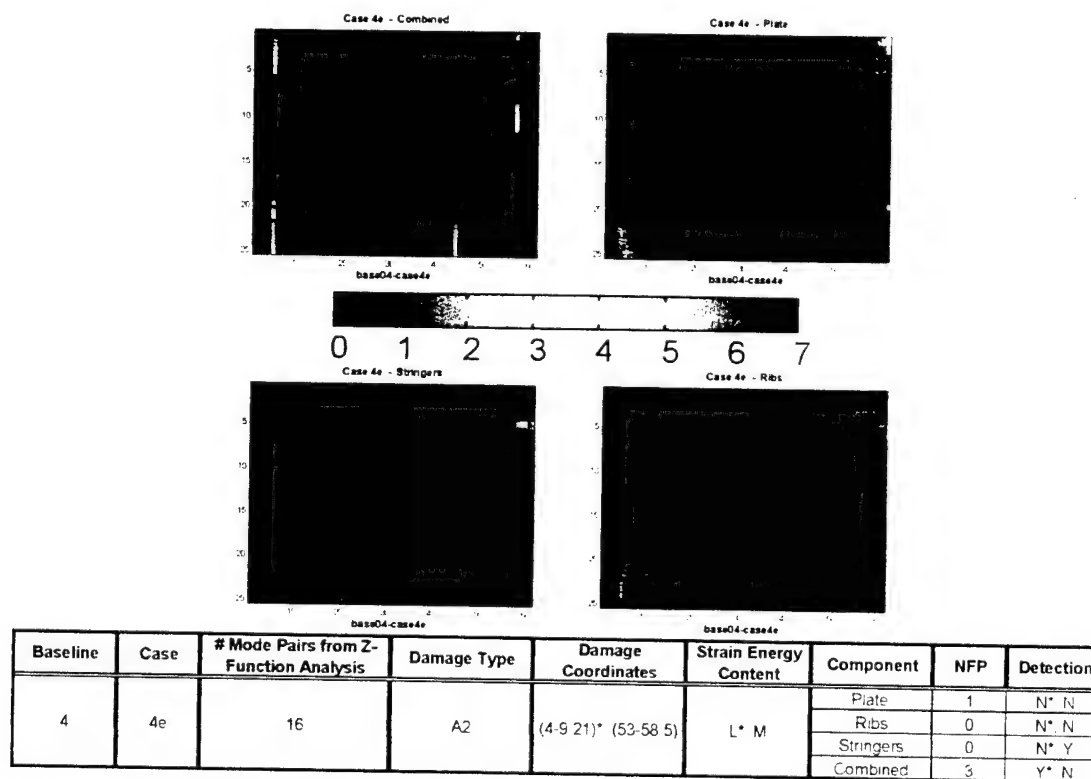
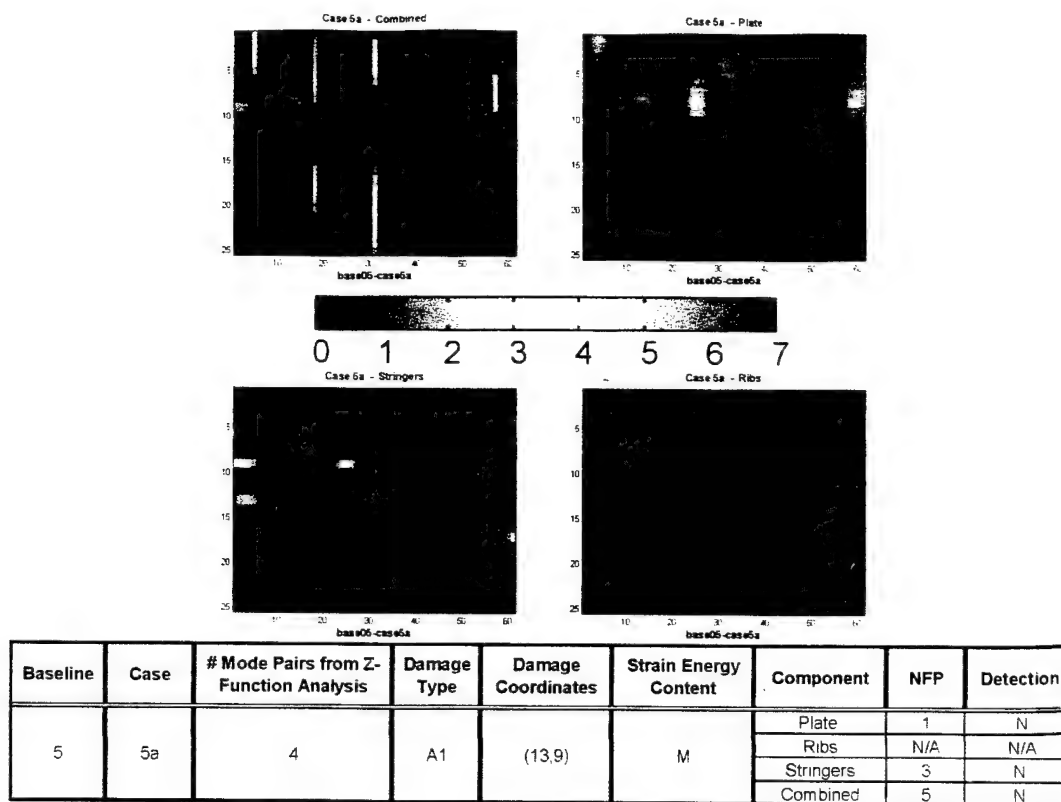
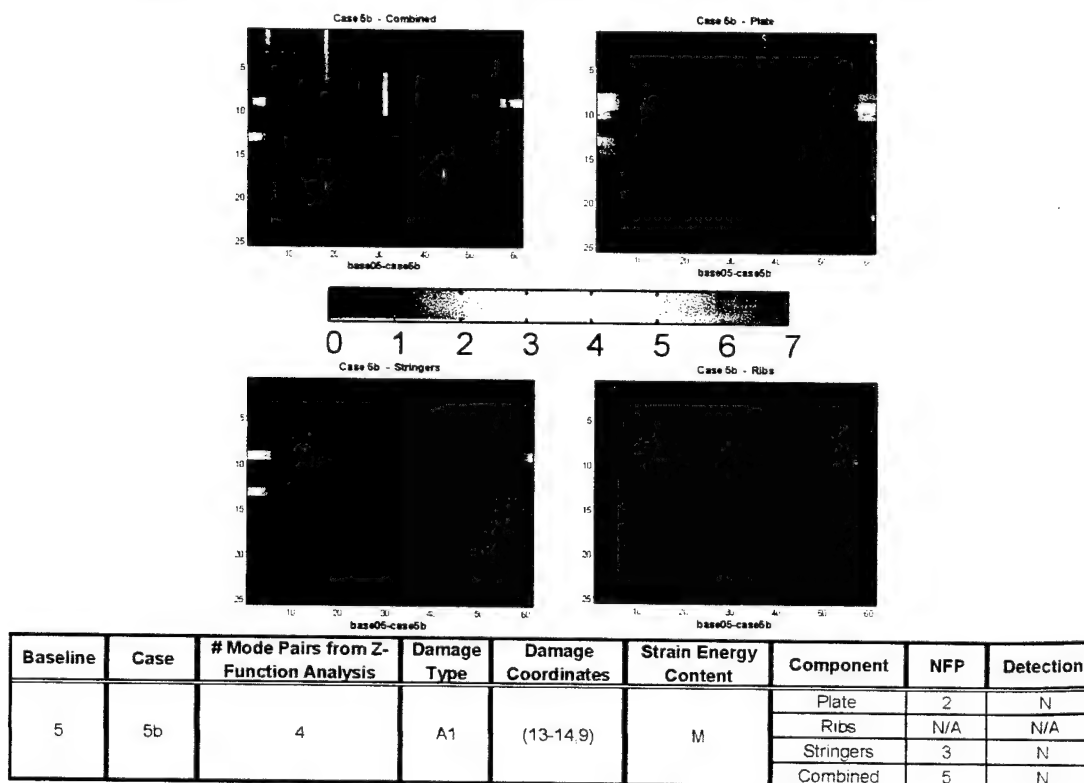


Figure D.10 Damage Map Results for Case 4e with Baseline 4.

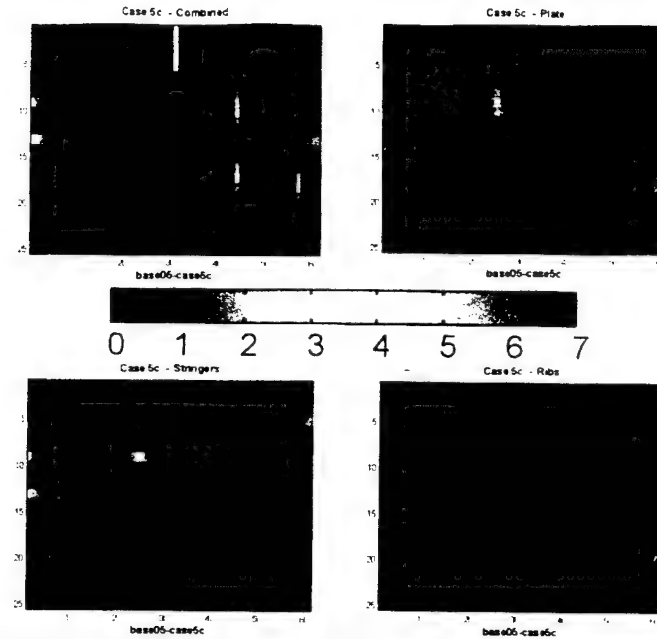


**Figure D.11 Damage Map Results for Case 5a with Baseline 5.**



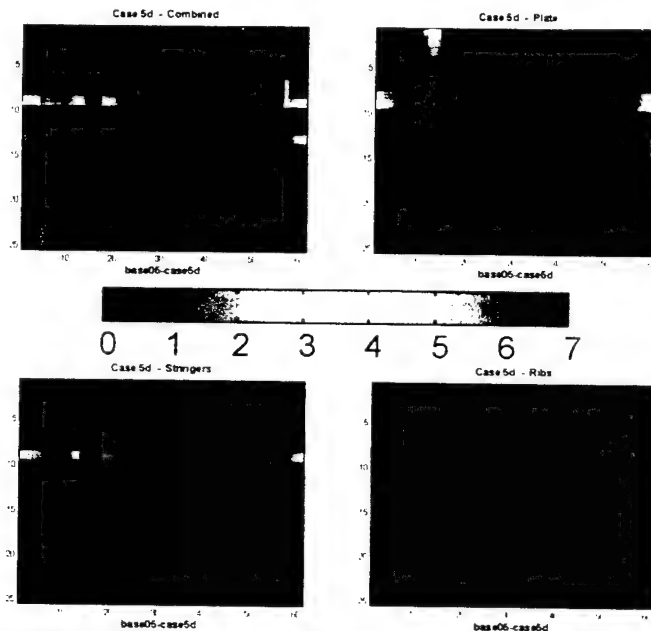
**Figure D.12 Damage Map Results for Case 5b with Baseline 5.**





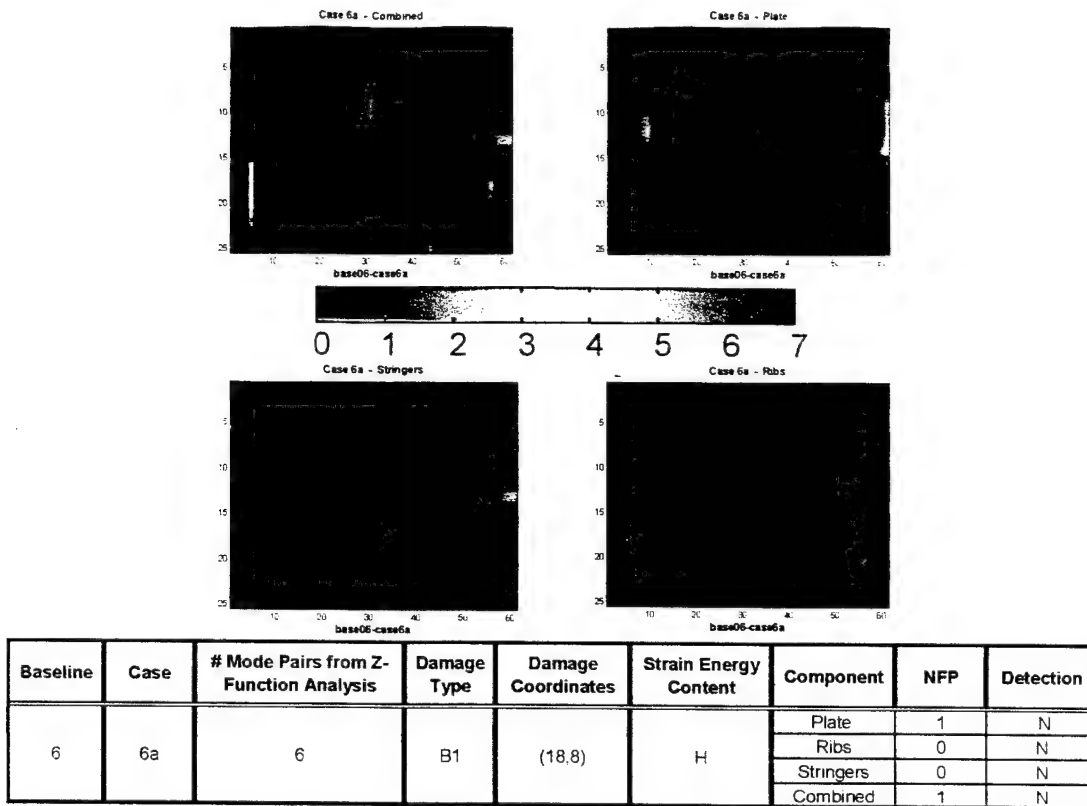
Baseline	Case	# Mode Pairs from Z-Function Analysis	Damage Type	Damage Coordinates	Strain Energy Content	Component	NFP	Detection
5	5c	5	A1	(12-14,9)	M	Plate	0	N
						Ribs	N/A	N/A
						Stringers	3	N
						Combined	6	N

Figure D.13 Damage Map Results for Case 5c with Baseline 5.



Baseline	Case	# Mode Pairs from Z-Function Analysis	Damage Type	Damage Coordinates	Strain Energy Content	Component	NFP	Detection
5	5d	2	A1	(12-16,9)	M	Plate	4	N
						Ribs	N/A	N/A
						Stringers	2	Y
						Combined	4	Y

Figure D.14 Damage Map Results for Case 5d with Baseline 5.



**Figure D.15 Damage Map Results for Case 6a with Baseline D.**

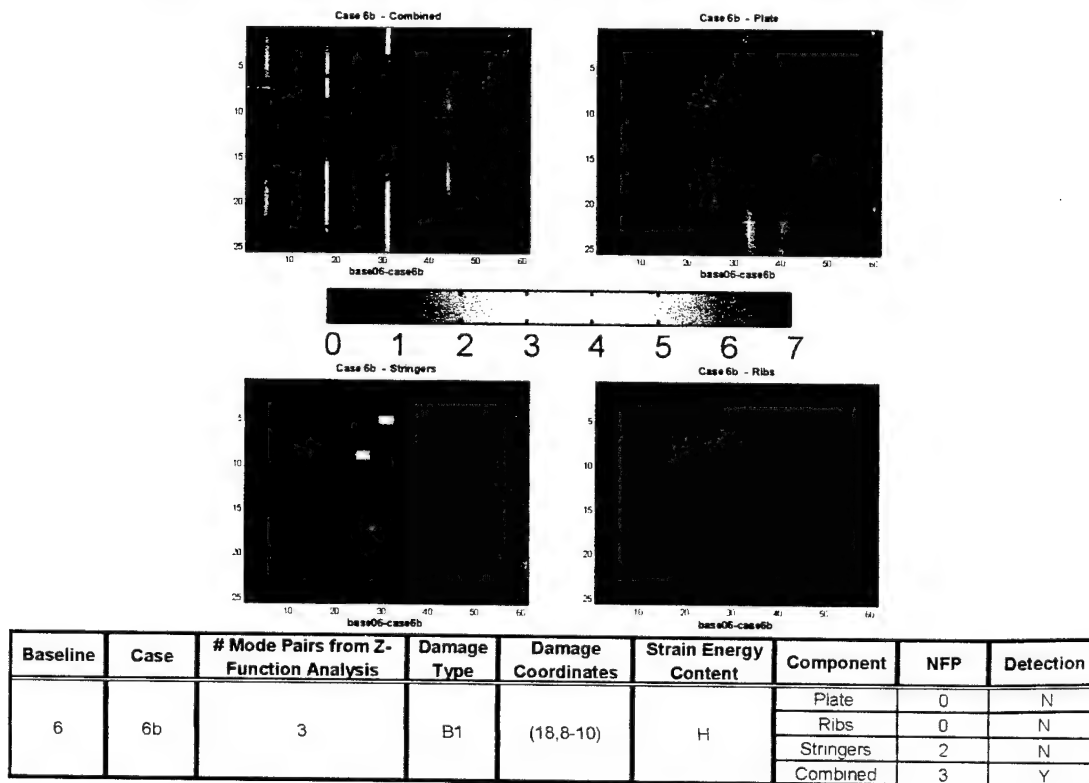


**Figure D.16 Damage Map Results for Case 6b with Baseline D.**

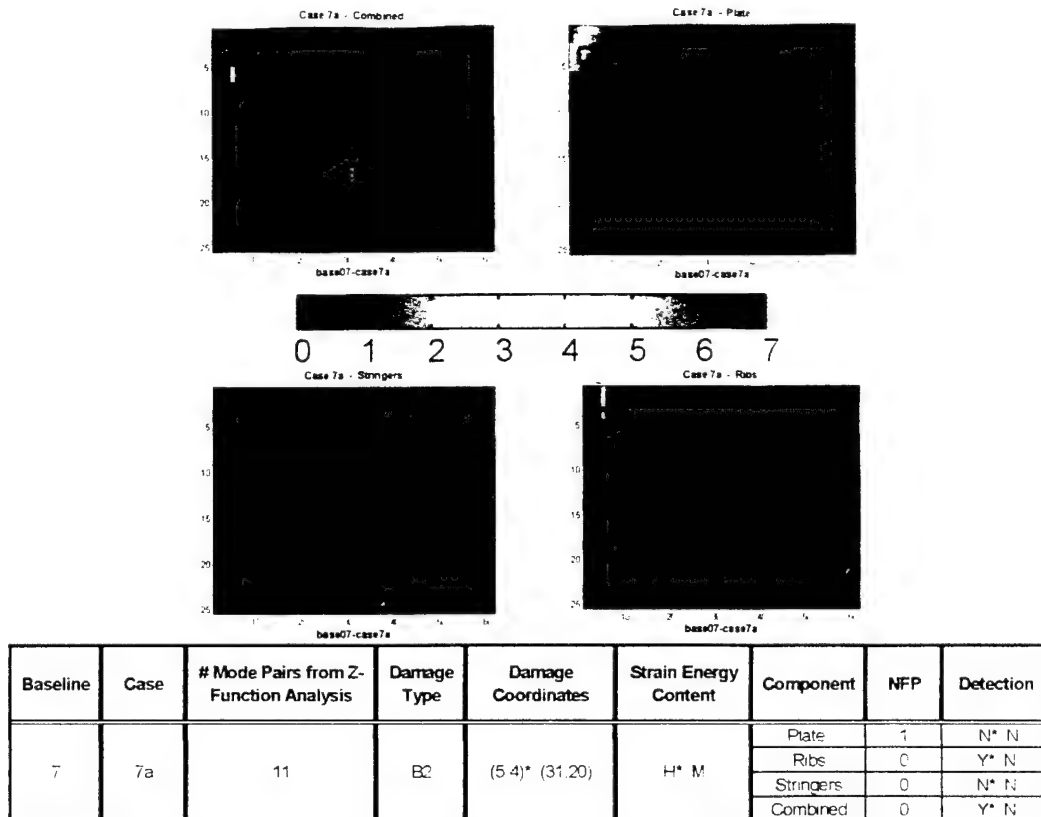


**Figure D.17 Damage Map Results for Case 7a with Baseline 7.**

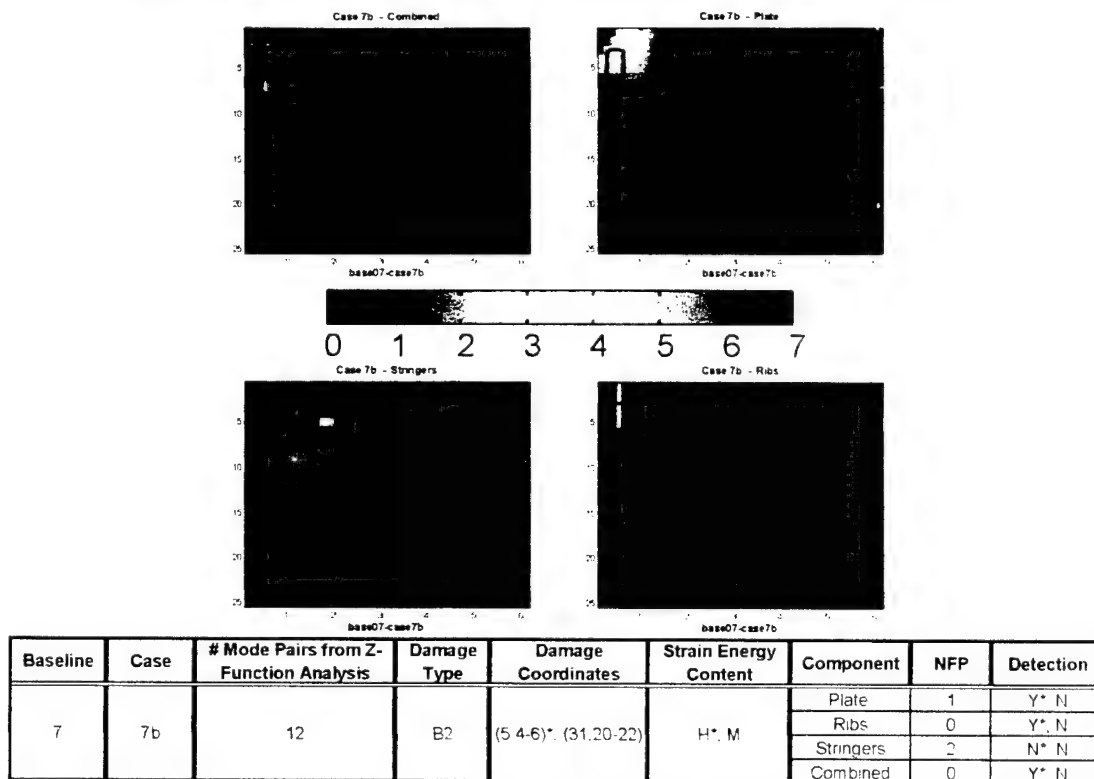


**Figure D.18 Damage Map Results for Case 7b with Baseline 7.**

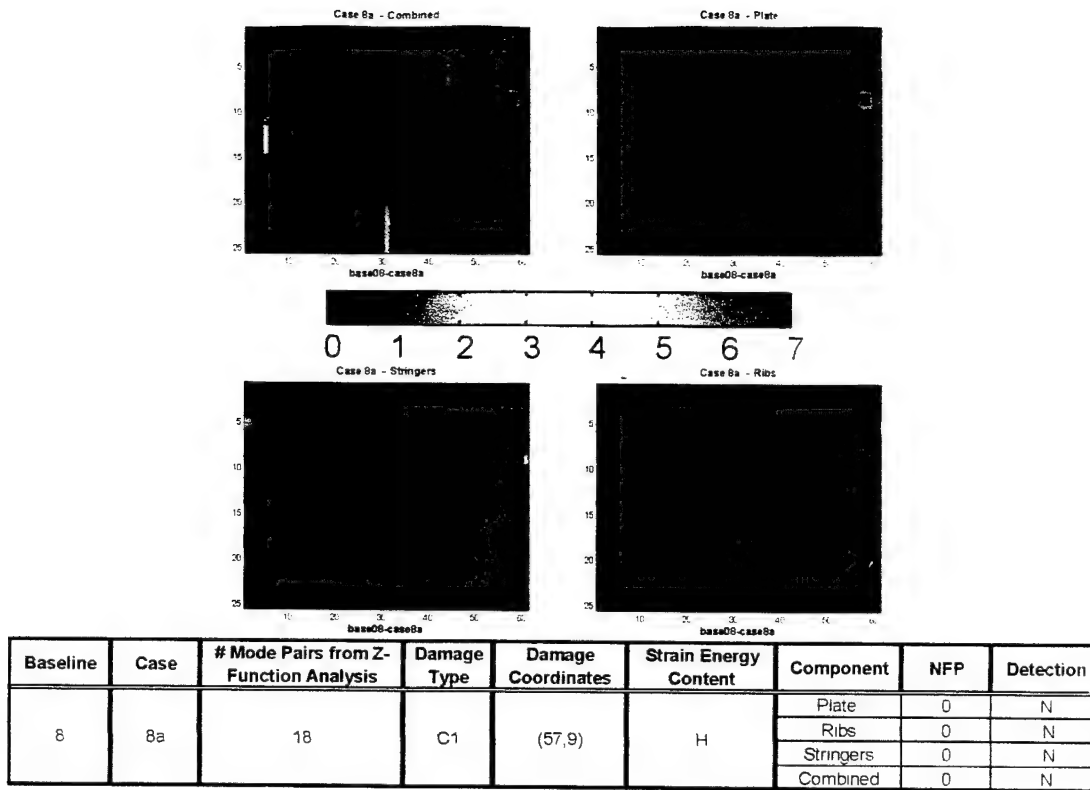


**Figure D.19 Damage Map Results for Case 8a with Baseline 8.**

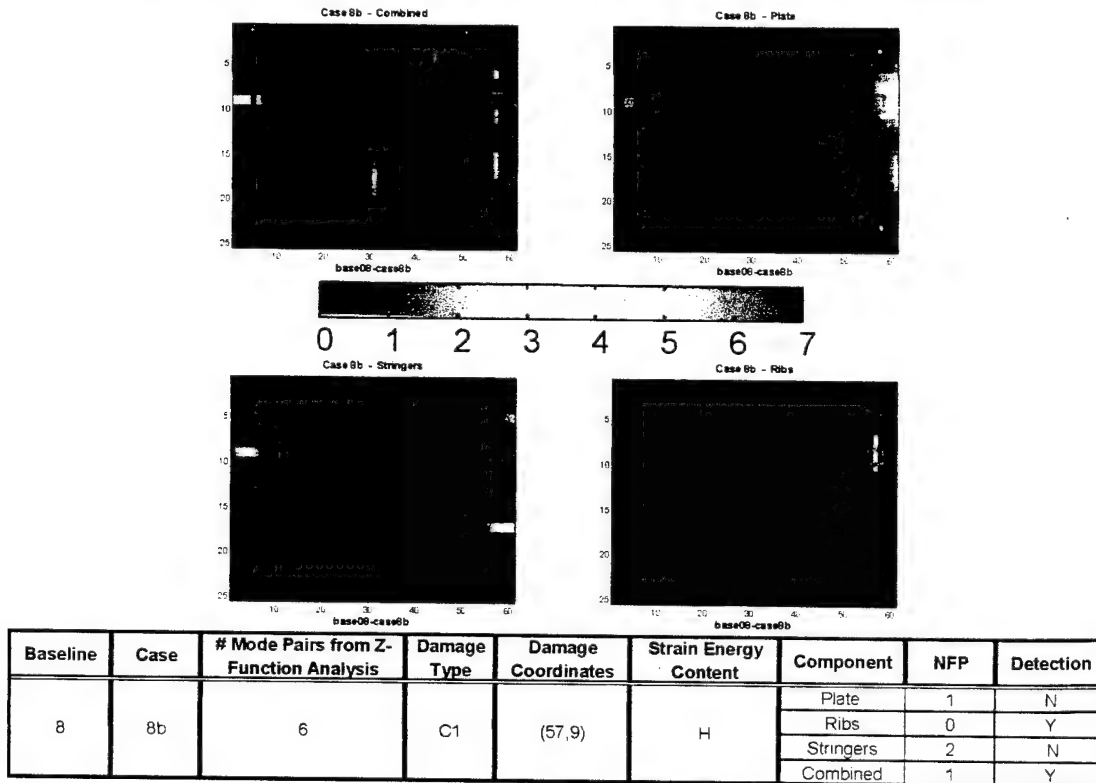


**Figure D.20 Damage Map Results for Case 8b with Baseline 8.**

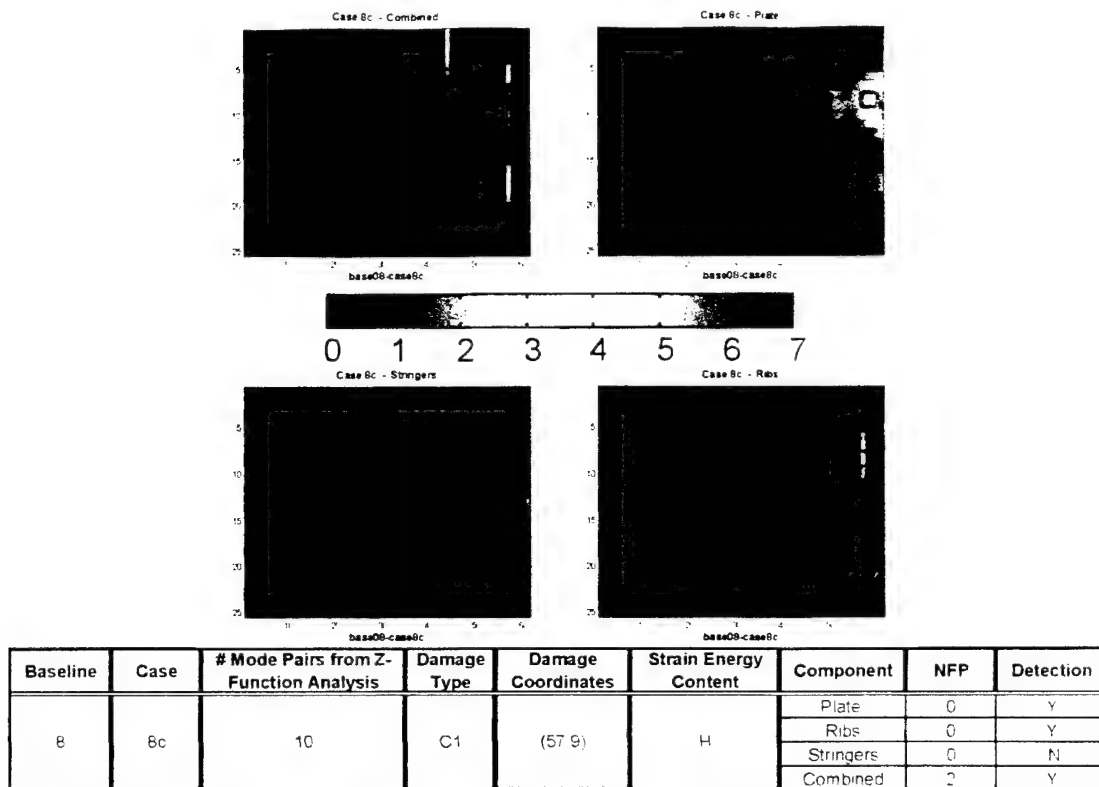


**Figure D.21 Damage Map Results for Case 8c with Baseline 8.**

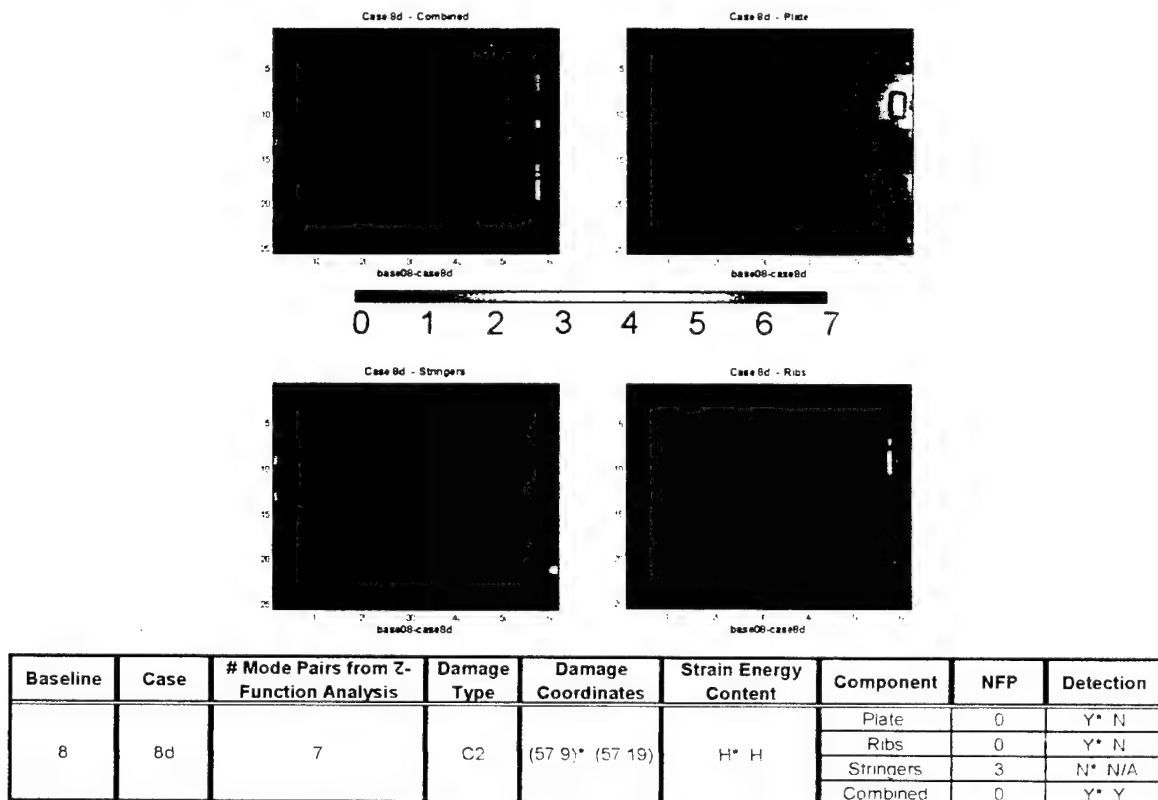


**Figure D.22 Damage Map Results for Case 8d with Baseline 8.**

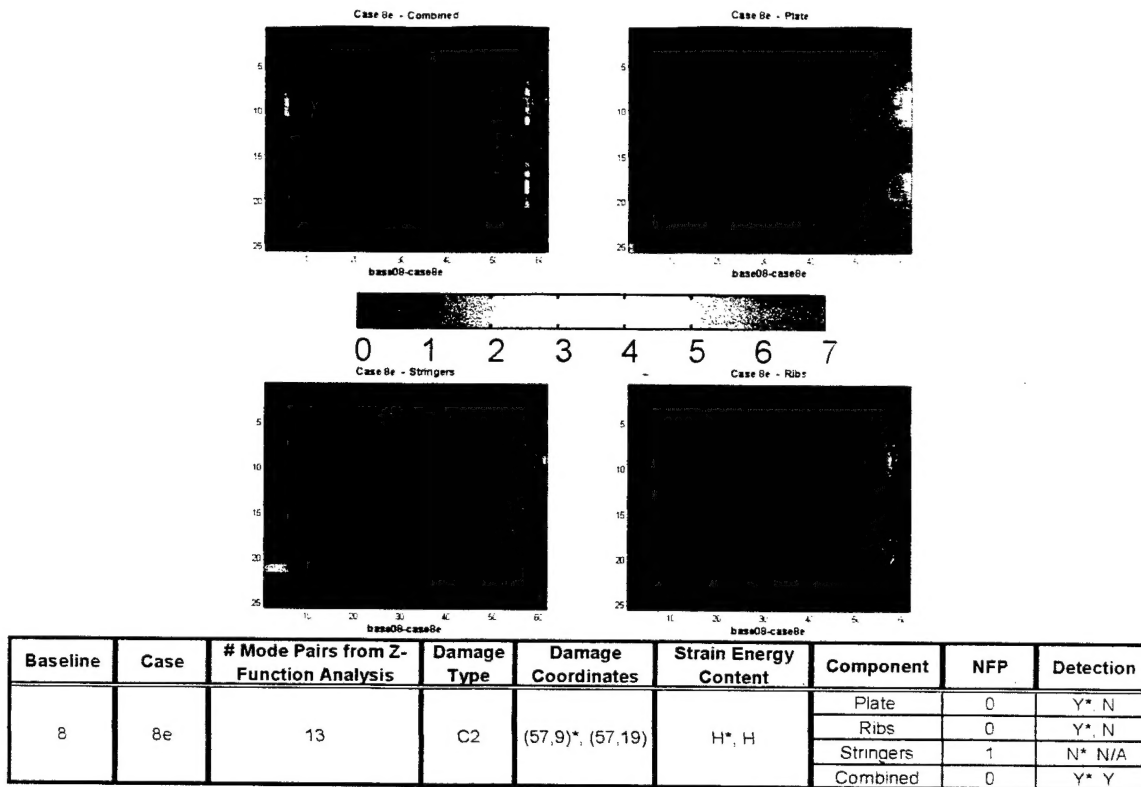


Figure D.23 Damage Map Results for Case 8e with Baseline 8.

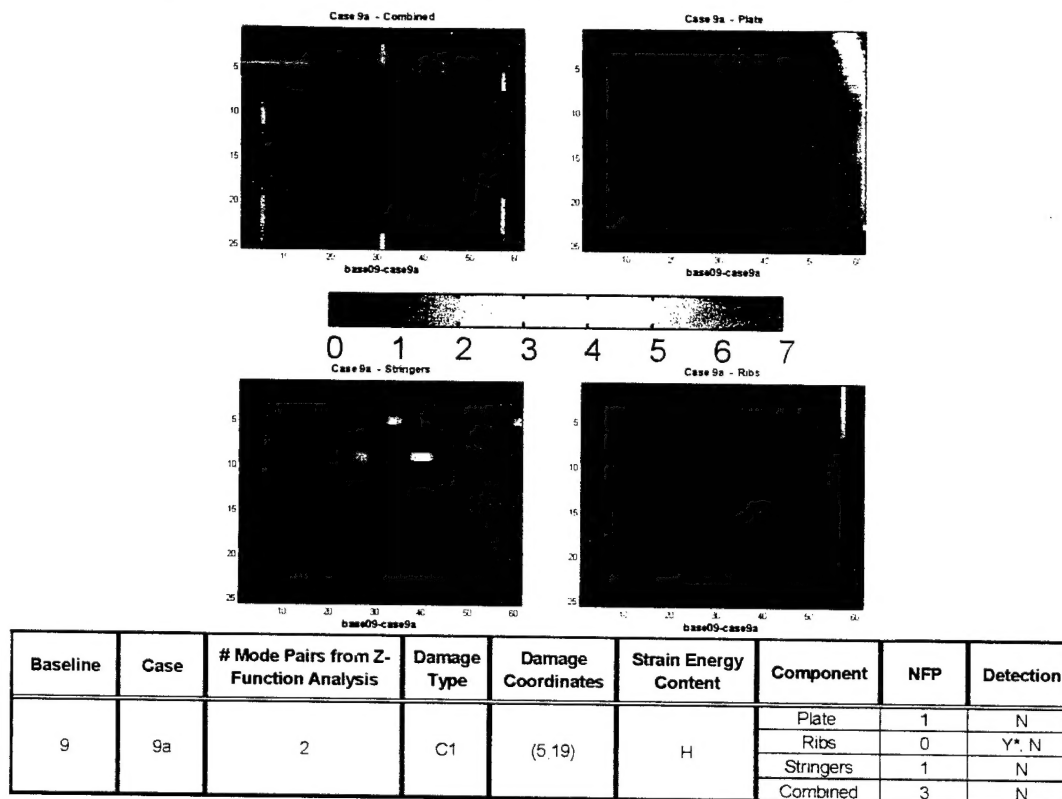
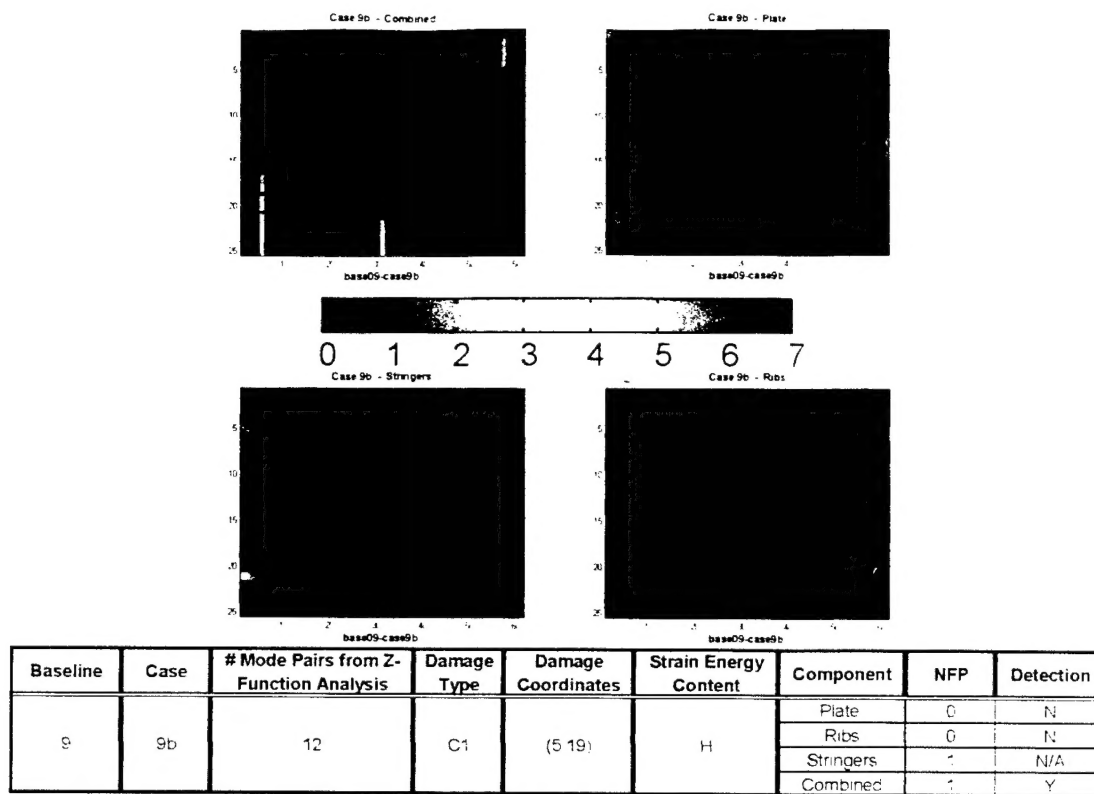
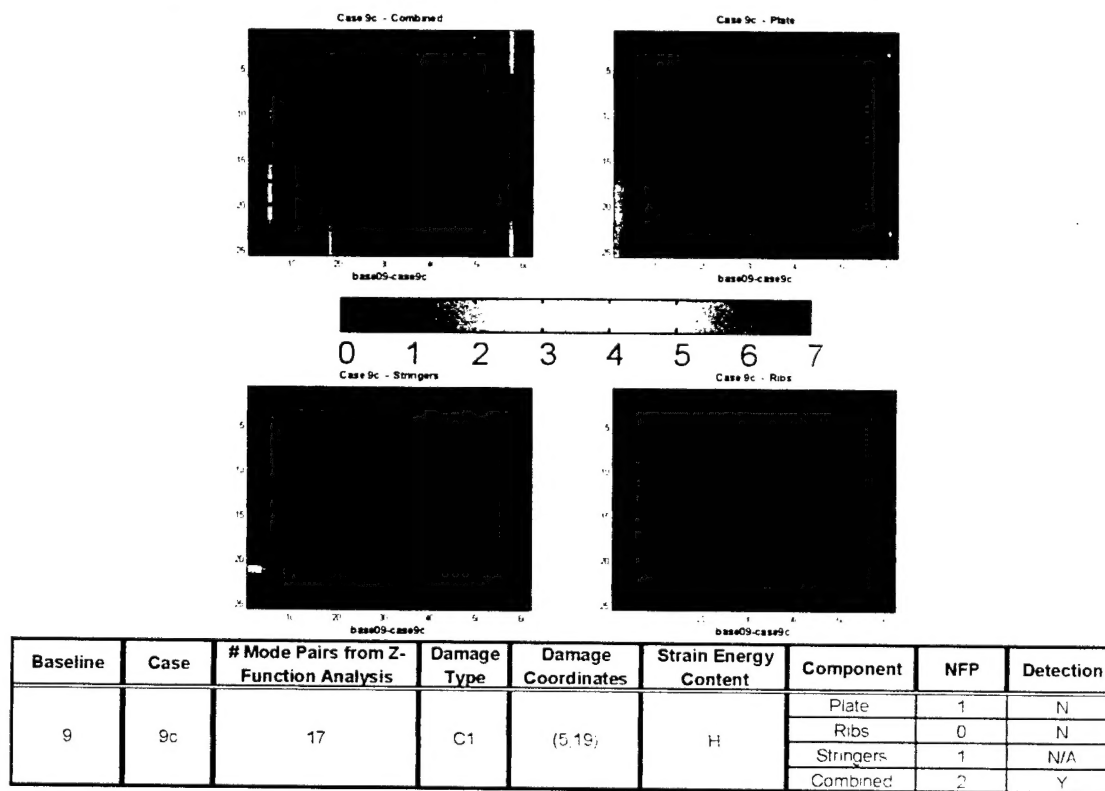


Figure D.24 Damage Map Results for Case 9a with Baseline 9.



**Figure D.25 Damage Map Results for Case 9b with Baseline 9.**



**Figure D.26 Damage Map Results for Case 9c with Baseline 9.**

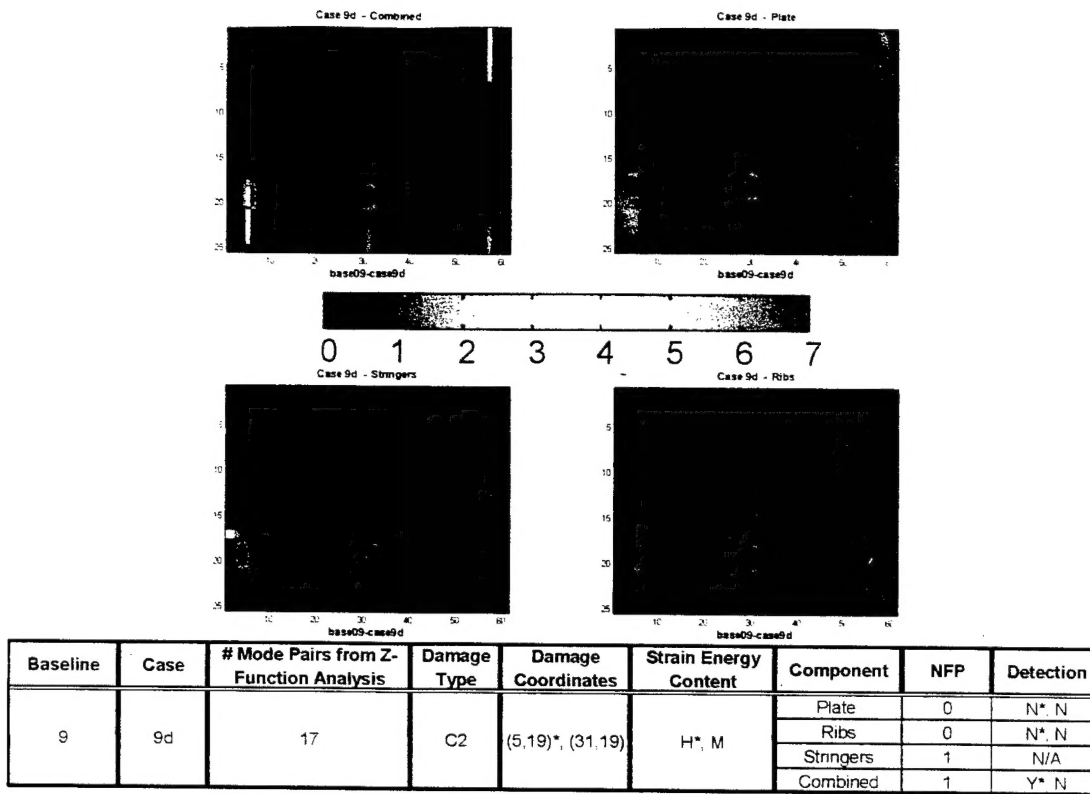


Figure D.27 Damage Map Results for Case 9d with Baseline 9.

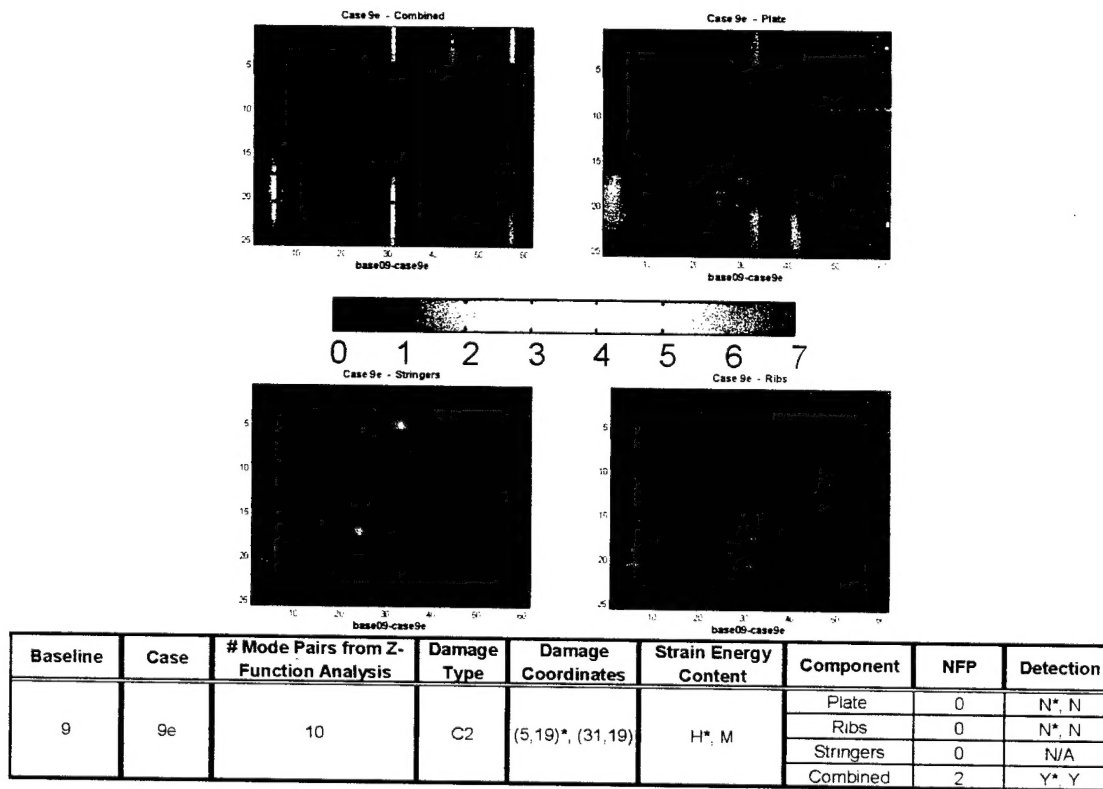


Figure D.28 Damage Map Results for Case 9e with Baseline 9.



